






# A high-fidelity spectral/hp element LES study of Formula 1 front-wing and exposed wheel aerodynamics

by Jean-Eloi William LOMBARD

December 20, 2017

Imperial College London
Department of Aeronautics

This thesis is submitted for the degree of
Doctor of Philosophy of Imperial College London

# Decleration

I declare that all of the work that is contained within this thesis has been undertaken by the author.

# Copyright Decleration

The copyright of this thesis rests with the author and is made available under a Creative Commons Attribution Non-Commercial No Derivatives licence. Researchers are free to copy, distribute or transmit the thesis on the condition that they attribute it, that they do not use it for commercial purposes and that they do not alter, transform or build upon it. For any reuse or redistribution, researchers must make clear to others the licence terms of this work

"There's no sense in going further — it's the edge of cultivation,"
So they said, and I believed it — broke my land and sowed my crop —
Built my barns and strung my fences in the little border station
Tucked away below the foothills where the trails run out and stop.

Till a voice, as bad as Conscience, rang interminable changes
On one everlasting Whisper day and night repeated—so:
"Something hidden. Go and find it. Go and look behind the Ranges—
"Something lost behind the Ranges. Lost and waiting for you. Go!"

So I went, worn out of patience; never told my nearest neighbours —
Stole away with pack and ponies—left 'em drinking in the town;
And the faith that moveth mountains didn't seem to help my labours
As I faced the sheer main-ranges, whipping up and leading down.

March by march I puzzled through 'em, turning flanks and dodging shoulders,
Hurried on in hope of water, headed back for lack of grass;
Till I camped above the tree-line—drifted snow and naked boulders —
Felt free air astir to windward—knew I'd stumbled on the Pass.

'Thought to name it for the finder: but that night the Norther found me—
Froze and killed the plains-bred ponies; so I called the camp Despair
(It's the Railway Gap to-day, though). Then my Whisper waked to hound me:—
"Something lost behind the Ranges. Over yonder! Go you there!"

Then I knew, the while I doubted—knew His Hand was certain o?er me.
Still—it might be self-delusion—scores of better men had died—
I could reach the township living, but ... He knows what terror tore me ...
But I didn?t ... but I didn?t. I went down the other side,

Till the snow ran out in flowers, and the flowers turned to aloes,
And the aloes sprung to thickets and a brimming stream ran by;
But the thickets dwined to thorn-scrub, and the water drained to shallows,
And I dropped again on desert—blasted earth, and blasting sky...

I remember lighting fires; I remember sitting by ?em;
I remember seeing faces, hearing voices, through the smoke;

I remember they were fancy—for I threw a stone to try 'em.
"Something lost behind the Ranges" was the only word they spoke.

I remember going crazy. I remember that I knew it
When I heard myself hallooing to the funny folk I saw.
'Very full of dreams that desert, but my two legs took me through it ...
And I used to watch ?em moving with the toes all black and raw.

But at last the country altered—White Man's country past disputing—
Rolling grass and open timber, with a hint of hills behind—
There I found me food and water, and I lay a week recruiting.
Got my strength and lost my nightmares. Then I entered on my find.

'Thence I ran my first rough survey—chose my trees and blazed and ringed 'em—
Week by week I pried and sampled—week by week my findings grew.
Saul he went to look for donkeys, and by God he found a kingdom!
But by God, who sent His Whisper, I had struck the worth of two!

Up along the hostile mountains, where the hair-poised snowslide shivers—
Down and through the big fat marshes that the virgin ore-bed stains,
Till I heard the mile-wide mutterings of unimagined rivers,
And beyond the nameless timber saw illimitable plains!

'Plotted sites of future cities, traced the easy grades between 'em;
Watched unharnessed rapids wasting fifty thousand head an hour;
Counted leagues of water-frontage through the axe-ripe woods that screen 'em—
Saw the plant to feed a people—up and waiting for the power!

Well I know who?ll take the credit—all the clever chaps that followed—
Came, a dozen men together—never knew my desert-fears;
Tracked me by the camps I'd quitted, used the water-holes I'd hollowed.
They?ll go back and do the talking. They'll be called the Pioneers!

They will find my sites of townships—not the cities that I set there.
They will rediscover rivers—not my rivers heard at night.
By my own old marks and bearings they will show me how to get there,

By the lonely cairns I builded they will guide my feet aright.

Have I named one single river? Have I claimed one single acre?
Have I kept one single nugget—(barring samples)? No, not I!
Because my price was paid me ten times over by my Maker.
But you wouldn?t understand it. You go up and occupy.

Ores you'll find there; wood and cattle; water-transit sure and steady
(That should keep the railway rates down), coal and iron at your doors.
God took care to hide that country till He judged His people ready,
Then He chose me for His Whisper, and I've found it, and it?s yours!

Yes, your "Never-never country"—yes, your "edge of cultivation"
And "no sense in going further"—till I crossed the range to see.
God forgive me! No, I didn't. It's God's present to our nation.
Anybody might have found it but—His Whisper came to Me!

Rudyard Kipling, The Explorer (1898)

# Abstract

Computational fluid dynamics is the test bed, for in-silico experiments, before a part is first built however the state-of-the-art relies on low-order Reynolds averaged Navier-Stokes (RANS) or Detached Eddy Simulations (DES) and their turbulence models that require fine tuning of many parameters. They are ill-suited for tackling the complex interaction between the wake of a Formula One front wing and the highly unsteady bluff-body wake of the rolling wheel. This thesis describes the effort made towards assessing the spectral/hp element LES as an alternative method for better for informing the process of the aerodynamicists.

Results from the computation of the flow on a rounded wingtip give further insight into the complexity of the flow revealing numerous vortical structures merging into a trailing vortex. A direct numerical simulation of the unsteady wake of an idealised rolling wheel at $Re_D = 1000$ reveals the flow structures associated to the shedding at the top of the wheel, the symmetry breaking as well as the meandering of the jetting-vortices adding to our fundamental understanding of the wheel wake. In particular the DNS allows for a thorough survey of the wake structures in the immediate wake, less than half a diameter, both the jetting vortices and the shedding at the top of the wheel occur but experiments struggle to instrument. Finally preliminary results for the computation of the flow about the front-section of the MP4-17D are reported and compared to experimental results as well as state-of-the-art RANS computation.

The CAD geometries, the mesh and initial conditions as well as the exact code used to run them are made openly available for each of the cases reported in this thesis for the fluids community to continue building on these results.

# Acknowledgements

I would like to thank Professor Sherwin, Dr. Taylor for sharing their drive during this ambitious project. I would like to thank Dr. Hoëssler for his invaluable insight, unwavering moral support through sometimes challenging times.

This manuscript would not be what it is without the constructive criticism of my assessors. The aeronautical community thrives thanks to leaders such as Professor Bearman and Professor Sims-Williams. Thank you.

I would like to thank professors Pénélope Leyland, Peter Schmid, Aimee Morgans, Francois Gallaire, Per Olof Person, ZJ Wang, as well as doctors Xu, Pegrum, MacCarthy for their support, encouragement and the fascinating discussions we had.

I would like to thank the McLaren Aero team and in particular the CFD Technology team. Adam, Athanasios, Francesco, Giampaolo, Petros, Robin, Simone and Guillaume, it has been a pleasure learning from you and stealing your queues on ICE3.

I would like to thank the friends I made at Imperial college Hui, Dani, Lisa, Jo, Curtis, Lionel, Laurent, Bastien, Dirk, Thibeault, Justin, Olga and Simon for reminding me that even if we spend most our time perplexed by the complexities of our research there are still people that think the earth is flat.

I would like to thank my friends Ulugbek, Javier, Greg, Artour, Anne, Daniele, Christophe, Alex, Fred, Astrid, Karine, Celine, Tif for their encouragement and astute suggestions.

I would like to thank my sponsors, McLaren, the Royal Aeronautical Society, the Aeronautics Department at Imperial college and my family, not necessarily in order of contribution.

I would also like to thank Bernie for refusing to fund my racing years through the feeder series towards Formula One but instead suggested I contribute to the sport as an engineer.

I would like to give a special thanks to my brother and my family including Laura Gabrielli and Jessica.

Finally I would like to thank Patrizia Gabrielli who, through her love, relentlessly supported me during these beautiful but sometimes challenging London years.

To Colette & Günther Ruch,
Paulette Pasche & Prof. William A. Blanc,
Christina Holder & Pr Robert P. Lombard,
Jessica & Laura Gabrielli,
dad, mum and titi and,
To Patrizia Gabrielli.

# Contents


**1 Introduction** **1**

1.1 Key aerodynamic developments and today's open challenges . . . . . 2

1.1.1 From streamlined to winged cars . . . . . 3

1.1.2 Front-wing aerodynamics . . . . . 5

1.1.3 The challenge posed by open rotating wheels : main contribution to drag. . . . . 10

1.1.4 Summary of aerodynamics main challenges . . . . . 15

1.2 State of the art of F1 aero design and limitations . . . . . 16

1.2.1 Track testing . . . . . 17

1.2.2 From aeronautical to automotive wind-tunnels . . . . . 19

1.2.3 Applications of CFD: from shock capturing to sub-grid scale modelling to informing F1 aerodynamicists. . . . . 21

1.3 How might high-fidelity CFD contribute to F1 aerodynamics? . . . . . 24

1.3.1 Representing and meshing complex geometries . . . . . 25

1.3.2 Low dispersion/dissipation and fast convergence . . . . . 27

1.3.3 Under-resolved DNS, implicit LES or no-model LES . . . . . 28

1.3.4 Numerical efficiency ready for next-generation exa-scale facilities . . 29

1.3.5 Post-processing . . . . . 29

1.4 Main Contributions . . . . . 30

1.5 Thesis outline . . . . . 31

**2 Fundamental** **33**

2.1 Conservation of mass and the Navier-Stokes equations . . . . . 33

2.1.1 Non-dimensionalisation . . . . . 34

2.2 Spatial discretisation : the spectral/*hp* element method . . . . . 35

2.2.1 Spectral/hp element discretisation . . . . . 35

2.2.2 Fourier-Spectral/hp element discretisation . . . . . 38

2.2.3 Three reasons that make the spectral/hp element method attractive for next-generation exa-scale facilities . . . . . 38

2.2.4 Summary of the spacial discretisation method and its benefits . . . 42
2.3 Temporal discretisation . . . 43
2.4 Boundary conditions . . . 44
2.5 A note on the sources of error . . . 45
2.6 Key recent and ongoing developements . . . 46

**3 From DNS to LES** **49**
3.1 Low dispersion/diffusion error of the spectral/hp element method . . . 50
3.1.1 Low dispersion/diffusion error . . . 50
3.1.2 Isentropic vortex advection : comparison between high- and low-order codes . . . 52
3.1.3 Burgers turbulence : high resolving power . . . 53
3.2 High-order meshing of complex geometries . . . 56
3.2.1 How to prepare a geometry . . . 56
3.2.2 Low-to-high order meshing : spherigons and prism splitting . . . 57
3.2.3 Direct high-order meshing : NekMesh . . . 58
3.3 De-aliasing : maximising the potential of the method . . . 60
3.4 Spectral Vanishing Viscosity (SVV) . . . 62
3.5 Summary of Chapter 3 . . . 65

**4 Wing-tip vortex** **67**
4.1 Introduction . . . 67
4.2 Literature review . . . 70
4.3 Computational Methodology . . . 74
4.3.1 Nektar++: a high-order spectral/*hp* element framework . . . 74
4.3.2 From DNS to SVV-iLES: filtering with Spectral Vanishing Viscosity 75
4.3.3 Geometry and mesh generation . . . 78
4.3.4 Initial and boundary conditions . . . 81
4.3.5 Temporal evolution . . . 83
4.4 Results and Discussion . . . 83
4.4.1 Wing Surface . . . 86
4.4.2 Propagation of the vortex core in the near-wake . . . 87
4.5 Conclusion . . . 92
4.6 Outlook . . . 93

**5 Rolling Wheel** **95**
5.1 State of the art . . . 96
5.2 Case definition and numerical setup methodology . . . 108

5.2.1 Numerical formulation and validation . . . 110
5.3 Dynamics of the Rolling Wheel Wake based on DNS . . . 111
5.3.1 Time-averaged flow field . . . 112
5.3.2 Time-averaged force coefficients . . . 112
5.3.3 Power Spectral Density of the Force Coefficients . . . 113
5.3.4 Dynamic mode decomposition of the near-wake . . . 115
5.4 Conclusion and Outlook . . . 120

**6 McLaren MP4-17D Front-Section** **121**
6.1 Motivation . . . 121
6.2 Near field wake of the MP4-17D front-wing . . . 122
6.2.1 Instantaneous flow field . . . 123
6.2.2 Near-wake survey . . . 124
6.2.3 Summary and outlook . . . 125
6.3 MP4-17D isolated wheel. . . . 125
6.3.1 Comparison of streamwise velocity profile in z-planes above the moving road . . . 126
6.3.2 Total pressure wake survey. . . . 127
6.3.3 Summary of the isolated wheel of the MP4-17D . . . 127
6.4 MP4-17D front section. . . . 137
6.4.1 Vorticity field . . . 138
6.5 Chapter conclusion and outlook . . . 138

**7 Conclusion and Outlook** **141**

# Chapter 1

# Introduction

This research presented in this thesis is motivated by a vision to improve the state-of-the-art CFD for Formula One design based on the capability to :

1. incorporate a higher level of physical based modelling,
2. effectively deploy on peta-scale, and future exa-scale, HPC resources and,
3. to be suited to both academic environments and early stage production in industry.

This vision, shared between the Sherwin Lab and McLaren Racing equally aims to fuse dynamic data from next generation high-fidelity CFD together with wind-tunnel and track. Two challenges are identified as areas where current state-of-the-art CFD methods employed in F1 industry could benefit from further insight : the formation of a wing-tip vortex and the unsteady detached wake of the rolling wheel. More importantly, the greatest challenge is the high-fidelity modelling using high-order spectral/$hp$[1] element wall resolved LES simulation, of the interaction between wing-tip vortices and rolling wheels of the front-section of the McLaren MP4-17D. This challenge is chosen as an embodiment of the overall technical ambition because it requires improvements in meshing and post-processing together with improved efficiency in leveraging current peta- and future exa-scale HPC infrastructures.

In what follows, the evolution of aerodynamic influence in Formula One, from the first wings to 1999 McLaren MP4-17D, is presented together with the tools that have supported these developments emphasising the gap between requirements for further improving aerodynamic efficiency of a Formula One and available tools. An argument is then made for spectral/hp element based high-fidelity CFD to fill this gap and enable Formula One engineers to further improve aerodynamic efficiency of their cars.

[1] "hp" refers to the ability of increasing resolution by decreasing the mesh size "h" or increasing the polynomial expansion "p" within a given element.

## 1.1 Key aerodynamic developments and today's open challenges

Aerodynamics has always been a key performance differentiator in Formula One. Until the 1960's the aim was to streamline the body of the car under the constraints of the regulations but also of the thermal management of the engine. From the 1968 season onwards, aerodynamics principles were also employed for downforce generation, or negative lift, with the appearance of wings (1968) and then downforce promoting underbodies, usually referred to as *ground force* cars. Considering the flow around a car and neglecting the flow regimes associated with cooling and exhaust flow, the parts of a 2017 Formula One car can be classified as follows

1. streamlined elements (such as the roll-over cage, nose, side-pods) that are designed for attached flow.

2. downforce generating elements such as wing, strakes, winglets, vortex generators, floor, skirts, diffuser, etc

3. guiding elements, such as bargeboards, that produce both pressure gradients as well as vortical structures

4. drag inducing components such as the wheels, suspension systems, cameras, etc. These can be at least partially be streamlined but most often result in bluff body flows.

During the first seventy years of the sport, Formula One aerodynamics evolved from an offshoot of aircraft design to a specialisation in itself. This was particularly true from the end of the 60's with the development of ground-effect thanks to close collaboration between Imperial College and leading F1 teams such as BRM, Brabham and Williams. Close collaboration between academia and industry also allowed for an efficient technology transfer when early commercial CFD tools were developed first at Imperial College and then, as they moved towards RANS modelling, into the aerodynamic departments of the F1 teams at the end of the 90's. Section 1.2 an overview of the aerodynamic development of the Formula One front-section[2] is presented. It is followed by a survey of the state-of-the-art tools used for aerodynamic optimisation and particular emphasis is cast on the CFD tools and the challenges their offer that need to be overcome for further optimising aerodynamic efficiency of a Formula One.

[2]defined as the first half of the car starting from the nose

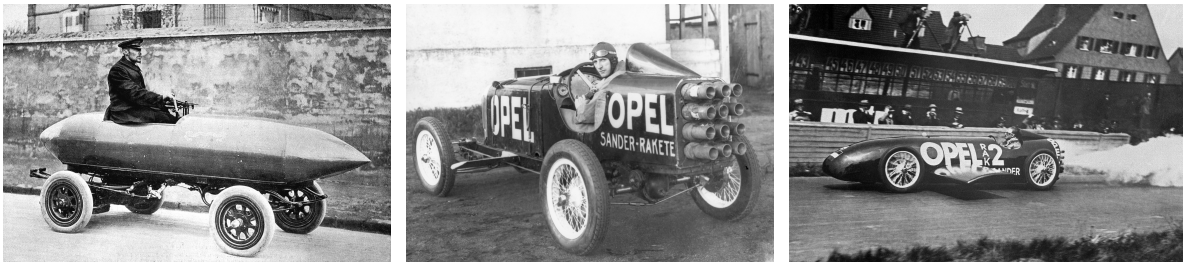



**Figure 1.1** – The streamlined electric vehicle la Jamais Contente (left). First attempt at a land-speed record with rocket engined cars with he Opel RAK1 (middle), note the small wings either side of the body to provide downforce. The Opel RAK2 (right), leverages much larger wings to improve handle at the higher velocities (roughly 230km/h). Both wings had positive camber. Source : (n/a, 2017*a*)

### 1.1.1 From streamlined to winged cars

The importance of aerodynamics in automotive design was already appreciated at the end of the XIX$^{\text{th}}$ century when competitors of the coveted Land Speed Record put a great deal of effort into streamlining their racers. *La Jamais Contente* (Figure 1.1 (left)), an electric vehicle, was the first road vehicle to break the 100[km/h] barrier and is a potent example. The rocket powered Opel RAK1 (Figure 1.1 (middle)) and RAK2 (Figure 1.1 (right)) were the first automobiles to see positive camber wings attached to their chassis to compensate for the positive lift of the rest of the vehicle.




**Figure 1.2** – Modified 1956 Porsche 550 Spyder by Michel May (left). Note the wing mount on the McLaren M2A at Firestone tyre test in Riverside California prior to 1966 season. And (right) the Ferrari 312 with a wing designed by Mauro Forghieri following the advice of Michel May. Sources : (Ferrari, 2017) and (n/a, 2017*b*)

In 1956, a Swiss student from the ETHZ first raced his modified Porsche 550 spyder with a wing in view of improving downforce (Figure 1.2 (left)). This is the first known example of a race car being fitted with a negative camber wing that is now commonplace in racing car design. He later joined Ferrari's Formula One team and his collaboration with Mauro Forghieri led to the first winged Ferrari Formula One car the 312 (Figure 1.2 (right)) . This also marks a shift in objectives for racing cars from drag-reduction through

streamlining only to a compromise between streamlining (drag reduction) and increased downforce through lifting surfaces, ground effects and then compressibility effects.

Aerodynamics have been a key player in McLaren DNA since the first entry into the championship from Bruce McLaren's team for the 1966 season. It builds on the lessons learned from M2A development car designed by Robin Herd that joined the McLaren from the National Gas Turbine Establishment where he had participated in the development of the Concorde (Wikipedia, 2017) (Figure 1.2 (middle)). During a test day in Zantvoort in November 1965 the M2A was fitted for the first time with a rear-wing producing downforce. A reported three seconds a lap improvement motivated the use of the wing for the 1966 M2B. However, challenges in cooling the Serenissima engine, used from the Belgium Grand Prix onwards in the season, prevented the use of the rear-wing.

### From unsprung to sprung wings

It wasn't until the 1968 season that wings, fixed to the unsprung parts of the car, were raced for the first time with the Lotus 49b (Fig. 1.3 a). As the wings grew in size the stronger loading increased the risk of failure on the suspensions arms (Fig. 1.3 b at the Montjuic Park Barcelona GP). From the Monaco GP in 1969 onwards, the wings fixed to unsprung parts of the wheel were banned motivating Lotus to envisage a spoiler design (Figure 1.3 c)).

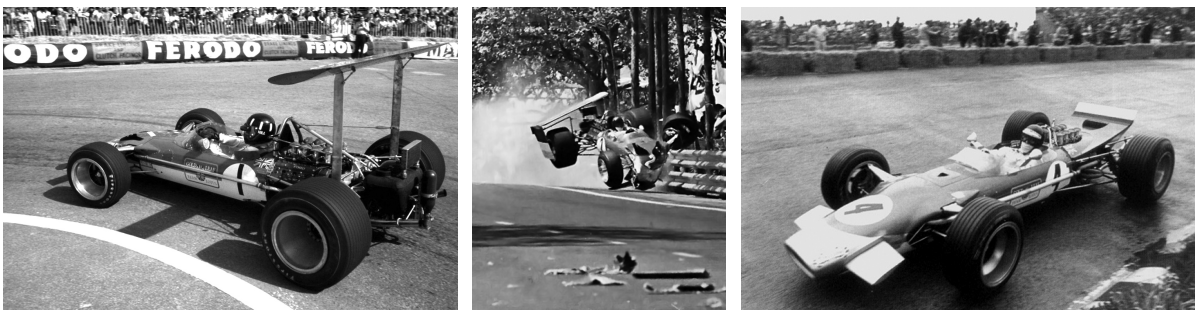



**Figure 1.3** – From unsprung to sprung wings during the 1968 season and first front-wings on Lotus 49h (c) (Bisset, 2015)

### Gurney flap

Before getting into the details of the evolution of the front wing we should emphasise the importance of one last modification to isolated wings during the 70's. The Gurney flap, typically 1-4% of the chord length and positioned vertically to the chord at the trailing edge, was invented by Dan Gurney for the Indy 500 of 1970, to improve the downforce of a given profile (Figure 1.4). By generating a low pressure region in the wake of the

gurney the flow can be re-attached, similarly to a flap. For the front-wing of the MP4-19 which is used as a base for the model we investigate in Chapter 5 the gurney flap helps keep attached the flow over a wider range of attitudes of the front-wing.




**Figure 1.4** – 1971 AAR Gurney Eagle for the Indy 500(Brown, 2017). Note the gurney flap on the rear wing.

### 1.1.2 Front-wing aerodynamics

The first full-width front-wing was introduced by Ferrari in 1974 (Figure 1.6 a). Between the 1968 season and 1974, the only noticeable difference to front wing design was the introduction of small end-plates at either extremity of these front wings to minimise induced drag from the roll-up vortex at the tips of the wings. The March 711 of 1978 (Figure 1.7) was a radical exception to the full-width front-wings of the 1970's that favoured small end-plates with parabolic profile aimed at reducing induced drag with an elliptical wing profile. Barnard introduced a two element front-wing with the MP4-2 (Figure 1.6 b) to further increase the downforce of the front-section, similarly to flaps from aeronautical applications. Tyrell introduced the high-nose front-wing (Figure 1.6 c), with the Tyrell 019. This is, arguably, the first time aerodynamic efficiency of the front-wing was optimised for the entire car. Prior to that front-section aerodynamic optimisation was performed locally on the front-wing itself by sacrificing wing-span on the front-wing in view of improving the mass flow towards the floor and diffuser.

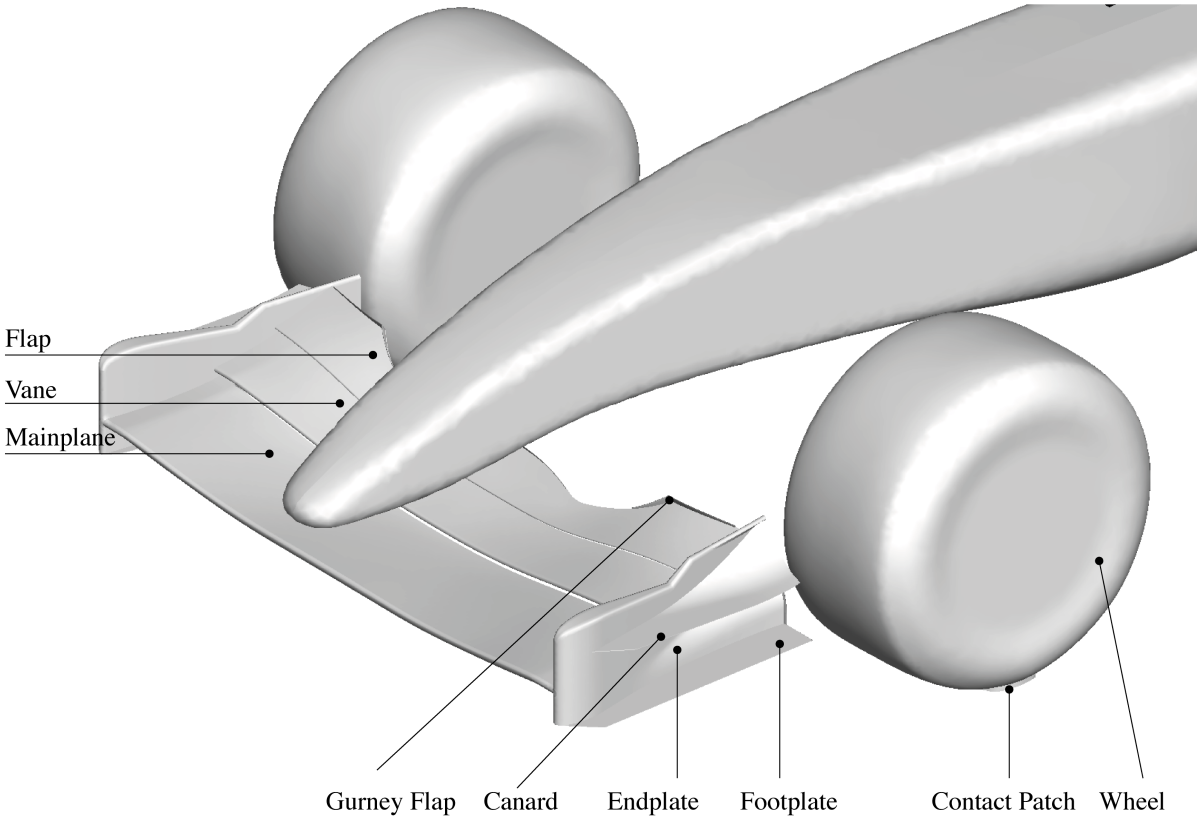



**Figure 1.5** – Different elements of the MP4-17D front-wing.

### Evolution of the endplate

Until the 1998 change in regulations (Figure 1.8 a), the wing-tip vortices generated by the front-wing where essentially perceived as a source of induced drag. Until then the endplates had been aligned with the interior of the wheel (Figure 1.8 b). As the new rules reduced the track of the car, the wake of the endplates now impinged directly the middle of the wheel. It was soon understood that sacrificing maximum span in favour of using the endplates as vane guides by avoiding direct incidence onto the rotating wheel was beneficial for reducing the drag (Figure 1.8 c). To compensate for this loss of span small strakes, or canards, were added at the exterior of the end-plates to induce vortex suction on these small aspect-ratio wings. This work started the incredible development of the endplate section with strakes followed by the introduction of footplates on the trailing edge that generated a systems of a least two more vortices. The endplate was then modified from a straight section to semi-circular design increasing the intensity of the interior footplate vortex on the MP4-14 (Figure 1.8 c). In addition to a growing footplate, the MP4-17D featured a canard, that together with the endplate, and footplate, was responsible for generating a system of four main vortices, studied experimentally by Pegrum (2006) and




**Figure 1.6** – First full-width front-wing raced on the Ferrari 312B3-74 (right) for the 1974 season. 1984 Barnard designed McLaren MP4-2 was the first F1 car to race a multi-element front-wing (as well as the famous "coke-bottle" rear). Similarly to a multi element wing used for aircraft (flaps and slats) that both increase total surface of the wing and especially larger amounts of camber. Compared to a single element with similar camber the multi-element wing exhibits separation at a higher angle of attack. First front wing with a high-nose (to increase mass flux towards floor yet allow for the full-width wing to be as close as possible to he ground to leverage ground effect : 1990 Tyrell 019 (tyr, 2017)

numerically in Chapter 6.

The end-plate contributes to increasing aerodynamic efficiency of the front-section in two ways: it prevents flow leakage from the pressure to the suction side of the wing at the wing-tip and helps direct the flow around the front wheels (either in-board before 2009 or outboard after). Since then, the double role of the end-plate has motivated complex designs generating multiple trailing vortex system.

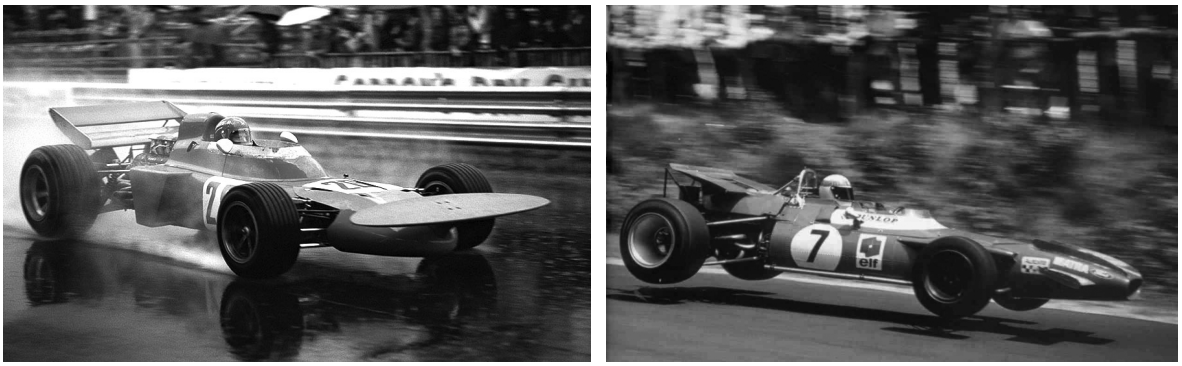



**Figure 1.7** – March 711 with elliptical front-wing (top) and 1970 Ferrari 312B (bottom) with rudimentary end-plate. Two early solutions aimed at minimising wake drag (by reducing the formation of the wing-tip vortices)(History, 2017)

Our motivation to use a model based on the MP4-17D was two-fold. Firstly, thanks to the availability of the CAD geometry from McLaren Racing we could reproduce an accurate representation of the experimental study conducted by Pegrum (2006) in the rolling-road equipped Campbell wind-tunnel at Imperial allowing for a more quantitative study of the correlation between wind-tunnel PIV data and CFD results.

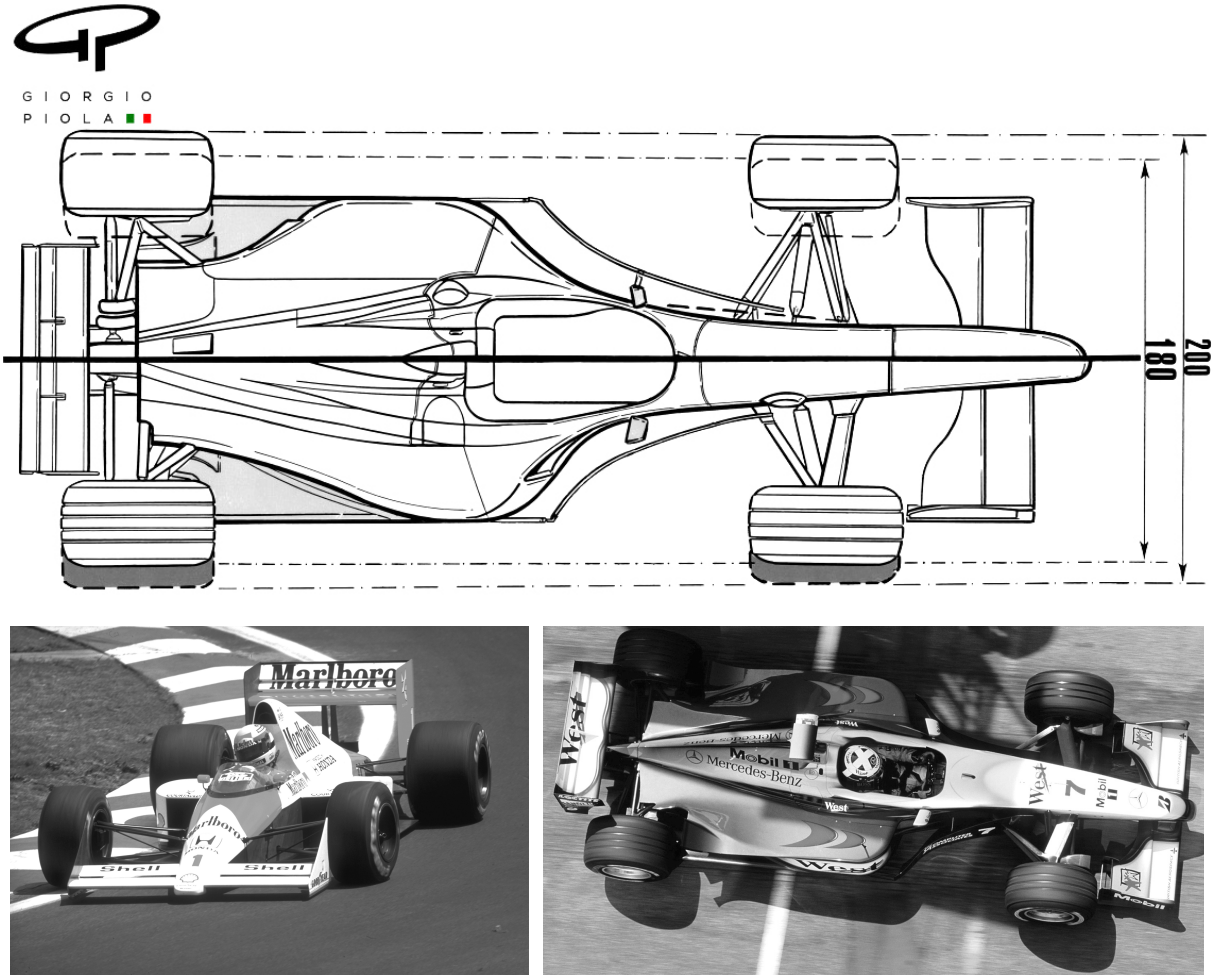



**Figure 1.8** – Change of regulation in width of the F1 cars from 200cm to 180cm (and the front-wing from 160 to 140cm, for 1998 meant the end-plate (or wing-tip) of the front-wing was now impinging the middle of the wheel. Contrary to its predecessor (the MP4-12) the end-plate was now used as a turning vane to manage the flow around the front-wheel (so-called in-wash front-wing). The growing complexity of the end-plate also allowed for generating increasingly complex vortical systems. Whereas a trivial endplate used until 1998 would generate two vortices from both the highest and lowest edges of the end-plate, the addition of a footplate, as shown on the right, produced at least three main stream-aligned vortices.

### y-250 vortex

The regulations change of 2009 introduced a *neutral-section* 250mm each side of the symmetry plane of the front-wing where no lifting-profile is allowed (Figure 1.10). The shorter span vanes and flaps thus had tips at 250mm from the symmetry plane of the car. The change in wing-profile on the main plane between the neutral and lifting region produces a complex systems of co-rotating vortices generally referred to as the $y_{250}$ *vortex*. Two key challenges in numerically modelling the $y_{250}$ vortex are its accurate modelling of the roll-up of the shear layers and tracking the evolution of the vortex as it advects

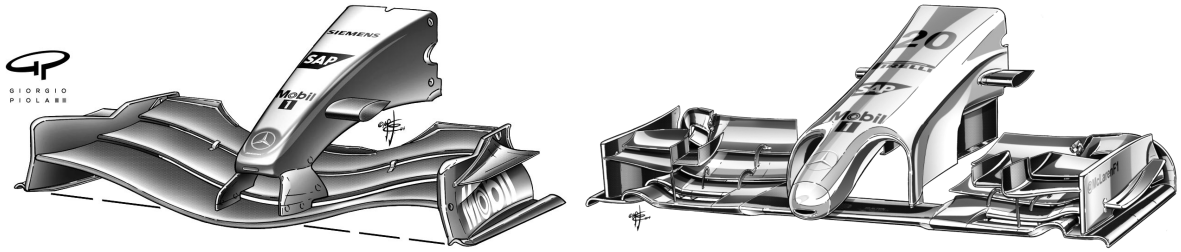



**Figure 1.9** – MP4-17D front-wing (left) and MP4-29 front-wing (right)(Piola, 2017*b*)

downstream through the suspension systems, around the barge-boards and side-pods all the way to the rear-wing and diffuser assembly. We should emphasise the large scales associated with this vortex which render its numerical modelling difficult due to the strong dissipation of state-of-the-art CFD tools used in Formula 1. The main plane of the front-wing has a chord of roughly 20[cm], producing a vortex that can remain coherent for the better part of the 4[m] length of the car. The combination of stringent local accuracy requirements near the wingtip where the vortices are generated together with the large extent of the coherent vortex render its modelling a challenge. This is one of the main motivations for investigating the possible benefits of using numerical schemes with low dispersion/diffusion errors which are then better able to propagate vortices over large space-time scales.

So far we have presented aerodynamic developments as isolated, local, elements of the car. Even though the first front-wings were optimised *in isolation*, such as the elliptic front-wing of the March 711 (Figure 1.7) it was already becoming apparent that the interaction between an aerodynamic element and the rest of the car required the understanding of their mutual interaction. An early example is the Forgheri rear-wing, that needed as much clean-air as possible, motivating a re-design of the rear end of the 312B3, that became the 312T. This is one of the first examples demonstrating the importance of *coupled* optimisation for overall performance gain of the car; by both increasing overall downforce while reducing drag as well as avoiding over-heating of the engine. This coupling of the flow between elements is one of the reasons why it is not possible to optimise a front-wing without a rolling wheel. More generally the *highly coupled* nature of F1 design requires a general understanding of both lifting surfaces and bluff-bodies operating together in ground effect. In this thesis, however, we focus only on the front-end of the car where the interaction of the vortex dominated flow from the front-wing with the bluff-body rotating wheel serves as a canonical test case for most of F1 incompressible aerodynamics.

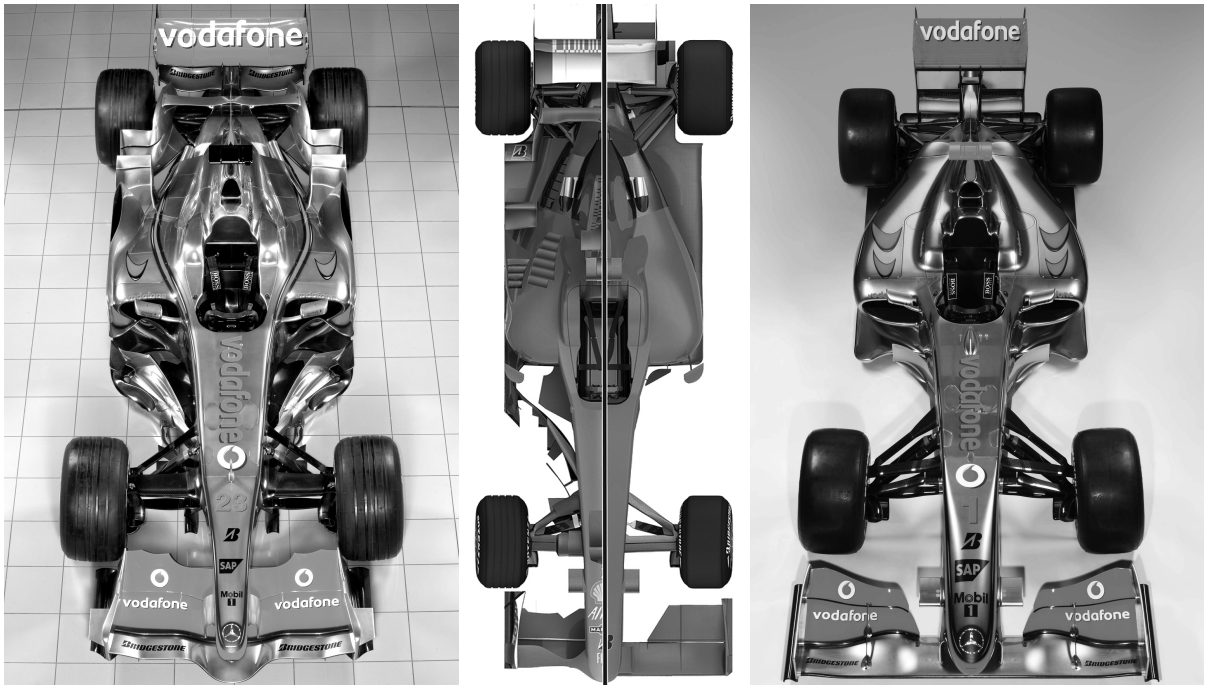



**Figure 1.10** – Regulation changes for 2009 with wider front-wings enabling out-wash end-plates as well as the 250mm neutral region each side of the symmetry plane producing the $y_{250}$ vortex(Piola, 2017*a*)




**Figure 1.11** – y250 vortex generated by 2013 Redbull RB9.

### 1.1.3 The challenge posed by open rotating wheels : main contribution to drag.

#### Overview of the aerodynamics of the rolling wheel

The immediate wake, that we consider to be within half a diameter of a rotating wheel, is dominated by two phenomena. First are shear instabilities between the oncoming flow

and the flow entrained by the rotating wheel which leads to a complex vortex shedding at the top of the wheel and the so-called *jetting vortices* nearby the contact region as the air escapes laterally when it reaches the high-pressure region upstream of the contact patch. These jetting vortices extend some distance laterally but remain in close proximity to the ground. They can negatively affect the flow in both the underbody and the rear-wing and diffuser assembly. As was shown with the Sauber C22 under tight cornering Sawley & Richter (1997), or high yaw angles, the interaction of the front-wing with the wheel wake can even hinder the performance of the rear-wing.

These two phenomena were already reported by Fackrell (1974) who employed both smoke-visualisation and total-pressure surveys. Since their seminal work, few authors have ventured towards describing the wake structure. Cogotti (1983) proposed a model consisting of three counter rotating vortex pairs, the relative intensity of which was not clearly defined. Saddington *et al.* (2007) experimentally investigated the wake of a rotating Formula One wheel by means of laser doppler anemometry and added to the models proposed by Bearman *et al.* (1988), Cogotti (1983) and Mercker & Berneburg (1991) by reporting two pairs of counter rotating vortices at the top of the wheel and nearby the contact region. More importantly they reported the two top vortices being entrained and merging into the bottom ones by $x = D$ downstream of the wheel centre, where $D$ is the wheel diameter. By $x = 2.5D$ they measured a similar wake consisting of two counter rotating vortices nearby the ground similar to that reported by Bearman *et al.* (1988). This behaviour was confirmed by both Pegrum (2006) and MacCarthy (2010).

Apart from the extreme competitive environment of Formula One, the automotive industry only recently developed a keener interest in wheel aerodynamics that, together with the underbody flow contribute from twenty to forty percent of the total aerodynamic drag (Wolf-Heinrich Hucho, 1993, Leclerc, 2008). Aerodynamic development of the car has mainly focused on the visible body-work which, together with packaging constraints, has led to convergence in optimum design shape. As the room for improvement vanishes, aerodynamicists are looking into the more challenging flows associated to the rotating wheels and engine/brake cooling. Wind-tunnel PIV measurements are considered state-of-the-art and allow for efficient survey of the unsteady flow features about a car. However it is challenging to instrument the tunnel to survey the velocity field within the wheel well. Even for open-wheel race-cars, such as Formula One, the intricate suspension system complicates surveys of the region between the wheel and the chassis through which the y-250 vortex systems develops.

Another challenging aspect of wheel studies is the nature of the flow itself where the flow-physics around the contact patch play a dominant role however access to this region, is complicate challenging because it is precisely between the rotating wheel and the rolling

ground plane. From a numerical point of view the rotating wheel and, in particular, the treatment of the contact patch are also a challenge. The vanishing gap between the rotating wheel and the rolling road requires careful modelling to avoid introducing stringent CFL restrictions. Also, the geometric approximations of this region pose a challenge for imposing consistent boundary conditions.

The importance of the rotation was already emphasised by Fackrell (1974). As shown in Figure 1.13 by the smoke visualisation the separation line at the top of the wheel is moved forward. The stagnation point is moved towards the ground and the jetting vortices are more pronounced leading to a taller but narrower wake at the top of the wheel and wider wake in the contact region. Purvis (2003) showed that increasing the size of the contact patch increases the width of the lower part of the wake but did not seem to significantly affect the upper-portion. It should be noted that the experiment was run with polyurethane foam wheels resulting in a non-physical contact patch (different deformation than a pneumatic tyre) and faster, uneven wear. Loading the wheel results in increasing the angle at which the jetting vortex leaves the contact regions. As the loading is increased, the vortex jet angles with respect to the ground plane is increased.

Car designers attempting the world land-speed records in the 30's, such as the 1937 Mercedes-Benz W125 Rekordwagen shown in Figure 1.15, already appreciated the importance of wheel drag. This motivated the use of fairings to effectively prevent most of the high-velocity flow impinging directly on the rotating wheels.

#### Reducing wheel drag by modifying the shape of the car around the wheels

Formula One is defined as an open-wheel racing category and as such, the wheels contribute to roughly 40% of the drag (MacCarthy, 2010). This significant contribution has been key motivation for using the front-wing and, more generally, the bodywork to control the location of the wake of the wheels. The 1955 Lancia-Ferrari D50 is early attempt at interpreting the open-wheel rule where the sidepods were used to avoid strong recirculation regions that create a low-pressure region in the wake of the front-wheels.

#### Controlling the wake by modifying the wheel geometry itself

Except for modifications of the body work around the wheel, at least three notable attempts have been made at influencing the wake of the wheels by modifying their shape.

The Tyrell P34 featured two sets of smaller front-wheels thus reducing the exposed surface while keeping the same contact surface and mechanical grip. The second attempt at reducing drag was tried by Ferrari, and then Toyota, in 2007 in the form of wheel fairing controlling more carefully the flow through the axle of the wheel that had mostly

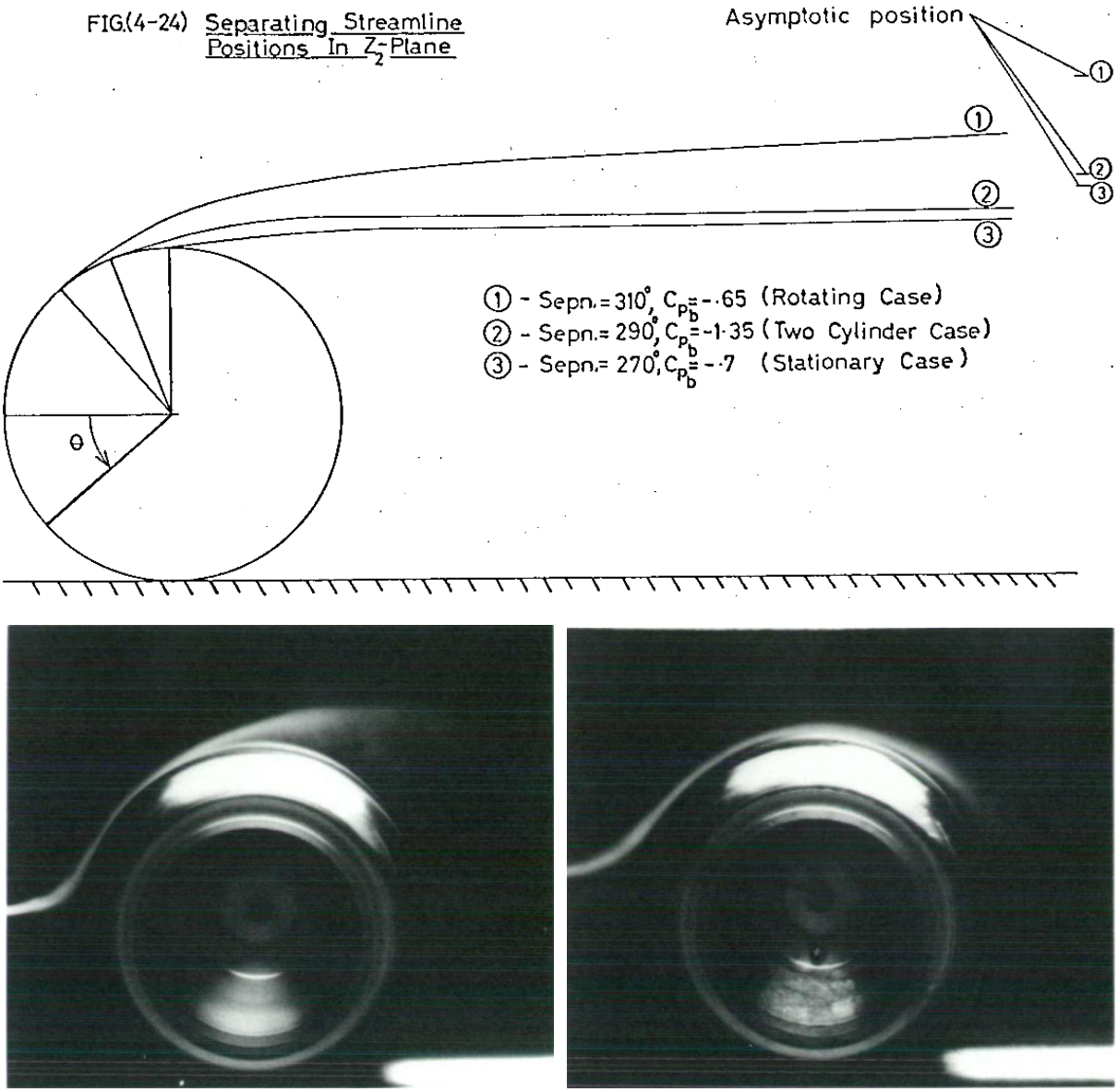



**Figure 1.12** – Fackrell rotating wheel in wind-tunnel, smoke visualisation rotating (left) and non-rotating (right) from Fackrell (1974).

been used until then for cooling the brake assembly. Finally, the third idea at reducing the wheel drag was introduced by Williams for the FW35 in the form of blown wheel axles. Flow through the hub cavity of the wheel can reduce drag by up to 3% MacCarthy (2010). Enough flow, however, is required to avoid oxidation of the brake assembly that would result in rapid wear. These devices showed non-linear benefits to the overall drag of the car that are still poorly understood despite being used as of 2017.

These three techniques aim at reducing the overall drag of the Formula One by modifying the size and shape of the highly unsteady wake.

In summary rotating wheels are the largest contributor to drag for open-wheel rac-

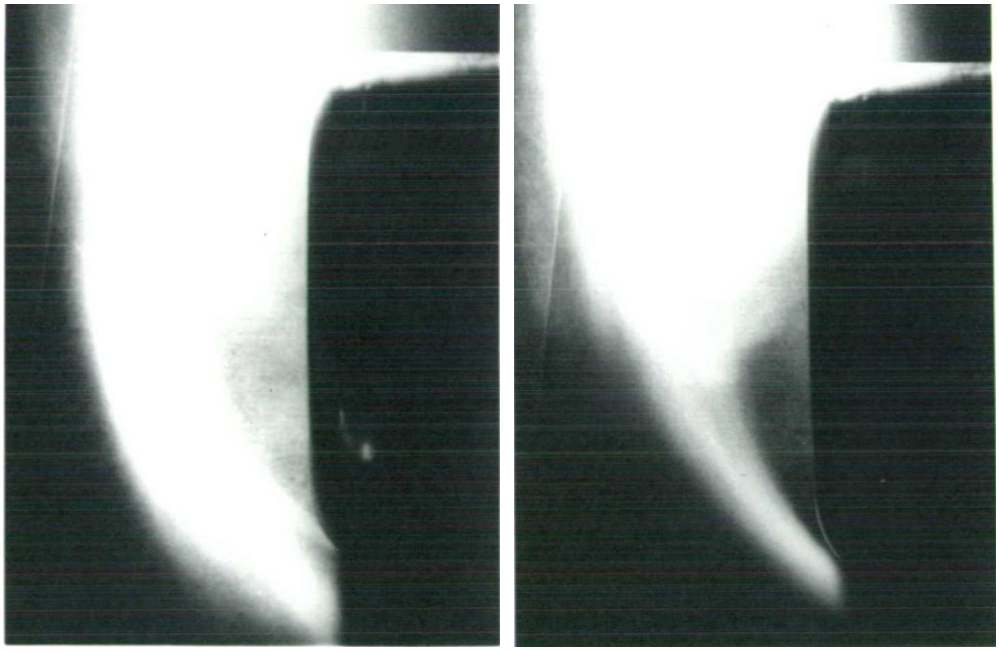


**Figure 1.13** – Fackrell rotating wheel in wind-tunnel, smoke visualisation, stationary (left) and rotating (right). Source: Fackrell (1974)

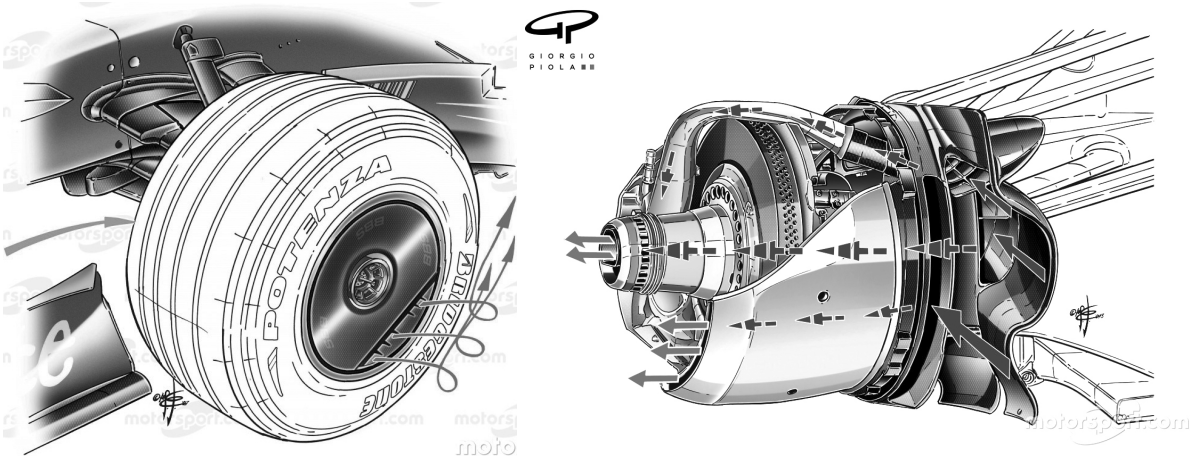



**Figure 1.14** – Ferrari 2007 front-wheel hup-cap, or fairing, (left) and 2013 Williams FW35 blown wheel nut (right) (Piola, 2017*a*).

ers such as Formula One and, together with the underbody, are the main contributor of drag for contemporary road-vehicles. So far little effort has been invested in aerodynamic considerations of the wheels leading us to believe there is potential benefit for aerodynamic efficiency improvement. Because the flow around a rotating wheel is still poorly understood we also believe the first step towards improving aerodynamic efficiency rests on improving the underpinning understanding of the flow features typically associated to a rotating wheel. We then see two main avenues of investigation towards optimising

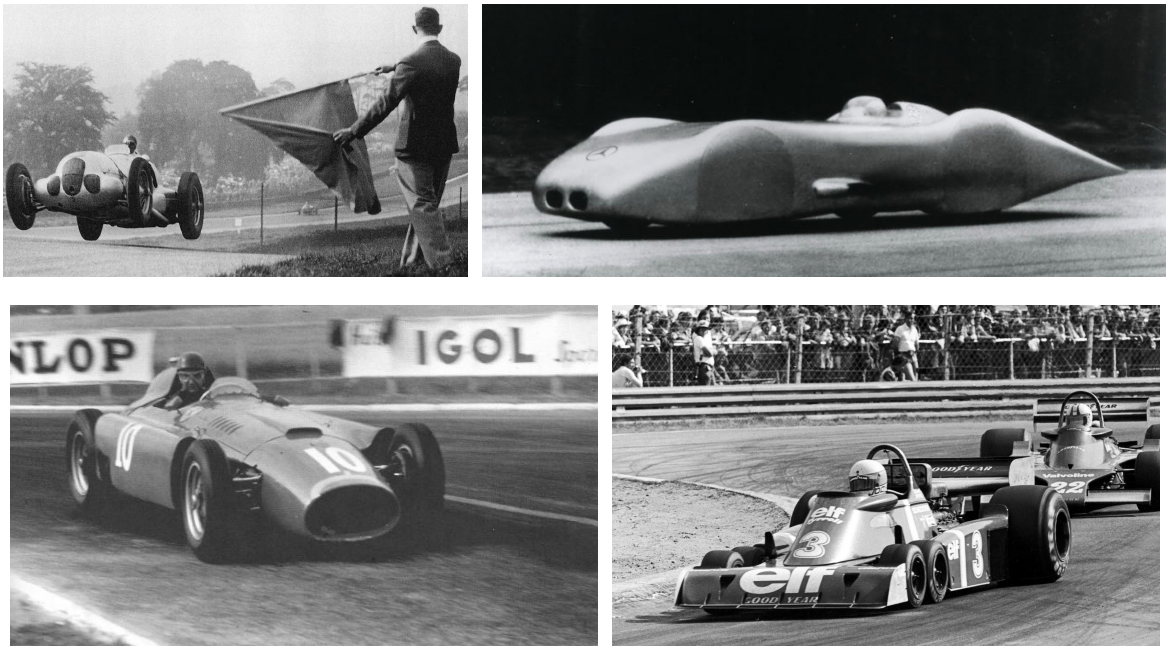



**Figure 1.15** – The 1937 Mercedes-Benz W125 Rekordwagen on its record 431[km/h] run on an autobahn still holds the record for the fastest car on a public road is an early example of attempts at reducing the drag from the open wheels. The Rekordwagen is modified version of the GP winning Mercedes-Benz W125 and 1955 Lancia-Ferrari D50, as well as Tyrrell P34 (Ballaban, 2017, Ferrari, 2017, tyr, 2017).

aerodynamic efficiency of vehicle wheels. Firstly the wheel wake itself can be optimised. Even in the strict framework of 2017 F1 regulations, it is still possible to leverage wheel nut blowing as well as active or passive, closed or open loop, flow-control mechanisms, thanks to ducting related to brake and calliper cooling. Fairings, like those that completely preclude air from flowing through the axle or partial fairing such as those first raced by Ferrari on the F2007 (Figure 1.14) and modifications to the geometry of the wheel spokes in terms of both their shape and number, should equally be considered in investigating local benefits to the wheel wake. The second avenue of investigation should focus on modifying the body of the vehicle so that the interaction between the wheel flow (wake and upstream with the front wing for example) is globally optimised. The work presented in this thesis, and in particular the work presented in Chapter 4 and 5 can be considered as an attempt to address these issues.

### 1.1.4 Summary of aerodynamics main challenges

In summary aerodynamic development of Formula One since the 60's has emphasised two key points. Firstly, the ever growing interest in optimisation of the drag and downforce of the entire car as opposed to that of individual components. Therefore there is a need for

taking into account the non-linear increase in total car drag despite the drag of individual components decreasing. An example of this non-linear interaction is given by Katz & Garcia (2002) for the front-wing of an Indy car (Figure 1.16). This non-linear increase in lift (or drag) requires modeling the flow interaction between the front-section with the rest of the car with low levels of dispersion/diffusion errors. Secondly there still remains room for improving the underpinning understanding of the fundamental flow physics of a rotating wheel.

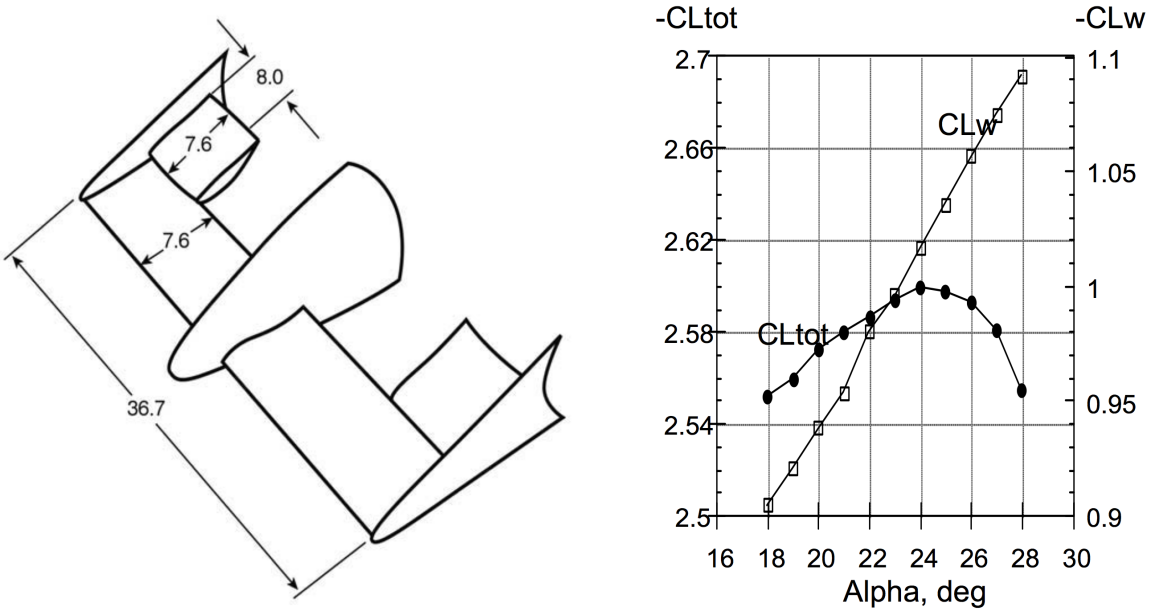



**Figure 1.16** – Non-linear increase in total car downforce despite linear increase of front-wing downforce as its angle is increased computed with a panel method. Past 24° the wake of the front-wing impinges the rear-wing(Katz & Garcia, 2002).

We will describe the evolution of the tools that have been developed in order to enable the technological innovations discussed previously.

## 1.2 State of the art of F1 aero design and limitations

The first aero-driven design cycles, in the 1960s, consisted in simply building parts, fitting them to a chttps://www.mclaren.com/formula1/ar and testing it on a track and the impact of this modification on performance was quantified by differences in lap-time. This is how the advantage of negative camber wings, the gurney flap and sharp underbodies favoring ground-effect were developed. From the 60's onwards it was understood that building models and testing their aerodynamic efficiency in the controlled environment of a wind-tunnel sped up design cycles. These efforts, pioneered by Imperial College (in collaboration with BRM, Shadows, Arrows, Williams, Lotus, etc) were made possible thanks

to developments in wind-tunnel technology such as the moving ground plane. These early developments marked the beginning of a dialogue between leading academic institutions and Formula One teams. Jointly they developed new tools specifically engineered for improving aerodynamic efficiency of Formula One cars. In turn, these new cars posed more questions requiring yet further development of the tools. This mutually beneficial dialogue pushing the frontiers of aerodynamics has impacted positively not only the motorsport and aerodynamic communities but also the transport sector at large as well as bio-technologies (Cantwell *et al.*, 2015, Tzortzis *et al.*, 2015).

In the following we will provide an overview of the methods used to assess and quantify the aerodynamic performance of a design presented by chronological order of their use. An actual design cycle would rather favour first testing a variety of solution computationally, before building a few scaled models to be tested in a wind-tunnel and a fewer still full-scaled parts to be tested at racing weekends on the track.

### 1.2.1 Track testing

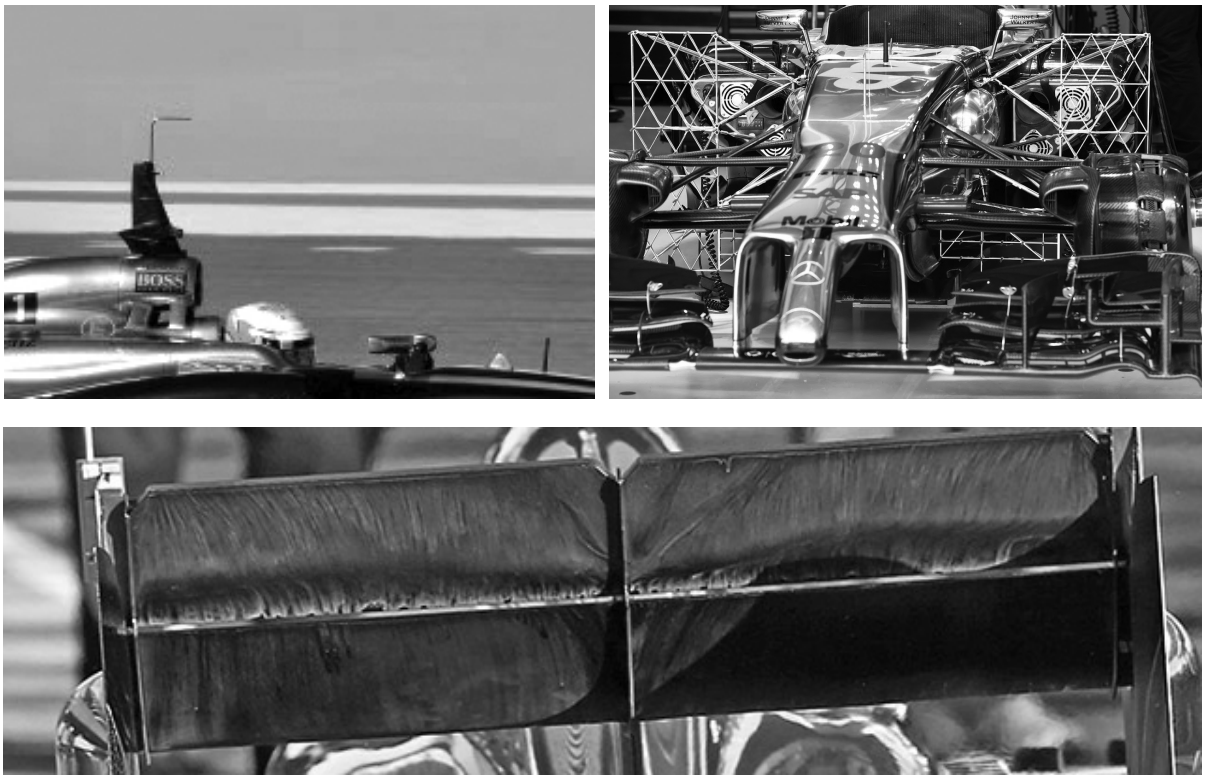



**Figure 1.17** – Mclaren MP4-29 with pitot tube mounted about the roll-structure in a) and aero-rake in b) as well as flow-viz paint applied to the rear-wing(Somerfield, 2017)

Originally track testing simply consisted of modifying the body-work of a car and then estimating the impact it had on performance by quantifying the difference in lap-time. A

good perspective on early aerodynamic testing is given in a Keith Howard interview of Robin Herd CBE, first chief designer at McLaren(Howard, 2004) :

> The M2 [Figure 1.2 b)] was built to take an aerofoil and we actually ran it in a test at Zandvoort. On his first lap with it fitted, Bruce was three seconds faster. We took it off again: three seconds slower. Back on again: three seconds faster. It was very difficult to believe, and that's one of the reasons we didn't get in earlier with wings in races. Plus there were journalists around during the test and we didn't want them taking note, so we actually hacked up the wing and put it in the bin to persuade them it didn't work! It was mildly irritating that Ferrari and then Brabham came along with them when we had done it first. I wanted to attach the M7's wings to the suspension uprights, but the feeling was that that was asking for trouble, which events showed it was.

Technological developments have allowed for a greater number of sensors being deployed:

1. *pressure taps*: mounted in holes drilled into the chassis
2. *pitot tubes*: generally mounted upstream of the cockpit or above the roll-structure (Figure 1.17 a))
3. *aero-rake*: More recently, aero-rakes allow insight into individual aerodynamic components of the car. Mark Taylor was pioneered the aero-rakes at McLaren. They are generally placed alongside the nose of the car, downstream of the wheels to quantify the wake structure behind the front-section of the car. They are also used to assess the performance of the floor and diffuser when they are placed downstream of the rear-end of the car. An example of aero-rake, developed by Mark Taylor for the MP4-29 is shown in Figure 1.17 b)
4. *flow-viz*: McLaren pioneered the use of *flow-viz* paint in 2010 which is sprayed on the surface of interest and then dries as the car is driven around the track. The dried paint betrays the flow structures on the surfaces of interest. This technique was originally employed in wind-tunnels.
5. *cameras with tufts*: to assess stall characteristics of wing-elements on the front-wing when subject dynamic yaw and pitching.
6. *infrared cameras*: are used to measure the temperature of the tyres, and more generally their thermal management to better understand the effect of the flow

about and in the wheel ducts. Tyre temperature is critical for harnessing wear rate that can have an impact on contact patch shape and size.

### 1.2.2 From aeronautical to automotive wind-tunnels

The end of the XIX$^{\text{th}}$ century saw tremendous interest in controlled powered flight with denser than air craft. Already then, building and crash landing prototypes was expensive and so means of investigating aerodynamic properties of different shapes before they were fitted to an aircraft were pursued. The first wind-tunnel built and operated in 1871 is most often credited to Frank H. Wenham(AIKEN, 1981). His 12 feet long (3.65[m]) and 18 inch (0.45[m]) square tunnel allowed for the first investigation of the lift and drag of various shapes. He is also famously reported strong lift to drag ratios ($c_L/c_d > 5$) for less than 15° incidence. His team also made the first investigations into the influence of aspect ratio on wing performance. Building on this experience Sir Hiram Maxim built a larger wind tunnel, with a three foot square test section and reported higher lift to drag ratios of 14 for cambered airfoils at 4 degrees of angle of attack. More importantly for automotive aerodynamics he was the first to report aerodynamic interference:

"The various members constituting the frame of a flying machine should not be placed in close proximity to each other(AIKEN, 1981)".

The Wright brothers also recognised the advantage of testing designs for their wings in a wind-tunnel when they realised previous reported data was inaccurate. Building there own open-return sixteen inch ($\approx 0.41[m]$) square wind-tunnel and quantifying lift and drag for many different profiles they were equipped with the most complete database of the era which, together with their pioneering three-axis control system to compensate for aerodynamic induced instability of the aircraft, eventually led them to the first powered flight in 1903.

Prandlt had the first closed return wind-tunnel build in Göttingen originally intended for improving the design of airships(Prandtl, 1920).

Tunnels for full-scale models were originally designed, either based on the Göttingen wind tunnel (closed) or the Eiffel (opened). The first tunnel, for road cars, was build by Daimler in 1938 (Wolf-Heinrich Hucho, 1993). Pininfarina opened their first wind-tunnel in 1972 that was extensively used by Cogotti (1983). Despite being quite expensive to build, wind-tunnels are mainly costly to operate requiring large fan power. Also building reduced-scale models is cheaper and faster leading to greater flexibility. These reasons motivated the construction of many reduced-scaled wind-tunnels from the 70s onwards, such as the Mira quarter-scale.

In the late 60's in the United Kingdom, the Donald Campbell wind tunnel of the

Aeronautics Department of Imperial College, was the first to include a moving ground plane with boundary layer suction originally intended for aerodynamic research for sea-planes. By the end of the 60's Professor Peter Bearman together with Professor John Harvey used this then unique wind-tunnel to investigate aerodynamics of cars in the most accurate model of a car/road interaction yet. It was then used by Fackrell (1974), sponsored by Dunlop, to investigate the basic aerodynamics of a rotating wheel which to this day still remains a reference study. As a side note, the same Donald Campbell wind tunnel was used by Lotus to develop the T78 ground-effect F1 car that was financed by Honda for development of the Honda Civic and later used by MacCarthy (2010) for his PhD investigation into wheel aerodynamics. These wind-tunnels were also used by BRM, Shadow, Arrows and Williams. In 2004, a three-axis traverse system was fitted to the tunnel and it was this facility that was used by Pegrum (2006) for his investigation of the aerodynamics of both an isolated rotating Formula One wheel and the MP4-17D simplified front-section presented in Chapter 6.

In contemporary wind-tunnels, such as the Toyota Motorsport wind-tunnel in Cologne or the Sauber wind-tunnel in Hinwil, the car is mounted to a robotic arm capable of both changing the attitude of the model as well as record the lift, drag, side force as well as the three moments. The walls and ceiling can be adaptable to further reduce blockage effects which is one of the technologies that was developed for motorsport modeling rather than aerospaceLarger than the Donald Campbell and Honda wind-tunnels at Imperial, these can accommodate 60% scale models and are fitted with pneumatic tyres and sensors, below the rolling metal belt that can measure the pressure and the shape of the contact patch region. The absolute accuracy of the wheels being mounted directly on the model is greater than for wheels mounted on stings. Typical blockage ratios are in the range of 5-7%. Boundary layer management for wind-tunnel testing of racing cars is extremely important for accurately modeling ground-effect. Since, as a first approximation, the car does not encounter a boundary layer on the track (in the absence of wind), the boundary layer must be removed by a suction patch just upstream of the moving ground plane where the boundary layer doesn't grow anymore because the belt speed is synced to that of the airflow. The models are also equipped with pressure taps and the tunnels are equipped with automatic traverses to enable efficient acquisition of flow structures by means of particle image velocimetry (or PIV), a non-intrusive optical technique for measuring flow velocity. Contrary to the aircraft industry where a sting is mounted to the tail of the aircraft, they are typically mounted through the roll-over hoop to avoid interference with the diffuser for example. The robotic sting allows for yawing, pitching and rolling as well as controlling the ride height. Contrary to CFD, wind-tunnels can give important information regarding the dynamic behavior of the car under braking for example, as the

model can be pitched down simulating a braking procedure and the effect of the dynamic evolution of the flow on the forces and moments can be recorded. These tunnels were built with insight developed at Imperial, and except for their larger size differ in one mostly by the moving ground that is emulated by highly polished steel belt supported by air bearings (introduced by MTS). Suction bellow the belt allows to compensate for the suction from the front-wing and the underbody/diffuser of the car operating in ground effect. Modern steel moving belts can operate up to 80[m/s], as opposed to the 25[m/s] limit of the synthetic moving ground plane in the Donald Campbell wind-tunnel at Imperial College.

**Summary of state-of-the-art automotive wind-tunnels strengths and limitations**

In summary the pioneering development of wind-tunnels for automotive research and developement at Imperial College with the full-width moving ground plane, boundary layer suction, three-axis traverse, six-component load cells and PIV have allowed for the most comprehensive body of knowledge about road car aerodynamics. In turn this has led to a competitive advantage for the Formula One teams working in close collaboration with the researchers of the aeronautics, and other, departments. As the front-wing and suspension systems becomes ever more complex access to a clean plane for visualising the laser sheet from the PIV becomes more challenging. More generally wind-tunnels are indispensable for investigating the aerodynamic forces on a car throughout its operational envelope, however quantification of the entire flow field for a given operational condition is best suited for CFD. In the next section an early example of this scenario, where an oddity is appreciated in the wind-tunnel and then investigated further with CFD is given before the short-comings of state-of-the-art CFD in Formula One are underlined.

### 1.2.3 Applications of CFD: from shock capturing to sub-grid scale modelling to informing F1 aerodynamicists.

The first efforts to leverage computers for engineering might be considered to be the work on shock physics by Richard Feynman and Hans Bethe at Los Alamos during World War II as they supported the design of the first atomic bomb. Richtmyer invented artificial viscosity, in 1948, to capture shocks in the computations without the solver diverging(Rider, 2014). The 1965 Scientific American article by Harlow & Fromm reporting the results of the unsteady Navier-Stokes computation about a square rod is arguably the *first engineering application* of Computer Experiments in Fluids Dynamics. They motivated the simulation of the *von-Kármán street* as a design tool for the replacement of the Tacoma Narrows Bridge that had been victim of vortex induced vibration. Two years later, the

shorter *computational fluid dynamics* was coined by Fromm & Harlow (1963).

During this period, Joseph Smagorinsky published his 1963 paper generalising Richtmyer-Von Neumann artificial viscosity to three dimensions and laying the foundations for both *climate modelling* and *Large Eddy Simulation*. And so the connection between shock-capturing for numerical simulation of nuclear weapon induced shocks and sub-grid scale modeling for turbulence was established. It is interesting to note the hostility of the community at Los Alamos towards artificial viscosity that was considered an ad-hoc hack where the values of the coefficients in the artificial viscosity were merely knobs that required fine-tuning. To this day there remains criticism towards artificial viscosity with arbitrary knobs such as the two coefficients required for the spectral vanishing viscosity that is used as one of the main enablers for computing high-Reynolds number flows with spectral/hp element methods.

Bifurcating from climate modeling, aeronautical industry proved to be a fertile ground for the development of CFD methods. In the 1980's Euler-equation based CFD was used to optimise the shape of 2D profiles by minimising shock induced drag. By the end of the 1980's, the first whole-aircraft models could be computed with these methods to optimise the location of the nacelle relative to the wing by understanding the interference the nacelle had on the lift characteristics of the wing. By the early 90's the first 2D RANS codes were developed an it was only at the end of the 90's that the first whole-aircraft computations where achieved thanks to 3D RANS codes. In the context of automotive aerodynamics, inviscid computations were used by Katz & Dykstra (1994) to optimise the design of a Le Mans prototype car. Since the wheels are not exposed there are fewer regions of detached flow and so it was believed that panel-methods could inform the designer for further streamlining the prototype. By the end of the 90's the first Formula One teams were investigating the possible benefits of leveraging 3D RANS based CFD to locally optimise the flow of the front-section of the car. In 1997, for example, in collaboration with the EPFL, Sauber (Sawley & Richter, 1997) investigated the flow around a simplified front-section. To the authors best knowledge these are the first publicly disclosed results of a 3D CFD analysis of a Formula One front-section. In the United Kingdom, similar developments were pursued between leading F1 teams and institutions such as Cambridge and Imperial. Kellar *et al.* (1999*b*,*a*) report a joint CFD and experimental study of the simplified front section of a 1998 Formula One car. This study already successfully aimed towards improving the understanding of the non-linear interaction between the front-wing and the rotating wheel.

By the early 2000's, F1 teams had both low-order 3D RANS based software available and the computational resources to run the first full car simulations. This allowed for the first visualisation and understanding the impact of modifications of the front-wing on the

rear wing for example which, until then, could only be quantified through lift and drag measurement in the wind-tunnel. In 2001, Benetton Formula One already used Star-CD to simulate a full car with 1 million elements at a resolution of 1[mm] over the front-wing. In 2003, the Sauber C22 was reported to suffer from loss of downforce during high yaw angle turns and the rolling belt equipped wind-tunnel at the Swiss Aircraft and Systems Company that the team was using before it built their own was only capable of yaw angles up to 4.5°. Thanks to a 100 million element RANS computations of the whole car at a yaw angle of 6° the influence of the front-tyre wake was found to be detrimental to the loading of the rear wing (Larsson *et al.*, 2005*b*). This second example of non-linear interaction between aerodynamic devices on a car motivates both further research and development into the understanding of wheel wakes and the development of high-fidelity CFD software capable of correctly modeling these complex flow interactions.

Automotive CFD evolved as a tool for early concept phase and component design in the 90's to complete system design and interaction assessment in the early 00's. However since then efficiency of the design cycle as well as the size and quality of the mesh investigated has increased drastically from a few million elements in the early 00's to several hundred million today. The underlying method, mostly low order finite-volume, has remained unchanged.

**Summary of state-of-the-art automotive CFD strengths and limitations**

In summary, since 1965, integration of CFD in a design cycle has helped reduce the time of the *vehicle development process*, from an average of 60 months in the 90's to 18 months in the 00's(Larsson *et al.*, 2005*a*). Similarly in aircraft development process, CFD has allowed for better optimisation of the interaction between components such as the nacelle and the wing as well as helped reduce the number of wind-tunnel tests by roughly 50% since the 1980's(Jameson, 2015) However the numerical methods underpinning most commercial and academic CFD codes date back to the 80's and 90's and are generally limited to low, second- or third-order accuracy and optimised for boundary modeled cases. These codes are ill-equipped to deal with unsteady vortex dominated and transitional flows encountered in the design of super laminar wings, high-lift systems, rotorcraft and formation flying. Complete aircraft in landing configurations as well as Formula One cars are two examples of niche markets where breaking out of the plateau that CFD has been experiencing for the past 30 years is a pre-requisite. LES of industrially relevant cases at high enough Reynolds number are feasible provided the CFD codes are based on at least the four following principles proposed by Wang *et al.* (2013) :

1. ability to mesh complex geometries (unstructured grids)

2. high-order algorithms for low dissipation for resolving unsteady features over large space-time scales

3. sub-grid scale models for wall-bounded flows (not isotropic)

4. massively parallel efficiency as well as locally approaching peak flop performance on each core.

In the following sections we will highlight how the spectral/hp element code `Nektar++` has been developed following these principles and tested on pertinent industrial test cases.

## 1.3 How might high-fidelity CFD contribute to F1 aerodynamics?

The evolution in Formula One aerodynamics since the 60's has opened challenges presented in Section 1.1. The three main avenues taken by Formula One engineers to improve the understanding and aerodynamic efficiency of the cars, namely track-testing, wind-tunnel experiments and CFD was presented in Section 1.2. Particular emphasis was put on the strengths and limitations each of these methods and four key necessary objectives have been defined for future CFD technologies to allow for the continued improvement of Formula One design. In this section we motivate how high-fidelity spectral/hp element LES, together with state-of-the-art wind-tunnel and track testing, might overcome these challenges .

Since the 90's individual elements of the body work of a Formula One have been optimised leveraging CFD. Initially the aim was to test a large number of simple parts, such as rear-wings element profiles, and then building a wind-tunnel component. By the end of the 90's the first RANS computations already aimed at gaining further insight into the non-linear interaction between the front-wing and rotating wheel. However, the flow around a rolling wheel for example is still poorly understood and this can be partially explained by the challenges posed by such investigations. It was only in 1974 with Fackrell (1974) efforts that the importance of the rolling in contact with the road was shown thanks to a wind-tunnel equipped with a rolling belt. A full width-rolling belt increases the cost of both building and operating a wind-tunnel. Secondly instrumenting the wind-tunnel to quantify the flow field is a challenge because the flow is sensitive to the perturbations introduced by the pressure probes for example. This is one of the main motivations for leveraging non-intrusive techniques such as PIV. However a key region of interest for the rolling wheel is the contact patch region where the flow is complex and still poorly understood because it is difficult to instrument. It was only in 2006 with

the novel approach of MacCarthy (2010) that the first velocity surveys of the very-near ground plane around the contact patch were measured thanks to rolling the wheel in a water tunnel. For similar reasons it is not presently possible to quantify the flow on a race-track closer than 0.5D downstream of the wheel (and not in the contact region). These challenges contributed to the motivation of leveraging CFD for assessing the entire 3D flow-field around the rolling wheel in contact with the ground.

### 1.3.1 Representing and meshing complex geometries

Maintaining geometric flexibility was one of the key objectives in developing the spectral/hp element method and it should be emphasised that this project was largely influenced by the ability of `Nektar++` to compute solution over complex geometries thanks to its support of prisms, tetrahedra, hexahedra and pyramids. Research in high-order meshing has made significant progress but is not yet mature. As industry moves towards high-fidelity CFD with methods such as the spectral/hp element method our experience has lead us to outline four main challenges :

1. minimising modelling error : assessing if the CAD model is representative of the operational window of the part in question

2. minimising representation error : generating CAD curvature conforming meshes.

3. maximising mesh quality : automating the process and so defining quality metrics to avoid for, example, stringent CFL restrictions

4. minimising mesh count : automated mesh adaptation through h-, p- or r-refinement.

#### Minimising modelling error

Minimising modelling error will become increasingly important since small discrepancies between the mesh geometry and the actual car on the track can have large effects on the aerodynamic properties of the car.

A priori the geometry of the wings and the entire front-wing can be, as a first approximation assumed to be straight forward as long as the tolerance used during the CFD analysis of the CAD model remain the same through the production process. The nature of the tip of a wing has a strong influence on the nature of the vortical structures rolling up. For example a blunt edge will produce a great number of co- and counter-rotating vortices than a rounded wingtip (such as that studied in Chapter 4). CAD modelling and meshing might favour simplifying the geometry in favour of a blunt tip however if

manufacturing of the actual wing produces a more rounded profile there might be discrepancies in the meandering of the $y_{250}$ vortex. Aerodynamic loading leads to both static and dynamic deformation as well as change in attitude due to the driving (change in yaw and attack angles). The change in surface quality of the road, for example when the car is driven over curbs the effective ride height of the front-wing is strongly influenced and large dynamic deformations of the front-section are observed. Because the wings work in ground effect configuration they are extremely sensitive to any of these variations.

Also the discrepancies between the CAD model used in CFD and the built car in racing conditions can come from the deformation of portions of the car that *a priori* might assumed to be negligible, such as the the nose that supports the front-wing. It is designed not only to be able to serve as a crash structure but also to optimise the flow around the car. Small deformations in the nose might significantly affect the ground clearance of the front-wing and so strongly influence its aerodynamic properties. Vanity panels and the small gaps between suspensions elements and the chassis provoke leakage.

Regarding the wheel, there are also many challenges to be overcome by CFD in order to accurately compute flow fields representative of racing conditions. The geometry itself of the wheel is highly sensitive to loading with a varying size and shape of the contact patch as well as the possibility of the appearance of centrifugal effects and standing waves that can modify the shape of the entire tyre (not only in the region of the contact patch) as well as thermal loading. Finite element models of the wheel geometries can be used to assess the results of these effects and provide CFD with a geometry as pertinent as feasible. Also the roughness of the slick tires or the presence of grooves in the rain-tires might have a large influence on the aerodynamic properties of the exposed rotating wheel.

In summary it should be stressed that modelling error associated to geometric simplifications associated to the CFD model and geometric discrepancies due to static and dynamic aero loading will become increasingly important as high-fidelity CFD converges towards DNS.

### CAD accurate mesh

In boundary layer research accurate representation of the surface is paramount because small discrepancies can provoke the onset of transition and so, more importantly for Formula One, can lead to delayed, or promoted detachment of the flow. This is particularly important in regions of the flow where it detaches over smooth curvatures surfaces such as the rolling wheel.

#### Automation

An automated meshing pipeline is quintessential for integration of the spectral/hp element method into a CFD led design workflow. The work presented in this thesis helped inform the needs of automated high-order meshing however most mesh were generated manually with a workflow presented in Chapter 3. One of the open challenges for automated high-order meshing is the ability to quantify the quality of a mesh to produce relevant mesh for the case under consideration as well as an efficient mesh that does impose artificially stringent CFL restrictions.

#### Adaptation

Mesh adaptation is paramount for improving the quality of the solution while reducing the computational cost. In this project, both h- and p-refinement were used to produce mesh-independent solutions. This pragmatic approach is costly in terms of man-hours requiring highly skilled engineers familiar with the challenges posed by high-order CFD. The `Nektar++` supports the development of p- h- and r-refinement and progress is made towards automating the adaptation.

#### Summary of high-order meshing challenges and opportunities

Presently, the ability to mesh complex geometries is a challenge for high-order methods and `Nektar++` is the only high-order software capable of meshing complex geometries with both prisms, tetra-hedra and hexa-hedra. Together with h- and p-refinement strategies presented in Chapter 3 the current pipeline has allowed for the computation of the flow over geometries representatives of F1 such as the simplified MP4-17D front-section presented in Chapter 6. Persson & Peraire (2006) have been prolific contributors to the field of high-order meshing and the interested reader is referred to Turner *et al.* (2016, 2017) for a detailed explanation of the latest `Nektar++` meshing functionalities.

### 1.3.2 Low dispersion/dissipation and fast convergence

The globally $C^0$ continuous spectral/hp element method based on the classical Galerkin formulation offers attractive dispersion diffusion properties for advecting flow features over large space/time scales in that both dissipation and dispersion errors are low relative to low-order methods.

This property is best evidenced by the canonical case of the advection of a Gaussian vortex or the isentropic vortex (for the spectral/hp element method based on a Discontinuous Galerkin formulation) presented in Section 3.1.2. It is believed that this intrinsic

property of the method might be beneficial for computing vortex dominated flows such as the wake of a Formula One front-wing where the wingtips, strakes, guide vanes and endplate produce a large number of vortices.

In Chapter 4 the results of the computation of a wing-tip vortex over a rounded tip NACA 0012 profile are shown and demonstrate that the spectral/hp element method is not only competitive for advection of Gaussian vortices but also for more industrially relevant cases such as the wingtip vortex thanks to the low dissipation/dispersion properties.

Finally, an extreme example of the importance of the low dispersion/dissipation properties of the spectral/hp element method is the modelling of the production and tracking of the $y_{250}$ vortex. It is generated (mainly) by the interaction between the ground, the FIA section and the flap elements, on a streamwise extent of roughly 25cm but can be seen to extend past the driver or roughly 2[m] downstream.

### 1.3.3 Under-resolved DNS, implicit LES or no-model LES

Modelled boundary layers correlate well when the detachment point is fixed, for example by a strong geometric kink, and the turbulence state of the boundary layer can be readily anticipated by either considering the boundary layer fully turbulent or akin to a tripped boundary layer. These conditions often hold when modelling cruise conditions for aircraft, but when considering take-off and landing configurations for example the high-angle of attacks of the flaps might produce detaching boundary layers. The strong vortices at the tips of the deflected flaps also introduce strongly three dimensional flow where the detachment point is not fixed and so turbulence modelling of the boundary layer might not verify the hypothesis on which they are based.

The flow about a Formula One front-wing is akin to the high-lift configuration of an aircraft in that a large number of vortices are produced by the tips of the numerous profiles. The importance of the accurate modelling of the formation of these vortices is emphasised by the fact that a significant amount of downforce on a front-wing is vortex induced. The cores of the vortices with their low pressure regions, when in proximity to a surface produce non-negligible forces on this surface.

Building on these observations an argument can be made for avoiding an ill-suited turbulence model in favour of an ad-hoc numerical stabilisation. This pragmatic approach is not always well received in the turbulence modelling community and understandably so. This echoes how the artificial viscosity introduced by VonNeumann & Richtmyer (1950) was received by the community of physicists at Los-Alamos.

The computation of the wingtip vortex in Chapter 4 acts as a demonstrator for this approach where the artificial viscosity introduced thanks to the spectral vanishing viscos-

ity, first introduced by Tadmor (1989) yields the best, publicly available, correlation to experimental data.

Building on this success the spectral vanishing viscosity spectral/hp element method, hereafter referred to as high-fidelity spectral/hp element LES was used to investigate other flows sensitive to realistic modelling of the boundary layer detachment. In regions where the detachment occurs over a smooth high-radius of curvature region small changes in the modelled detachment point can have significant impact on the shape of the wake and consequently on both lift and drag. Also in region of the front-wing where vortices are generated accurate modelling of the shear is quintessential (and isotropic flow that is sometimes used as a hypothesis for justifying RANS models clearly does not hold). Furthermore, because of ground effect and more generally because the front-wing is so complex each element operates in a disturbed flow field. Finally wings are designed to operate close to their peak lift, or close to stall so small discrepancies in detachment can result in the wrong prediction of the state of stall of a front wing that in turn negatively affects the prediction of the flow of any element in its wake.

### 1.3.4 Numerical efficiency ready for next-generation exa-scale facilities

Effectively leveraging the resources of next generation high performance computing facilities is a prerequisite. The spectral/hp element method is believed to be particularly well suited for these new mixed architectures for at least three reasons :

1. can operate on the plateau of the roofline model and not limited by memory cache bandwidth

2. the time to solution with given error is believed to be shortened

3. the compact nature of the discretisation offers good scaling capabilities.

The spectral/hp element method and the reason for these attractive properties and the underlying numerics are presented in Chapter 3.

### 1.3.5 Post-processing

There is an additional importance consideration that has sometimes been overlooked when assessing next generation CFD codes, namely the ability to effectively post-process the data. In this context post-processing is regarded as more than averaging in that stability analysis, for example, can be readily studied within the same framework.

The methods developed here and our collaboration with Jordi (2015) regarding co-rotating vortex stability is a precursor to the tremendous potential offered by high-fidelity methods in terms of assessing the stability of co-rotating vortices for example. Accurately modelling the vortices of a wing-tip and then of a front-section is only the first step in assessing their stability. Indeed the streamwise aligned vortex dominated wake is subject to strong positive and negative pressure gradients as it flows around the wheel and as such is susceptible to breakdown. The corresponding loss in total pressure results in loss of downforce if the breakdown occurs nearby a lifting surface and from a drivers perspective can modify the balance of the car. As reported by Hoëssler (2011) the spectral/hp element method is expected to be particularly useful for investigating the stability of vortical systems because of its strong resolving capability and low dispersion/diffusion error.

Hoëssler (2011) demonstrated the potential benefits predicted by Hein & Theofilis (2004) but the computation of a representative baseflow remained a challenge. The PhD project of Jordi (2015) developed the adaptive SFD to successfully compute steady state solutions for two co-rotating Batchelor vortices. One of the aims of this present thesis is to develop the LES capabilities of `Netkar++` so that high-fidelity flow solutions can be fed into the adaptive SFD to obtain a baseflow and ultimately compute the stability of the flows.

During the course of this project, a collaboration with Cambridge led to developing interpolation routines for feeding PIV data from a water tank towing experiment into CFD domain to compare the evolution of the trailing vortices of both a delta-wing and a simplified Formula One front-wing.

Beyond the realm of F1, the knowledge and tools developed during the course of this project can be directly applicable to improving efficiency of transport for road-cars (Evstafyeva *et al.*, 2017, Longa, 2018), tubes (Prince, 2015), trains , high-lift configurations of aircraft and optimisation of wing design for cruising (Grazia, 2016).

## 1.4 Main Contributions

The focus of the research presented in this thesis is to investigate numerically the airflow around wings, isolated wheels and ultimately around the idealised front-section of a Formula One. The flow around a wing tip is studied and particular emphasis is given to accurate modelling of the wing-tip vortex system. The wheels are modelled either as truncated cylinders with adequate boundary conditions associated with the rolling or basic standard wheel configurations (similar to the Fackrell (1974) wheel). Finally the combination of a wheel and a front-wing are studied to assess the interaction between the complex vortical structures with the rolling wheel wake. A variety of computations where

carried out both to assess the evolution of `Nektar++` from an academic DNS tool towards a revolutionary LES tool deployable into industry.

## 1.5 Thesis outline

This thesis is based on the last 4 years of intense collaboration between the methodology department of McLaren F1 led by Dr. Mark J. Taylor and then Dr. Julien F.A. Höessler and the Sherwin Lab ending in October 2017. The development associated with the `Nektar++` framework are presented in Chapter 2 and 3. Because each flow studied is quite different we have chosen to break with traditional thesis structure and include separate literature reviews in each chapter so that they are better self-contained. Analysis of the wing-tip is presented in Chapter 3, the rotating wheel in Chapter 4 and the Formula One front-section is Chapter 5. Finally conclusions and recommendations for further work are presented.

# Chapter 2

# Fundamentals of the spectral/hp element method

## 2.1 Conservation of mass and the Navier-Stokes equations

The phenomena considered in this thesis are associated to the dynamics of fluids about bodies of geometric scales ranging from $O(10^{-4})$[m] to $O(1)[m]$. The mean free path of air molecules at ambient temperature (23°C) and pressure ($1.013 \cdot 10^5$Pa) is estimated to be of the order of $6.6 \pm 0.1 \cdot 10^{-8}$[m](Jennings, 1988). As such, the scales associated to the motion of the fluid about the bodies considered are at least three orders of magnitude larger than the mean free path of air, which is why the *continuum hypothesis* holds.

The state of a moving fluid can defined by the distribution of fluid velocities at any given time $t$ and position $(x, y, z)$ by $\mathbf{v} = \mathbf{v}(x, y, z, t)$ and two thermodynamic quantities such as pressure $p(x, y, z, t)$ and density $\rho(x, y, z, t)$. The other thermodynamic quantities, such as temperature, can be defined by these two thanks to the equation of state.

In the following few sections we will introduce non-dimensional quantities used to describe the flows of interest before the spatial and temporal discretisation for the spectral/hp element method are presented. Emphasis is cast on why this computational method is expected to be competitive against more traditional low-order methods ubiquitous in Formula One as of 2017. The chapter will then be concluded by a few notes regarding the different forms of errors that arise when discretising and solving these flows. Finally the key ongoing developments of `Nektar++` most of which are expected to be used by the future developments of this project are presented. Chapter 3 will then focus solely on the key developments that have taken place and are still being pursued for deploying high fidelity CFD modelling into Formula One.

### 2.1.1 Non-dimensionalisation

Considering a flow about the wingtip presented in Chapter 5 we need only consider the kinematic viscosity $\nu$. The wingtip itself is defined both by the geometry and a length scale. If we look at two wingtips of identical shape, only the length of the the cord $c$ defined as the distance between the leading and trailing edge then the flow itself about these wings is defined by the velocity at any given point. Because density is assumed to remain constant throughout the flow, compressibility effects are neglected. The kinematic viscosity $\nu$ has units of $m^2.s^{-1}$, the length scale $L$ has units of $m$ and the velocity $U_\infty$ of $m.s^{-1}$ so the only non-dimensional combination of these quantities is the definition of the *Reynolds number*:

$$Re_L = \frac{U_\infty L}{\nu}$$

where $U_\infty$ is the inflow velocity.

For unsteady flows a time-scales can be associated to the dynamics of the system as discussed in Chapter 5. For the rotating wheel of diameter $D$ immersed in a fluid of kinematic viscosity $\nu$ at a freestream velocity $U_\infty$ the wake exhibits shedding frequency $f$. This frequency can be non-dimensionalised as the *Strouhal number* :

$$St_D = \frac{fD}{U_\infty}$$

The reported velocities throughout this thesis are normalised by the inflow velocity $U_\infty$ as $U/U_\infty$, $V/U_\infty$ and $W/U_\infty$. The pressure is also non-dimensionalised and the total pressure coefficient, defined by $CP_0 = (\frac{1}{2}\rho\mathbf{v}^2 + p)/(\frac{1}{2}\rho U_\infty^2)$ which simplifies to

$$CP_0 = 2p + u^2 + v^2 + w^2$$

for an incompressible fluid.

In addition to these two non-dimensional numbers force coefficients associated to the drag, lift and side-force can defined, respectively, as:

$$c_D = \frac{2F_D}{U_\infty^2 A} \qquad c_L = \frac{2F_L}{U_\infty^2 A} \qquad c_S = \frac{2F_S}{U_\infty^2 A}$$

where $F_D$, $F_L$ and $F_S$ the respective forces integrated over the surface of interest and $A$ is a reference area.

## 2.2 Spatial discretisation : the spectral/*hp* element method

To compute the flow field about geometries relevant to Formula One we numerically compute solution to the incompressible Navier-Stokes equations. From the 1940's the solutions to partial differential equations (PDEs) for engineering applications were sought for using low order finite-element, finite volume or finite difference methods. These methods were attractive in that the grid-refinement, or h-type refinement allowed for greater resolution in regions of complex geometry or flow-physics. The fully spectral methods offered no geometrical flexibility but good convergence properties which is why they were used in fundamental research for cases such as boundary layers over flat-plates. Towards the end of the 1960's Orszag developed the spectral method where the solution for periodic problems was expanded on a Fourier basis and the solution to non-periodic problems were expressed with polynomials. The spectral element method introduced by Patera (1984), the p-type method as well as the spectral/hp element method introduced by Karniadakis & Sherwin (2005) used throughout this thesis retain the convergence properties of the spectral method while allowing for greater geometrical flexibility required for Formula One geometries. In addition to the accuracy and convergence properties, as well as low diffusion, the spectral/hp element method has a number of attractive properties stemming from its data structure as implemented in `Nektar++`. Although more details are given in (Cantwell *et al.*, 2015), the compact and localised nature of the data structures involved, relative to low-order finite volume or finite element methods, reduces the requirements in terms of memory bandwidth between cores during computation and increases on-node performance yielding good scaling properties. As will be discussed further the spectral/hp element method, as implemented in `Nektar++` is future-proofed for the move towards next generation exa-flop scale (hereafter referred to as exascale HPC) facilities that leverage mixed architectures (CPU+GPUs) further increasing the number of compute cores. Following our paper presenting `Nektar++` we focus here only on solving the incompressible Navier-Stokes equations. As a starting point for the key features of `Nektar++` as well as other domains of research where progress is being made we refer the interested reader to Cantwell *et al.* (2015).

### 2.2.1 Spectral/hp element discretisation

We consider a computational domain $\Omega$ which is a two- or three-dimensional finite element mesh. Individual elements $\Omega_e$ (a triangle or quadrilateral in two-dimesions, a prism, tetrahedra pyramid or hexahedra in three dimensions) tesselate the space $\Omega = \cup\Omega_e$ and

the intersection between any two elements is defined by $\Omega_{e1} \cap \Omega_{e2} = \partial\Omega_{e1e2}$. To solve the Navier-Stokes equations we consider solutions discretised in space $u^\delta$ that respect continuity across elements, i.e. in a subspace $u^\delta \in V_N \subset C^0$. Within each element the solution can be represented as

$$u^\delta(\mathbf{x}) = \sum_{n=1}^{p} \hat{u}_n \phi_n \left( [\chi_e]^{-1}(\mathbf{x}) \right) \tag{2.1}$$

where $\chi_e : \Omega_e \to \varepsilon$ is a parametric mapping from each element $\Omega_e$ to a standard reference space $\varepsilon \subset [-1, 1]^3$ (hexahedra, prisms, pyramids or tetrahedra):

$$\Omega_e \rightarrow \varepsilon \tag{2.2}$$

$$\chi \mapsto \mathbf{x} = \chi_e(\xi) \tag{2.3}$$

For tetrahedra, prisms and pyramids one or more of the coordinates is collapsed creating singular vertices (Karniadakis & Sherwin, 2005). These mappings support deformed and curved elements, so that a conforming mesh about a curved surface will have elements with curved edges and faces in $\Omega$, but once mapped to the elemental reference region both edges and faces are straight. In Equation 2.1 $\phi_n(\xi)$ where $1 \leq n \leq N_p$ with $N_p = p * p$ for quads and $N_p = 0.5P(P+1)$ for triangles is a set of polynomials forming a tensorial basis of one-dimensional bases segments in the elemental reference regions and $\xi$ are the quadrature points. The choice of this basis can be modal or nodal in nature and is usually based on a modified hierarchical Jacobi basis that supports boundary-interior decomposition of the form :

$$\phi_p(\xi) = \begin{cases} \frac{1-\xi}{2} & \text{for} \quad p = 0 \\ \left(\frac{1-\xi}{2}\right)\left(\frac{1+\xi}{2}\right) & \text{for} \quad 0 < p < P \\ \frac{1+\xi}{2} & \text{for} \quad p = P \end{cases} \tag{2.4}$$

The advantage of this form of basis is that there are only two polynomials $p = 1$ and $p = P$ that do not vanish at the boundary between adjacent elements and so, increasing the polynomial order within an element does not result in increasing the number of non-vanishing polynomials at the boundary. From a computational perspective this is attractive since increasing the polynomial order of the computation means only those on the boundary need to be communicated to adjacent elements which contributes to the good scaling properties of the spectral/*hp* element method. In this sense the spectral/*hp* element method is *compact*. Finally the coefficients $\hat{u}_n$ in Equation 2.1 are determined by imposing a restriction $R = \mathscr{L}u^\delta$ that its $L^2$ inner product with respect to the test

functions $\Psi_n(\mathbf{x})$ is zero. For the Galerkin projection used throughout this work, the test function $\Psi_n$ are the same as the trial functions $\phi_n = \Psi_n$.

Generalising this process to all elements, the global solution $u^\delta(x)$ can be expressed by *global assembly* :

$$u^\delta(x) = \sum_{i=0}^{N_{DOF}-1} \hat{u}_i \Phi_i(x) = \sum_{\text{elements}} \sum_{p=1}^{p=P} \hat{u}_p \phi_p^e(\xi)$$

where the $\hat{u}_i$ are the global mode coefficients and $\hat{u}_p$ the local (elemental) mode coefficients.

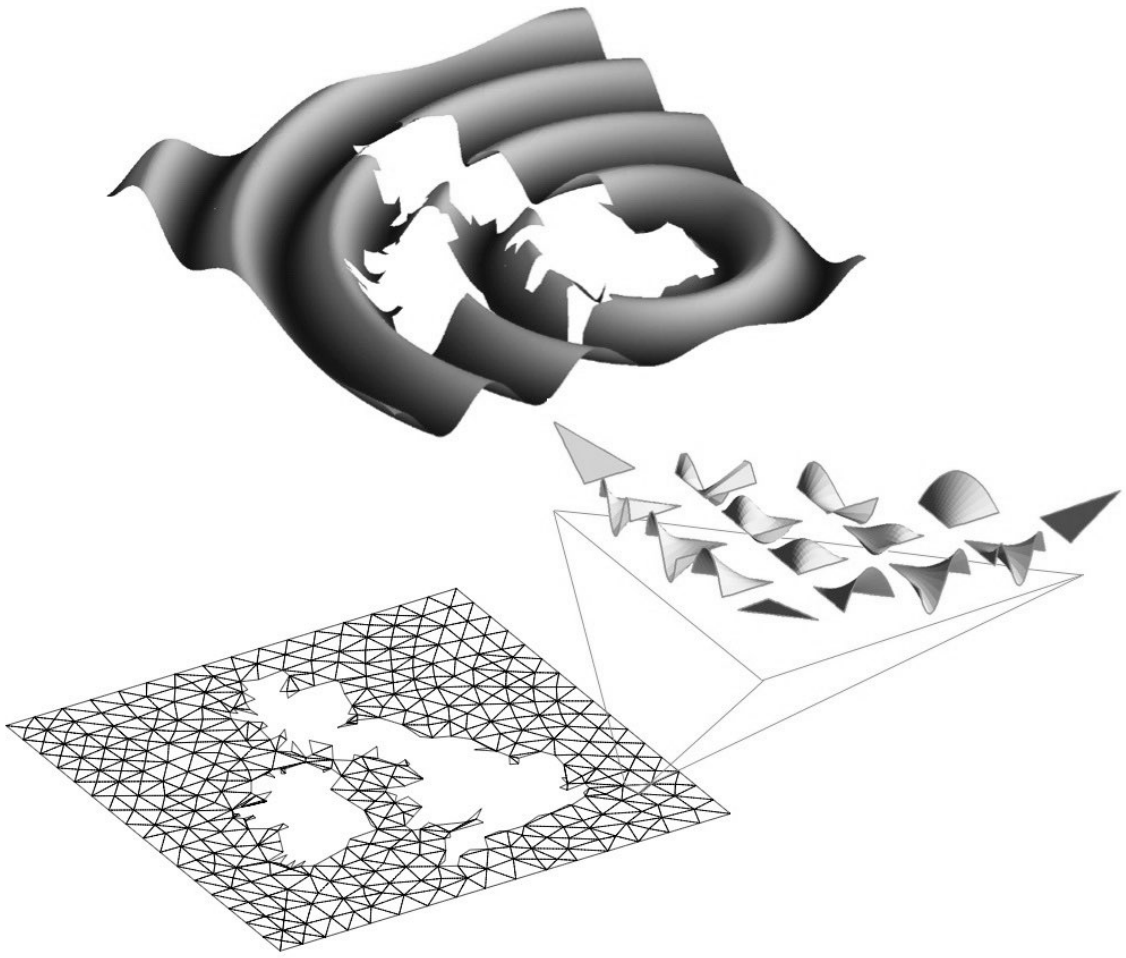


**Figure 2.1** – Spectral/hp element discretisation of the British Isles. Source : Karniadakis & Sherwin (2005)

The `IncNavierStokesSolver` used throughout this study solves the Navier-Stokes equations following this scheme of spatial discretisation together with two-forms of temporal discretisation. The interested reader will find compelling information for using or developing `Nektar++` in Cantwell *et al.* (2015) as well as on http://www.nektar.info

### 2.2.2 Fourier-Spectral/hp element discretisation

In cases where there exists a periodic-direction, such as an infinite cylinder, a developing boundary layer over a flat plate or simplified Formula One rear-wing setup neglecting the end-plates, it is advantageous to discretise the periodic direction with a Fourier expansion. This approach was proposed by Karniadakis (1990) and implemented into `Nektar++` in a parallelised form by Bolis *et al.* (2014), the details of which can be found in Bolis *et al.* (2016). For example a bi-dimensional spectral/*hp* element method is used to discretise the non-periodic x-y plane and a Fourier expansion is used to discretise the homogeneous direction z. The general solution in this basis would the have a form :

$$u^{\delta}(x, y, z) = \sum_{pqk} \Phi_{pq}(x, y)\Phi_k(z)\hat{u}_{nk}$$

This effective spatial discretisation has been recently used in the studies by Rocco *et al.* (2015) and Xu *et al.* (2016*a*, 2017*a*).

### 2.2.3 Three reasons that make the spectral/hp element method attractive for next-generation exa-scale facilities

In this section the three perceived benefits that motivated the project for deploying this method into industry are presented, namely:

1. spectral convergence
2. low bandwidth requirements and good scaling for peta- and exa-scale HPC facilities
3. highly efficient usage of each core.

#### Attractive convergence properties

Arguably the most cited motivation for using spectral/hp element methods in CFD computations is the so-called *exponential rate of convergence* increasing the polynomial order within each element offers. Contrary to lower-order methods, where the rate of convergence is controlled by the underlying order of the method, for the spectral/hp element method both mesh size and polynomial order can be varied. For sufficiently smooth solution, (i.e. that do not exhibit discontinuities) Babuška & Suri (1994) have shown the exponential rate of convergence to hold. That is the solution convergence to the analytical solution faster than any order. It is, therefore, more cost-effective considering a fixed number of degrees of freedom, in terms of CPU time and hardware, to increase the polynomial order $P$ at the detriment of mesh size $h$. In the more global setting of CFD methods, and

in particular when comparing against low-order methods the argument is slightly more complex. For a given number of degrees of freedom and a given simulation time it might be advantageous for the spectral/hp element method to operate with a higher polynomial order however this also increases the computational cost. In short a low-order mesh with a much finer grid might be less demanding in resources than a high-order method on a coarse grid because the high-order method would require more compute resources. The argument for high-order methods would then be that the spatial convergence rate is faster than the increase in cost and so for long simulation time computations it might still be advantageous to leverage the spectral/hp element method.

A simple example to demonstrate the attractiveness of the convergence properties of the spectral/hp element method can be found, for example, in Ekelschot (2016) that we reproduce here to keep the argument self-contained.

Consider the unsteady advection problem

$$\partial_t u + \mathbf{a}\nabla u = f \qquad \text{in} \quad \Omega = [-1, 1]^3$$

with $\mathbf{a} = (1, 1.5, 2)^T$. We impose an initial condition $\mathbf{u}(\mathbf{x}, t = 0) = \sin(\pi x)\sin(\pi y)\sin(\pi z)$ and a time-dependant boundary conditions given by

$$\mathbf{u}(\mathbf{x}, t) = \sin(\pi(x_{\partial\Omega} - t))\sin(\pi(y_{\partial\Omega} - t))\sin(\pi(z_{\partial\Omega} - t))$$

where $x_{\partial\Omega}$, $x_{\partial\Omega}$ and $x_{\partial\Omega}$ are the coordinates on the boundary of the domain $\partial\Omega$. The $L_2$ norm is then computed relative to the analytical solution

$$\mathbf{u}(\mathbf{x}, t) = \sin(\pi(x - t))\sin(\pi(y - 1.5t))\sin(\pi(z - 2t))$$

at a given time $t = 0.3$. The error is computed on different mesh where either $h-$ or $p-$ were used for the refinement. The solution for $P = 7$ polynomials and 8 hexahedral elements is shown in Fig. 3.1 a). The faster rate of convergence of the $p-$ refinement ($\circ$) rather than h-refinement ($\bullet$) is shown in Fig. 3.1 b). Further examples can be found in Vermeire *et al.* (2017). In the context of this project, a step towards a comparison of high- and low-order methods has been since the results of the high-order methods are now openly available for comparison.

**How compactness might be attractive for memory bandwidth limited HPC facilities**

In this section we briefly emphasise two additional benefits inherent to the spectral/hp element method and of particular interest for deploying large scale LES into exa-scale

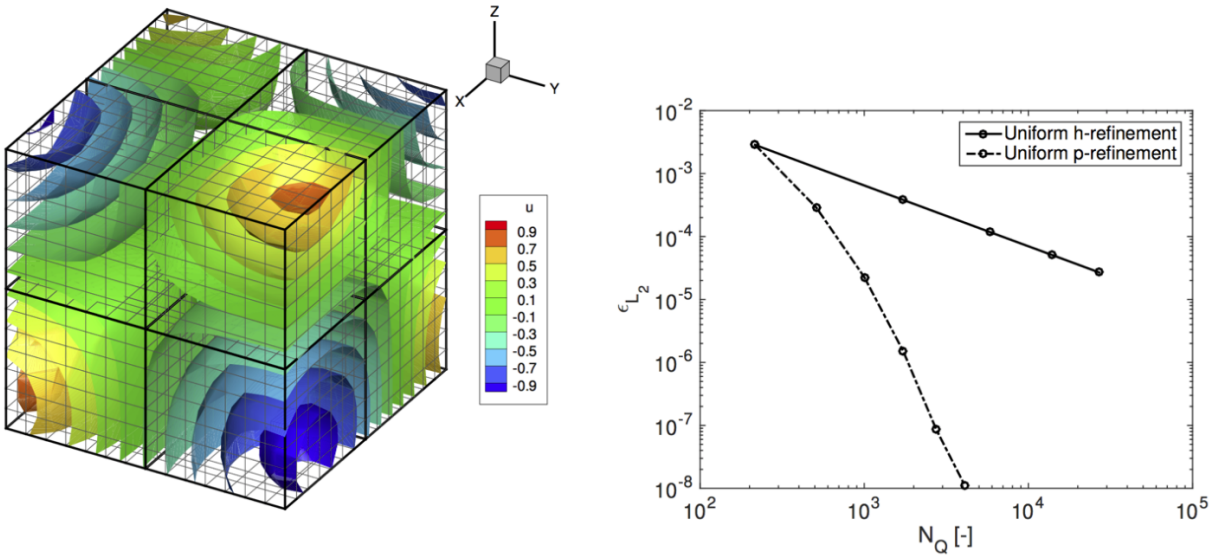



**Figure 2.2** – Faster convergence of the $L_2$ error with respect to the analytical solution with p- (○) rather than h- refinement (●) for an advection problem. Source: Ekelschot (2016).

facilities for industry.

Thanks to compact nature of the spectral/hp element method the actual data required to be communicated between elements is smaller as each data point contains more information. This is an argument for scaling. As computer scaling becomes infinite, by all practical measures ($> 100K$ cores), the constraint becomes one of bandwidth between processors.

The same argument holds for accessing the data from the cluster. Moving the mesh and session files from a PC terminal to a cluster is quite fast because they are small. However large amounts of data are typically required for the analysis of the unsteady flow behind the MP4-17D front section for example. This is a problem for both retrieving data from HPC but also when post-processing, for example slices or iso-contours. Some of these features are directly implemented in `Nektar++` allowing for post-processing software to only render the scene without actually computing the iso-contour themselves thereby avoiding to load the entire flow field. This post-processing method allows for a reduction in bandwidth and memory required by post-processing software for visualising a given flow structure.

Lower number of DOFs are required for the same accuracy (especially in smooth regions of the flow). Even if Fluent or Star-CCM+ can scale to 100K cores they require many more DOFs per core. Also because information is less dense (i.e. each DOF contain less information) these computations produce much larger data sets. In the limit of infinitely large computing facilities the bottleneck in HPC CFD will be memory bandwidth and not compute power.

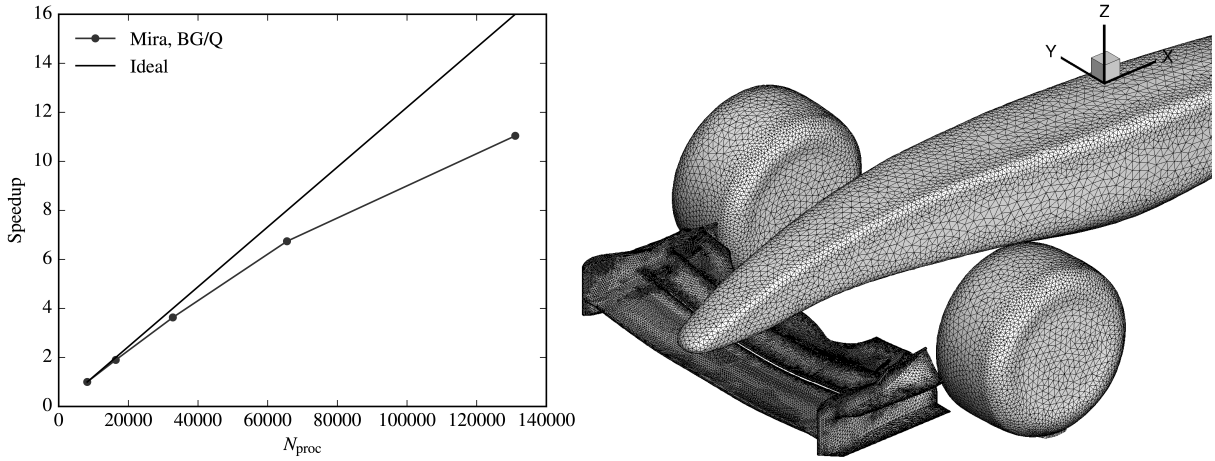



**Figure 2.3** – Scaling (•), relative to ideal scaling (−), of the McLaren MP4-17D test case on the peta-scale Blue Gene/Q supercomputer MIRA which was ranked as 9th fastest computer in the world as of November 2016 by Top500 project(https://www.top500.org).

### More efficient use of each core : the roofline model

Following the argument of Moxey *et al.* (2016*b*), on exa-scale systems with increasing core counts and more complex memory hierarchies data must be managed ever more efficiently to attain peak performance of each core. Effective use of state-of-the-art HPC facilities requires both efficient use of each core and efficient use of the available bandwidth. This becomes more important as computations scale from $O(10^15)$ FLOPS today towards $O(10^18)FLOPS$ by 2018.

For high-order methods and the spectral/hp element method in particular, most of the runtime is spent evaluating a dense matrix-vector multiplications which typically are more memory compact. In essence the dense nature of the matrices in the matrix-vector multiplications inherent to the spectral/hp element method offer a good ratio of operation intensity per bandwidth used. Colloquially, for every byte moved onto a given CPU of the HPC system a large number of operations are executed. The means of assessing the performance of a code can be understood using a roofline model (Figure 2.4) where the computation of the MP4-17D in Chapter 6 would correspond to $App_2$.

Ongoing development within the high-order community aims to further improve this inherent efficiency of the spectral/hp element method by collecting linear algebra operators on a single core (Moxey *et al.*, 2016*b*).

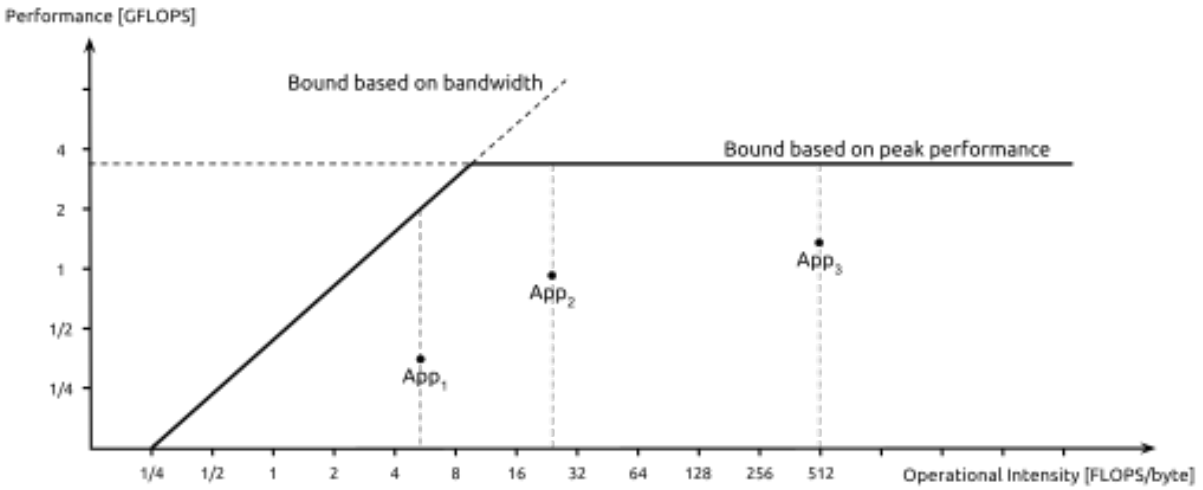



**Figure 2.4** – Low order codes are expected to operate in the bandwidth limited regime (App1), whereas high-order methods, thanks to their compact nature, are expected to operate closer to the peak efficiency of each CPU (App2). Source: adaptation of Williams *et al.* (2009).

### 2.2.4 Summary of the spacial discretisation method and its benefits

In summary we have shown the the spacial discretisation of the spectral/*hp* element method is particularly attractive because:

1. the discretisation is compact: thanks to the bubble/interior decomposition there are only two modes (in 1D) that do not vanish at the boundary.

2. contrary to commercial low-order methods, the polynomial order $P$ can be chosen on the fly, at run-time: a computation can be executed at order $P = 4$ and then if the resolution is deemed insufficient, it can be restarted at $P = 5$ by simply changing the expansion order in the session file.

3. for sufficiently smooth solutions $p$-refinement allows for an exponential rate of convergence (Babuška & Suri, 1994).

4. As we will see in Section 3.4 for practical industrial applications under-resolution prevents the solution from being smooth enough. However boundary-interior decomposition allows for reduced memory access and communication between elements (or partitions) which is attractive for deployment of this method onto ever larger HPC facilities.

Before discussing how the mapping $\xi_e$ between local regions (possibly with curved faces and edges) and standard regions (with straight sides and faces) is used for obtaining

CAD conforming curved elements we briefly present the temporal discretisation in Section 2.3 and the pre-conditionners used to accelerate the convergence of the iterative solvers.

## 2.3 Temporal discretisation

Most of the computations presented here employed a second-order accurate Implicit-Explicit (IMEX2) scheme (Maday *et al.*, 1990) . However the explicit time-stepping for the diffusion operator restricts the time-steps. A semi-implicit sub-stepping scheme (Xiu *et al.*, 2005) has been used since release `Nektar++ v4.0` that enables larger time-steps. A starting point for further reading regarding the time-stepping schemes available in `Nektar++` can be found in the User Guide. In the following paragraph we quantify the advantage of leveraging the implicit time-stepping scheme as opposed to the second-order implicit-explicit scheme.

#### Time-step restrictions and Courant-Friedrichs-Lewy conditions

Within the spectral/hp element method, similarly to the Courant-Friedrichs-Lewy conditions for low-order methods, with a fully explicit time-integration scheme the time-step is limited by (Karniadakis & Sherwin, 2005):

$$\Delta t \leq \frac{\alpha_{\Im} h_{\min}}{\max(|V^e(t)|) c_\lambda P^4} \tag{2.5}$$

where $\alpha_{\Im} \approx 0.723$ for the third order Adams Bashforth scheme and $c_\lambda$ depends on the quadrature points used ($c_\lambda \approx 0.2$ for Gauss-Lobatto-Legendre). $P$ is the polynomial order of the basis and $h_{\min}$ the size of the smallest element. The strong limitation this condition imposes is a motivation for semi- or fully implicit time-integration schemes.

Three key points of paramount importance for the computations undertaken throughout this study should be emphasised :

1. the velocity $V^e(t)$ is the velocity within the deformed element. However the mapping towards the standard element yields a standard velocity $V^{std.}(t)$ that may be greater. Strongly deformed elements might introduce stringent restrictions in time-steps even in regions of the flow where the velocity as measured in the deformed element, does not seem important.

2. the velocity $V^e(t)$ also depends on time. Therefore high frequencies within an element can contribute to generate numerical noise or general under-resolution. For LES this also negatively affects the maximum allowable time-step for numerical stability.

3. finally the maximum time-step scales as $\Delta t \sim P^{-4}$ which means that, for unsteady simulation, the attractive convergence properties of the spectral/hp element method are accompanied by stronger time-step restrictions as the polynomial order is increased.

**Summary of the the time-integration schemes used and their effect on the solution**

In summary, the semi-implicit time-stepping scheme allows for larger time-steps and reduced computational effort which are of paramount importance when the multi-scale geometries produce multi-scale flow physics such as the $y_{250}$ on a MP4-29 vortex. Further improvements in relaxing the CFL restriction are envisaged by locally adapting the polynomial expansion and/or the elements of the mesh.

## 2.4 Boundary conditions

The spatial discretisation discussed in Section 2.2.1 requires adequate boundary condition for the well-posedness of the problem. Throughout this project we use five different types of boundary conditions:

1. classical Dirichlet boundary conditions for the vanishing velocity at the solid wall surface. This condition was used for the wing itself in the wingtip case as well as for imposing the rotation of the idealised wheel, and

2. classical Neumann boundary condition for slip boundaries used for the wall of the wind-tunnel in the wingtip case or the MP4-17D case where only the normal components of the velocity is required to vanish, and

3. the non-penetrative boundary condition of the contact patch used for the rolling wheel case where first the solid body of rotation is prescribed before adding a second condition of non-permeability (i.e. the velocity component normal to the surface of the contact patch vanishes), and

4. high-order outflow boundary(Dong *et al.*, 2014) condition to ensure the energetic structures advecting to the outflow cannot add momentum to the domain by reverse flow. This boundary condition was essential in successfully modelling the $y_{250}$ where a region of the recirculating wheel that is not represented in the computational domain introduced instabilities. This outflow boundary was modified to take into account a prescribed pressure field and,

5. finally mapped boundary conditions allowing for the possibility of embedded simulations or combining experimental and numerical work(Serson & Meneghini, 2015). This was the case for the computations of the delta-wing wake in collaboration with Cambridge.

Details of the implementation of these boundary conditions can be found in both Karniadakis & Sherwin (2005) and www.nektar.info.

## 2.5 A note on the sources of error

In view of better understanding the quality of the computed solutions it is constructive to introduce a model to assess the total error:

$$\varepsilon_{\text{Total}} = \varepsilon_{\text{Proj.}}\varepsilon_{\text{Diff.}}\varepsilon_{\text{Disp.}}\varepsilon_{\text{Time}}\varepsilon_{\text{BCs}} \tag{2.6}$$

where the projection error $\varepsilon_{\text{Proj.}}$ is introduced with the initial conditions when they are projected from either an analytical expression, such as in the Taylor-Green vortex case or through interpolation from a RANS or DES/LES solution as in the McLaren MP4-17D test case. The dispersion and diffusion errors $\varepsilon_{\text{Diff.}}\varepsilon_{\text{Disp.}}$ are produced by both the underlying CG scheme as well as from under-resolution that is produced by a number of aliasing terms as well as the action of the artificial viscosity. The $\varepsilon_{\text{Time}}$ error are produced by the truncation of the time integration scheme and, finally the boundary condition errors $\varepsilon_{\text{BCs}}$ are introduced, when an analytical solution of interpolated solution from a previous RANS or DES/LES computations are used, for example when an embedded simulation is performed.

For the Taylor-Green vortex case presented in Chapter 3 the dispersion and diffusion errors dominate in the better resolved cases but the projection error of the original solution might be more important for the coarsest computations.

For the MP4-17D computation presented in Chapter 6 there are large errors when the RANS solution is projected onto the mesh and so $\varepsilon_{\text{Proj.}}$ is believe to be dominant.

Finally in the computation of the $y_{250}$ the BCs interpolated from the DES to make-up for the missing endplate introduce considerable error.

This simplistic model just serves as a reminder for the dominant source of error polluting a computational solution.

## 2.6 Key recent and ongoing developements

In this section we briefly presented the Continuous Galerkin formulation of the spectral/hp element method that has been employed for the computations presented in this thesis. Because the objective of this thesis was the development of the entire CFD package for deployment in the Formula One industry we will only discuss the modifications to the spectral/hp element `Nektar++` that have taken place during the course of this project however the `Nektar++` community is active in many other fields (Cantwell *et al.*, 2015) and to name a few developments we mention :

1. development and validation of SVV for hexahedra, tetrahedra and prisms as well as for Fourier modes. The first application of the SVV filter is reported in Chapter 4 based on Lombard *et al.* (2016) and was used in Bao *et al.* (2016), Serson *et al.* (2016),Xu *et al.* (2016*a*, 2017*a*),

2. prism splitting Moxey *et al.* (2015*b*),

3. p- adaptationEkelschot *et al.* (2017) , paving the way for r- adaptation Moxey *et al.* (2016*c*) (Ekelschot, 2016),

4. underpinning improvements in implementation Moxey *et al.* (2016*a*),

5. more recently NekMesh Turner *et al.* (2016, 2017),

6. developing the stability solver for HPC Bolis *et al.* (2016),

7. motivating the use of HDG to improve the efficiency of CG Yakovlev *et al.* (2016),

8. developing encapsulated SFD for determining steady states of complex flows,Jordi *et al.* (2014) together with a detailed reporting of this research in Jordi (2015),

9. together with fundamental aspects of ensuring the `Nektar++` framework can continue to be developed sustainibly by a growing community of users Cohen *et al.* (2014),

10. time-stepping Vos *et al.* (2011) and

11. and finally activities of the research group in the field of electro-cardiology led by Dr. Cantwell have resulted in further development of the code that has been used throughout this project Cantwell *et al.* (2014)

and to name a few key studies underpinning the use of spectral/*hp* element methods for high-fidelity computation of Formula One related flows we name :

1. improve the understanding of the advantage of h- or p- refinement Cantwell *et al.* (2011),
2. de-aliasing study underlying the influence of *geometric aliasing*,
3. the work by Moura *et al.* (2015, 2016, 2017) regarding the natural dissipation and resolution power of both CG and DG. He also underlined similarities between CG+SVV and DG and
4. as well as understanding how best to leverage HPC resources Bareford *et al.* (2016).

These developments of the spectral/hp element framework `Nektar++` together with underpinning studies just mentioned have allowed for new contributions to diverse fields outside of the motorsport context of this thesis. To name a few :

1. boundary layer flow (Xu *et al.*, 2014, 2016*a*,*b*),
2. transition to turbulence work towards laminar-flow control for aeronautical applications (Xu *et al.*, 2017*a*,*b*),
3. flow control Rocco & Sherwin (2015), Rocco *et al.* (2015) and
4. cardiac electrophisiology Tzortzis *et al.* (2015).

In the following Chapter 3 we will focus on the key developments of the spectral/hp element method, implemented into `Nektar++`, that rendered high-fidelity LES over the MP4-17D front-section possible demonstrating the industrial worthiness of the high-order methods.

# Chapter 3

# The evolution of Nektar++ from DNS to high-fidelity LES

In Chapter 2 we defined the governing equations of the flow as well as described the spatial and temporal discretisation used by the spectral/hp element method. More importantly we discussed how this method aligns well with peta- and anticipated exa-scale HPC facilities thanks to its compact nature. We also showed how, thanks to the local basis chosen, the order of the computation can be chosen at run-time by changing one line in the session file as opposed to having to run a completely different version of the code and/or recompile it on the HPC facility. We also presented a classical case of fast convergence properties that motivated the development of spectral and then spectral/hp element methods at the beginning of their development. Combined these developments promoted spectral/hp element methods to be used in a setting of Direct Numerical Simulation limited to academia during the end of the 90's and 00's with for example the harbour problem Karniadakis & Sherwin (2005).

Three further attributes of the spectral/hp element method make it a compelling candidate for resolving the highly unsteady flow around a Formula One car and, more generally, around bluff bodies and lifting surfaces :

1. highly developed meshing capability,

2. low dispersion/diffusion error and

3. no-model accounting for the sub-grid scales.

These three properties are quintessential when aiming to accurately model the development of multiple interacting vortical structures generated by a Formula One front-wing interacting with the rotating wheel and then advecting towards the rear-wing and diffuser assembly. Demonstrating that the spectral/hp element method can track multi-scale flow

features over large spacetime scales has been one of the key objectives of this study. In the following few sections we will report the developments incorporated in the `Nektar++` framework to build on the highly capable DNS solver into the highly capable LES solver it is as of `Nektar++` v4.4.

## 3.1 Low dispersion/diffusion error of the spectral/hp element method

In Section 2.2.3 we showed why the spectral/hp element method is attractive in terms of convergence. Steady computations this is sufficient, however for unsteady computation it is equally important for a code to have low dispersion/diffusion error. For sufficiently smooth solutions the continuous Galkerin formulation of the spectral/hp element method, used throughout the work present in this thesis, offers much lower numerical dispersion/diffusion that its low-order counter-parts. This property explains why fully spectral or spectral/hp element methods are favoured for direct numerical simulations of transition to turbulence in a boundary layer for example(Xu *et al.*, 2017*a*).

### 3.1.1 Gaussian vortex advection : low dispersion and diffusion error.

The constant advection about the origin of an off-centred 2D Gaussian in the $[1,1]^2$ domain is a classical test case used for assessing both the spatial and temporal accuracy of a solver :

$$\begin{aligned} \partial_t u + \nabla \cdot \mathbf{F} u &= 0, && (3.1)\\ \mathbf{F}(u) &= \mathbf{V}(u), && (3.2)\\ \nabla \cdot V &= 0, && (3.3)\\ \mathbf{V} &= (V_x, V_y)^T && (3.4) \end{aligned}$$

and exact solution of the velocity field $u(x,y,t)$ at time $t$ given by:

$$u(x,y,t) = \exp\left(-41\left[(x - 0.3\cos(2\pi t))^2 + (y - 0.3\sin(2\pi t))^2)\right]\right)$$

which corresponds to a Gaussian of standard deviation $\sigma = 0.11$ rotating about the origin with a radius of 0.3. Dirichlet boundary conditions with vanishing velocity are used for the four borders of the domain where the maximum value of the velocity from the Gaussian does not exceed $O(10^{-9})$. The $\Omega = [1,1]^2$ domain is then discretised using either 128,

32 or 8 triangular elements within which the local solution is approximated by first-, third- and eighth-order polynomials respectively. The solution is then advanced in time for five full rotations about the origin. The results, reported in Fig. 3.1, emphasise the lower diffusion of the final solution for the higher-order discretisation (8 elements at P=8) rather the lower (128 elements at P=1), motivating the use of a high order discretisation in this case for minimising the error. Note that the second order Implicit-Explicit time-integration scheme introduces a negligible phase average error compared to the diffusion error of the spatial discretisation.

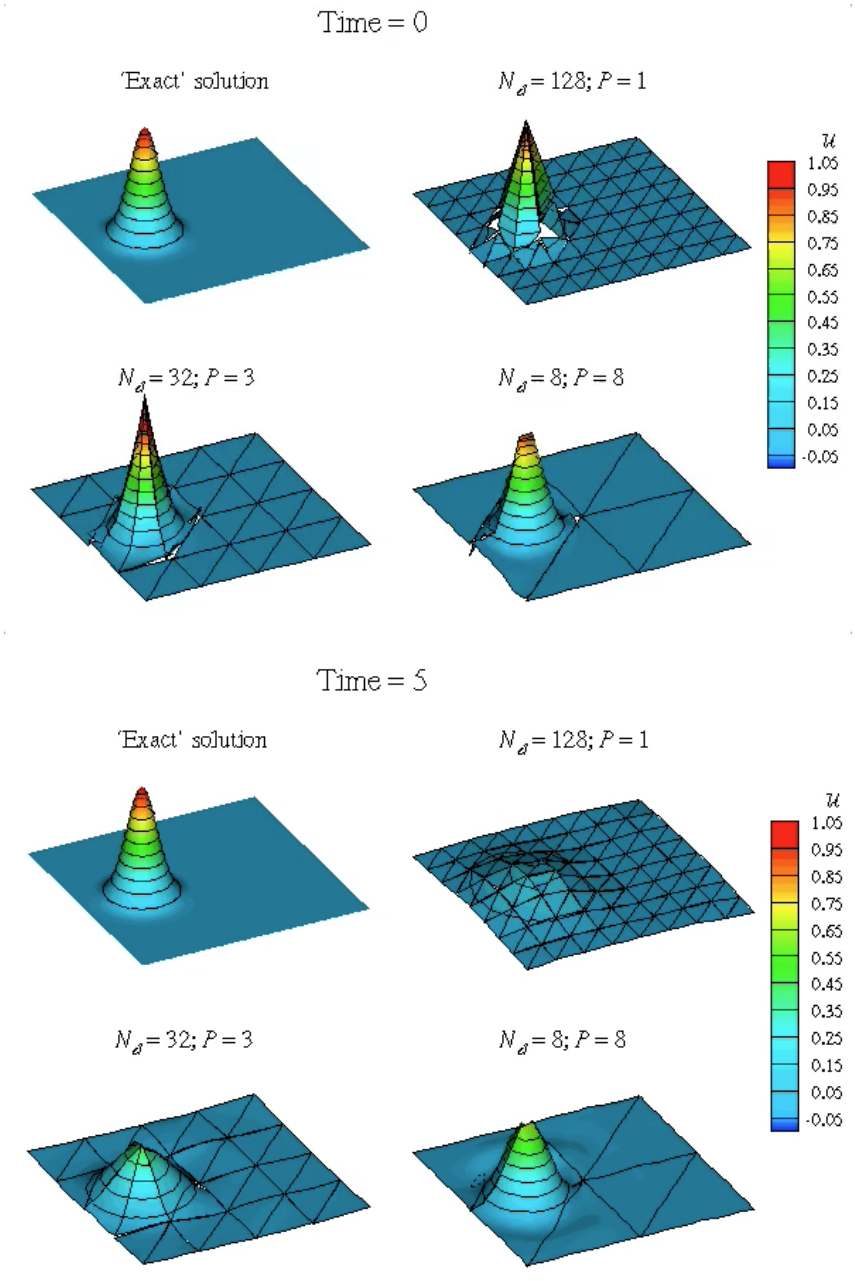



**Figure 3.1** – Advection of the Gaussian vortex

### 3.1.2 Isentropic vortex advection : comparison between high- and low-order codes

Vermeire *et al.* (2017) compare the diffusion and dispersion error for an advecting isentropic vortex of a high-order spectral/hp element method against second- and third-order STARC-CCM+. Contrary to `Nektar++`, PyFR is based on the flux reconstruction scheme introduced by Huynh which generalises the DG formulation used by `Nektar++`. Similarly to the Gaussian vortex, the isentropic vortex has an analytical solution of Euler's equation at all times allowing for a straightforward comparison of error between different codes. In the $\Omega = [-40, 40]^2$ domain with periodic boundary conditions, the initial flow field is given by :

$$\rho = \left[1 - \frac{S^2 M^2 (\gamma - 1e^{2f})}{8\pi^2}\right]^{\frac{1}{\gamma-1}}, \tag{3.5}$$

$$u = \frac{Sye^f}{2\pi R}, \tag{3.6}$$

$$v = 1 - \frac{Sxe^f}{2\pi R}, \tag{3.7}$$

$$p = \frac{\rho^\gamma}{\gamma M^2} \tag{3.8}$$

with $u, v$ the velocity components, $p$ the pressure, $\rho$ the density, $M$ the freestream Mach number, $R$ the radius, $S$ the vortex strength, $S = 13.5$ and $\gamma = 1.4$ and $f = (1 - x^2 - y^2)/2R^2$. The simulation is run for fifty flow-throughs. For the PyFR computation $80^2$ quadrilateral elements with $P = 5$ polynomials are used for the spatial discretisation and a five stage fourth-order Runge-Kutta scheme is used for time-stepping. Both the second- and third order STAR-CCM+ computations were performed on a $480^2$ quadrilateral mesh. The second-order computation used an implicit second order time-stepping scheme. For the third-order STAR-CCM+ computation a Monotonic Upstream-Centered Scheme for Conservation Laws (MUSCL) scheme is used.

The results of the comparison of the density contours after $t = t_c$, $t = 5t_c$, $t = 10t_c$ and $t = 50t_c$ are shown in Figure 3.2. The $P = 5$ solution from the PyFR solver is qualitatively identical to the analytical solution after $t = 50t_c$ whereas both second- and third-order STAR-CCM+ computations show considerable discrepancy in terms of both diffusion and dispersion error with the amplitude of vortex severely affected as well as its position relative to the analytical solution. Vermeire *et al.* (2017) further report the PyFR computation to be five orders of magnitude more accurate than the third-order STAR-CCM+ case at one order lower cost that is measured as the price of the hardware used multiplied by the number of seconds it was used.

Together with the Gaussian vortex, these two test cases motivate the attractiveness of high-order methods that are believed to offer better accuracy for a given computational case. This however might not be true for non-smooth solutions where the attractive properties of the spectral/hp element methods do not hold. In this scenario the increase in computational resources required for a higher-order computation are not offset by an increase in the accuracy of the solution. In the next section we discuss recent results from (Moura *et al.*, 2017) that seem to indicate that even in cases of under-resolved computations, i.e. where the convergence properties of the high-order methods aren't as good, a higher-order discretisation still contains a more accurate solution.

### 3.1.3 Burgers turbulence : high resolving power

The advection of the isentropic vortex is a case of a smooth solution that can be well captured by the spectral/hp element method and shows an exponential rate of convergence as the polynomial order is increased. However if the isentropic vortex cannot be well resolved it may lead to instability of the simulation. Another classical example of this phenomena where a flow feature is not captured by the mesh and can lead to numerical instability is the Burgers equation. A shock forms at the origin and, because of the sharp, local gradient, strong oscillations can be seen in the velocity profile. These oscillations, are akin to Gibbs phenomena whereby spurious oscillations are produced in the partial Fourier series approximation of a discontinuous function. Increasing the number of Fourier modes (in spectral space) or increasing the order of the polynomials within elements does not suppress this behaviour.

Following Moura *et al.* (2015), the inviscid Burgers' equation is force with a white-in-time function F(x,t) :

$$\partial_t u + \frac{1}{2}\partial_t u^2 = \frac{A_F}{\sqrt{\Delta t}} \sum_{N \in \mathbb{N}_F} \frac{\sigma_N(t)}{\sqrt{|N|}} \exp\left(i \frac{2\pi N}{L} x\right) \tag{3.9}$$

where $\mathbb{N}_F = \{\pm 1, ..., \pm N_c\}$ where for wavenumber $k > k_c = 2\pi N_c/L$, the cut-off wavenumber, the forcing vanishes. $A$ is the forcing amplitude and $\sigma_k$ is a standard Gaussian random function with $\Delta_t$ the time step and $L$ the domain length of the computation. This forcing is used to reproduce a -5/3 slope in the inertial range of the energy spectrum $E(k) \sim k^{-5/3}$ mimicking that of the Navier-Stokes turbulence.

The main argument to make is that in the wake, for a given number of degrees of freedom it might be beneficial to aim for higher $p$. This result however has not been shown for actual geometries (only 1D forced Burgers turbulence and 3D "Euler turbulence").

The spectral/hp element seems to be a pertinent candidate for investigating the evo-

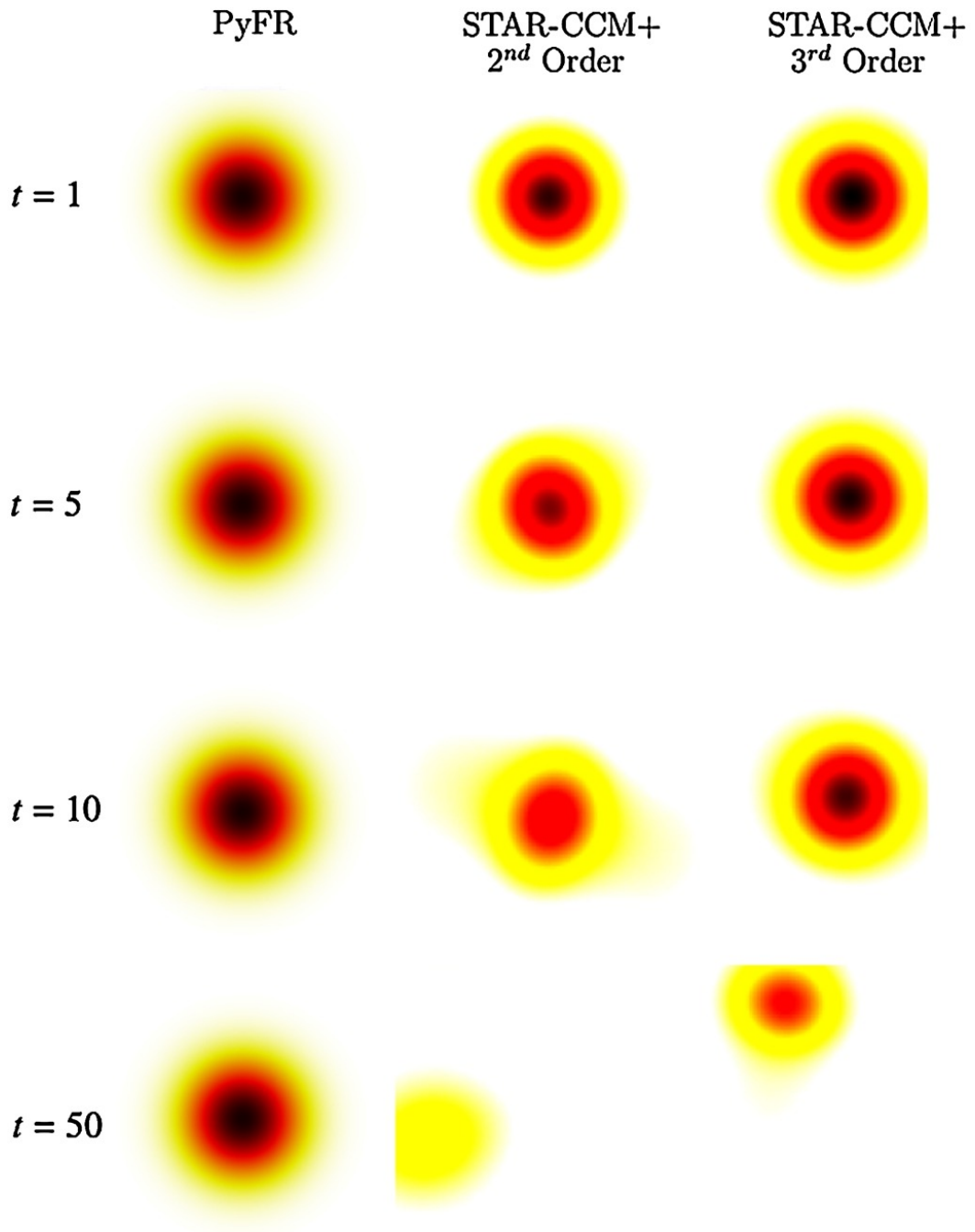



**Figure 3.2** – Lower diffusion and dispersion error for the isentropic vortex case with high-order methods, such as PyFR on the left, compared to 2nd and 3rd order spatial discretisation for STAR-CCM+. Source: Vermeire *et al.* (2017).

lution of important flow features over large spacetime scales because of their inherent low diffusion/dispersion error. The $y_{250}$ vortex produced by the front-wing with a cord of roughly 20cm develops in conjunction with vortices shed from the flap and vane, before interacting with the suspension elements, the wheel wake and the side-pods over a

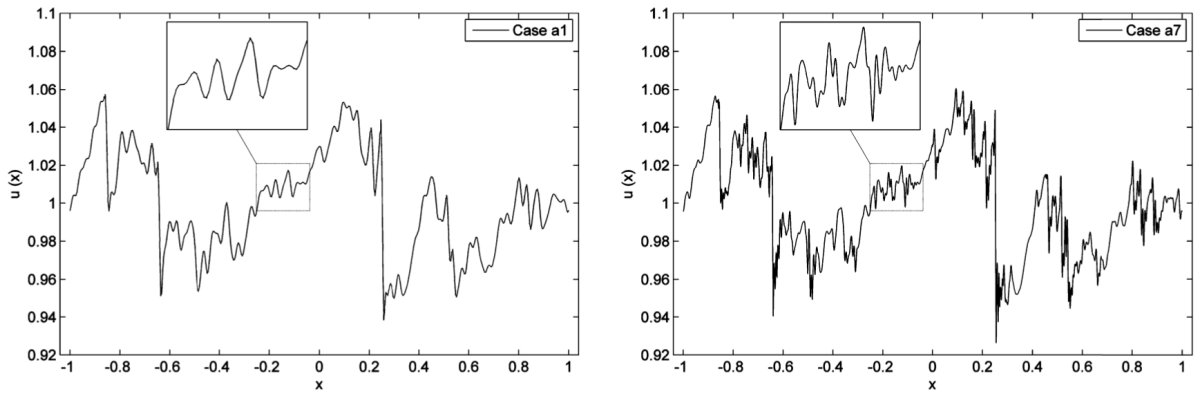



**Figure 3.3** – Comparison between the solutions on two mesh of the forced Burgers turbulence where the mesh in b) is four times coarser than the mesh in a) for the same global degrees of freedom. The higher resolution of the solution with the higher p-refinement (but lower h-refinement) highlights the advantage of leveraging a higher order discretisation even in the case of 1D under-resolved turbulence (Moura *et al.*, 2017)

distance of 2m. The stability of this vortex and a characterisation of its meandering is considered to be an important indicator of the aerodynamic efficiency of a Formula One front-section(Nakagawa *et al.*, 2016). To be able to model this phenomena requires accurate modelling on the sub-millimetre scale. Effectively this problem requires resolving more than three orders of magnitude difference in geometric scales as well as large time-scales. These co-rotating vortices are known to be sensitive to pressure gradients as well as to the presence of other vortices as well as noise (Hoëssler, 2011). In view of these challenges a numerical method with low dispersion/diffusion appears to be a promising candidate.

When the project was initiated in 2012, `Nektar++` had been shown to be an enabling tool for investigating vortex development and stability at low Reynolds number. It was possible to run the wingtip case, presented in Chapter 4 at a Reynolds number, based on the wing cord, of $Re_c = 1 \cdot 10^4$.

The Reynolds number, based on the cord of the mainplane of the front-wing is typically of the order of $2 \cdot 10^4$ and the flow producing the $y_{250}$ for example requires resolving the complex geometry of the front-wing, suspension system, rolling wheel, sidepods, barge-boards and floor.

Thus the ambition of resolving the flow over a Formula One front section was two fold. Firstly we should generate a curved mesh of the Formula One front section and, secondly it would be necessary to improve the numerical stability of the spectral/hp element to mimimic the small dissipation scales associated to high-Reynolds number flows but not resolved.

In the next three section we first describe the evolution of the meshing pipeline that

is now capable of generating a high-order, or curved, mesh over a Formula One front section. We then describe the two developments that are used to stabilise the method when running a LES, namely de-alasing and the spectral vanishing viscosity.

## 3.2 High-order meshing of complex geometries capturing geometries with same accuracy as flow important for transitional behaviours

The first step in modelling the flow around a Formula One is obviously the ability to accurately represent the geometry in CAD software, followed by the ability to accurately discretise the surface and the volume in suitable manner for the numerical scheme. After seventy years of CFD, meshing remains an important bottleneck in the overall CFD workflow, and this is particularly true for high-order meshing. Unlike linear solvers, which use meshes consisting of straight-sided elements, high-order solvers require curved elements that align to the underlying geometry. In order to capitalise on the high-order discretisation, the mesh should also be coarse. The combination of these two factors makes high-order generation for geometries as complex as those considered in Formula 1 extremely challenging. The last ten years have seen a strong push in the development of high-order meshing capabilities however, in most cases, these meshing pipelines are not integrated in a coherent package together with a solver. These tools, such as Gmsh, have however proved invaluable since a plethora of open fluids flow problems exists where the geometries are not complex. For industrial application however, a close integration between the meshing pipeline and the solver is required so that the entire CFD workflow can be automated. In the next few paragraphs we report the efforts made in this direction and give an overview of meshing capabilities `NekMesh` offers as of `Nektar++ v4.0`.

### 3.2.1 How to prepare a geometry

Before discussing the two avenues we have investigated for meshing Formula One geometries, it should be stressed how important an adequate preparation of the geometry is for high-fidelity meshing and high-fidelity CFD simulations. Because the high-fidelity simulations presented in this thesis do not rely on wall modelling, accurately representing the geometry with curved elements at the surface is all the more important.

For a tool to be integrated properly into an industrial setting, it must be carefully integrated into the existing workflow. CAD representation of a geometry is the first means for a Formula One engineer to express his idea and, more importantly this idea, or

design, will be assessed by means of computational and wind-tunnel experiments. In order for a this idea to be machined in view of testing it in a wind-tunnel care must be given to the CAD drawing at the conception stage. Similarly, for computational experiments, and in particular for high-fidelity CFD where minute differences in geometry can, for example, provoke early detachment of the flow, it is paramount that a constant dialogue between CAD and CFD engineers is supported. This will be particularly crucial when transitioning from a low- to high-order CFD workflow. The experience acquired during this project motivates the following suggestions in terms of CAD design :

1. avoid duplicate CAD surfaces,
2. avoid holes (i.e. missing CAD surfaces in particular in regions of the geometry where simplifications where made for example in the brake ducting.),
3. trailing edges should be blunt edges with 1mm thickness (on the scale of a car),
4. prefer radius of curvature of more than 1mm or simplify them to sharp leading edges,
5. avoid fillets that might introduce small radius of curvature,
6. avoid gaps smaller than 5mm,
7. be mindful of the sensitivity of the wheel flow to the modelled geometry of the deformed tire.

### 3.2.2 Low-to-high order meshing : spherigons and prism splitting

In the following two paragraphs we discuss the meshing process used throughout most of this project. This method has been coined *a posteriori high-order meshing* by Turner *et al.* (2017) because it is essentially a two step procedure where first a linear, or low-order, mesh is produced with commercial code before it is deformed to conform to a high-resolution representation of the geometry and the boundary layer is refined.

#### Spherigon patches

The meshing pipeline used throughout this thesis is summarised in Figure 3.4. `Star-CCM+` is used to produce volumetric meshes composed of both prisms on the boundary layers and tetrahedra in the rest of the volume. This *linear mesh* is coarse compared to the corresponding mesh used for low-order solutions of the flow over a given geometry. The

high order polynomial within each element can however, recover the resolution if desired. At this point, the boundary layer mesh is composed of a single *macro* prism whose height is of the same order of magnitude as the local boundary layer thickness $\delta_{99}$. `Star-CCM+` is also used to prepare a higher-resolution surface mesh of the curved regions (such as the mainplane of the front-wing). The resolution is typically five to ten times higher and mainly depends on two factors: local curvature relative to the size of the macro prism and relative size of the prism element to the thickness of the surface. Spherigon patches are then applied to the triangular surface of the prism in Cartesian coordinates in contact with the surface (Figure 3.5). Towards the trailing edge of the main-plane for example the size of the triangular face of the prisms is greater than the distance between the intrados and extrados. This is particularly true if both the intrados and extrados are part of the same regions. When the spherigon patches are applied to the intrados, the normals from the extrados might be mistakingly taken leading to degenerate elements. To avoid these elements a routine to remove the curvature from degenerate elements should be executed between the application of the spherigon patches and the boundary layer splitting. For a deeper discussion regarding spherigon patches we refer the interested reader to Section 3.2.2 of Hoëssler (2011).

#### Prism splitting

Prism splitting is the second step in this workflow (Figure 3.4). The original prism that has now been curved by the spherigons patches is then split with a growth rate starting from the surface to resolve as much of the boundary layer flow physics as can be afforded. The great advantage of this prism splitting is that it cannot produce degenerate elements if the spherigon curved prism was not degenerate adding much appreciated robustness to the workflow because the prism is split in element space before it is mapped to the cartesian space. Details relating to this method as well as the mesh produced for both the wingtip and McLaren MP4-17D test case can be found in Moxey *et al.* (2015*a*).

### 3.2.3 Direct high-order meshing : NekMesh

The main drawback of spherigon patches is that they are simply a way of smooth a rough surface, and do not necessarily align to the CAD surface. Direct high-order mesh generators have seen a growing interest since the early work of Persson & Peraire (2009) and are reaching levels of maturity compatible with deployment into Formula One industry. Within the `Nektar++` community David Moxey, Michael Turner and Joaquim Peiro have been the main instigators of this thrust (Turner *et al.*, 2016, 2017, D. Moxey & Sherwin, 2013). High-fidelity modelling of fluid flows can only be as good as the high-fidelity rep-

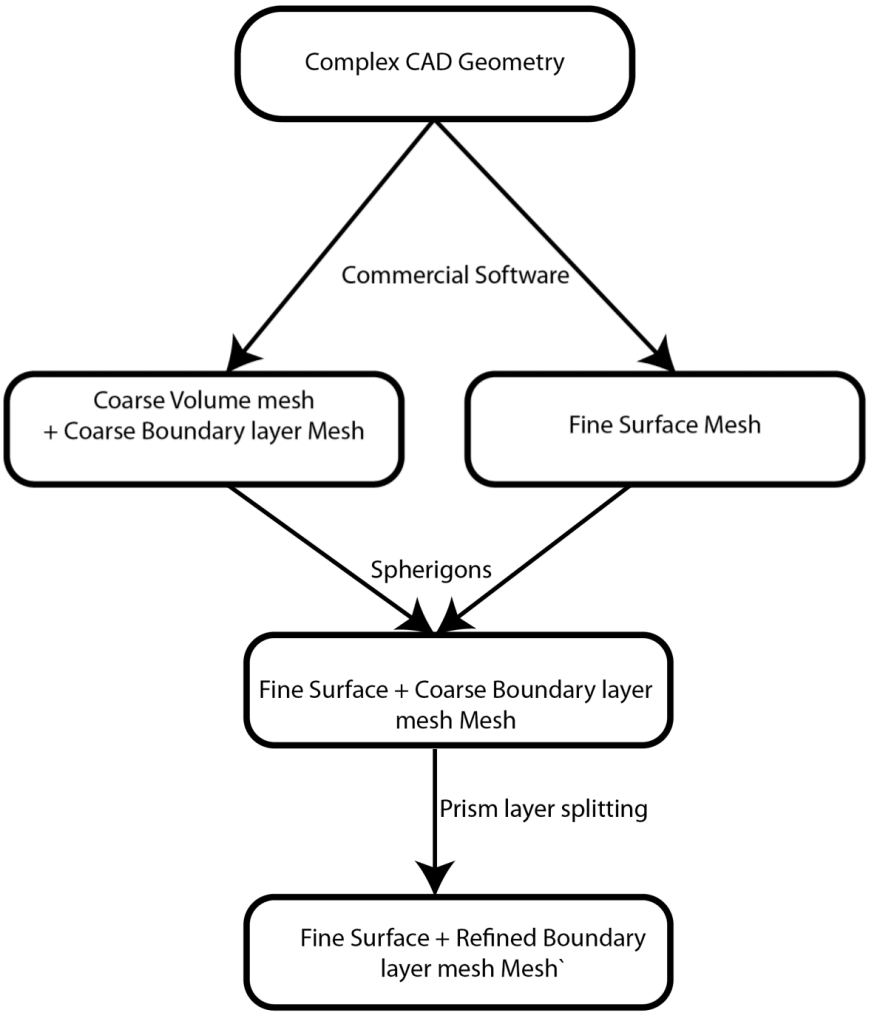



**Figure 3.4** – Meshing pipeline

resentation of the geometry producing the flow features. The subtle development of the three-dimensional boundary layer on the rounded wingtip of the wingtip case for example requires accurate modelling of the curvature too accurately modelling the detachment of the boundary layer as it rolls up into a system of vortices generally referred to as *the* wingtip vortex. There is no point in aiming to compute the detachment over a curved surface if it is represented by linear elements that represent non-negligible discontinuities in curvature since these might artificially provoke detachment. This is also the case for mesh generated in the aim of assessing transition towards turbulence such as (Xu *et al.*, 2017*a*). Despite high-order meshing being subject to intense research accompanying the development of high-order solvers, during the course of this project it was still necessary to be an expert in high-order methods to generate valid high-order mesh. The time-scales required in generating a valid mesh for an expert user remains a challenge and a bot-

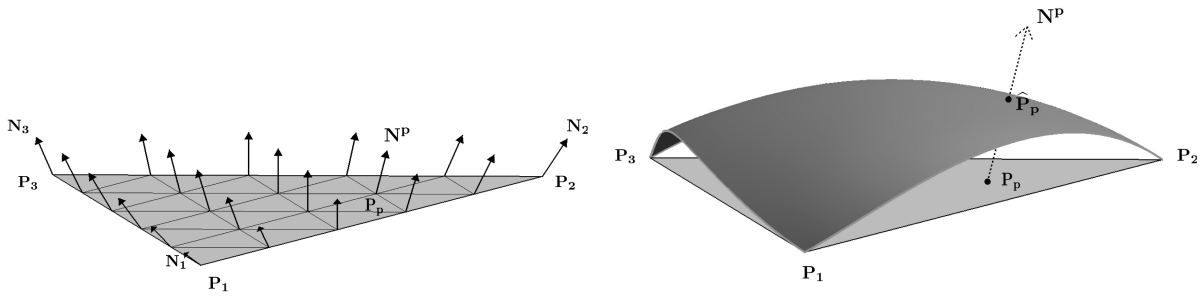



**Figure 3.5** – The first step in the high-order meshing procedure is to deform the boundary layer macro-prisms (i.e. there is only one layer of prisms in the low-order mesh). The higher resolution mesh is used by the spherigon patches to inform with the definition of the normals at a finer level so that the macro-prism is deformed. Note that this procedure only conserves $C^0$ tessellation of the surface producing, in regions of low resolution, non-physical kins that can, in turn, affect the boundary layer flow by promoting transition.

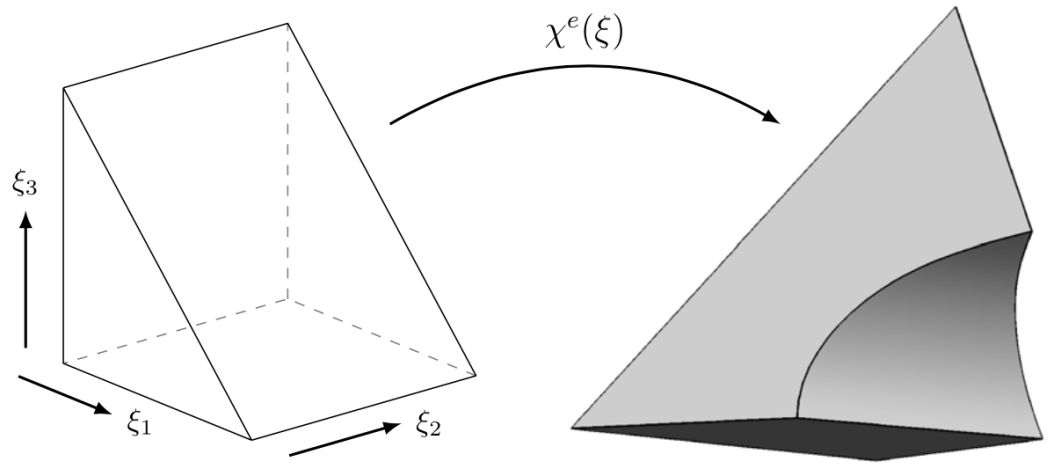



**Figure 3.6** – Element mapping $\chi^e(\chi)$ from the element in standard space $\Omega_{st}$ to the cartesian space $\Omega^e$.

tleneck in a *high-fidelity vehicle development program*. `NekMesh` aims to overcome these challenges. The interested reader is referred to Turner (2017).

## 3.3 De-aliasing : maximising the potential of the method

De-aliasing, over-integration of the linear operators or consistent integration of the non-linear operators refers to using more quadrature points than would otherwise be necessary for representing a polynomial approximation to a solution in a given element. For example integrating a polynomial of order $\mathscr{P}_{2P}$ requires at least $Q_{\min} \geq P + 3/2$ Gauss-Lobatto-Legendre polynomials for exact integration. As correctly de-aliasing to avoid adding spurious solutions during integration simply requires knowing the knowing the polyno-

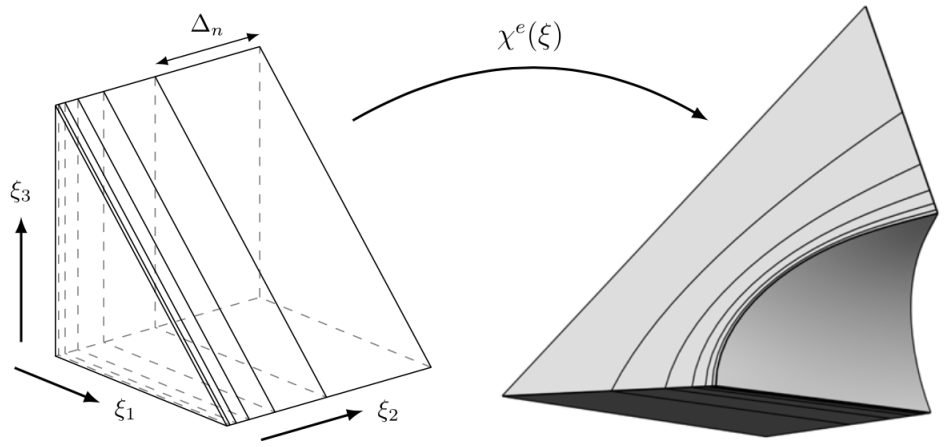



**Figure 3.7** – Once the prism is split into multiple prisms in the standard region it is isoparametrically mapped by $\chi^e(\xi)$ to the cartesian space $\Omega^e$ ensuring the prisms splitting hasn't introduced degenerate elements.

mial order of the integrand. The convection term of the incompressible Navier-Stokes is non-linear of order 2. For a curved element, the integration operator is performed on the standard region with an isoparametric mapping between the curved space and the standard region. This mapping introduces an additional order to that of the equation under-consideration. For the incompressible Navier-Stokes equations, over a curved mesh, the non-linearity is of order 3.

The comparison between two different quadratures, with global de-aliasing and without, is contrasted by computing the $L_2$ norm of the differences in velocity fields :

$$L_2(u_Q, u_{\text{exact}}) = \sqrt{\sum_{i=0}^{N} \left[(u_Q)_i - (u_{\text{exact}})_i\right]^2 w_i}$$

where $w_i$ are the quadrature weights, $(u_Q)_i$ is the solution at point $i$ for a quadrature $Q$ and $(u_{\text{exact}})_i$ is the solution at the same point $i$ when using exact or global-dealiasing for the integration.

### Geometric aliasing and the importance of global aliasing (or consistent integration)

In summary to this section we emphasis the importance of global de-aliasing (or consistent integration) of the Navier-Stokes equations onto curved elements by employing at least $Q_{\min}$ quadrature points, given by :

$$\boxed{Q_{\min} \geq P_{\text{expansion-order}} + \frac{P_{\text{non-linearity-order}} + P_{\text{order of Jacobian}} + 3}{2}} \tag{3.10}$$

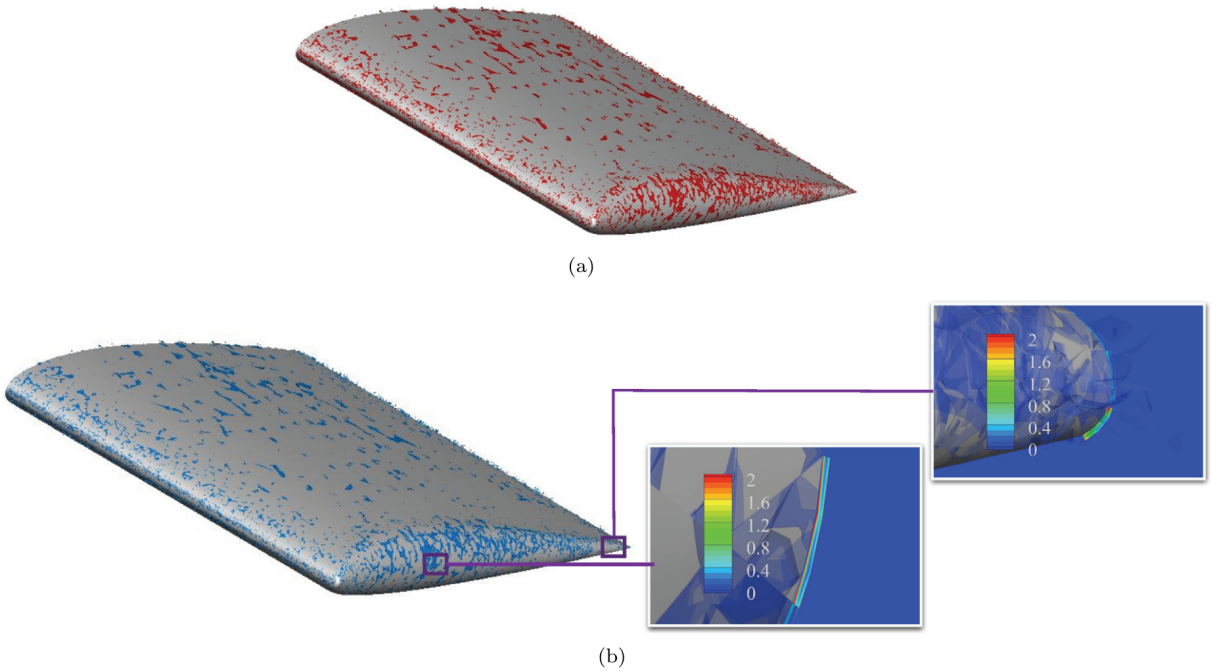



**Figure 3.8** – Aliasing error of the non-linear term a) and total aliasing error in b) between a solution computed with and without global de-aliasing (or consistent integration of both the non-linearities from the PDE as well as from the geometric factor).

**Example** For example, considering the solution of the Incompressible Navier-Stokes, that have second-order non-linearities ($P_{\text{non-linearity-order}}$ ), on a mesh of prisms (the tetrahedra are not deformend) of the wingtip case from Chapter 4 with $P = 4$ would require at least :

$$Q_{\min} \geq 4 + \frac{4+3}{2} = \frac{15}{2}$$

For a consistently integrated solution of a 3rd order solution (with P=4) in the curved prismatic elements forming the boundary layer mesh $Q_{\min} = 8$ quadrature points are required.

## 3.4 Spectral Vanishing Viscosity (SVV)

When length scales associated to physical dissipation are not resolved they need to be *modelled* de-aliasing does not suffice to avoid spurious oscillations of the solution and ultimately numerical instability. The focus of our investigations will be around implicit LES, i.e. where the diffusion through the grid is used to model these scales, instead of a sub-grid scale model as found in explicit LES. However, traditionally implicit LES relies on the assumption of a diffusive method as typically found at lower orders. Due to the low diffusion and dispersion of the spectral/hp method, when running an under-

resolved simulation we therefore require a source of artificial viscosity to stabilise the simulation and provide a modelling effect. In this work we consider the spectral vanishing viscosity (SVV) kernel, which is a modification to the Laplacian term in the Navier-Stokes equations and allows us to filter unwanted energy from high-order modes and stabilise the simulation. In the below we give a brief overview of the formulation and how this aligns with the spectral/hp element method.

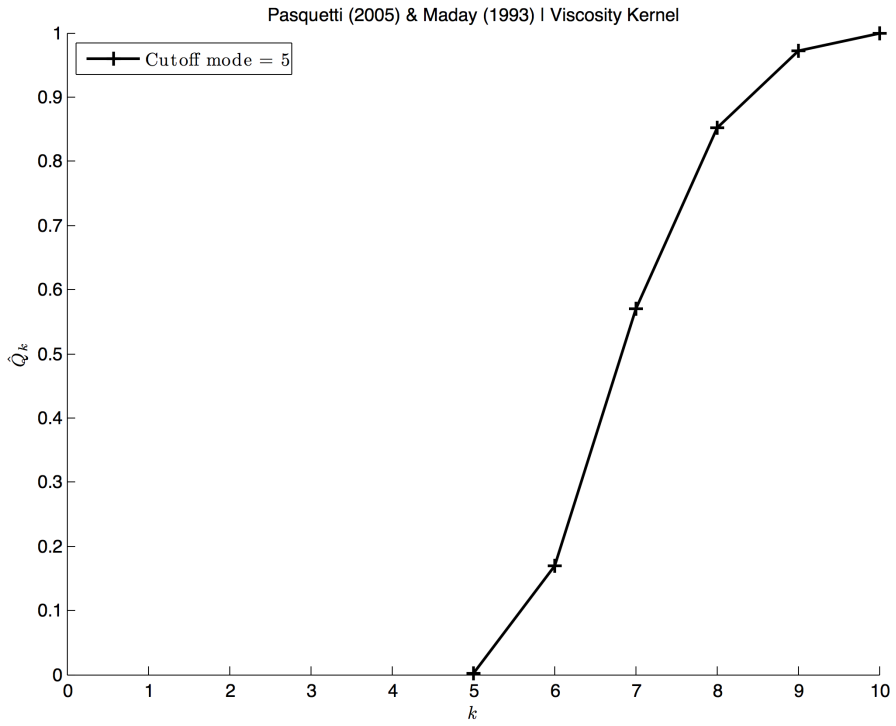



**Figure 3.9** – Spectral Vanishing Viscosity kernel for n=11 modes with a cut-off at m=5.

Following the original introduction of SVV by Tadmor (1989) we consider the inviscid Burgers' equation

$$\partial_t u(x,t) + \partial_x \left( \frac{u^2(x,t)}{2} \right) = 0 \tag{3.11}$$

with initial conditions $u(x, t = 0)$ on a periodic $[-\pi, \pi]$ domain. Spontaneous jump discontinuities, or shocks, may develop leading to numerical instability. The unique physical solution requires adding a condition on the entropy for example but in the context of the Spectral Vanishing Viscosity we are only interested in obtaining a solution by augmenting the problem with numerical smoothing that prevents spurious oscillations about the shock. The key attractiveness of the SVV is that it succeeds in introducing sufficient viscosity for numerical stability all the while preserving the spectral convergence properties of the underlying spectral or spectral/hp element method. This was proven in Tadmor

(1989) and motivates our interest for the SVV in the context of the spectral/hp element method. The numerically stabilised inviscid Burgers' equation can then be written as :

$$\partial_t u(x,t) + \partial_x \left( \frac{u^2(x,t)}{2} \right) = \varepsilon \partial_x \left( Q_\varepsilon \partial_x u \right) \tag{3.12}$$

where $\varepsilon \in \mathbb{R}^+$ and $Q_\varepsilon$ is a viscosity kernel whose form we will defined shortly. In the present context of spectral/hp element method the elemental operator associated to the SVV takes, in Dim dimensions the form:

$$S^e_{VV}(\mathbf{v}, \mathbf{u}) = \varepsilon \sum_{i=1}^{\text{Dim}} (\partial_{x_i} \mathbf{v}, Q_{\text{Dim}} * \partial_{x_i} \mathbf{u})_{\Omega^e}$$

where $(,)_{\Omega^e}$ is the Legendre inner product in the elemental region $x \in \Omega^e$, $\mathbf{v}$ a $C^0$ continuous test function and with $\mathbf{u} \in C^0$.The viscosity kernel $Q_\varepsilon$ is non-linear and vanishes for the lowest modes defined in Pasquetti (2005) by $Q_\varepsilon = \exp[-(k-n)^2/(k-m)^2]$ for $k > m$ and zero otherwise where $k \in [1, ..., n]$ are the modes and $m$ is the cut-off mode from which the SVV does not vanish. The shape of the resulting kernel for a case with n=11 modes and a cut-off at m=5 is given in Figure 3.9.

Moura *et al.* (2016) have shown evidence of the similarity between DG discretisation and CG+SVV. They also proposed an alternate kernel formulation that aims to maintain a constant Peclet number regardless of the local size of the element, polynomial order or advection velocity.

Artificial viscosity is an attractive and straighforward means for suppressing artificial oscillations associated with high polynomial order representations of discontinuities.

**In summary** the spectral vanishing viscosity is particularly attractive for stabilising an under-resolved DNS all-the-while preserving the spectral accuracy of the underlying method.SVV is not detrimental to the spectral convergence properties of the underlying spectral/*hp* element method. For the kernel used throughout this study it is important to bear in mind that to keep the desired spectral convergence properties of the underlying CG-based spectral/*hp* element method the cut-off parameter $k_c$ should also be increased, otherwise, relatively more and more modes have added dissipation and so convergence is negatively affected. This can be considered a shortecoming of the original kernel introduced for SVV and motive alternate kernels such as the *power kernel* does not have this property introduced by Moura *et al.* (2016).

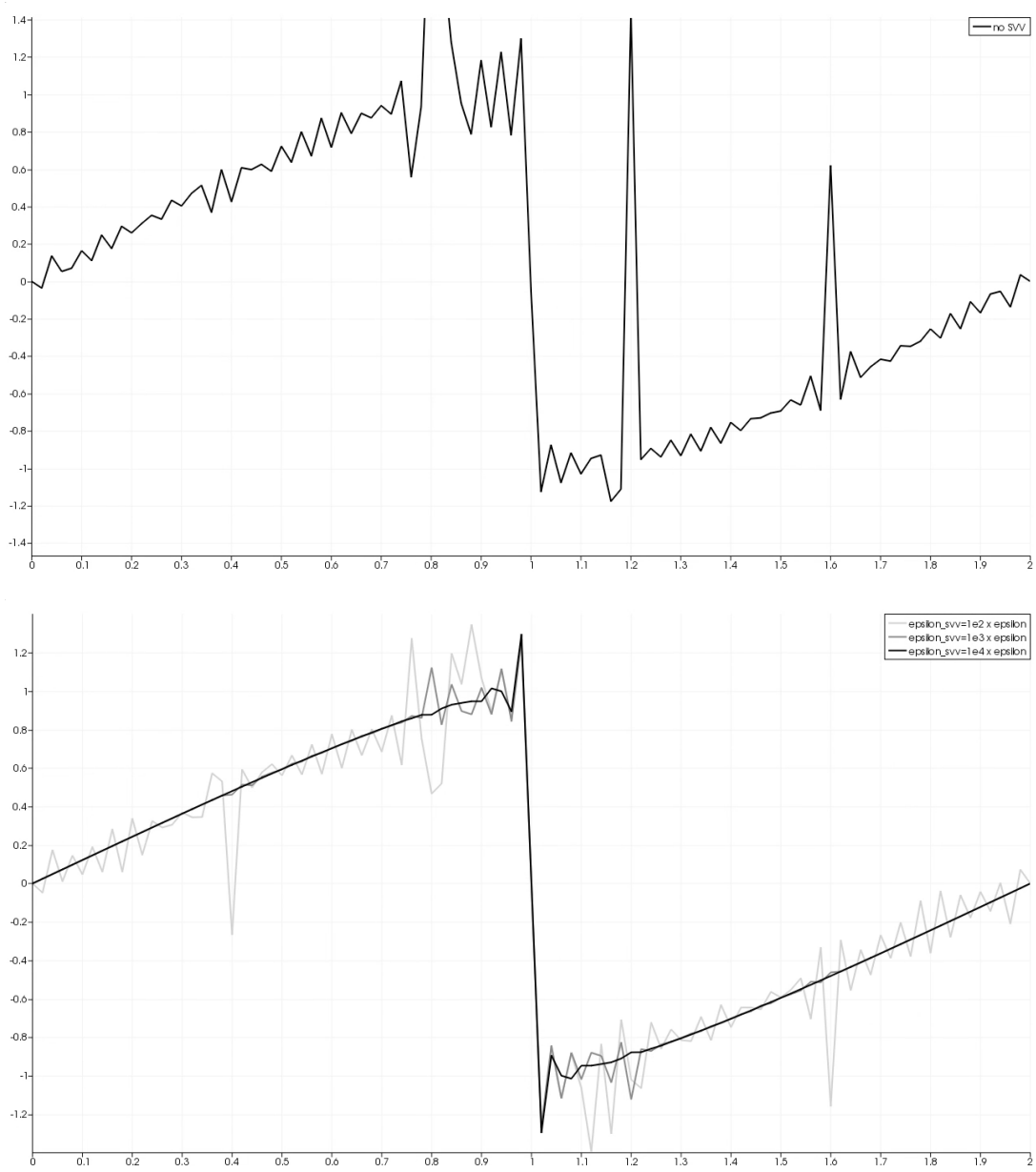



**Figure 3.10** – Diverging solution to the inviscid Burgers' equation after t=0.5 with five equi-spaced elements and 15th order polynomials (top). Solution to the inviscid Burgers' solution with added Spectral Vanishing Viscosity with $\varepsilon_{SVV}/\varepsilon = 10^2, 10^3$ and $10^4$ as the line gets darker.

## 3.5 Summary of Chapter 3

In summary this chapter has exposed examples of flows where the spectral/hp element method is particularly attractive because of its low dispersion/diffusion properties. We then showed how the meshing pipeline was developed towards the complexity required by a 2017 Formula One front-section. Finally we exposed the de-aliasing and SVV required for high-fidelity LES. In the following chapter we will present results of the computation of the wingtip vortex developing over a NACA 0012 profile with a rounded wingtip and

compare these results to independent experimental data.

# Chapter 4

# The rounded wingtip

## 4.1 Introduction

Understanding the development and growth of wingtip vortices over lifting surfaces is an ongoing research topic both in academia and industry. From an academic perspective, fundamental open questions remain, such as the possible re-laminarization of the vortex as it is shed from the wing Chow *et al.* (1997) and the origin of meandering Devenport *et al.* (1996), Jacquin *et al.* (2001), Heyes *et al.* (2004), the low-frequency movement of the vortex core and the evolution of the vortex structure. Vortices shed from lifting surfaces pose challenges to model in many an industrial context such as wind turbines, helicopter blades, high-lift configuration of aircraft and high-performance automotive industry Uzun *et al.* (2006), Uzun & Hussaini (2010), Rossow (1999), Ghias *et al.* (2005), Dacles-Mariani *et al.* (1995). Developing a better understanding of the near-wake of the vortex, lying within one chord length of the trailing edge of the lifting surface, is therefore essential in understanding the complex flow-structure interactions of interest in these problems. The far-field properties of these vortices are also a challenge for the aeronautics industry, where their persistence imposes strict limits on distances between landing aircraft Spalart (1998). For these reasons we are interested in refining modeling methods for investigating the growth of the vortex in the near-field.

Conceptually, the simplest approach to ensure that the flow physics are accurately simulated is to perform a direct numerical simulation (DNS), in which all necessary scales are resolved at a given Reynolds number. For cases at even moderately high $Re$ however, this approach is clearly unfeasible. To demonstrate this, let us assume the Kolmogorov hypothesis holds for this flow and as a very rough approximation that the length scale $l_0$ associated to the largest eddies is of the same order as the chord length $l_0 \approx c$. The number of grid points needed to resolve the Kolmogorov length-scale relates with the Reynolds number as $\eta \sim Re^{-3/4}$ , meaning that three-dimensional simulation of a uniformly tur-

bulent flow requires a resolution of $Re^{9/4}$ grid points. For aeronautical test cases, where $Re$ is typically $O(10^6)$ or $O(10^7)$, we therefore require $O(10^{14})$ to $O(10^{16})$ grid points to resolve the flow. Even accounting for variations in geometry which may permit varying resolution throughout the domain, based on the current rate of advancement of high-performance computing (HPC) facilities, resolving fully developed three-dimensional flow at high Reynolds number in a timely manner will continue to be well out of reach for the foreseeable future.

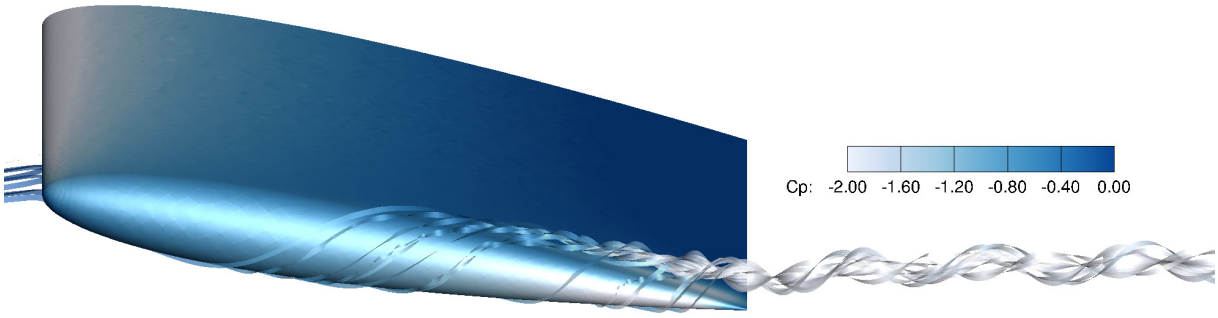



**Figure 4.1** – Wingtip vortex developing over a NACA 0012 profile with rounded wing cap in a wind tunnel, modeling the experimental setup of Chow *et al.*Chow *et al.* (1997) Both wing surface and streamlines are colored by static pressure coefficient $C_p = 2 \cdot (p - p_\infty)/\rho_\infty U_\infty^2$ where $U_\infty^2 = 1$ and $\rho_\infty = 1$.

Consequently, there has been ongoing development of modeling methods where small turbulent scales are not explicitly computed. Traditional Reynolds Averaged Navier Stokes (RANS) methods, alongside more recent advanced such as the Reynolds Stress methods Churchfield & Blaisdell (2013), have been developed to simulate both the complex three-dimensional transitioning boundary layer on the wing and the highly curved flow within the vortex. More computationally-intensive methods, such as LES and Lattice Boltzman VLESSatti *et al.* (2012) have also been developed or adapted to investigate such flows, in correlating the simulated results to experimental data. The lattice Boltzman method has been used in conjunction with a modified $k - \varepsilon$ two-equation turbulence model as well as turbulence wall shear stress model were used to perform a VLES where the walls were the turbulent flow at the wall was modelled.

The key feature of these studies is in their use of reduced equations or turbulence models, all of which require parameters to tune their performance. Since the underlying physical processes that dictate the development and evolution of vortices is not well understood, it is therefore difficult *a priori* to determine appropriate settings for these models. The aim of this work is therefore to demonstrate how an implicit LES method, in which the number of parameters is comparably very small and is used to provide additional stability, can successfully be used to obtain accurate comparisons against experimental data. We appreciate that there may be different views of the definition of implicit LES.

We have adopted the definition of Sagaut (Sagaut, 2001), who explicitly refers to SVV as an implicit LES model and states that *"using a numerical viscosity with no explicit modeling are all based implicitly on the hypothesis [...] the action of subgrid scales on the resolved scales is equivalent to a strictly dissipative action."* The only influence of the sub-grid scales on the resolved scales is therefore dissipative.

Many existing LES codes are based on finite volume, linear finite element or Cartesian grid methods. We will instead investigate the viability of the spectral/*hp* element method, which lies in the class of high-order finite element methods. These methods are widely used in academia, as they offer attractive properties such as exponential convergence and low dissipation error for sufficiently smooth solutions (Bolis *et al.*, 2014). This is significant, as faithfully modeling the wingtip vortex in the far wake is of particular interest in many research communities and industries. It is implied that accurate modelling of the far field vortex requires precise modelling of the vortex onset in the near field using high precision, low dissipation schemes (Churchfield & Blaisdell, 2011, Dacles-Mariani *et al.*, 1996, Chow *et al.*, 1997, Duraisamy & Baeder, 2006, Satti *et al.*, 2011). However, these methods have not been widely applied for the type of industrial, high-$Re$ cases that we consider in this work. Such methods are generally perceived as difficult to implement, as a range of specialised preconditioners, mesh generation procedures, parallel communication strategies and stabilisation approaches are needed to successfully complete a simulation.

In this paper we present the SVV-iLES formulation, which utilises the spectral vanishing viscosity approach to stabilise numerics Tadmor (1989). We show how the issues of implementation and mesh generation can be overcome, as well as highlight the benefits that these schemes can have for industrial problems, both in terms of resolution power relative to existing studies and computational efficiency. To demonstrate the viability and robustness of the scheme, we consider the test case presented by Chow *et al.* (Chow *et al.*, 1997), in which the flow over a NACA 0012 wingtip has been investigated with precise experimental measurements. This case has subsequently become a benchmark for vortex dominated flows. To this end we perform an SVV-iLES, at the highest Reynolds number considered so far for this case, and correlate our results to the experimental data. As in previous numerical studies, in order to reduce the computational cost we have chosen to run the computation at a lower Reynolds number. In this work we set $Re = 1.2 \cdot 10^6$, as compared to the experiment which uses $Re = 4.6 \cdot 10^6$.

In the following section we will briefly report the experimental and numerical methods that have been developed and evaluated for investigating the nascent wingtip vortex, as well as the key findings of these studies. We then discuss the key features of the SVV-iLES method in Section 4.3 and the numerical methodology for our simulations. The evaluation of the SVV-iLES, by close comparison with the extensive data from the experiment of

Chow *et al.*(Chow *et al.*, 1997) and numerical results of Uzun *et al.*(Uzun *et al.*, 2006), is presented in Section 4.4 before we conclude in Section 4.5 with a brief overview of the key findings.

## 4.2 Literature review

We begin with a brief presentation of existing work in the investigation of wingtip vortices; other thorough reviews of this field can be found in Rossow (Rossow, 1999), Spalart (Spalart, 1998) and Green & Acosta (Green & Acosta, 1991). Firstly, experimental studies are considered and a summary of the types of flow dynamics that exists for these cases is presented. We then discuss results obtained by numerical simulations before emphasizing the possible drawbacks of an explicit subgrid-scale model in the context of complex flows, such as the wingtip vortex and highlight the originality of the method employed in this study.

### Experimental methods

For the wingtip vortex the Reynolds number is computed from the chord length $c$ as $Re_c = cU_\infty/\nu$, where $U_\infty$ is the free stream velocity and $\nu$ is the kinematic viscosity. Giuni (Giuni, 2013, Giuni & Green, 2013) and Giuni & Benard (Giuni & Benard, 2011) investigated the initial formation and development of the wingtip vortex on a NACA 0012 rectangular wing with both square and rounded wingtips at $Re_c = 7.4 \cdot 10^5$ for angles of attack $\alpha = 0°, 4°$ and $12°$. They reported that for a given fixed angle of attack, a 'more' axisymmetric vortex sheds from the rounded wingtip with stronger vorticity within its core compared the square-tip wing. They also reported that for the $\alpha = 12°$ case the axial velocity excess is higher for the rounded wingtip. This region is surrounded by a region of axial velocity deficit corresponding to rolling up of the vorticity sheet. The weaker axial velocity excess for the square wingtip is believed to be a consequence of the more numerous secondary vortices generated by the square wingtip.

Defining the center of the primary vortex as the location of the streamwise helicity peak, they investigated the meandering of the vortex in the near field. Two distinct modes of behaviour were observed: for the squared wingtip, the meandering decreased with the distance from the trailing edge whereas for the rounded wingtip case, the meandering grew quasi-linearly with distance from the trailing edge. This has also been reported by Devenport *et al.* (Devenport *et al.*, 1996) and Giuni *et al.* (Giuni & Green, 2013). However Jacquin *et al.* (Jacquin *et al.*, 2001) concluded vortex meandering to be insensitive to free stream unsteadiness in the wind tunnel. Fabre & Jacquin (Fabre & Jacquin, 2000, Fabre *et al.*, 2002) and Dieterle *et al.* (Dieterle *et al.*, 1999) suggested meandering

might also be influenced by the destabilization of a vortex by secondary vortex of opposite sense. Jacquin goes further by reporting that the various co-operative interactions between primary and secondary vortices affected the same range of frequencies as meandering. Zuhal (Zuhal, 2001) and Zuhal & Gahrib (Zuhal & Gharib, 2001) investigated the correlation between number and strength of secondary vortices and the amplitude of meandering. McAlister (McAlister & Takahashi, 1991) investigated the wingtip vortex of NACA 0015 with both rounded and square wing cap reporting the maximum azimuthal velocity of the vortex to be independent of Reynolds number but dependent on the angle of attack.

Finally, Chow *et al.* (Chow *et al.*, 1997) performed an extensive experimental and numerical study of the wingtip vortex over a rounded NACA 0012 profile in view of defining a benchmark for numerical models. They reported merging of the secondary and tertiary vortices into the primary within one chord length of the trailing edge. From this distance onwards, the vortex had an axisymmetric structure with a jet-like axial velocity profile (i.e. the axial velocity within the vortex core was greater than the freestream velocity). The peak jetting velocity was measured to be $1.77U_\infty$ at the trailing edge and by three-quarters of a chord length downstream of the trailing edge it was measured to be $1.7U_\infty$. Pressure taps were placed on the wing-surface to assess the state of the boundary layer, both under the primary vortex where a strong suction region is present and at different spanwise locations, allowing for insight into the three dimensional boundary layer. They also reported skin-friction lines to gain understanding into the attachment and detachment lines of the strongest vortices in the near wake, as well as low amplitudes of meandering because of both a relatively large angle of attack of $\alpha = 10°$ and measurements at relatively short distances from the trailing edge. Devenport *et al.* (Devenport *et al.*, 1996) reported meandering amplitude growing linearly with distance from trailing edge.

### Numerical methods

Presently, RANS based methods with linear eddy viscosity models, such as $k-\omega$ SST and $k-\epsilon$, remain commonplace for industrial flow simulation (Churchfield & Blaisdell, 2013). For vortex dominated flows, and more generally flows with strong curvature, these models may struggle due to the largely unsteady dynamics of the flow. Large discrepancy with experimental data, exceeding 100% error on $C_p$ distribution in the vortex core, as well as drastic under-prediction of the jetting within the core have been reported by Churchfield *et al.* (Churchfield & Blaisdell, 2009*a*). These results have motivated the development, over the past 30 years, of more complex closure models tailored for highly curved flows such as the wingtip vortex. We present a brief overview of this development.

Dacles-Mariani *et al.* (Dacles-Mariani *et al.*, 1995) ran a $5^{\text{th}}$ order compact (i.e. 7

point stencil instead of 11) biased upwind scheme for the advection term and second order scheme for the viscous term. Here they underline the necessity for low numerical dissipation. They ran a modified version of the one-equation Baldwin-Barth turbulence model where they modified the production term to avoid overproduction of eddy viscosity in the vortex core. They successfully captured a secondary structure and computed the axial velocity profiles of the core to within 3% of experiment but under-predicted the core pressure by more than 25%. It should also be stressed that Dacles-Mariani *et al.* (Dacles-Mariani *et al.*, 1993) used experimental data to setup both inflow and outflow boundary conditions for their RANS simulation. Linear eddy-viscosity being too dissipative, Craft *et al.* (Craft *et al.*, 2006) developed a non-linear eddy viscosity model (EVM). This more advanced model still suffered from a more severe decay of the turbulent stresses than measured experimentally. Duraisamy and Iaccarino (K. Duraisamy, 2005) modified the eddy viscosity coefficient of the $v^2 - f$ turbulence model and compared their results favorably for axial surplus compared to the baseline Spallart-Allmaras and Menter's $k-\omega$ SST models. The wingtip vortex exhibits a peculiarity in the turbulence structures where the stress and strain are out of phase which renders questionable the use isotropic eddy-viscosity based prediction methods such as (k-$\omega$, etc). Churchfield *et al.* (Churchfield & Blaisdell, 2008, 2009*b*, 2011, 2013) modified the Spalart-Allmaras model to account for streamline curvature and successfully modeled the lag between the mean strain rate and respective Reynolds stress. This method produced the best correlation with experiment, for a RANS based method, but proved costly (relative to other simpler RANS methods) and so their use may be restricted to flows dominated by vortices. They also showed that without the accurate modeling of the three dimensional boundary layer the developing vortex remained challenging to compute accurately even for the advanced RANS models correcting for the high degree of curvature in the flow.

In an attempt to develop increasingly robust models, more advanced numerical methods such as Large Eddy Simulation (LES) and Very Large Eddy Simulations (VLES) have been proposed to investigate unsteady features of the flow as well as aero-acoustic properties. Fleigh *et al.* (Fleig *et al.*, 2004) developed a compressible LES to investigate far-field broadband noise generated by the nascent vortex on a rotating wingtip at Reynolds $Re_c = 1 \cdot 10^6$ and reported computed power and thrust coefficients for the windmill blade within 3% of experimental data. Ghias (Ghias *et al.*, 2005) reported a compressible LES of NACA2415 with square tip run at $Re_c = 10^5$ where they employed a dynamic sub-grid scale model but did not present the correlation of their data with experiment. Uzun *et al.* (Uzun *et al.*, 2006, Uzun & Hussaini, 2010) numerically investigated Chow's experiment with a compact finite differencing LES with implicit spatial filtering at $Re_c = 5 \cdot 10^5$. Their results were included in the following comparison of our simula-

tions with experimental data. Jiang *et al.* (Jiang *et al.*, 2008) reported results for a LES simulation of Chow's experiment at the experimental Reynolds number of $Re_c = 4.6 \cdot 10^6$ but did not compare the results with experiment. The lattice Boltzman method was used in conjunction with a modified $k - \varepsilon$ two equation turbulence model and wall shear stress model to perform a VLES. Despite good correlation with the experimental results of Chow *et al.* (Chow *et al.*, 1997) for the suction of the vortex on the surface of the wing the method over-predicted the jetting phenomena within the vortex by 23% at streamwise location $x/c = -0.114$ and 12% at $x/c = 0.456$. So far these more advanced modeling methods have generally been used for simulations at lower Reynolds numbers (Jiang *et al.*, 2008, Uzun & Hussaini, 2010) or have not not been compared against experimental data in the way they will be in the present study (Uzun *et al.*, 2006).

**Motivation and contributions of present study**

Modeling unknown physics by leveraging a sub-grid scale model outside of its operational window can be seen as a substantial drawback for explicit sub-grid scale models, which tend to rely on a wide range of parameters to dictate their behaviour. The two-equation eddy-viscosity $k-\omega$ *SST* turbulence model introduced by Menter (Menter, 1994) in 1994, for example, relies on 9 modeling constants. Menter underlines, in this paper, the strong sensitivity of the resulting computed flow to variations of 5-10% of these constants and further stressing *"None of the available theoretical tools (dimensional analysis, asymptotic expansion theory, use of direct numerical simulations (DNS) data, renormalization group (RNG) theory, rapid distortion theory, etc.) can provide constants to that degree of accuracy."* Leveraging these many parameter sub-grid scale models, such as $k - \omega$ SST and more recently Reynolds Stress Relaxation models (Churchfield & Blaisdell, 2013), in complex flow cases therefore requires an *a priori* knowledge of the flow physics. This is often infeasible, particularly when complex geometries are present and the length scales of both flow and geometry vary substantially. For example, in engineering applications such as flow over a Formula 1 car, different sets of parameters may be required to accurately model the various flow dynamics that are induced by the variations in geometry across the body of the the car. This includes the vortex dominated flow of the wing-tip regions of a front wing, regions of the front wing where the flow is mostly two-dimensional, and the rotating wheel that impinges on the moving road. It may therefore be impossible to obtain values for these parameters that capture the desired flow features across the entire car.

The aim of this paper is to show that regularized high order spectral/*hp* element methods, without an explicit sub-grid model, can be applied to produce results that compare favorably against experimental data, by considering flow over a three-dimensional geome-

try of practical interest. The SVV-iLES approach, which we will present in the following section, requires the choice of two regularization parameters: one to dictate the level of artificial viscosity, and another for a cut-off wavenumber. These are chosen through experimentation, such that the computation does not diverge but do not require assumptions regarding the physics of the flow. We discuss this methodology in the following section before showing results of the NACA 0012 wingtip vortex case.

## 4.3 Computational Methodology

In this section, we give a brief summary of the computational methodology used for the NACA 0012 wingtip simulations. We begin by outlining the Nektar++ spectral/*hp* element framework in which the solver is implemented (Cantwell *et al.*, 2014). We then outline the types of regularization that are necessary to perform the computations and prevent the simulation from diverging, along with the mesh generation procedures that are used to generate a curvilinear boundary layer mesh for the geometry. Finally, we discuss initial and boundary conditions as well as resolution requirements in space and time for the simulations.

### 4.3.1 Nektar++: a high-order spectral/*hp* element framework

High-order finite element methods often suffer from the stigma of difficulty of implementation, which in turn means that despite their attractive numerical properties and the ability to resolve difficult cases such as the one presented here, they are frequently under-used. Nektar++ is a framework designed to address this problem by providing a modern development environment for these methods. It is highly parallel, providing a range of efficient preconditioners and has support for a variety of solvers including the incompressible Navier-Stokes equations. For a summary of functionality one can see for example Cantwell *et al.* (Cantwell *et al.*, 2014), or for more details on the method itself, the reference book by Karniadakis & Sherwin (Karniadakis & Sherwin, 2005).

In the following sections, we outline the modifications made to Nektar++ in order to adapt the existing DNS solver, making it suitable for an iLES approach through regularization. Furthermore we outline the other challenges that need to be addressed in order to more generally make spectral/*hp* element methods viable for these problems.

### 4.3.2 From DNS to SVV-iLES: filtering with Spectral Vanishing Viscosity

Running cases at high-Reynolds number on an under-resolved mesh requires close inspection of the source of errors. The highly non-linear nature of the underlying equations leads to a complex interactions of these errors, which when left uncorrected leads to a diverging solution. Broadly, we have found that the two most important aspects are:

1. consistent integration of non-linear terms;

2. artificial dissipation to prevent divergence of the flow in the presence of under-resolution.

We now explain each point in more detail. The incompressible Navier-Stokes solver used in Nektar++ directly integrates the underlying equations through the use of an operator splitting scheme in combination with a consistent boundary condition for the pressure Poisson equation (Karniadakis & Sherwin, 2005). In this scheme, nonlinear terms are computed explicitly at each quadrature point, which depending on the element type uses a form of Gauss quadrature. These nonlinear terms are then multiplied by the elemental basis functions and integrated in order to compute the $L^2$ inner product, as is required in the continuous Galerkin formulation. However, since Gauss quadrature will only produce exact values for integrals of polynomials of degree $O(2P)$ at a simulation polynomial order of $P$, aliasing errors are introduced due to the quadratic nonlinearity present in the Navier-Stokes equations. When simulations are adequately resolved, this aliasing error usually does not affect the robustness of the simulation. However, when under-resolution is used for implicit LES, this aliasing effect leads to a significant buildup of error as the simulation progresses in time, and usually causes the simulation to abruptly diverge.

We note that the nonlinear terms of the Navier-Stokes equations are consistently integrated if the elements are straight-sided. In this case, the Jacobian of the mapping which defines the coordinates of the element is affine with constant determinant. However, where the element is curved, this mapping is an isoparametric polynomial expansion, which when incorporated into integrands, leads to an additional source of aliasing error. In this work, we do not take this source of error into account. A more detailed description of these aliasing errors, as well as means of suppressing them, can be found in (Mengaldo *et al.*, 2014). Whilst it is true we could likely suppress aliasing errors using SVV, which we describe below, it would require stronger diffusion together with a lower cut-off mode, leading to reduced accuracy of the overall solution. Additionally, since the SVV operator is

anisotropic, whereas dealiasing is isotropic, the two do not completely overlap. Therefore a reduced amount of regularisation can be achieved using dealiasing.

In regards to the second point, we first note that the energy spectrum of the flow consists in a resolved range of wave numbers, the large eddies, and an un-resolved range, the turbulent or dissipative scales, for higher wave numbers. Because of this cut-off the higher wavenumber dissipative scales are not resolved for LES. The energy build-up at high-wavenumber and the coupling through the nonlinear term down to lower wave numbers may lead to unstable computations at worst and erroneous energy spectra at best.

Spectral Vanishing Viscosity (SVV), first introduced by Tadmor (Tadmor, 1989) for spectral Fourier methods, aims to damp the high-wavenumber oscillations without impeding the physics of the flow at lower wavenumbers, thereby stabilising the simulation and preserving the accuracy of the solution. In this approach one adds an additional reaction term of the form

$$\epsilon_{\mathrm{SVV}} \frac{\partial}{\partial x} \left( \hat{Q} \star \frac{\partial u}{\partial x} \right)$$

where $\epsilon_{\mathrm{SVV}}$ is a constant, $\star$ denotes the convolution operator and $\hat{Q}$ is a kernel dictating which modes receive damping. This approach was extended to the Navier-Stokes equations by Kirby & Sherwin (Kirby & Sherwin, 2006), Karamanos and Karniadakis (Karamanos & Karniadakis, 2000) and has been extensively used by Pasquetti *et al.* (Pasquetti, 2005), Severac and Serre (Severac & Serre, 2007), Xu *et al.* (Xu, 2006) as well as Lamballais *et al.* (Lamballais *et al.*, 2011).

We also stress that the oscillations stabilized by the SVV method are sub-element oscillations. The intrinsic nature of the spectral/*hp* element methods results in degrees of freedom within each element. When the solution field is under-resolved, it is no longer guaranteed to be smooth. This therefore leads to the development of spurious high-frequency oscillations in the polynomial representation of the solution inside each element, arising from Gibbs phenomena occurring between two connected elements. The aim of SVV stabilisation is to prevent these sub-element oscillations, since they may lead to oscillations occurring in neighbouring elements and ultimately to divergence of the computed solution.

In the context of the simulations presented here, we introduce artificial damping as an implicit sub-grid scale model through the Spectral Vanishing Viscosity (SVV). We appreciate that there may be different views of the definition of implicit LES. We have adopted the definition of Sagaut (Sagaut, 2001), who explicitly refers to SVV as an implicit LES model and states that *"using a numerical viscosity with no explicit modeling are all based implicitly on the hypothesis [...] the action of subgrid scales on the resolved scales*

*is equivalent to a strictly dissipative action."* The only influence of the sub-grid scales on the resolved scales is therefore dissipative.

The key point in SVV filtering is that, due to the shape of the kernel $\hat{Q}(k)$,

$$\hat{Q}(k) = \begin{cases} \exp\left(-\frac{(N-k)^2}{(M-k)^2}\right), & k > M, \\ 0, & k \leq M, \end{cases}$$

artificial viscosity for any mode number $k$ is only applied above a cut-off mode $M$. For the higher modes, the total viscosity can thus be expressed as $1/Re + \epsilon_{SVV}$.

The SVV operator was incorporated into the velocity correction scheme of the incompressible Navier-Stokes equations inside Nektar++ by following the approach presented by Kirby & Sherwin (Kirby & Sherwin, 2006), where the elemental Laplacian operator is convolved with the kernel $\hat{Q}$. The computational cost is therefore negligible since the only cost involved is during setup. However, we note that the addition of SVV can lead to higher iteration counts in the conjugate gradient method used to calculate the intermediate pressure field and perform the velocity correction. This effect can be mitigated through the use of appropriate preconditioning strategies (Sherwin & Casarin, 2001).

In our SVV-iLES method the parameters do not adapt automatically to the flow (i.e. without the input of an experienced user), although methods have been proposed to overcome this constraint by implementing an adaptive SVV diffusion (Karamanos & Karniadakis, 2000, Kirby & Karniadakis, 2002). These methods however still require the same number of parameters to be calibrated on a case-by-case basis and increase the computational runtime cost, as the matrix systems which represent the diffusion operator need to be rebuilt whenever either parameter is changed. We have therefore not considered such approaches here. Also note that we do not use spatially-variable SVV diffusion coefficient or wall functions to limit the amount of damping near solid walls.

As reference, the values of the SVV parameters used by different groups, including the simulations performed here, are reported in Table 4.1. Since we do not have a detailed *a priori* knowledge of the flow features and, consequently, of the sub-grid flow physics, we have chosen our SVV parameters arbitrarily so that they ensure a non-diverging solution. For other simpler cases in the literature, more effort has been made to more rigorously quantify the use of specific SVV parameters (Lamballais *et al.*, 2011). For the sake of comparison however, we report the parameters used in previous studies and stress that our choice aligns reasonably closely with that of previous studies. We recognise greater exploration is necessary for more complex cases. Research along these lines is presently being conducted by *et al.* Moura *et al.* (2015).

| | $M$ | $\epsilon_{\text{SVV}}$ |
|---|---|---|
| Tadmor(Tadmor, 1989) | $\frac{1}{3}N$ | $1/N^2$ |
| Pasquetti(Pasquetti, 2005, 2006, Pasquetti *et al.*, 2008) | $\{\sqrt{N}, \frac{1}{3}N, \frac{1}{2}N, \frac{3}{5}N\}$ | $\{1/N, 1/4N, 4/N\}$ |
| Xu(Xu, 2006) | $\{N-2, \frac{2}{3}N\}$ | $1/N$ |
| Karamanos(Karamanos & Karniadakis, 2000) | $\frac{15}{21}N$ | 1/N |
| Kirby(Kirby & Karniadakis, 2002) | $5\sqrt{N}$ | 5/8 |
| **Present study** | **0.5N** | 0.1 |

**Table 4.1** – Different values for the SVV parameters (diffusion $\epsilon_{\text{SVV}}$ and cut-off mode $M$) where $N = P - 1$ for a discretization of polynomials of order $P$.

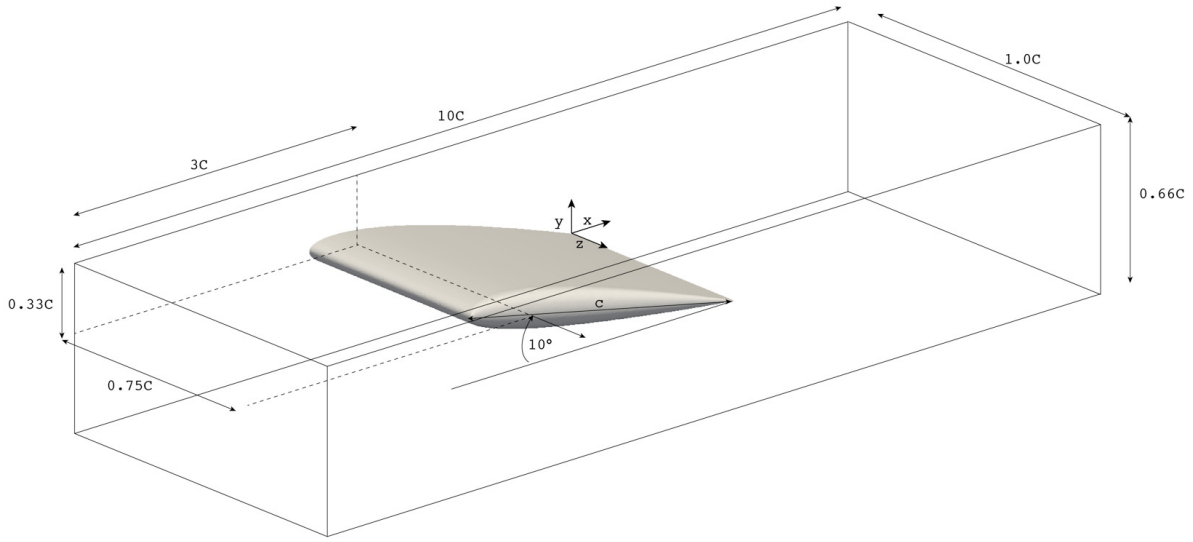



**Figure 4.2** – Computational domain representing the test section in the wind tunnel used by Chow *et al.* (Chow *et al.*, 1997) for their experiment.

### 4.3.3 Geometry and mesh generation

The rectangular wing investigated numerically has a NACA 0012 profile, with a rounded wing cap (consequently a longer semi-span where the wing is thickest) and a blunt trailing edge. The semi-span, without the cap is, $b = 0.91[m]$ and the chord is $c = 1.22[m]$ which correspond to an aspect ratio of $A = 0.75$. The boundary layer tripping mechanism (Chow *et al.*, 1997) used in the experiment is not reproduced in the mesh. We represent the test section of the low speed wind tunnel located in the Fluid Mechanics Laboratory of NASA Ames Research Center used by Chow *et al.* (Chow *et al.*, 1997) for the experimental work, by a $0.66c \times c \times 10c$ cuboid domain as shown in figure 4.2. We do not model the wind tunnel sections upstream and downstream of the test section. A Cartesian coordinate system $(x, y, z)$ is used to locate point within the computational domain with its origin the wingtip trailing edge, where $x$ is aligned with the streamwise direction and $y, z$ are

the two transverse ordinates.

Regarding the interference between the primary vortex and the wind tunnel walls, Chow *et al.* decided to use as large a model as possible while still avoiding severe viscous interaction between the wall and the primary vortex through significant growth and/or separation of the boundary layers on the wind tunnel walls. The authors of the experiment warn against large inviscid effects (mirror effects) due to the close proximity of the wall that most likely influence both the primary and secondary vortices. It should also be noted that the significant blockage created by the large wing in the relatively small wind tunnel section accelerates the flow around the wing. Hence the absolute angle of attack, perceived by the wing, is around 2° higher than the angle of attack prescribed by the geometry.

**Meshing methodology** When considering complex geometries, even generating a linear, straight-sided mesh poses a significant challenge. We have therefore turned to commercial mesh generators, which provide a robust approach to generating linear straight-sided meshes, but generally lack support for high-order elements. We note that for high-order simulations, elements which lie on the boundary must be curved so that they align with the underlying geometry. Using straight-sided high-order elements can significantly alter the physics that form near boundaries and thus downstream of the boundary.

The commercial software we use first imports the CAD geometry, in this case the wing, and makes a fine tessellation of the surface. This tessellated surface is then used to produce the surface mesh. As we have the meshed surface and the original IGES (or CAD) geometry, but not the intermediary tessellation, we are presently unable to add the necessary curvature to the linear mesh by interrogating the CAD geometry directly. To smooth the mesh we adopt an alternative, patch-based technique known as spherigons (Volino & Thalmann, 1998) which rely on surface normals that are obtained from a fine triangulation generated by the commercial software.

The robust high-order three step mesh generation procedure used is summarized in Fig. 4.3 and the interested reader should refer to Moxey *et al.* (Moxey *et al.*, 2015*a*) for further details. Our meshing procedure generates a coarse single-element boundary layer of prisms which are curved using spherigons at the wing surface, with straight-sided tetrahedra filling the rest of the volume. Each prism is split using an isoparametric method in the wall-normal direction, which allows us to achieve the desired wall normal resolution whilst preventing the self-intersection of the boundary layer elements. The tetrahedra grow from the prism layer in a controlled manner in regions of interest, such as the vortex path, where we impose a regular element size to avoid introducing additional mesh induced error.

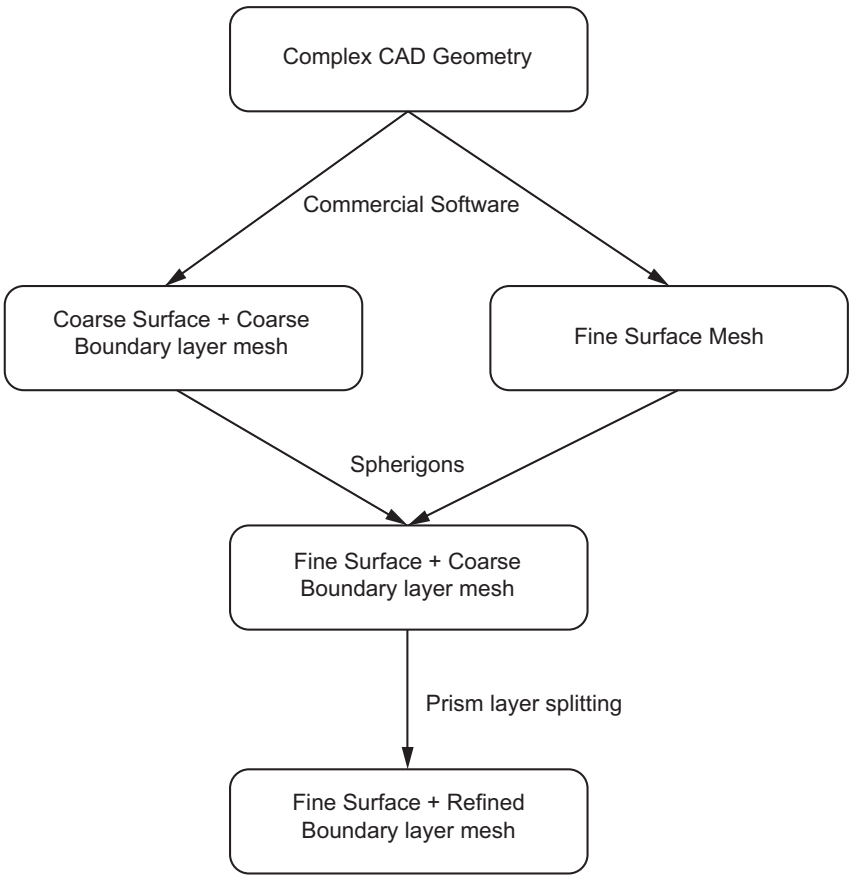



**Figure 4.3** – Robust three-step meshing procedure.

| Method | DOF ($\cdot 10^6$) |
|---|---|
| RANS (modified Baldwin-Barth)(Dacles-Mariani *et al.*, 1997) | 2.5 |
| RANS (Lag RST)(Churchfield & Blaisdell, 2013) | 13.8 |
| LES (Uzun *et al.*, 2006) | 26.2 |
| iLES (Jiang *et al.*, 2008) | 26 |
| **Present study** | **16.7** |

**Table 4.2** – Comparison of mesh used by different methods, converted to degrees of freedom (DOF)

**Comparative degrees of freedom** The implicit diffusion from the SVV operator preserves the convergence properties of the underlying scheme. It does not degrade the exponential rate of convergence of the accuracy of a solution achievable for a sufficiently smooth field (Xu, 2006). We have focused on using our anisotropic prism refinement technique to capture the wall-normal near-wall resolution. In this region we have measured that across the wing surface, the placement of the closest grid point satisfies $y^+ < 1$. With this level of resolution, we can accurately capture the sub-viscous layer of the flow field and resolve the high shear of the boundary layer profile. However the resolution of subsequent elements is not enough to, for example, capture the extremely fine scale of the turbulent boundary layer characteristics. Additionally, for computational reasons, we clearly cannot resolve with a similar level of accuracy in the wall-tangential direction. We do appreciate that this may very well play an important role in capturing the flow in the region of the vortex roll-up. We discuss this further in the presentation of our results.

The present mesh is composed of 243000 elements of which 24500 are prisms around the wing surface and 218500 are tetrahedra growing from the three prism layers to the wind tunnel walls. The prism layer represents roughly 20% of the total number of degrees of freedom. Running this computation with $5^{\text{th}}$ order polynomials (i.e. $6^{\text{th}}$ order accuracy in space) amounts to roughly 16.7 million degrees of freedom; around 40% fewer degrees of freedom than used by Uzun *et al.* (Uzun *et al.*, 2006) for their LES. Table 4.2 compares degrees of freedom for our SVV-iLES method with other studies of this case.

### 4.3.4 Initial and boundary conditions

The simulation is impulsively started from $u/U_\infty = 1$ throughout the domain, except at the no-slip boundaries where $u/U_\infty = 0$, at a low $Re_c \approx 10$. We then gradually increase the Reynolds number by a factor of 10, each time waiting for two convective time units defined as $t_c = c/U_\infty$, until the simulation reaches the desired Reynolds number. To improve computational efficiency the polynomial order $P$ of the discretization is increased with Reynolds number, with $P = 2$ for $Re_c = 10$ and $P = 6$ for $Re_c = 1.2 \cdot 10^6$. At the

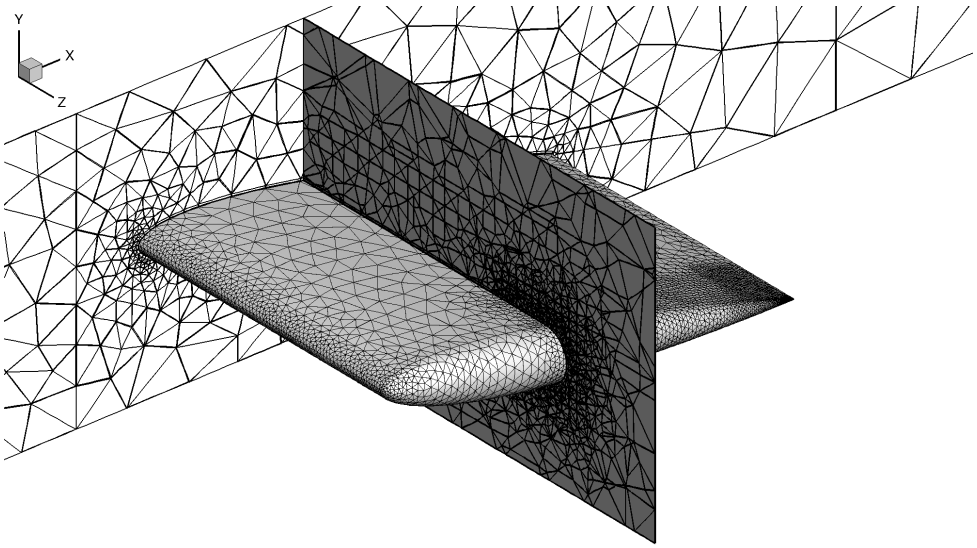



**Figure 4.4** – Overview of the coarse surface mesh and two planes, spanwise cut at the root of the wing and streamwise cut around mid chord. For sake of clarity quadrature/collocation points within each surface element are not shown here.

outflow, we impose the boundary condition developed by Dong *et al.* (Dong *et al.*, 2014) that balances the kinetic energy influx through the outflow boundary condition to prevent instability. The computational setup differs from the experimental setup in three ways. We discuss these and their possible influence on the results in the following paragraph.

Firstly, the boundary layers developing on the wind tunnel walls are neglected, by using a free slip condition. The primary vortex is located sufficiently far away so that the viscous interaction between the primary vortex and the wind tunnel walls is much weaker than the interaction between the primary vortex and the wing surface via the secondary structures.

As a first approximation, the wall acts, inviscidly, as a symmetry condition. Since the computed location of the vortex is similar to the experimental data, the inviscid interaction between the vortex and the wind-tunnel walls is assumed to be of similar intensity. Secondly, as with other LES studies, we do not model turbulence at inflow. As we shall see in the results section, despite the lack of a turbulent inflow we still see good comparisons against experimental data. Finally the boundary layer on the wing is not tripped. The tripping of the boundary layer near the leading edge has been reported to increase the diameter of the vortex (measured by the peak to peak distance of the vertical velocity) by 30% (McAlister & Takahashi, 1991). McAlister also report that adding a boundary layer trip changes the streamwise component of the velocity from a small excess to a large deficit at the position $x/c = 4$; however we do not observe the vortex that far downstream. The tripping of the boundary layer might affect the interaction between the primary and secondary vortices and has been reported to decrease the inboard movement

of the primary vortex along the span (McAlister & Takahashi, 1991).

### 4.3.5 Temporal evolution

The Navier-Stokes equations are integrated in time using a second-order accurate stiffly-stable implicit-explicit scheme (Karniadakis *et al.*, 1991). The advection term is explicitly integrated, whereas the viscous term is implicitly integrated. This therefore relaxes the sometimes stringent, diffusion stability condition $\Delta t \propto \Delta x^2/\nu$. The CFL restriction $\Delta t \propto \Delta x/u$, where $u$ is the advection velocity within each cell, remains however. Because the mesh we consider is coarse, we assume numerical error is dominated by error from the spatial discretization. The time step used for the computation normalized by the convective length scale of the chord $t_c$ is $\Delta t/t_c = 1.6 \times 10^{-6}$ which translates into a maximum normalized sampling frequency of $3 \cdot 10^5$. For spectral/$hp$ element methods using a second order implicit-explicit time integration scheme, the analog to the CFL definition imposes a restriction on the maximum timestep of the form(Karniadakis & Sherwin, 2005) $\Delta t < \Delta x/(\max_{\Omega^e \in \Omega}\{|V^e|P^2\})$ where we assume $\max|V^e| \sim U_\infty$. For the present mesh, where the smallest mesh element is $10^{-4}c$ and using $5^{\text{th}}$ order polynomials, the timestep restriction is of the order of $10^{-5}t_c$. In practice, since the velocity in some regions can be significantly larger than $U_\infty$, we use a timestep one order of magnitude smaller.

## 4.4 Results and Discussion

In this section, the performance of the SVV-iLES method is evaluated by simulating the development of the wingtip vortex in the near field and comparing the results against the experimental study by Chow *et al.* (Chow *et al.*, 1997) as well as the previous LES by Uzun *et al.* (Uzun *et al.*, 2006).

We define the *near field* to be the region above and below the wing and up to one chord length downstream of the trailing edge. In this context the *mid-field* is the region from $c$ to $10c$ and the *far-field* is at a distance of more than $10c$ from the trailing edge. To put the challenge of accurately computing the vortex into perspective, we outline the typical tracking distances of interest for different applications. The automotive industry is interested in tracking the vortex for roughly $20c$. For wind turbines and helicopters blades, with an aspect ratio of roughly 10, the study of the interaction between the rotor blades and the preceding blades that leads to noise and structural vibration, requires tracking the wingtip vortex over more than $60c$ for one revolution. In this study an effort is made to characterize the performance of the modeling method both in the three-dimensional

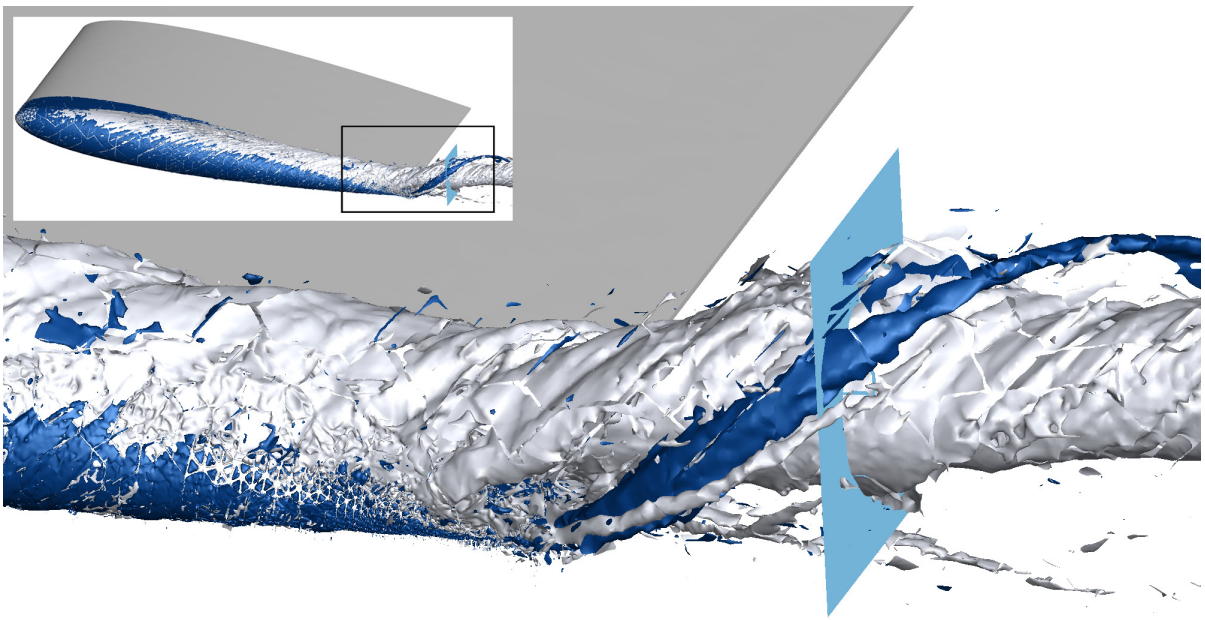


**Figure 4.5** – Contours of iso-helicity showing the interaction between the primary (in light grey) and a secondary vortex of opposite rotational sense (in blue, or dark grey). The light grey/blue plane denotes the location of the streamwise cut $x/c = 0.125$ at which results are compared with experiment in Figs. 4.10-4.11.

turbulent boundary layer and in the rollup wake. It is supposed that accurate modeling of the vortex in the near field downstream of the trailing edge pre-supposes an accurate modeling of the three-dimensional boundary layer roll-up on the wing surface.

The vortex can loosely be defined as the region in which the fluid has high helicity, low relative pressure and an axial velocity surplus. Different methods have been developed for defining the center of a vortex, but these can prove challenging to apply in the near wake where the vortex is forming as a consequence of the shear layer roll-up. These methods include helicity peak correction, vorticity peak, $Q$-criterion, zero in-plane velocity and axial velocity peak. It has been shown that the helicity peak correction method is best suited for estimating the vortex core radius, axial velocity peak and swirl velocity peak. Giuni & Benard (Giuni & Benard, 2011) assert that the centering method chosen should depend on the key aspect of interest but the robustness of these methods is not sufficient for identifying the vortex as it develops from the shear layer roll-up and interacts with secondary structures. For this reason the method of the manual location of the vortex core by identifying local pressure minima has been favored. This method has also been used by Chow *et al.* so this source of error should be taken into account when appreciating the discrepancy between reported core locations (Fig. 4.8) in this region.

The flow over the wingtip develops into a highly skewed three-dimensional boundary

layer that rolls up and detaches into a rapidly rotating vortex, at a distance of around $0.5c$. This forms an increasingly low pressure region in the vortex core that gradually accelerates the fluid entering the core into a jet characterized by a notable normalized axial velocity surplus. This strong vortex is thought to be laminar and persistent, extending many chord lengths downstream of the trailing edge. The challenge from a modeling perspective comes from the three-dimensional boundary layer, the detachment and the strong curvature induced both by the geometry and by the many interacting vortical structures. Two key regions of the flow are used to assess the performance of the SVV-iLES method against the experimental data of Chow *et al.* (Chow *et al.*, 1997): the wing surface and the vortex core. These two regions are of particular interest because they radically differ in nature. Most classical turbulence models can capture turbulent boundary layers well, but few of these can accurately model the vortex core where curvature of the streamlines is high (Bradshaw, 1973).

In the second region of interest, the vortex core, the key feature to reproduce is the low pressure region driving the jetting phenomena or the normalized axial velocity surplus. Inside this region, the high value of $u_{\max}/U_\infty$ at the trailing edge, and the low decay within the first chord length downstream of the trailing edge at $x/c = 0.867$ is a challenging feature to capture. We will therefore compare our results, as well as those from previous computations, against the reported experimental values of $u_{\max} = 1.77U_\infty$ and $1.59U_\infty$ respectively from Chow *et. al.* (Chow *et al.*, 1997). Uzun *et al.* (Uzun *et al.*, 2006) underpredict the peak normalized and time averaged axial velocity by more than 20%, albeit at a lower chord Reynolds number $Re_c = 5{\cdot}10^5$. The $k-\omega$ based RANS computation by Churchfield *et al.* (Churchfield & Blaisdell, 2011) report a 150% error, with respect to the experimental data by Chow *et. al.* (Chow *et al.*, 1997), in the $C_p$ distribution within the vortex at $x/c = 0.867$. Even the $k-\omega$ SST-RC RANS (Churchfield & Blaisdell, 2011), that predicts the $C_{p_0}$ at $x/c = 0.867$ with less than 10% error, has nearly 20% error for the estimation of the axial velocity surplus and 30% error for the static pressure in the core at $x/c = 0.867$.

The results from SVV-iLES and evaluation with respect to experiment for the two regions of interest is presented in the next section. All results presented here have been time-averaged over three chord convective length or $1t_c$. We assume the flow is fully developed when the $C_p$ distribution on the wing-surface at the span-wise location $z/c = 0.899$ converges to a smooth curve.

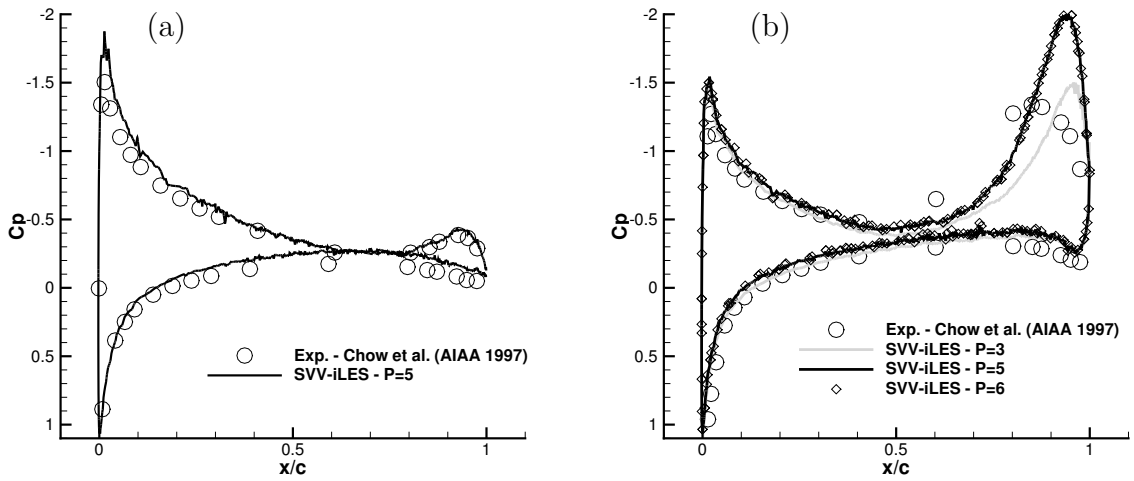



**Figure 4.6** – Comparison with experiment (Chow *et al.*, 1997) of time-averaged $C_p$ distribution over $3t_c$ time units as a function of streamwise position, with the leading edge in $x = 0$, at spanwise location $z/b = 0.833$ (a) and $z/b = 0.899$ in (b) where we also show the results from the uniform grid-refinement study (convergence in $P$). The number of mesh degrees of freedom for $4^{\text{th}}$, $6^{\text{th}}$ and $7^{\text{th}}$ order accurate in space are 5.7M, 16.7M and 25.3M respectively. The 50% increase in number of degrees of freedom when using $7^{\text{th}}$ instead of $6^{\text{th}}$ does not significantly affect the pressure distribution on the wing at the spanwise location $z/c = 0.899$.

### 4.4.1 Wing Surface

#### $C_p$ distribution

Chow *et al.* (Chow *et al.*, 1997) reported the pressure distribution at two spanwise locations. The first cut, at $z/b = 0.833$, is situated inboard of the vortex core where its influence is mild, whereas the second is located at the vortex core in $z/b = 0.899$. At this position, the presence of the vortex leads to a distinctive pronounced suction region. The extent of this region upstream depends on the shape of the roll-up layer. The presence of the vortex reduces the pressure in this region which translates into an increase in lift.

Despite a relatively good agreement with experiment for the $C_p$ distribution at the spanwise location $z/c = 0.833$ (Fig. 4.6a), at the spanwise location of the developing primary vortex (Fig. 4.6b), the SVV-iLES computed results under-predict the vortex suction from $x/c = 0.5$ to $x/c = 0.9$ and significantly over-predict the suction for the last $0.1c$. Coarse tangential resolution, in the first 0.5c, may have led to a strong SVV dissipation that which in turn significantly damped the early growth of the vortex over the wing surface. The sudden change in trend at $x/c = 0.9$ might be due interaction between the primary and a secondary the secondary vortex. With this exception however, the main features of the flow are well captured.

It should be noted that the instantaneous field is noisy because of the unsteady nature of the boundary layer at this high Reynolds number and is obviously reduced as we average

over longer time intervals, which explains the residual noise in the $C_p$ distribution (Fig. 4.6a-b). The use of the spherigon mesh smoothing technique in the representation of the geometry may also lead to some higher frequency oscillations and thus less smoothness in the distribution. Adding further diffusion from the SVV may help in removing some oscillations. However, additional diffusion might lead to an artificial reduction of the Reynolds number.

**Resolution study**

Although this test case is computationally expensive to simulate, we have performed a limited $p$-refinement study of the flow physics, using the $C_p$ distribution as a benchmark for observing convergence and providing a form of self-validation. In these tests, the polynomial order was varied, comparing the $P = 5$ results that we present here to results at $P = 3$ and $P = 6$. The resulting $C_p$ distributions, presented in figure 4.6b, show very little difference between the $P = 5$ and $P = 6$ cases, despite a 50% increase in the total number of degrees of freedom. However, there is a significant difference between that of $P = 3$ and $P = 5$. Whilst there is still variation between the experimental results and both $P = 5$ and $P = 6$, we can at least conclude that in terms of polynomial order the simulation is well-resolved.

We note that this type of refinement is good in that it is hierarchical and so all the degrees of freedom at lower polynomial orders are contained within the higher order simulations. It does not, however, guarantee that there cannot be regions which are still not captured and so the basic features of the flow will remain reasonably similar. Further work is therefore required to generate a larger sequence of meshes to study the effect of refinement in terms of element size. However, given the significant undertaking of this type of study and the convergence we have obtained in $p$, we do not consider this here and use the $P = 5$ results in the coming section.

### 4.4.2 Propagation of the vortex core in the near-wake

In the vortex core we track the normalized time-averaged axial velocity, the static pressure and at the location of the vortex both in the spanwise direction ($z$) and normal to the suction side direction (positive $y$), as shown in figures 4.7 and 4.8. Therefore both time-averaged pressure coefficient and axial velocity have not been corrected for the error stemming from possible meandering. In this section we also presents an overview of the development of the vortex in the near wake. A comparison shown for both streamlines and time-averaged normalized axial velocity at two crossflow locations: over the wing towards the trailing edge at $x/c = -0.114$ and in the near wake at the $x/c = 0.125$. These results

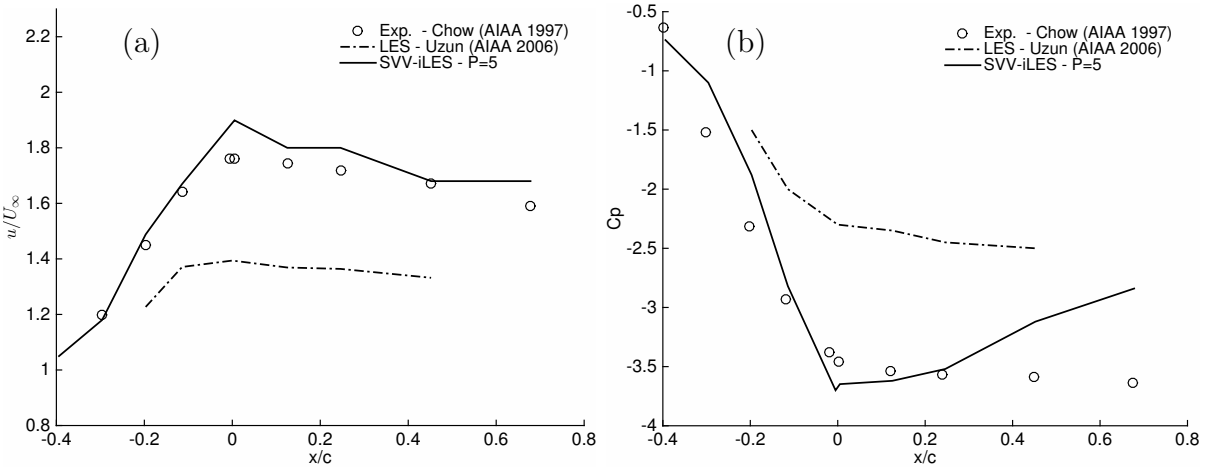



**Figure 4.7** – Comparison with experiment (Chow *et al.*, 1997) and previous LES by Uzun *et al.* (Uzun *et al.*, 2006) of the progression of (a) axial velocity and (b) $C_p$ distribution in the vortex core. The origin, $x/c = 0$, is taken to be the position of the wingtip trailing edge.

are shown in figures 4.9 and 4.10.

**Normalized axial velocity in the vortex core.**

The progression of the axial velocity of the vortex can also be affected by the presence/absence of a boundary layer trip as reported by McAlister (McAlister & Takahashi, 1991): for $Re_c = 1.5 \cdot 10^6$ a NACA 0015 profile at angle of attack $\alpha = 12°$ the streamwise component of the velocity in the vortex core has a small jetting behavior (¡ 5% velocity excess) without the trip and a significant 20% deficit ($u/U_\infty \approx 0.8$) when a boundary layer trip is added to the leading edge. In Fig. **??** we report the streamwise progression of the normalized axial velocity. Our modeling adequately resolves the strong jetting behavior measured experimentally. We do however over-predict the peak axial velocity in the vortex core by 6% with respect to the experimental value.

**Static pressure within the vortex core.**

In Fig. **??** we report the streamwise progression of the vortex core static pressure. Despite a relative error of less than 10% over the wing surface the error grows linearly downstream of the trailing edge reaching 30%. Accurately capturing the low pressure region within the vortex core and sustaining this low pressure even just one chord distance downstream of the trailing edge is particularly challenging. The linear increase in pressure is most likely the result of either too coarse a mesh within the vortex core and/or too strong a contribution from the SVV. When the grid is too coarse to adequately capture a gradient the SVV filter damps out part of its kinetic energy. Neglecting compressibility effects, this resulting decrease in jetting velocity increases the pressure (or decreases the suction

of the vortex).

**Vertical position of the vortex core.**

The vertical location of the primary vortex core is computed to be 20% lower than both the experiment and previous LES (Fig. 4.8a). The change in attitude as the vortex leaves the proximity of the wing surface follows a similar trend, with the core remaining at the same distance above the wing surface from streamwise location $x/c = -0.4$ from the trailing edge, to the trailing edge $x/c = 0$ and then showing a pronounced upward trend from the leading edge to the experimentally reported $x/c = 0.4$ location downstream of the leading edge. Fig. 4.9a shows the computed cross-section of the vertical vortex profile above the wing surface, with the same position measured experimentally (fig. 4.9b) and in the previous LES result of Uzun *et al.* (fig 4.9c). Despite a discrepancy regarding the vertical position of vortex core, we seem to be qualitatively agreeing with the experimental results. In particular, the shape of our computed vortex is closer to the isotropic round shape of the experimentally obtained vortex, particularly when compared to the previous LES result. The topology of the flow in the region $0.03 < y/c < 0.06$, with the presence of a secondary vortex, is also qualitatively closer to the experimental results than the previous LES. We should note however that the location of the SVV-iLES computed structures is different with respect to those measured experimentally. Whilst it is difficult to explain this discrepancy without a further series of detailed simulations, one possible explanation is in the tangential grid spacing. We note that for computational reasons, this is clearly not as fine as the wall-normal direction, and this may therefore play a key role in influencing the detachment location and therefore vertical position of the vortex core. It is also interesting to remark how accurate the LES results from Uzun *et al.* are at predicting the vertical position of the vortex core above the wing despite significantly different flow topologies (Fig. 4.9a and Fig. 4.9c).

**Spanwise position of the vortex core.**

The spanwise position of the computed vortex core is compared against both the experimental data of Chow *et al.*(Chow *et al.*, 1997) and previous LES results by Uzun *et al.* (Uzun *et al.*, 2006). Three key features of flow can be assessed by this figure: the location of the origin of the primary vortex, the location at the trailing edge and the evolution of the vortex as it leaves the vicinity of the surface of the wing. There is good agreement between experimental data and both LES regarding the position of the vortex at the trailing edge. There is, however, a significant discrepancy regarding the origin of the vortex. Indeed both Chow *et al.* (Chow *et al.*, 1997) (circles in Fig. 4.8b) and Uzun

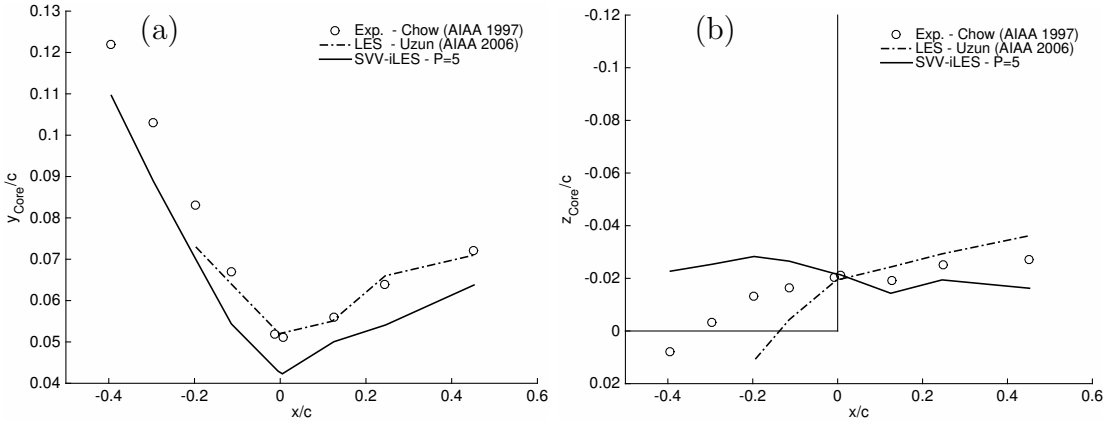



**Figure 4.8** – Comparison with experiment (Chow *et al.*, 1997) and previous LES by Uzun *et al.* (Uzun *et al.*, 2006) of the vertical position of (a) the vortex above the wing and (b) spanwise location. The origin, $z_{core}/c = 0$ and $y_{core}/c = 0$ is taken to be the position of the wingtip trailing edge. The position of the wing is identified with the rectangle in b).

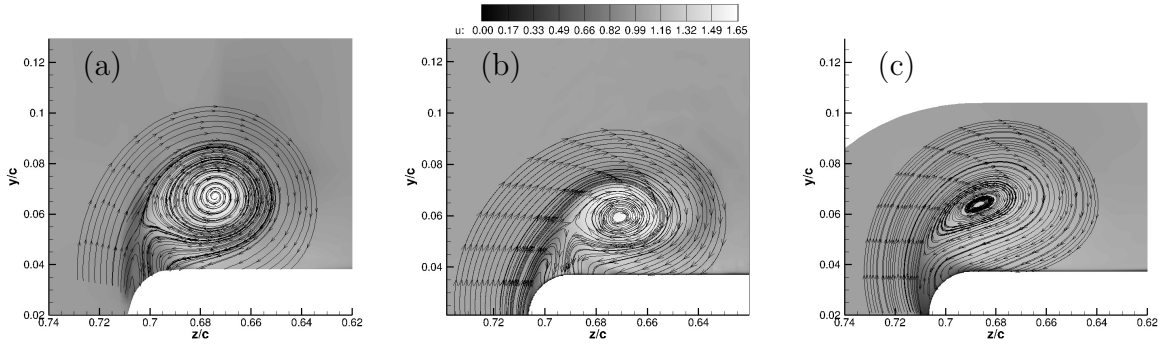



**Figure 4.9** – SVV-iLES computed streamlines and normalized time-averaged axial velocity at the crossflow plane $x/c = -0.115$ downstream of the trailing edge in b) compared against experimental results from Chow *et al.*(Chow *et al.*, 1997), in (a) and previous LES results by by Uzun *et al.*(Uzun *et al.*, 2006), in (c).

*et al.* (Uzun *et al.*, 2006) (dot-dashed line in Fig. 4.8b) report the origin of the primary vortex in the region of the wing cap whereas the present results show the origin to be on the suction side of the wing around mid-chord. McAlister & Takahashi (McAlister & Takahashi, 1991) as well as Thompson (Thompson, 1983) reported the origin of the vortex on the suction side of a NACA 0015 profile for a similar case. McAlister & Takahashi (McAlister & Takahashi, 1991) also report tripping the boundary layer decreases the inboard movement of the primary vortex along the span without altering its distance above the wing. This may offer possible insight into the difference in spanwise trajectory between Uzun's LES computed vortex which has a more pronounced inboard movement than Chow's experiment.

The most interesting feature of the flow that can be analysed with Fig. 4.8b is the evolution of the vortex as it leaves the vicinity of the surface of the wing. The experimental

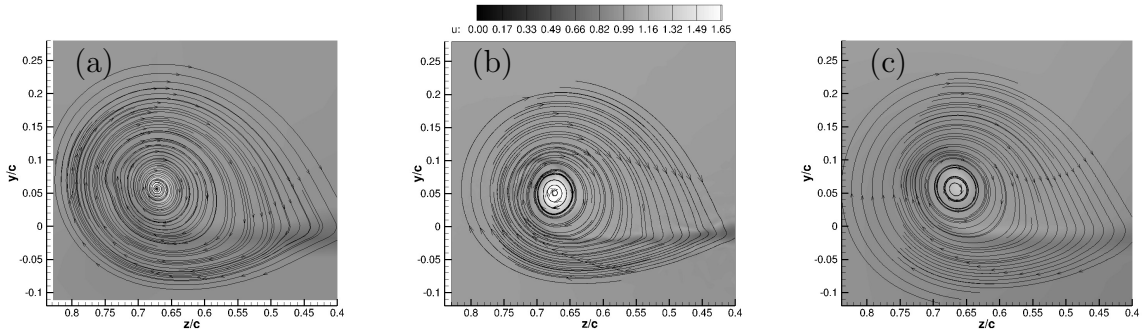



**Figure 4.10** – SVV-iLES computed streamlines and normalized time-averaged axial velocity at the crossflow plane $x/c = 0.125$ downstream of the trailing edge in b) compared against experimental results from Chow *et al.* (Chow *et al.*, 1997), in (a) and previous LES results by by Uzun *et al.* (Uzun *et al.*, 2006), in (c). Fig. 4.5 acts as a companion figure to locate the $x/c = +0.125$ with respect to the primary and secondary vortices with a three dimensional perspective of the flow in this region. Fig. 4.11 complements Fig. 4.10b in aiding the identification of the secondary vortex with respect to streamlines and also the streamwise component of the vorticity.

results of Chow *et al.* show two distinct kinks at $x/c = 0.125$ and then $x/c = 0.452$. This is particularly evident when comparing against the previous LES of Uzun *et al.*, where the progression of the vortex core moves steadily inboard. We believe these kinks are the result of the interaction between the primary vortex and a secondary vortex orbiting around it. Evidence of this secondary vortex can be seen in both the comparisons of the streamwise-normal streamlines shown in Fig. 4.10a with the notable presence of a flat spot in the region $0.72 < z/c < 0.75$ and $0.01 < y/c < 0.07$. Our numerical results also show a similar flat spot, albeit in slightly different position, in region $0.72 < z/c < 0.75$ and $0.06 < y/c < 0.1$. By plotting the streamwise component of the vorticity vector in this region we can correlate these flat spots to a weaker, counter rotating, secondary vortex (Fig. 4.11a). In Fig. 4.11b we enlarge this region of interest to evidence the weaker, counter rotating vortex in light grey. In these two figures the primary vortex appears in dark grey. This secondary, weaker, counter rotating vortex can also be seen when visualising the iso-helicity surfaces. In Fig. 4.5 the primary vortex appears in grey and the secondary vortex in dark grey (or blue if visualised in color). The light grey (light blue) surface represents the spanwise location $x/c = +0.125$ at which the comparison is made between experiment, previous LES and present results for Fig. 4.10-4.11. It is also interesting to note that the computed secondary vortex seems to be out of phase, in the streamwise direction, with respect to the experimentally computed vortex. Indeed it appears in the II quadrant whereas in the experimental results it appears in the III quadrant (when viewed as in Fig. 4.10-4.11).

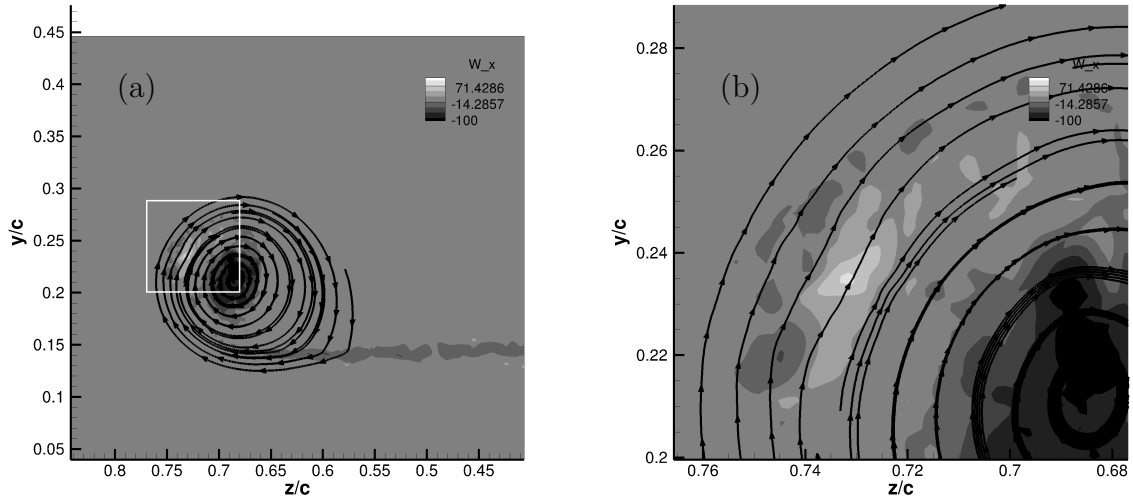



**Figure 4.11** – Streamwise component of the vorticity vector $\Omega_x$ at location $x/c = +0.125$. Both primary vortex, in dark grey, and secondary vortex in light grey in the II quadrant are visible with an overview of the flow in a) and the detail of the location of the secondary vortex in b). These figure acts as a companion to Fig. 4.10b.

## 4.5 Conclusion

The SVV-iLES workflow, developed for computing unsteady vortex-dominated flows, has been assessed by comparing numerical results with experimental data by Chow *et al.*(Chow *et al.*, 1997) for a NACA 0012 wingtip vortex test case, at a higher Reynolds number than any LES study performed to date. Overall, the results show the potential of this method to resolve the large scale features of the flow, without the use of explicit turbulence and sub-grid scale models. The use of an implicit LES presents a notable advantage over these methods, given that only two parameters are needed to control regularization and stability of the numerics.

Our results show better correlation with experimental results than previous numerical results, both in terms of the static pressure distribution, prediction of the jetting velocity, vortex spanwise location and the ability to resolve the secondary vortex interaction with the main wingtip vortex. In particular, we note that the results presented here show a good agreement in the roll-up region where both the static pressure and velocity magnitude agree within 10% of experiment. We also observe that although the mesh used in this study is coarser than ones reported in other studies, as highlighted in Tab. 4.2, and the Reynolds number is larger than previous investigations, the results of this study demonstrate that the SVV-iLES method can still accurately capture the essential features of the flow. However we do note that unsteady simulation obviously requires significantly more compute resource as compared to steady RANS simulations. We additionally obtain a qualitatively good agreement of the modeling of the vortex roll-up, and predict the

secondary vortex and its interaction with the primary vortex over the wingtip. We believe this can be attributed both to the lower diffusion and dispersion properties of the spectral/*hp* element method and to the use of an isoparametric refinement technique which provides adequate wall-normal resolution in the sub-viscous layer of the boundary region.

There are however some clear differences between the results presented here and experimental data. It is clear that the suction peak on the wing appears further downstream ($x/c = 0.95$ instead of the experimental value of $x/c = 0.85$). There is also a visible difference in the location of the secondary vortex at location $x/c = 0.867$ downstream of the trailing edge. These points seem to indicate that despite successfully modeling the secondary vortex, the interaction between the primary and secondary vortex is not yet accurate enough to reproduce experimental results. The *p*-refinement study presented here shows that, whilst our results are well-resolved in terms of the polynomial space, a small increase in polynomial order does not generally lead to a better correlation with the experimental data. This is likely due an under-resolution of the wall-tangential directions across of the surface of the wing and in particular in the first $0.5c$, where the primary vortex originates. Therefore, whilst a large increase in polynomial order would hopefully yield a better correlation with the experimental results, a more efficient approach to achieve convergence is likely to be a combination of both mesh and *p*-refinement. It is therefore clear that, together with improving the smoothness of the surface mesh and a further increase in Reynolds number to match the experiment, future studies should include additional local refinement in terms of element size in order to hopefully attain a closer agreement with the experimental results.

In summary, the SVV-iLES method has been shown to be a compelling alternative for computing complex unsteady vortex dominated flows, such as the wingtip vortex, motivating its use for complex industrially relevant cases where high-fidelity computational fluid dynamics can become an enabling technology.

## 4.6 Outlook

This test case is interesting because it is computationally intensive enough to require HPC resources (as of 2017) but simple enough that the resources required are within reach of most labs. From a point of view of the flow physics the wing-tip vortex is not yet fully understood, in particular the relative importance of the secondary vortex reported Lombard *et al.* (2016). Furthermore it is an interesting test bed for improving the understanding of next generation CFD codes and in particular high-order codes such as `Nektar++`. As such we believe the following studies would greatly benefit both the

academic and industry sectors wishing to deploy these methods into their development cycles :

1. rigorous study of the relative importance of spatial error against time-integration error. Within the framework of F1 design, as of time of writing, most computations are highly under-resolved in space. As such we make the assumption that the time-integration scheme either the second-order implicit/explicit IMEX2 scheme of the semi-Lagrangian implicit time-integration scheme do not dominate the error. However this assumption should be checked and in the case of the wingtip vortex where spatial resolutions closer to DNS will soon be achievable it should be stressed that time-integration errors might start to dominate. This likely scenario should motivate the development and testing of higher-order time-integration schemes to ensure the benefit of high-order spatial discretisation is not wasted,

2. obviously more advanced artificial viscosity methods, or physically motivated subgrid-scale models can best tested on this case. Already in the framework of low-order RANS based computations the solutions is highly sensitive to the turbulence closure model and,

3. finally a study regarding the effective Reynolds number is worthy of being undertaken. In the limit of no artificial viscosity and high- or DNS resolution the CG method offers no additional viscosity than that prescribed by the kinematic viscosity. However in flows where the hp-mesh does not resolve the diffusive length-scales it is not yet clear how much the artificial viscosity introduced by SVV affects the Reynolds number. A secondary effect of SVV is introducing strong fluctuations in regions of the flow where it affects the highly under-resolved modes. These fluctuations might act towards provoking bifurcations in the flow at lower Reynolds number, similarly to what was reported by Henningson *et al.* (1993) when investigating bypass transition, than might be expected with a finer mesh without artificial viscosity. Despite having being used as a stabilisation tool for many years since its introduction by Tadmor (1989), its use as an artifiicial viscosity for mimicking subgrid scale dissipation in highly unsteady flows over complex geometries is only being tested with the work presented in this thesis.

# Chapter 5

# The dynamics of the rolling wheel near wake.

Despite forty years of ongoing research, the wheel wake is still not fully understood. In its simplest form, the wheel can be modeled by a finite aspect ratio cylinder rolling on a moving ground plane. This idealised description already brings about three of the main challenges of the rolling wheel analysis: the modeling of the rotation of the wheel, the modeling of the moving ground plane and the modeling of the intersection between the two. Similarly to a large number of bluff bodies, and contrary to streamlined bodies, most of the drag of a wheel results from the large separated wake leading to a low base pressure and large pressure fluctuations (Bearman, 1980). Therefore, advancing the understanding of the underlying mechanisms of this near wake is paramount for reducing the bluff-body drag to a minimum. In conjunction with these efforts, a growing body of research is devoted to the control of the bluff-body wake an example of which is given for the canonical case of the D-shaped bluff body (Dalla Longa *et al.*, 2017) or the Ahmed body (Evstafyeva *et al.*, 2017, Rouméas *et al.*, 2009). This chapter aims to describe the investigations carried out on fundamental aspects of highly unsteady wake of the rolling wheel by means of Direct Numerical Simulation (DNS). As part of this investigation, the q-criterion is used to identify the vortical structure associated to the dynamic modes computed by Dynamic Mode Decomposition first introduced by Schmid & Henningson (2001). This generalisation of the method to fully three-dimensional flows allows for visualisation of the modes associated to the shedding at the top of the wheel, the meandering of a set of vortices in the very-near wake responsible for the symmetry breaking in the spanwise direction. A low frequency mode is associated with the slow meandering of the jetting vortices. Finally, for the first time, the shear is extrapolated onto the rotating wheel surface from the DMD modes to establish a map of regions on the rolling wheel body where each mode is most active. Quantification of the shear produced by motion at a

given frequency further emphasises the different flow mechanisms responsible for the rich frequency content of the power spectral density of the force coefficients.

In the following few paragraphs we will highlight the challenges accompanying the study of the rolling wheel in contact with a moving ground plane and the insights brought about by experimental and numerical investigation over the past fifty years.

## 5.1 State of the art

The rolling wheel of diameter $D$ and width $W$ is essentially a low aspect ratio bluff body producing a large and highly unsteady wake. Despite strong interest from the automotive industry and open-wheel racers, such as Formula One, since (Fackrell, 1974) effort few studies have been published in the open literature. The automotive industry strives to reach ever more challenging emission standards set by ambitious policy makers triggering growing demand for a better understanding of the underpinning fluid dynamics of the wheel. For a road car operating at highway/motorway cruise conditions the wheels and underbody are responsible of 10-40% of the total aerodynamic drag. For open wheel races such as Formula One the rotating wheels are responsible for roughly 40% of the drag. We start by considering the open literature and where additional studies can help enlighten the fluid dynamics of this problem. The flow about a rolling wheel exhibits three types of separation: 1) separation resulting from the adverse pressure gradient on the circumference of the cylinder, 2) primary separation from the rotating sharp edges and secondary separation along the flat sides and, 3) primary and secondary separation on the moving ground plane.

In conjunction with early experimental research, efforts were made to develop analytical models of the flow about wheels (Fackrell, 1974, Bearman & Fackrell, 1975). It was soon realised that despite offering insight for two dimensional flows, such models did not hold for three-dimensional wheel (Bearman & Fackrell, 1975).

In the context of growing electrification of the drivetrain of road vehicles reducing the drag becomes a decisive factor through its direct impact on the range of the vehicle. An example of this of this effort is demonstrated in D'Hooge *et al.* (2012) for the development of the Tesla Model S. Most studies focus on the aerodynamic of the front-wheels since, for automotive applications, they contribute strongly to drag of the vehicle because they are exposed to strongly yawed flow (Kothalawala & Gatto, 2016). The rear wheels also contribute strongly to the flow as they modify the flow in the underbody, diffuser and near wake region. Better understanding of their contribution to the near wake could possibly be used to reduce the base-pressure deficit in future work. These efforts were combined with optimisation of the rim design. Kandasamy *et al.* (2012) show that numerical simulation

of the rims based on sliding mesh, and not immersed boundary conditions, show the best correlation for different rim designs with experiment.

**Three-dimensional effects** The first study considering a cylinder of finite aspect ratio W/D was Wieselberger in 1922 and reported by Muttray in Zdravkovich (2003) showing that before the critical regime, $Re_D < 3 \cdot 10^5$ the drag of the truncated cylinder with rounded edges and an aspect ratio of $W/D = 5$ is consistently lower than the infinite span cylinder. This is attributed to the *venting* of the low pressure recirculation region in the near-wake. Venting is the addition of high momentum flow around the edges of the cylinder which would not be present in the case of an infinite cylinder where flow reaches the wake only by flowing above or below the cylinder. The flow departs from two-dimensionality already for aspect ratios as large as $W/D = 20$ as shown by Bearman (1980) and more strongly so as the $Re_D$ is increased. Even for infinite cylinder experiments the aspect ratio is limited by the size of the wind-tunnel and apparatus. At $Re_D < 200$ the flow remains bidimensional and the size of the domain does not seem to have much impact on drag measurement, however large variations in drag have been reported for $Re_D > 8 \cdot 10^3$ (Szepessy & Bearman, 1992).

For very small aspect ratio cylinders, or coin-shaped cylinder, the "wheel" becomes a streamlined body and so the drag is dominated by viscosity (Zdravkovich *et al.*, 1998). In this study it was also reported that rounded edges of the cylinder tips decreased the drag by 33%, relative to the blunt cylinder of same aspect ratio. It was suggested that the detachment over the blunt edge caused the increase in drag. This result was not consistent however with the study by Fackrell (1974) that reported lower drag for the blunt edged wheels. Further study into the effect of the aspect ratio was carried out by Zdravkovich *et al.* (1989) reporting spanwise symmetry breaking flow patterns for short cylinder with aspect ratios $W/D < 3$, consistent with most wheels.

The effect of the finite aspect ratio on the wake of the rolling truncated cylinder, in the present case $W/D = 0.4$ is significant. The finite width of the wheel allows for bypassing of the flow around the sides diminishing the length of the recirculation region. The separation point at the top of the wheel moves backwards as the aspect ratio decreases from infinity. Stapleford *et al.* (1969) studied the influence of the aspect ratio of a cylinder in contact with the ground and noted the increase in bypass flow around the shoulder edges as the aspect ratio of the cylinder is decreased considerably increasing the three-dimensionality of the flow.

**Effect of rotation** Cogotti (1983), Fackrell (1974), Mercker & Berneburg (1991), Stapleford *et al.* (1969) studied the influence of the rotation on the wheel reporting that

contact with the ground of the rolling wheel decreases both lift and drag. Using a laser sheet illuminating a the flow seeded with smoke, Fackrell (1974) examined the influence of the rotation on the location of the detachment point at the top of the wheel diminishing the region of suction at the top of the wheel in turn diminishing the lift in this region. In the region of the contact with the road however a strong pressure peak is associated with the entrainment of the fluid down towards the road forcing the flow out towards the sides of the contact region. Conversely the low pressure region downstream of the region of contact is further reduced by the rotation. The shedding at the top of the wheel and the strengthened jetting vortices at the bottom of the wheel lead to a taller and narrower wake for the rotating wheel compared to the non-rotating case as seen in the total pressure survey in a plane x/D=2.5 (Bearman *et al.*, 1988). Mercker & Berneburg (1991) in particular attribute this decrease in drag to the added momentum of the flow in the region of the jetting vortices and locally decreasing the pressure weakening the low pressure region immediately downstream of the body. The strengthening of the jetting vortices, also reported by Fackrell (1974) and more recently by Chauveau (2002) is referred to as *viscous pumping* and is responsible for the strong sensitivity of the rolling wheel wake to the modelling of the flow in and around the region of contact.

**Streamwise vortex models of the rolling wheel wake** have been proposed since Fackrell (1974) to explain the results of the total pressure survey in crossflow planes typically in the range $0.5 < x/D < 2.5$ downstream of both the stationary and rotating wheels. A large pair of counter rotating vortices associated to the jetting and a secondary weaker pair of vortices above them was reported. It was already acknowledged by both Fackrell (1974), Bearman *et al.* (1988) that this simplistic model did not account for the highly unsteady nature of the near wake. Cogotti (1983) built on these results and suggested the presence of a third pair of counter rotating vortices generated by the hub cavity. This vortex model of the wheel wake, consisting in three pairs of vortices, was confirmed by Mercker & Berneburg (1991) except for the sense of rotation of the top pair was opposite to that reported by (Cogotti, 1983, Fackrell, 1974). Saddington *et al.* (2007) studied a rigid 50% model of a Formula One tyre with LDA did not find evidence to support the presence of the hub vortices and suggested similar results to those of Fackrell (1974), Bearman *et al.* (1988). He reported the stronger pair of jetting vortices absorbing the top pair of vortices for $x/D > 1$. Wäschle *et al.* (2004), Wäschle (2007) suggested a more complex vortex structure of the near wake however since their study was based on RANS simulations unsteady features were not taken into account. In addition to these wake surveys on a fixed plane (typically in the range of $1 < x/D < 2.5$) studies of the wheel wake have focused on reporting the pressure distribution on the surface of the wheel.

With the first unsteady computation of an isolated wheel Chauveau (2002) showed the limit of these time-mean crossflow plane surveys. Studies of the impact of both turbulence models and shoulder and contact patch deformation show how sensitive the wake is to variations in shear which is obviously not taken into account by the pressure surveys. The tools developed and tested in this thesis and chapter in particular aim to address some of these limits.

The rolling wheels of ground vehicles contribute much more to the flow than drag however, in the context of Formula One and greener automotive, it is a key interest for designers which is why much of the work reported and presented in this chapter is heavily biased towards the objective of understanding which wake structure contributes most strongly to drag. Regards for safety for example deviate strongly from this objective but are nonetheless of prime importance. The wheel wells themselves have received attention (Fabijanic & George, 1996, Basara *et al.*, 2000) for safety considerations such as the spray caused by the wheel rotation (Gérardin *et al.*, 2014). The wake of a rolling wheel is also of interest for the reduction of road dust dispersion for industrial vehicles (Gérardin & Midoux, 2016).

**Effect of the edge shape** The present study is limited to a sharp edged cylinder however this model is not physical *per-se* in that actual manufactured wheel have a non-vanishing radius of curvature at the edge that can be further complicated by the presence of tread patterns and engravings.

The rounded wingtip produces a simpler structure of vortices that wrap up around the wingtip to a form vortex just above the suction extremity (Lombard *et al.*, 2016). The sharp edged wingtip, or square-tip, produces a larger number of stronger vortices on the edge surface that then interact differently with the main vortex on the suction side Chauveau (2002), Ghias *et al.* (2005). Mercker & Berneburg (1991) focused a study on the effect of the shoulder shape on the ensuing wake structure and reported that for sharp edged shoulder the sense of rotation of the two strongest vortices at the top of the wheel was opposite that reported by Cogotti (1983). More generally it can be argued that the shape of the shoulder mainly influences the flow by fixing the detachment point in cases with sharp, or at least sharper, shoulders. Wittmeier *et al.* (2014) compared full-scale and quarter scale tyres for wind-tunnel testing. Their results show that the flow and consequently the contribution to drag of the vehicle of the wheels is dominated by the bottom of the wheel that is not protected by the oncoming flow of the wheel well. They recommend the shape of the shoulder, in particular, to be as rounded as possible so as to avoid separation in this region. The sensitivity of the flow to geometry in this region is so strong that the three-dimensional printing of the brand on the tyre shoulder is responsible

for 1%.

**The challenge of the contact with the moving ground** Bearman (1978), Bearman & Zdravkovich (1978) studied the suppression of vortex shedding as an infinite span cylinder is brought in proximity with a stationary ground plane on which a boundary layer has developed. They show that the vortex shedding is shear driven and consequently that the shedding can be suppressed below a critical threshold of velocity, which for the infinite cylinder happens as it is well within the boundary layer of the flat plate ($z/D < 0.3$ for BL of $z/D = 0.8$ at the wheel centre).

For bluff bodies two non-dimensional numbers are typically used to quantify the flow: the drag coefficient $C_x = \frac{F_x}{\frac{\rho u_\infty^2 A}{2}}$ and the non-dimensional shedding frequency $St_D = \frac{f*D}{U_\infty}$ where $D$ is the diameter, Å a reference area, $\rho$ the fluid density, $f$ the dimensional frequency, $F_x$ the streamwise component of the force acting on the cylinder, $U_\infty$ the far-field velocity. Both $St_D$ and $C_x, y, z$ vary with Reynolds number.

The first bluff body in proximity with a ground to be studied was the cylinder reported by Wieselsberger (1921). As the gap between the infinite cylinder and the wall is decreased, the peak power spectral density of the velocity fluctuations remains at the same Strouhal number until the gap to diameter ratio decreases below $G/D = 0.3$. For lower gap values and, for the case of the cylinder in contact with the surface, the shedding is completely suppressed. Bearman & Zdravkovich (1978) further reported a positive lift (i.e. mean force acting on the cylinder repels it from the wall). Experimental work by Roshko (1954) conducted at the sub-critical $Re_D = 2 \cdot 10^4$ reported a decrease in the mean drag coefficient as the gap between the infinite span cylinder and the wall is decreased to zero while the drag increased. In an experimental study of the vortex shedding from a circular cylinder near a moving ground Nishino *et al.* (2007) showed that as the gap between the infinite cylinder and the moving ground decreases the drag decreases until reaching a plateau for a value of G/D of 0.35 after which the drag remains constant. This plateau effect wasn't previously reported for cylinder nearby fixed ground planes. Interestingly the experiments were repeated with a finite-length cylinder of aspect ratio 8.33 and the no shedding was measured regardless of the gap between the finite length cylinder and the rolling road. Nishino *et al.* (2007) suggest the plateau regime is provoked by the moving ground's absence of a growing boundary which suppresses the Kármán vortex shedding. They also concluded that the absence of variation in drag as the gap is decreased for the finite span cylinder is a result of the absence of Kármán shedding for all measured gap sizes. These experiments where conducted at two sub-critical Reynolds number $Re_D = 0.4 - 1 \cdot 10^5$. Leaving a gap between the rolling wheel and the moving ground plane can be an attractive solution for simplifying either the costly experimen-

tal setup or diminishing the complexity associated to the meshing of the contact region. Despite the wheel having an aspect ratio typically of $W/D < 1$. Nonetheless the study of two-dimensional cylinders in proximity to a stationary or moving ground plane can be informative to the wheel case. The study by Huang & Sung (2007) reported the suppression of the shedding near the gap with a moving ground-plane but not with the stationary ground-plane. Piccioni *et al.* (1997)'s study of a rolling motorbike wheel and fender emphasised the challenges of meshing the region of contact between the wheel and the road. Low aspect ratio wheels such as bicycle wheels are particularly sensitive to yawed inflow and effort is made by manufacturers to provide improved performance and handling in crosswind conditions (Godo *et al.*, 2009). Sprot *et al.* (2012) studied experimentally the effect of both tyre pressure and axle height (equivalent to loading of the tyre) and concluded that the more strongly deformed tyre, with a more pronounced bulge in the contact patch area, had the weakest drag for strongest deformation. Interestingly it was also reported that the wake was more strongly influence by the shape of the deformed shoulder (i.e. the bulge) than by the size of the contact patch itself.

A number of studies were conducted to investigate the influence of the gap between the cylinder and a ground plane, starting with the work of Taneda (1965) followed by Roshko *et al.* (1975), Bearman (1978), Bearman & Zdravkovich (1978) and more recently Lin (2002), REICHL *et al.* (2005) and Bimbato *et al.* (2011).

Although early studies such as Cogotti (1983) and Stapleford *et al.* (1969) seemed to indicate the contact of the rolling wheel with the moving ground plane had little effect on modifying the flow as compared to a case where the rolling wheel is close but not in contact with the road these views have been strongly contested by Sardou (1988). The modelling of the contact region by a *platform* or *contact patch* reported in Sawley & Richter (1997), Chauveau (2002) remains to this day the preferred method for meshes for boundary conforming codes. For non-conforming methods, such as that used by Pirozzoli *et al.* (2012) for example, there is no restriction on the size of the elements and so there is no artificial constraint for the mesh in the region of contact between the wheel and the road. Hobeika (2012) studied the effect of the wheel shape as it is deformed by the contact with the ground as well as the influence of different rim configuration finding that the tread patterns on the shoulder produced stronger vortex generation hence increasing the drag. Longitudinal grooves however decreased the drag when in the middle of the wheel and increased it when set closer to the shoulder.

**Reynolds number effects** The critical Reynolds number past which the drag and lift coefficients converged was estimated numerically by Chauveau (2002) for a sharp edged truncated cylinder, similar to the present model. Cogotti (1983) has shown experimentally

that the critical Reynolds number for a rotating wheel on a moving ground plane for a faired wheel with rounded edges is greater than $2 \cdot 10^6$.

**Unsteadiness** The drag is comprised of both skin-friction drag and pressure drag. The pressure drag is produced by the strong difference in pressure between the stagnation region ahead of the wheel and the low pressure in the base region.Due to strong shear in the stagnation region the wake is highly unsteady leading to strong fluctuations of the base pressure resulting in non-negligible fluctuations of both lift and drag. Similarly to the infinite span cylinder, the dependance of drag on $Re_D = \frac{U_\infty D}{\nu}$, where $U_\infty$ is the freestream velocity, $D$ the diameter of the wheel and $\nu$ the kinematic viscosity of the fluid is expected to be non-negligible because of the continuous curvature of the wheel and has been reported by Pirozzoli *et al.* (2012) with a drag coefficient $C_x = 2.35$ at $Re_D = 100$ and $C_x = 1.24$ at $Re_D = 500$.

The rolling sphere wake was investigated both experimentally and numerically by Rao *et al.* (2012, 2015), Hourigan *et al.* (2016) and, similarly to the results of Pirozzoli *et al.* (2012) for the rolling wheel, two transitions were reported. The first transition occurs at $Re_D = 139$ for the sphere and $Re_D \approx 300$ for the rolling wheel where the flow goes from a steady symmetric configuration consisting in two counter-rotating vortices to an unsteady flow dominated by the shedding of hairpin vortices from the top half of the cylinder or sphere (furthest away from the ground). The second transition, from a symmetric shedding of the vortex to a breaking of the spanwise symmetry, occurs at $Re_D = 192$ for the sphere and $Re_D|c2 \approx 500$ for the wheel For the rolling sphere, the dominant frequency associated to the hairpin shedding is $St_D = 0.117$ and $St_D = 0.050$ for the spanwise oscillations. For the rolling wheel, at $Re_D = 500$, i.e. just passed the critical Reynolds number for the symmetry breaking, the dominant spanwise frequency is $St_D, y = 0.25$ and the dominant frequency in the lift and drag coefficients is around $St_{D,x,z} = 0.1$. For the rolling wheel, as the Reynolds number is further increased towards $Re_D = 1000$, the $St_D, y = 0.25$ peak of $Re_D = 500$ broadens and is shifted towards higher frequencies to occupy the $St_D \subset [0.1 - 0.5]$ with two additional peaks appearing in $St_D = 0.03$ and $St_D = 0.9$. Similarly the lift and drag coefficients of the rolling wheel show broad peaks around $St_D = 0.25$, $St_D = 0.4$ and $St_D = 0.8$ with a lower frequency peak at $St_D = 0.02$.

Similarly to the rolling sphere, Khoury *et al.* (2010) analyse the flow field around a 6:1 prolate spheroid at $Re_D = 10^4$ where the major axis is perpendicular to the flow. The flow is still sub-critical but the transition occurs just as the flow separates. Interestingly they report the large-scale shedding Strouhal frequency of $St_D = 0.156$ which is below that of the wake of a sphere (at $St_D = 0.19$). They also report a Kelvin-Helmholtz instability

signal in the shear layer at a higher Strouhal range $3.2 < St_D < 3.4$ that are also higher than typically reported for a sphere ($1.9 < St_D < 2.4$ as reported by Constantinescu & Squires (2004)).

As highlighted by Carmody (1964) it is unlikely that a flow possessing distinct and large-scale periodic characteristics can be adequately described and understood in terms of a time-mean flow. One of the first studies to leverage PIV for non-intrusive near-wake analysis performed by Bearman (1997) reported major differences between the time-mean and instantaneous flows in a crossflow plane at a distance of 25% of the model car length downstream of the body. These early PIV results raised questions about the suitability of analysing the near wake of a bluff body with time-mean data and so equally questioning the pertinence of using time-averaged computational methods to assess these highly unsteady regions of the bluff-body wakes. Twenty years later these questions still remain relevant were shared by Axon *et al.* (1998), Sims-Williams (2001) with the first RANS computations of the wheel. This problem is still pertinent to bluff body flow analysis sixty years later as the tools for investigating the unsteady near-wake of bluff bodies still remain to be improved.

Despite pioneering efforts such as Chauveau (2002), it is only towards the end of the 00's that unsteady computations of the flow about a rolling wheel were attempted, mostly limited by both the computational cost and the immaturity of the underlying high-fidelity low-numerical-diffusion codes available. Because of the intrinsic unsteadiness of the flow about bluff bodies in general and rolling wheels in particular it can be attractive to use highly diffusive turbulence models associated to RANS computations to artificially stabilise the flow and improve the rate of convergence of the numerical solution. For computations of isolated wheels this can be an attractive approach. However when computing the flow about the front-section of a Formula One where numerous wing-tip vortices interact with the wake of the wheel, the added numerical diffusion might artificially weaken the strength of the vortices shed by the front-wing and negatively affecting the correlation between experimental and numerical data. The rigorous study comparison of three turbulence models for the flow about a Fackrell wheel by Basara *et al.* (2000) should be mentioned. The conclusion was that the flow field, and in particular the pressure distribution around the surface of the wheel were strongly sensitive to the turbulence model as well as to the mesh and none of the tested combinations was in agreement with experimental data. Chauveau (2002) performed the first Large Eddy Simulation (LES) of the flow over a rotating wheel. Whereas only half a wheel (with respect to the symmetry plane) was meshed for the steady state computations of the isolated wheel, the full wheel was meshed for the unsteady computation in order to allow for three-dimensional effects to develop. A key contribution to the understanding of the flow about a rotating Fackrell

wheel was the instantaneous flow fields in the $y = 0$ symmetry plane and in the a plane $x/D = 0.937$ downstream of the wheel with $x/D = 0$ corresponding to the centre of the wheel. These unsteady snapshots allowed, for the first time, the identification of both the fluctuation of the main vortices at the top of the wheel as well as their varying number. These were the first sets of results explaining why the sense of rotation and the number of vortices shed by the wheel have been so difficult to agree on. Because of the limited amount of available resources the author acknowledged that this seminal computation was under-resolved which is why a more quantitative analysis of these data could not be undertaken. It should however be stressed that this result is the first to conclude the necessity of performing unsteady computations for adequately representing the flow around a rolling wheel. Dassanayake *et al.* (2012) performed a qualitative numerical investigation of a Fackrell wheel with URANS, DES and LES using Fluent 13.0 and concluded that the LES offers the richest vortical structures (in terms of numbers). Salati (2012), Dassanayake *et al.* (2012) also performed an unsteady computation of the rolling wheel and show that LES offers the best correlation with experiment when compared against both DES and RANS. However, all three models correlate poorly for the pressure distribution on the wheel centre line. The poor agreement for the pressure distribution around the wheel, particularly for the LES, can be explained by the relatively low averaging time with respect to low frequency dynamics reported by Chauveau (2002), for example.

McManus & Zhang (2005) in collaboration with the BAR Honda F1 team, reported the first results from an unsteady computation of the flow about a rolling wheel over a moving ground plane and compared their results to the same Fackrell wheel geometry but with a stationary wheel using URANS. The authors only report time-averaged data: iso-vorticity magnitude surfaces of the time-averaged flow, as well as vorticity and velocity in a plane downstream $x/D = 1$. They also report strong sensitivity of the time-averaged flow to both mesh and turbulence model (Spallart-Allmaras and RKE). The flow was started from a uniform flow, allowed to develop for ten convective time units, based on the free stream velocity and wheel diameter and then averaged over 35 convective time units.

Berger *et al.* (1990) reported a *bubble pumping* mode associated with the oscillation of the point of wake closure in the streamwise direction at $St_D = 0.05$ for both a disk and a sphere. Duell & George (1999) also reported a bubble pumping mode at $St_H = 0.069$, where $H$ was the height of the Ahmed body.

Hashmi & Dimitriou (2006) showed the non-negligible effect of the skin friction on the wake stressing that the pressure distribution along the centre line of the wheel itself is not a good indicator of the performance of the modelling. Because of the non-linear saturation and feedback in the near wake, accurate surveys of the near wake might offer

better assessment of the quality of a given model. This point is a main driver for the approach presented in this chapter.

Axerio-Cilies *et al.* (2012) performed a comparative study between RANS, URANS, LES as well as experimental of a *stationary* representative Formula One wheel from the Toyota F1 car in 2007. This study aimed at further improving the understanding of the role of the numerical modelling methods on the wake of an isolated wheel. For the most complex case, with flow through the brake-ducts, callipers, etc, interest was driven by the wish to use *blown axles* during the 2007 season pioneered by Toyota and Ferrari. The study also stressed the importance of comparing the distribution of velocities in the wake as opposed to the more traditional approach of assessing different modelling methods by comparing the pressure distribution on the rolling wheel itself. Particularly in the context of numerical simulations using different codes with varying amounts of numerical dissipation which can significantly affect the interacting vortical structures produced by the distribution and fluctuations of shear on the body of the wheel.

**Numerical methods suitable for the highly unsteady flow about a bluff body.** The first published RANS computation of the rolling wheel on a moving plane is attributed to Axon *et al.* (1998) showing agreement with experimental results regarding the decrease in lift and drag for a rolling wheel compared to a stationary one and the presence of the strong pressure region ahead of the contact patch. It is stressed however that the detachment at the top of the wheel does not agree with experimental data suggesting the assumption of a fully developed boundary layer when using RANS closure models does not represent the state of the boundary layer over the smooth surface used by Fackrell (1974). Following the analysis of the influence of turbulence models used to close the RANS equations by Basara *et al.* (2000), Chauveau (2002) studied the suitability of both the Baldwin-Lomax and Spallart-Allmaras models. The parameters of the Baldwin-Lomax model had to be reduced until it vanished. Interestingly in all cases presented the moving ground plane boundary condition was relaxed to a free-slip boundary condition in order to decrease the resolution requirements to model the strong shear in the region of the contact patch. Finally it was reported that the excessively dissipative turbulence models decrease both the lift and drag coefficients of the rolling wheel. More recently, Newbon *et al.* (2017) studied both experimentally and numerically the effect of the upstream wake of a Formula One on a second car in an overtaking manoeuvre. In particular they show how the exposed rotating wheels of the upstream vehicle contribute strongly to the momentum deficit and so to the loss of downforce for the second vehicle.

Wäschle *et al.* (2004) compared two commercial codes ubiquitous in industry, Star-ccm+ and PowerFLOW to LDA measurements of both stationary and rotating isolated

wheels in a wind-tunnel. The authors found generally acceptable qualitative agreement between the two codes and the experiment. Wäschle (2007) also looked both experimentally and numerically at the effect of the wheel well on the rotation of the wheel showing a strong difference in wake structure between the rotating and non-rotating cases. These results show the importance of accurately modelling the rotation of the wheels in the wheel-wells for optimisation of the car as a whole. This is consistent with the results from Dimitriou & Klussmann (2006) showing the synergy between automotive and racing activities for the development of the understanding of rolling wheel wakes. Validation of numerical tools by aiming for better than 2% error between experiment and CFD (Axon *et al.*, 1998, Wäschle *et al.*, 2004, Kandasamy *et al.*, 2012) is important for improving the efficiency of the design cycle. These studies on specific aspects of the rolling wheel wake are complemented by studies of the wheel wake building and comparing numerical results with experimental work of Fackrell (1974) such as Mears *et al.* (2002, 2004), Issakhanian *et al.* (2010).

Because of the smooth nature of the separation at the top of the wheel, numerical models that rely less on wall-modelling and more on wall-resolving the dynamics, such as DNS using high-order methods are believed to offer unprecedented correlation with experimental data.

**What we neglect** For road and racing vehicles the wheels are not simplified truncated cylinders or variations of the Fackrell wheel. They include brake assemblies, suspensions systems and spokes all of which have a non-negligible influence on the wake. Leśniewicz *et al.* (2014) for example, together with PSA Peugeot Citroen, compare both *moving wall boundary* (i.e. solid body of rotation) and the *moving reference frame* showing that for a realistic wheel model including spokes and brake assembly the MRF model correlates better with experiment. They also reported reduced area drag for the case of a tyre with longitudinal treads $\Delta SC_x = -0.002$ (Wolf-Heinrich Hucho, 1993) . The effect of slip-streaming is also strongly influenced by the rolling wheels (Dominy, 1990). (Kothalawala & Gatto, 2016) performed both RANS and URANS computations on an isolated Fackrell (1974) wheel with a gap (similar to the original setup of Cogotti (1983) but with a gap between the road and the wheel $0.63 < h/D < 2.5$ which isn't representative of a wheel configuration but nonetheless informative regarding the effect yaw has on the recirculation bubble. Wäschle (2007) effect of rolling wheels on the Ahmed body and on models of real cars concluding that despite the increase in drag for the car resulting from the higher drag when the front-wheels rotate the rear wheels contribute towards decreasing the drag by entraining energetic flow in the recirculation region of the wake of the car increasing the base pressure.

In practical applications, there is often flow through the wheel associated with brake cooling and rims, etc which is not modelled in the current truncated cylinder case and is believed to have a strong influence on both the structure of the instantaneous flow and the time-averaged force coefficients. Landstrom *et al.* (2012), Kandasamy *et al.* (2012) and the influence of tread pattern has also been investigated by Hobeika (2012), Vdovin (2013). Cooling airflow also has an impact on the wheel aerodynamics (Landström & Löfdahl, 2011, Vdovin *et al.*, 2013, 2014) and more recently DeMarco *et al.* (2017), Extending this work to industrially relevant cases would require to complexify the geometry by including hub-cavities, spokes, roughness and tread patterns, tyre deformation, brake assembly, suspension assembly, wheel well and the rest of the body of the car. The experimental investigation by Brizzi *et al.* (2004) reported the quantification of the flow through the wheel. Sprot *et al.* (2011) studied the effect of hub flow through, or axle blowing, on the wake of a rolling wheel and how different flow through setups affecting both the drag and the shape of the wake. The flow ought to be complexified by including impinging flow at a yaw and camber angle as well as taking into account brake cooling ducts, noise/turbulence. The cooling flow through the brake duct assembly, studied by Dreyer *et al.* (2007) for example, is also neglected in this work despite its importance for both security and performance reasons. Finally in this study we have not investigated the influence of changing yaw angles let alone dynamic change in yaw angle which might also strongly modify the flow. Dynamic sweeps at varying attitudes are now commonplace for aero investigation of Formula One cars. Already Aschwanden *et al.* (2006) investigated LMP1 car aerodynamics with dynamic sweeps in the wind-tunnel mimicking the highly dynamic track conditions. They found that the fluctuation of aerodynamic coefficients varied significantly when pitch and heave oscillations at 20Hz were introduced into the model. The static wheel model of the truncated cylinder does not take into account the static deformation of the tyre due to loading, heating and rotation, let alone their unsteadiness. Mankowski *et al.* (2011) had interest in transient yaw fluctuations and reported strong sensitivity for reduced frequencies in the range of $0.3 < \omega_R = 2\pi L/U < 1.5$.

The effect of the interaction with a wing-generated vortex and the wheel and its wake is obviously the main challenge for designing open-wheel racers and studies such as Diasinos & Gatto (2008), van den Berg & Zhang (2009) look into the effect of the location and strength of the vortex generated by a wing of different span and angle of attack on the wheel wake.

A canonical example of a rolling wheel interacting with vortical structures shed from a front-wing is present in Chapter 6.

**In summary the open challenges regarding the rolling wheel in its simplest form require deeper insight into the dynamics of the very near wake as well as quantifying the shear on the rolling body.** Despite forty years of research in the field of wheel aerodynamics leveraging wind-tunnel, water-tunnel as well as computational simulations a clear understanding of the flow about a rotating wheel in contact with a moving ground plane still remains an open challenge. Building on the previously proposed models of the wake structure in the time-average sense (Fackrell, 1974, Cogotti, 1983, Broadhurst, 2007) and more recently insight regarding the dynamics of the flow (Croner *et al.*, 2013, Pirozzoli *et al.*, 2012) we aim to add to the discussion by identifying the flow structures associated to the previously reported dominant frequencies.

**Structure of this chapter** Previous studies of the wheel wake have either been conducted experimentally recording the wake in planes downstream of the wheel or numerically by recording averaged flow fields as well as averaged force coefficients. More recently the power spectral densities of the forces acting on the wheel have been reported however the flow structures associated to these frequencies have not yet been identified. The current study aims to shed light on the flow structures associated to the previously reported dominant frequencies. Dynamic mode decomposition (DMD) is used to extract these flow features. The wall shear stress has been extracted for each of these dominant DMD modes giving further insight into the effect of the wake on the wheel. These simulations provide a detailed view of the topology of the wake and the identification of the regions of strongest shear associated to each dominant frequency is believed to be helpful information in view of informing control strategies. The details of the numerical setup and method are presented in Section 5.2. The results of the extensive DNS are presented in Sec. 5.3 with a comparison of lift, drag and side-force coefficients in Sec. 5.3.1, the power spectrum density (PSD) of these coefficients. In Sec. 5.3.2, the results of the dynamical mode decomposition in Sec. 5.3.3 correlating wake structures to both the modes with high dynamical amplitude as defined by DMD and the peaks reported by the PSD. In Sec. 5.3.4 a flow field is reconstructed using only the mean flow and the three most dominant DMD modes and this reconstructed flow field is compared and contrasted with the prevalent streamwise vortex models.

## 5.2 Case definition and numerical setup methodology

We consider a wheel of diameter $D$, width $W = 0.4D$ rotating with a no-slip boundary condition at $\omega = 2U_\infty/D$ where $U_\infty$ is the velocity of both the inflow and the moving ground plane in a domain of dimensions $\Omega = [5D, 5D, 15D]$ with the center of the wheel

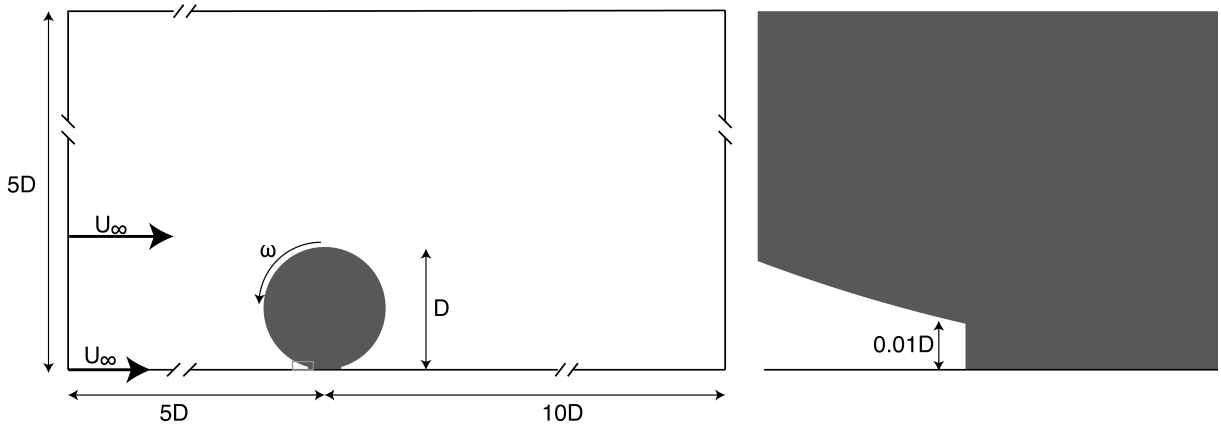



**Figure 5.1** – Geometry of the rolling wheel on the ground. Inset with close view of extruded patform of height $0.01D$ representing the contact between the wheel and the road.

at $5D$ from the inlet. This domain is identical to that validated by Pirozzoli *et al.* (2012). The Reynolds number based on the diameter of the wheel, defined by $Re_D = U_\infty D/\nu = 1000$ is considered where $\nu$ is the dynamic viscosity of the fluid is the key governing parameter when considering the flow over a rolling wheel without a gap. The simulation was advanced for $10^2 D/U_\infty$ allowing for sufficient development of the flow and time for resolving frequencies down to $St_D = 0.02$ . Following previous studies (Pirozzoli *et al.*, 2012, Stewart *et al.*, 2010*b*,*a*, Rao *et al.*, 2012) the compressible effects can be neglected for this flow. The incompressible Navier-Stokes equations are used to model this flow. To mimic the region of contact between the rolling wheel and the translating road a small platform of height $0.01D$ is inserted between the truncated cylinder representing the wheel and the rolling road. This modelling method, commonplace in academic studies, is also standard in both the motorsport and automotive industry. Because the flow, and in particular the jetting vortices, are sensitive to the shape of the tyre in the region of contact a rigorous analysis investigating different shapes and sizes (with respect to the diameter) would add to the general understanding of the scope and limitations of this modelling technique motivated by the limit of curvature conforming mesh in the vanishing gap between the wheel and the road.

To assess the influence of the flow around the rolling wheel we monitor the forces acting on the body that we consider to be the contact patch, the side walls or fairing and the wheel. These forces are decomposed into streamwise, spanwise and ground-normal components $F_x$, $F_y$ and $F_z$ respectively. In accordance with best practise these forces are non-dimensionalised by the frontal surface of the wheel as well as the inflow velocity as $C_{x,y,z} = \frac{2F_{x,y,z}}{0.4D^2U_\infty^2}$. The non-dimensional frequencies of the forces acting on the body are also of interest and these frequencies $f_{x,y,z}$ are also non-dimensionalised as the Strouhal

number $St_{D|x,y,z} = \frac{Df_{x,y,z}}{U_\infty}$.

In addition to these force histories we record three dimensional snapshots of the wake at a high sampling frequency of $St_{D|Sampling} = 20$.

### 5.2.1 Numerical formulation and validation

The open-source spectral/hp element library `Nektar++` (Cantwell *et al.*, 2014) is adopted to solve the incompressible Navier-Stokes equations. Pressure and velocity fields are decoupled by a stiffly-stable velocity correction scheme and time integration is achieved by a second-order accurate implicit-explicit scheme (Karniadakis, 1990). Both h- and p-refinement were conducted to assess the influence of the grid on lift, drag and side-force coefficients. The h-type refinement was achieved by increasing the number of elements on the surface whereas the p-refinement was achieved by testing the higher resolution grid at higher polynomial orders. The incompressible Navier-Stokes equations were then discretised by fourth-order polynomials for the u-, v- and w-components of the velocity field and third order polynomials for the pressure field the choice of which was informed by the grid independence study. In comparison to the previous DNS by (Pirozzoli *et al.*, 2012) where 120 elements were used to discretise the diameter of the cylinder a non-uniform grid was used in the present study with elements as small as 0.001D at the intersection between the wheel and the wheel shoulder to improve the resolution of the powerful shear layers evidenced in this region by the modal analysis.

To achieve best geometric fidelity in representing the curved surface of the wheel, each element was curved using spherigons(Volino & Thalmann, 1998) and seventh order polynomials. This numerical setup corresponds to the experimental setup of a rolling belt in a wheel tunnel where the boundary layer prior to the belt is removed through bleeding holes (Fackrell, 1974). Consequently it can be assumed there is no boundary layer upstream of the rolling wheel, except for that created by the pressure rise and jetting. The truncated cylinder was originally pioneered by (Fackrell, 1974) as the simplest geometry that could represent the flow around an actual rolling wheel. The straight side walls, or fairing, are used to prevent any through-flow between the faces of the wheel. However the main flow features of the rotating wheel, namely the detachments mentioned previously as well as the jetting vortices originally reported by Fackrell (1974) and further studied by (MacCarthy, 2010) were present for this simplified geometric model. Regarding the geometry it is important to stress the difference between the current setup and that used by (Pirozzoli *et al.*, 2012) in the contact region between the road and the rotating wheel. Whereas as (Pirozzoli *et al.*, 2012) modelled the contact region by a single line corresponding to the intersection of the cylinder with the ground plane we rather followed

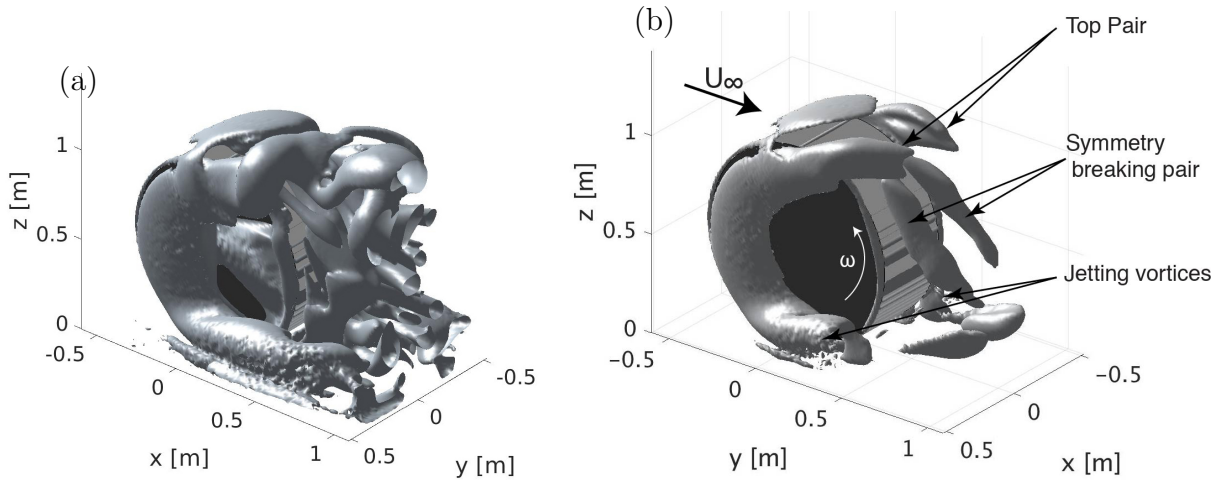



**Figure 5.2** – iso q-criterion at $Q = \cdot 10^{-5}$ of the instantaneous (a) and mean (b) flow field.

the recommendations based on the experimental work of (MacCarthy, 2010) motivating the importance of accurately modeling the size of the contact region. To this end, the contact region, or contact patch is modelled by extruding a straight angled parallelepiped platform from the ground plane of height $0.01D$ and of the same width as that of the wheel $W = 0.2D$. The boundary condition imposed to this platform was that of a pure rotation, similarly to that of the rest of the wheel, but with the added constraint of zero-normal flow to ensure no flow-through in the contact region. At the outflow plane the boundary condition developed by (Dong *et al.*, 2014), balancing the kinetic energy influx through the outflow boundary to insure stability was used. The computation was initialised by a uniform flow $(U_\infty, 0, 0)$ and $20tU_\infty/D$ were computed before the time-averaging was initialised and then recorded for $90tU_\infty/D$. The mesh consisted in $2 \cdot 10^5$ prismatic elements and $2.1 \cdot 10^6$ tetrahedral elements. The computation of a convective time-unit required 4h on 3840 ARCHER mpi ranks for a sixth-order accurate in space and second order time-integration scheme. The mesh, session file and initial condition are openly available upon request.

## 5.3 Dynamics of the Rolling Wheel Wake based on DNS

The Q-criterion (Dubief & Delcayre, 2000) of both the instantaneous snapshot and time-averaged flow field are represented in Figures **??**a) and **??**b) respectively.

### 5.3.1 Time-averaged flow field

The time-averaged flow field visualised by q-criterion reveals the presence of four pairs of vortices. Starting from the top of the wheel, or furthest away from the ground plane, a first pair of vortices is related to the unsteady detachment and roll-up of the flow over the tire shoulder as it moves from the high pressure stagnation region in front of the wheel to the side of the wheel. The two vortices visible in Figure **??**b) are the tails of the horseshoe vortices that can be seen in the instantaneous snapshot Figure **??**a). Close to the symmetry plane of the wheel another pair of counter-rotating vortices is visible. These two vortices have the opposite sense of rotation to the tails of the horseshoe vortices. Contrary to the horseshoe vortices that advect at a constant height of roughly $D$ from the ground plane, these two vortices contribute to the lower half $z < 0.5D$ recirculation region within $0.5D$ of the wheel. In the lower half of the wheel the wake is dominated by two pairs of vortices. The first pair is similar to the symmetric ones of the top *mixing vortices* and have a non-negligible angle with respect to the ground plane. The second pair of vortices in the lower half of the wake are the so-called *jetting vortices* already identified by Fackrell (1974). Similarly to Chauveau (2002) we report a sense of rotation of the jetting vortices opposite that of Cogotti (1983). Both the instantaneous and time-averaged flow fields reveal the presence of an as of yet unreported *secondary* counter-rotating vortex pair parallel to the jetting vortex and caused by secondary separation.

The steady re-attachement about the shoulder of the wheel in the front-half (for $x/D < 0$) have the same crescent shape reported by Zdravkovich *et al.* (1998).

It should be stressed that spanwise symmetry breaking (i.e. the time-averaged flow is not symmetric in the span wise symmetric) has been reported for many bluff bodies amongst which the rolling sphere but has not been investigated for the rolling wheel. The possibility of random switching between states in the wake together with low-frequency ($St_D < 0.05$) vortex meandering prevent the average from converging for the hundred convective time-units simulated. It does however offer some insight when analysed in conjunction with the DMD modes which can be seen as linear perturbations of the mean flow (assuming it representative of the steady state) (Chen *et al.*, 2012, Rigas *et al.*, 2014).

### 5.3.2 Time-averaged force coefficients

Since the seminal work of Fackrell (1974) followed by the work of Cogotti (1983), Mercker & Berneburg (1991), Chauveau (2002) and more recently Pirozzoli *et al.* (2012) emphasis has been put on understanding the wheel wake by reporting the number, and sense, of streamwise oriented vortices in a x-normal plane in the near-wake ($x < 0.5D$) of the wheel. However as reported by Chauveau (2002)who computed the first unsteady flow

| | $Re_D$ | $C_L$ | $C_D$ | $C_S$ |
|---|---|---|---|---|
| Fackrell & Harvey | $2.10^5$ | 0.28 | 0.51 | - |
| Pirrozzoli *et. al.* | $1.10^3$ | $1.01 \pm 0.01$ | $1.03 \pm 0.01$ | - |
| Present | $1.10^3$ | $0.36 \pm 0.01$ | $0.97 \pm 0.01$ | $0.00 \pm 0.02$ |

**Table 5.1** – Time averaged lift, $C_L$, and drag ,$C_D$, coefficients compared to both experiment and previous DNS.

about a rotating wheel these streamwise vortex based models are loosely representative of the actual flow. The highly unsteady and three-dimensional nature of the shedding mechanisms produce a varying number of vortices detaching from the surface at varying orientations on a wide range of time-scales which is believed to explain why, adding to the complexity of the experiment or the cost of the computation, there has been little agreement regarding the time-averaged values of the lift, drag and side-force coefficients. We nonetheless report them in Table 5.1 for sake of comparison with the previous DNS results at $Re_D = 1000$ (Pirozzoli *et al.*, 2012). Reproducing experiments is challenging because of the reported sensitivity of the wake to the geometry of the rolling wheel that varies for different loading, temperature, nature of the compound, etc. Numerically the challenge remains in both meshing and assigning physically relevant boundary conditions to the region of contact between the moving ground plane and the rolling wheel. These small variations in geometry of the wheel are believed to explain the differences in reported coefficients between the present DNS result and those from the DNS of Pirozzoli *et al.* (2012). We should also emphasise the effects of the rich dynamics in the sense of large spectrum of pertinent time-scales. The cost associated to both Pirozzoli *et al.* (2012) and the present DNS limit the frequencies investigated to a range of $St_D = [0.02, 4]$ but do not exclude the presence of lower frequencies (i.e. $St_D < 0.02$) having an effect on the time-averaging. The next section aims to give further insight into the wake, and in particular to the structures associated to a given frequency dominating the power spectral density of the force coefficients.

### 5.3.3 Power Spectral Density of the Force Coefficients

Pirozzoli *et al.* (2012) were the first to report the power spectrum density of the forces acting on the body of a rolling wheel on a moving ground plane computed from DNS at $Re_D = 1000$.

The streamwise drag coefficient $C_x$ (Figure 5.3, top) is dominated by the wake signal corresponding to the formation and shedding of the vortex loops at the top of the wheel around $St_{C_x} \approx 1/\pi$. Harmonics of this mode are also clearly visible at $St_D = 2/\pi$ and

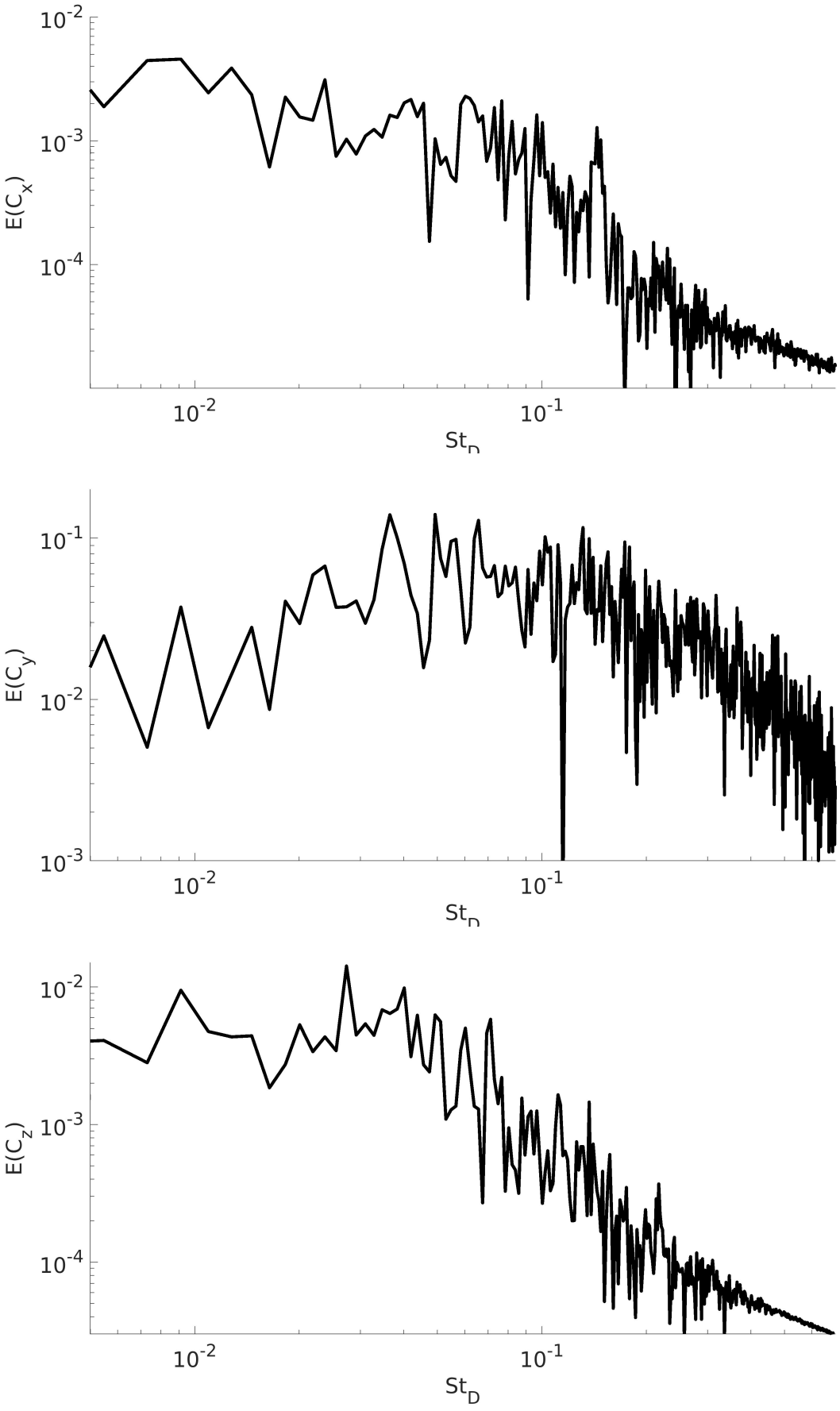



**Figure 5.3** – Unfiltered Power Spectral Density of $C_x$ (top), $C_y$ (middle) and $C_z$ (bottom).

$St_D = 3/\pi$. The power spectra density also confirms the lift coefficient $C_z$ (Figure 5.3, middle) is equally dominated by the pressure fluctuation brought upon the surface of the cylinder by the periodic shedding of the vortex loops. The non-linear saturation in the near wake also generates global modes which in turn affect the shedding mechanisms on the body of the rolling wheel. The spanwise component of the force coefficient $C_y$ betrays a dominance from the sinuous symmetry breaking mode at $St_{D|z} \approx W/\pi \approx 0.12$. In addition, and similarly to the rolling sphere case at $Re_D = 300$ the force signals equally exhibit a rich signal compatible with a chaotic behaviour of the wake.

Contrary to the spectra of the side-force coefficient, the spectra of both the lift and drag coefficients indicate there might be strong activity in the low-frequency range, below $St_D < 0.08$. For bluff bodies these low frequencies (ie lower than the shedding frequencies) are typically correlated to bubble pumping modes, or slow streamwise oscillations of the recirculation region (Berger *et al.*, 1990, Duell & George, 1999, Evstafyeva *et al.*, 2017).

The noise seen in the PSD is comparable to that reported by Rao *et al.* (2012), Pirozzoli *et al.* (2012) for the rolling sphere for a case where the Reynolds number is 20% larger than the critical Reynolds number at which the symmetry breaking is first apparent. This indicates the strong non-linear interactions between modes already in the very-near wake $x/D < 0.5$ for bluff bodies or the *rapid progression towards chaotic flow* as concluded by that study. Longer time acquisition is required for further improving the quality of the PSD.

### 5.3.4 Dynamic mode decomposition of the near-wake

In view of improving the understanding of the structure of the wake and in particular in view of correlating a coherent flow structure to given frequency identified in the PSD of the body force coefficients or sensing of the near wake we have applied the Dynamical Mode Decomposition (DMD) first introduced by (Schmid & Henningson, 2001).

In the following paragraph we recall the main hypothesis behind DMD as well as the main steps in obtaining the decomposition. The underlying assumption of DMD, and following the notation of Schmid & Henningson (2001), is that there exists a *linear mapping* $\mathbf{A}$ between a snapshot $\mathbf{v}(\mathbf{t} + \mathbf{\Delta t})$ at time $t + \Delta t$ and the snapshot $\mathbf{v}(\mathbf{t})$ at time $t$ where $\Delta t$ is assumed to be a constant sampling time. Because of the large range of frequencies identified by the power spectral densities of the body force coefficients (Figure 5.3) the DMD was computed for different $\Delta t \in [0.05, 1.4]$. The sequence of $N$ snapshots is then represented as a matrix

$$V_1^N = [\mathbf{v}_1, \cdots, \mathbf{v}_N]$$

where each column $i$ is a snapshot $\mathbf{v}_i$ at time $t = t_0 + i \cdot \Delta t$ where $t_0$ is the time of the first snapshot and $\Delta t$ the sampling time, supposed constant. The main hypothesis of the DMD is that over the time-horizon $N\delta t$ the time advancement operator $A$ is supposed to be linear

$$\mathbf{v}_{i+1} = A\mathbf{v}_i$$

For a sufficiently large number of snapshots, the n$^{\text{th}}$ snapshot is contented in the span of $V_1^{N-1}$, in other words:

$$AV_1^{N-1} = V_2^N = V_1^{N-1}S + re_{N-1}^T \tag{5.1}$$

where $r$ is a residual vector and $S$ is of the form of a companion matrix:

$$S = \begin{pmatrix} 0 & & & & a_1 \\ 1 & 0 & & & a_2 \\ & \ddots & \ddots & & \vdots \\ & & 1 & 0 & a_{N-2} \\ & & & 1 & a_{N-1} \end{pmatrix} \tag{5.2}$$

From a point of view of the flow physics the linear hypothesis is akin to a multi-scale argument which is the DMD is sensitive to the sampling frequency. A singular value decomposition is then applied to the sample sequence $V_1^{N-1} = U\Sigma W^H$ where $U$ are the POD modes of $V_1^{N-1}$. Equation 5.1 becomes :

$$S = U^H V_2^N W \Sigma^{-1}$$

The modal structures are extracted from the matrix $S$ in the same way the global modes are extracted from the eigenvectors of the Hessenberg matrix H with the DMD modes :

$$\phi_i = U y_i$$

where $\mu_i$ are the eigenvalues of $Sy_i = \mu_i y_i$ with $\Re(\log(\mu_i)/\Delta t)$ the growth rate and $\Im(\mu)$ the frequency.

In summary the dynamic mode decomposition has been applied to associate the coherent flow structures to the peaks from the PSD of the force coefficients. The DMD analysis correlates the dominant frequencies, as defined by those with the largest growth rate $\Re(\log(\mu_i)/\Delta t)$ in terms of dynamical importance, or weakest decay, to the dominant frequencies of the power spectral density reported in Figure 5.3. The four dominant frequencies identified by the DMD are $St_D = 1/\pi$ and $St_D \approx 2/\pi$ associated to the vor-

tex shedding at the top of the wheel and previously reported by Pirozzoli *et al.* (2012), $St_D \approx W/\pi$ corresponding to the meandering of the near wake which dominates the side-force and finally a previously un-reported low frequency $St_D = 1/4\pi$ frequency that dominates the drag/lift coefficients.

### $St_D = 1/4\pi$ jetting vortex meandering

The PSD of both lift and drag, reported in Figure 5.3 indicate a low frequency or roughly $St_D = 1/4\pi$, or lower, dominates. The force history gathered during the present computations span one hundred convective time units however and were limited by available resources. This low frequency therefore should be interpreted as an upper-bound for the the dynamic mode evidenced by the DMD. Figure 5.4 (bottom) shows that, contrary to the $St_D = W/4\pi$ and $St_D = 1/\pi$ modes where the flow structure associated to these frequencies are located, respectively, in the near wake on the top-half of the wheel and at the top of the wheel, the low frequency $St_D = 1/4\pi$ mode is most active in the lower part of the wake where the jetting vortices dominated, as can be seen from the peaks in shear (dark blue regions in Figure 5.4 (bottom right)), nearby the contact patch. The nature of the structures apparent in Figure 5.4 (bottom right) can be explained by the non-linear interaction between the modes in the near wake. The existence of this low frequency mode as well as the rich nature of the low frequency region in the PSD motivates future computations over over longer time horizons.

### $St_D = 1/\pi$ horseshoe vortex shedding

The dominant frequency for the symmetric shedding of the hairpin vortices at the top of the wheel in Figure 5.4 (middle left). Similarly to the rolling sphere (Rao *et al.*, 2012), the bottom half of the rolling wheel does not exhibit the same shedding as the top half because the entrainment of the fluid in the lower region works towards locally diminishing the shear and so avoiding the onset of the viscous instability, responsible for the shedding at the top of the wheel, as can be seen from the distribution of the shear on the wheel surface (Figure 5.4 (middle right)).

### $St_D = W/\pi$ the symmetry breaking mode

The analysis of the power spectral density of the side-force coefficient revealed a dominant frequency around $St_D = W/\pi$ and the DMD analysis (Figure 5.4 (top left) reveals this frequency can be associated spatially to the pair of counter rotating vortices generated as secondary detachments from the top of the wheel (as seen in the mean flow field

Figure **??**). The meandering of these two counter-rotating vortices and the associated shear on the body of the rotating wheel is responsible for the $y = 0$ symmetry breaking.

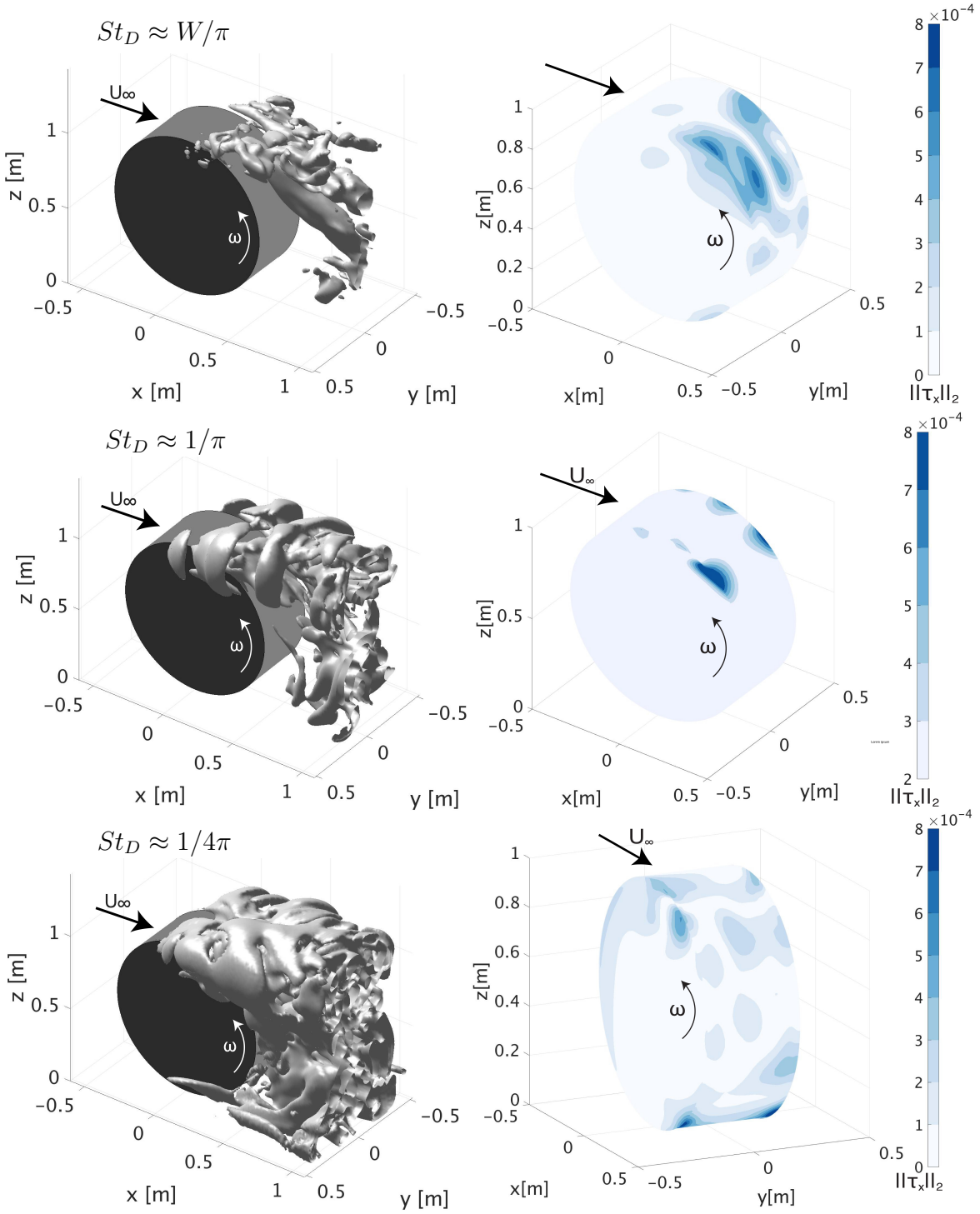



**Figure 5.4** – DMD modes associated to the symmetry breaking $St_D = W/\pi$ (top), the shedding of the hairpin vortices $St_D = 1/\pi$ (middle) as well as the low-frequency bubble-pumping mode $St_D = 1/\pi$ (bottom).

## 5.4 Conclusion and Outlook

The flow about a rolling wheel on a moving ground plane at $Re_D = 1000$ has been investigated numerically by means of a DNS. The vortices of the three-dimensional DMD modes were visualised by computing the q-criterion and the shear on the wheel surface associated to each DMD mode was computed revealing the regions where it is strongest. The three most unstable DMD modes were computed to be :

1. $St_D = 1/\pi$ associated to the periodic shedding of the symmetric horseshoe vortices at the top of the whee.

2. $St_D = W/\pi$ associated to the symmetry breaking because of the meandering of the secondary vortices at the top of the wheel.

3. $St_D = 1/4\pi$ a low frequency bubble pumping mode that seems to most strongly influence the surface of the rolling wheel through the meandering of the jetting vortices.

The location of the regions of strongest shear can be seen as potential candidates for placing sensors for informing flow control strategies that would target a specific dynamic mode.

In the more general context of automotive flows and motorsport in particular, the flow impinging the wheel is strongly modified by either a wheel well or front-wing. Chapter 4 and Chapter 5 have focused on the dynamics of the flows of the isolated elements and in the next chapter a canonical example of a Formula One front-section is investigated.

# Chapter 6

# The McLaren MP4-17D front-section

> If you asked any of the mechanics and engineers, who are working from early in the morning until 11 o'clock seven days a week, and have been for 10 years, they'd tell you there is no glamour in it for them.
>
> Bruce McLaren

## 6.1 Motivation

In this chapter we report numerical results of flows modelled with the high-fidelity spectrla/hp element LES of the McLaren MP4-17D front-section and compare them to experimental results of Pegrum (2006). The three sub-models considered are a wheel only, an isolated front-wing and both together.

In all three cases boundary-conditions on the ground-plane mimic a rolling road. Results will be correlated by comparing mean total pressure distributions $CP_0$ as well as mean streamwise velocity to the experimental data obtained in the Imperial College windtunnel by Pegrum (2006).

This increasingly complex vortex systems generated by Formula One front-wings since the early 00's aim at maximising the global efficiency of the front-wing. The 1998 change of regulations ushered in the development of ever more complex end-plates. Formula One aerodynamists quickly realised it was advantageous to load the tips of the wings to generate powerful vortices to manage the flow around the front-wheel. This is an interesting example of the non-linear optimisation of aerodynamic elements for a Formula One car. Because the front-wing conditions the flow for the rest of the car, increasing loading of the front-wing increases overall downforce levels but past a certain point (before

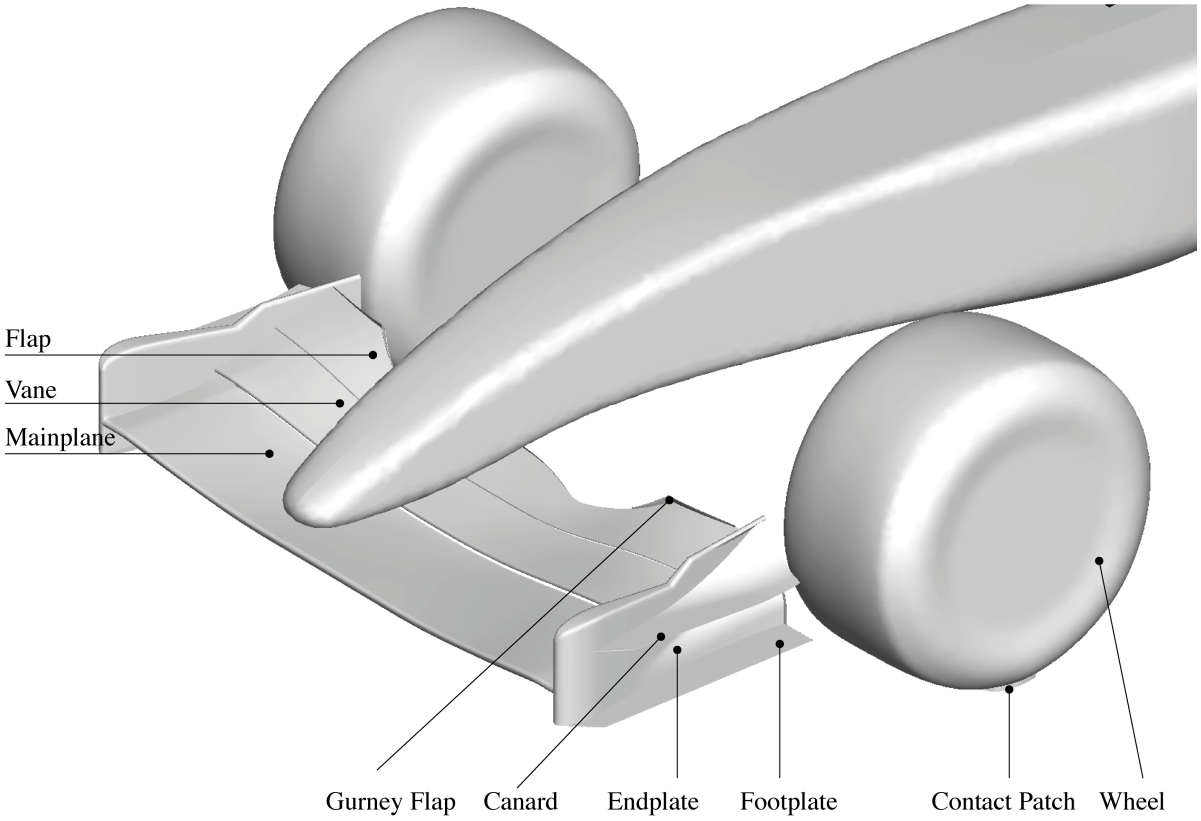



**Figure 6.1** – Different elements of the MP4-17D front-wing.

stall) it might be that the excessive upwash caused by the front-wing becomes detrimental to both the floor and the rear-wing. Front-wing design, and end-plates in particular, can also have a strong influence on the drag produced by the front wheels. Increasing the number of vortices on the end-plate might locally increase wake drag (from the front-wing) but decrease the overall drag of the car by reducing the of the front-wheels by modifying its wake. In the following we report the results of a comparison between preliminary LES and the experimental data in view of assessing the capability of high-fidelity CFD of correctly modelling the flow physics.

## 6.2 Near field wake of the MP4-17D front-wing

Formula One front-wings are designed to operate in a flow that is influenced by the rolling wheel immediately downstream of it and so it seems quite artificial to study the wake of an isolated front-wing. The motivation for the experimental study was to assess the topology of the wake immediately downstream of its trailing edge and then study how different ride-heights influenced the interaction between the strongest vortices shed by the front-wing.

The motivation of the numerical study builds on these objectives however, due to limited computational resources only one ride-height $h/c_{MP} = 0.48$ has been investigated as of time of print. The LES of this isolated front-wing can contribute to the understanding of the flow by offering data on the wing itself where it is impractical to access with PIV. Additionally, from a numerical point of view this test case is a more representative test than the wingtip presented in Chapter 4. In particular, the LES methodology developed during this thesis should enables dynamic boundary layer modelling on the strongly loaded wings as well as possible merging or breaking up of the vortices.

The Reynolds number is set to $Re_{C|MP} = 2 \cdot 10^5$ based on the chord of the mainplane. The mesh consists in $2{\cdot}10^5$ prisms and $1.84{\cdot}10^6$ tetrahedral elements. The initial condition was interpolated onto the high-order mesh from a RANS solution and the flow was time-averaged for 5 convective time-units of the mainplane $t_c = c_{MP}/U_\infty$ after letting the flow settle for five convective time units. One convective time-unit required 24h on 3840 mpi ranks of ARCHER.

### 6.2.1 Instantaneous flow field

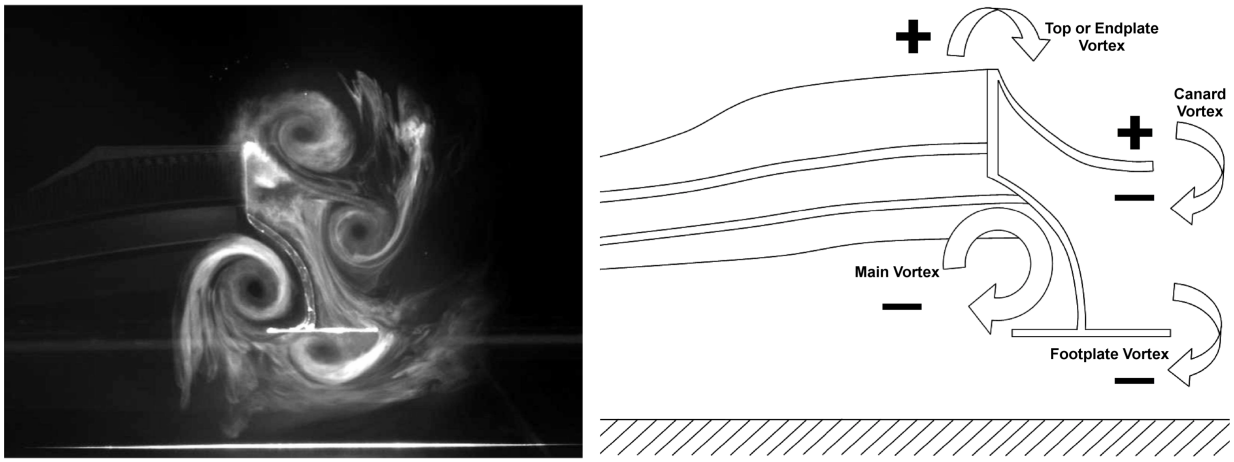



**Figure 6.2** – Laser-smoke visualisation (looking upstream) of the flow in a $y = -0.3$ plane directly downstream of McLaren MP4-17D front-wing without wheel at a ride height of $h/c_{mp} = 0.48$ and with a moving ground plane and $Re_{c|MP} = 2 \cdot 10^5$ (Pegrum, 2006).

Pegrum (2006) identified four main vortices produced by the front-wing: a top or end-plate vortex, a canard vortex, footplate vortex and the main vortex (Figure 6.2). A contribution of the LES towards the understanding of the flow around the MP4-17D front-wing can be seen in the total-pressure iso-contours (at $CP_0 = 0$) in Figure 6.3 which reveals :

1. the unsteady streaky structures on the suction side of the mainplane

2. the unsteady bluff-body wake of the gurney flap
3. that the end-plate (or top) vortex is generated by the merging of at least three vortices shed by the top of the endplate and, finally
4. the canard vortex is much weaker than the endplate, footplate and main vortex which is consistent with experimental results where it wasn't found

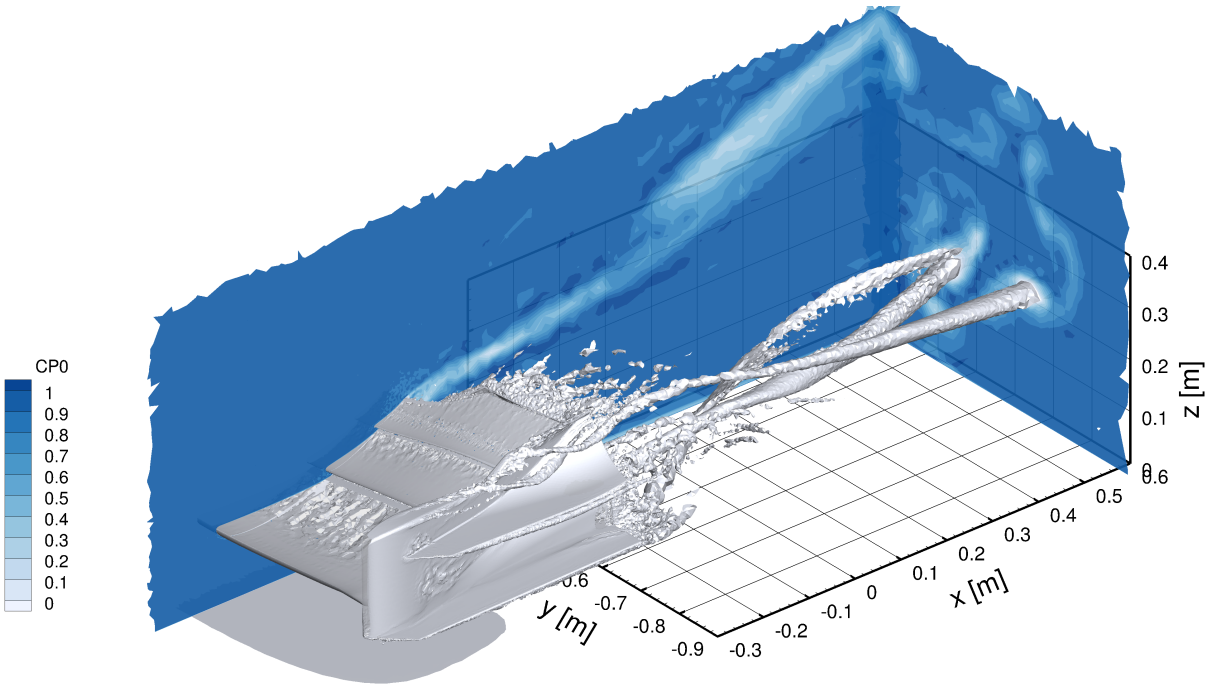



**Figure 6.3** – Instantaneous total pressure $CP_0 = 0$ iso-contour.

### 6.2.2 Near-wake survey

A state-of-the-art RANS computation was used to initialise the LES. The flow was then allowed to develop for ten convective time-units of the main-plane before it was averaged for another three convective time-units. The experimental data was averaged over a much larger time-horizon. This discrepancy in averaging contributes to explaining the larger apparent number of vortices in the top (or endplate) region. The agreement between CFD and experimental data is otherwise good in terms of the strength and location of the vortical structures at $x = -0.3$ Figure 6.4 (top). The wake of the wing is notably different however with a much lower pressure recorded in the experimental data. Further away from the wing, in $x = 0$ the main and footplate vortices (Figure 6.4, bottom) appear to be both closer to each other imposing a different interaction to that reported in experiment and seen further downstream at $x = 0.42$ where they have nearly merged in the CFD data but remain distinct in the experiment (Figure 6.5, bottom).

### 6.2.3 Summary and outlook

The LES confirm the experimental results and the presence of four well defined main vortices. The numerical data gives insight into the formation of the top (or endplate) vortex as the result of merging between at least three smaller vortices. Numerical results also confirm the two strongest vortices are the main and top vortices which dominate the two smaller canard and footplate vortices. A close view of the footplate vortex shows it developed under the footplate. Finally the numerical results also show no sign of vortex breakdown in the absence of the wheel which is consistent with the experimental results.

With additional computational resources, a rigorous mesh convergence study should be made. In particular, it should be seen if a finer mesh allows for a better correlation with experiment for the wing wake in the $x = -0.3$ plane. The vortex formation seems adequately resolved with the present mesh however the vortex interaction and the merging of the main and footplate vortices is obviously sensitive to viscosity and so it should also be checked that the numerical viscosity is not driving the faster merger. Finally the meandering of these vortices should be assessed by longer computations, more representative of the averaging time used for the experiment.

## 6.3 MP4-17D isolated wheel.

The purpose of these simulations of the isolated wheel is two-fold. Firstly one of assessing the required mesh resolution for resolving the flow physics in both the contact-patch region and the top of the wheel. The second is to compare these numerical results against the PIV data from Pegrum (2006). As mentioned earlier, in Chapter 5, it has been reported numerous times that the flow about a rolling wheel is highly sensitive to its shape which is why it is important to underline the difference in shape between the wind-tunnel model used by Pegrum (2006) (Figure 6.6) and the CAD model used for these simulations:

1. the size and shape of the contact patch cannot be matched because its records have been lost and so the same strategy as employed for the study of the idealised isolated wheel of Section 5.2 is used,

2. the pneumatic wind-tunnel model had four grooves,

3. the shoulder profile should be similar to that used in the simulation since both are modelled on the Michelin F1 tyre and

4. the CAD model is faired preventing any flow through the axle contrary to the wind-tunnel model.

The Reynolds number is set to $Re_{C|MP} = 2 \cdot 10^5$ based on the chord of the mainplane (from the complete model). The mesh consists in $5 \cdot 10^5$ prisms and $2.2 \cdot 10^6$ tetrahedral elements. The initial condition was interpolated onto the high-order mesh from a RANS solution and the flow was time-averaged for 5 convective time-units of the mainplane $t_c = c_{MP}/U_\infty$ after letting the flow settle for two convective time units. One convective time-unit required 10h on 7680 mpi ranks of ARCHER.

### 6.3.1 Comparison of streamwise velocity profile in z-planes above the moving road

It is apparent in the comparison of instantaneous snapshots of the streamwise velocity distribution in a plane $z/D = 0.04$ above the ground (Figure 6.7) that the wake is not correctly modelled. In particular, the magnitude of the reverse flow region is much weaker in the simulation than in the experiment. The extent of the jetting, however, seems to be captured, both extending towards $y = -0.4[m]$.

The time-averaged computations show a similar trend for the six plane locations $z/D = 0.04$, $z/D = 0.19$, $z/D = 0.34$ in Figure 6.9 and $z/D = 0.49$, $z/D = 0.64$, $z/D = 0.80$ in Figure 6.10. The difference of the flow between the faired wheeled used for the CFD and the hollow wheel of the experiment is particularly visible as indicated by the arrows in (Figure 6.10, top). The angle of the jetting vortex with respect to the ground plane also seems to be larger for the CFD results than for the experiment. Comparing both sides of the cambered wheel in Figure 6.8 it can be seen that the jetting vortex has a smaller angle with respect to the ground plane (i.e. it is closer to parallel to the ground) on the side of the wheel with the larger contact patch (left). This seems to indicate that, even if the camber for both the numerical and experimental wheels is the same, the numerical model of the deformed contact patch does not match the experimental one.

The survey of the near wake in close proximity with the ground, at $z/D = 0.04$ Figure 6.9 (top) confirms the findings of MacCarthy (2010) that, contrary to the suggestions of Mears *et al.* (2004) there is no evidence of negative jetting flow but rather a region of low velocity reverse flow. Peak velocity 20% higher than the free-stream are also reported in the jetting vortices corroborating the results of MacCarthy (2010).

The asymmetry in contact patch side produced by the camber of the wheel changes the angle at which the jetting vortex departs from the contact region. The side with the largest contact region produces a larger jet, that stays closer to parallel to the ground whereas the side with the smallest contact patch produces a smaller jet with a steeper angle. These results are consistent with those reported by MacCarthy (2010).

### 6.3.2 Total pressure wake survey.

The PIV data was recorded in three streamwise normal planes at $x = 0.2[m]$, $x = 0.3[m]$ and $x = 0.4[m]$ where the centre wheel of diameter $D = 0.66[m]$ corresponds to $x = 0[m]$. Similarly to the comparison streamwise component of the velocity in planes parallel to the ground, the total-pressure survey betrays a stronger jetting vortex for the CFD compared to the experiment. The jetting vortex also appears higher and further away from the wheel shoulder than in the experiment (Figure 6.11, top and middle). In the near wake station, at $x = 0.4$ the jetting still appear higher than in the experiment and the experimental wake appears taller. The averaging time of two-convective time units does most likely explains how clearly the top vortex pair is apparent in the CFD data. Finally the wake of the wishbone, which has not been modelled in the CFD geometry, is apparent in the experimental data (arrow in Figure 6.11, bottom).

Because of the setup in the wind-tunnel the PIV acquisition plane was only streamwise stations. As such there is no data reporting the evolution of the boundary layer, and in particular the detachment of the flow as it moves around the rolling wheel. The pane normal to the axis of rotation of the wheel (neglecting camber), show in Figure 6.12, gives insight into the nature of the flow. The stagnation point is located in (x,y)=(0.28,0.42). Contrary to what what previously reported by Fackrell (1974) (Fig. 4.24) the LES results seem to indicate a much earlier breakdown of the boundary layer (i.e. nearby, or at the stagnation point) rather than at 270° to 290° range (where the 0° would be at the stagnation point). Further analysis of the boundary layer, with finer DNS resolution which was not achieved during the course of this project due to funding limitations, would allow for a deeper understanding of the instability mechanisms in the boundary layer. The present results only show the breakdown is correlated with the adverse pressure gradient.

### 6.3.3 Summary of the isolated wheel of the MP4-17D

At this stage, the correlation between the CFD and PIV data is poor. The differences in geometry, in particular in the region of the contact patch, have been reported to have a large impact on the wake. For the isolated wheel this is already a challenge but for a wheel interacting with a front-wing ,or wheel well, for a road car the minute differences between numerical and experimental setups might lead to strong discrepancies between results for wake surveys. Both experimental and numerical models also omit the brake cooling assembly, suspension systems and more complex tread patterns which further complicate the model. The discrepancies between results cannot only be explained by differences in geometry. Additional computational resources ought to be deployed for a grid-convergence study of the CFD results. Because of certain slow dynamics of the

wheel wake identified in Chapter 5 it isn't yet clear what time-horizons are required for converged statistics of the flow.

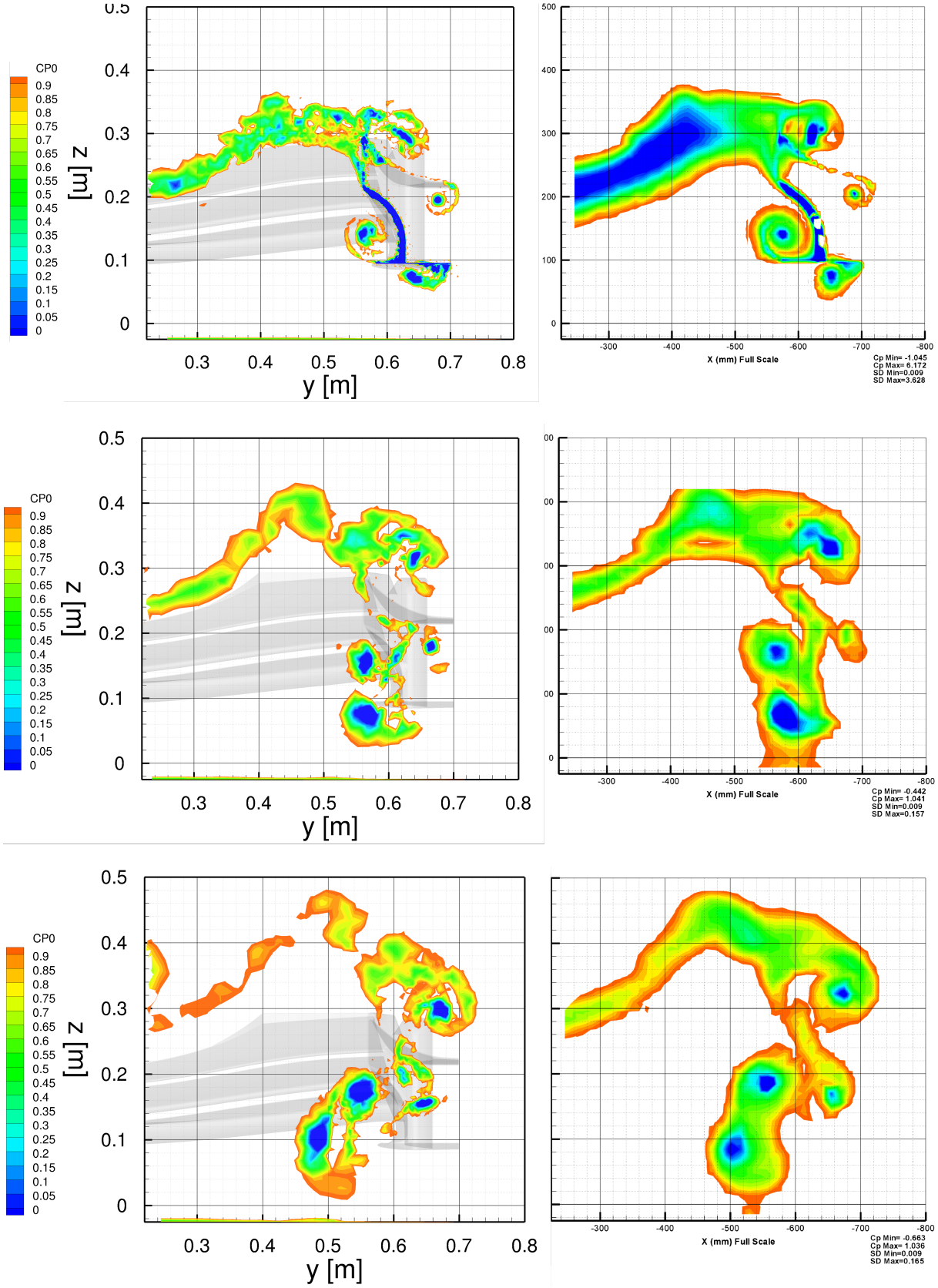



**Figure 6.4** – Time averaged total pressure distribution $CP_0$ downstream of the MP4-17D front-wing at a ride-height of $h/c_mp = 0.48$ with a moving ground plane at $x = -0.3$ (top), $x = -0.15$ (middle) and $x = 0$ (bottom) and $Re_c|MP = 2 \cdot 10^5$. High-fidelity LES (left), experimental results (Pegrum, 2006) (right)

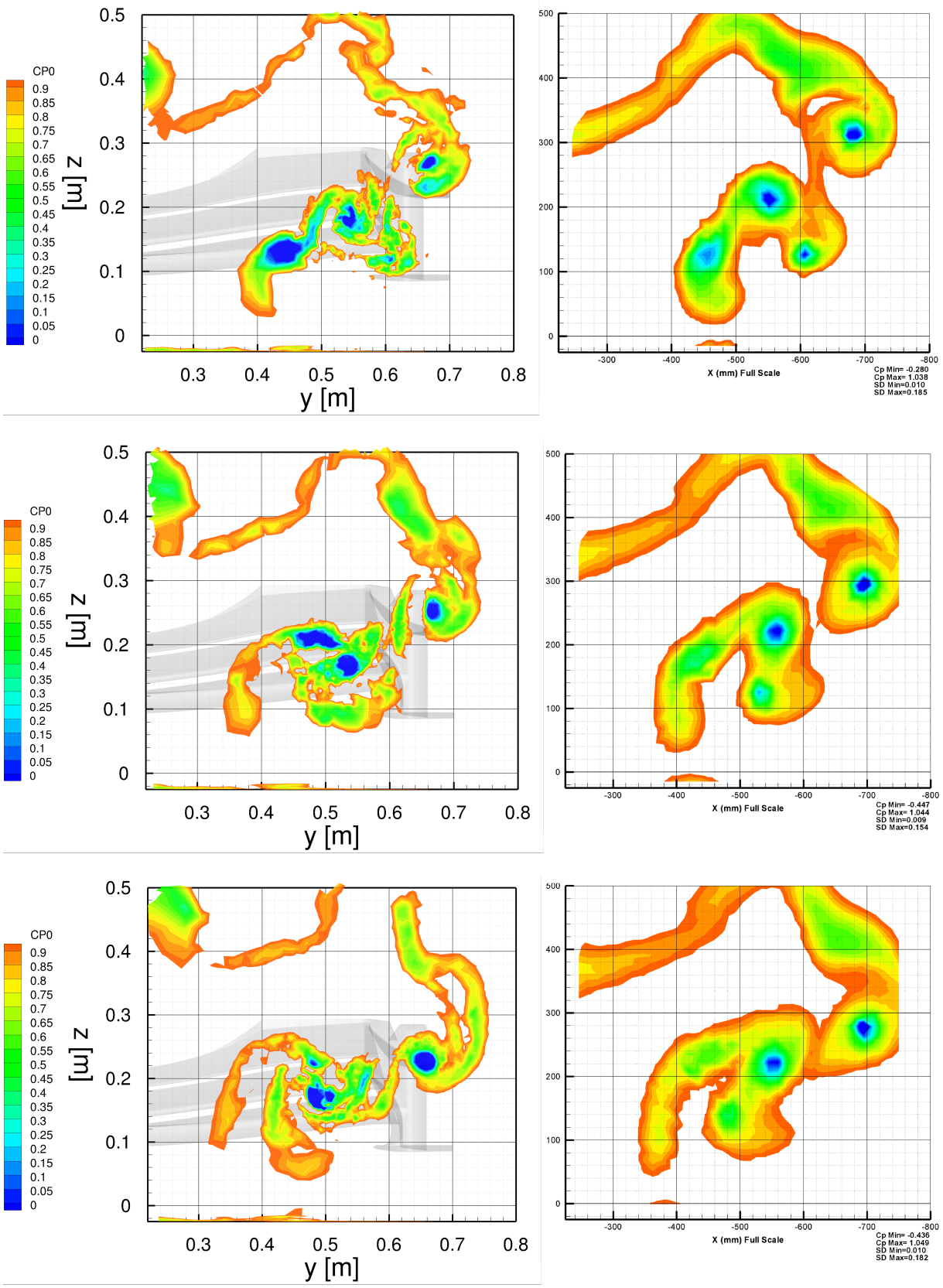



**Figure 6.5** – Time averaged total pressure distribution $CP_0$ downstream of the MP4-17D front-wing at a ride-height of $h/c_mp = 0.48$ with a moving ground plane at $x = 0.15$ (top), $x = 0.3$ (middle) and $x = 0.42$ (bottom) and $Re_c|MP = 2 \cdot 10^5$. High-fidelity LES (left), experimental results (Pegrum, 2006) (right)

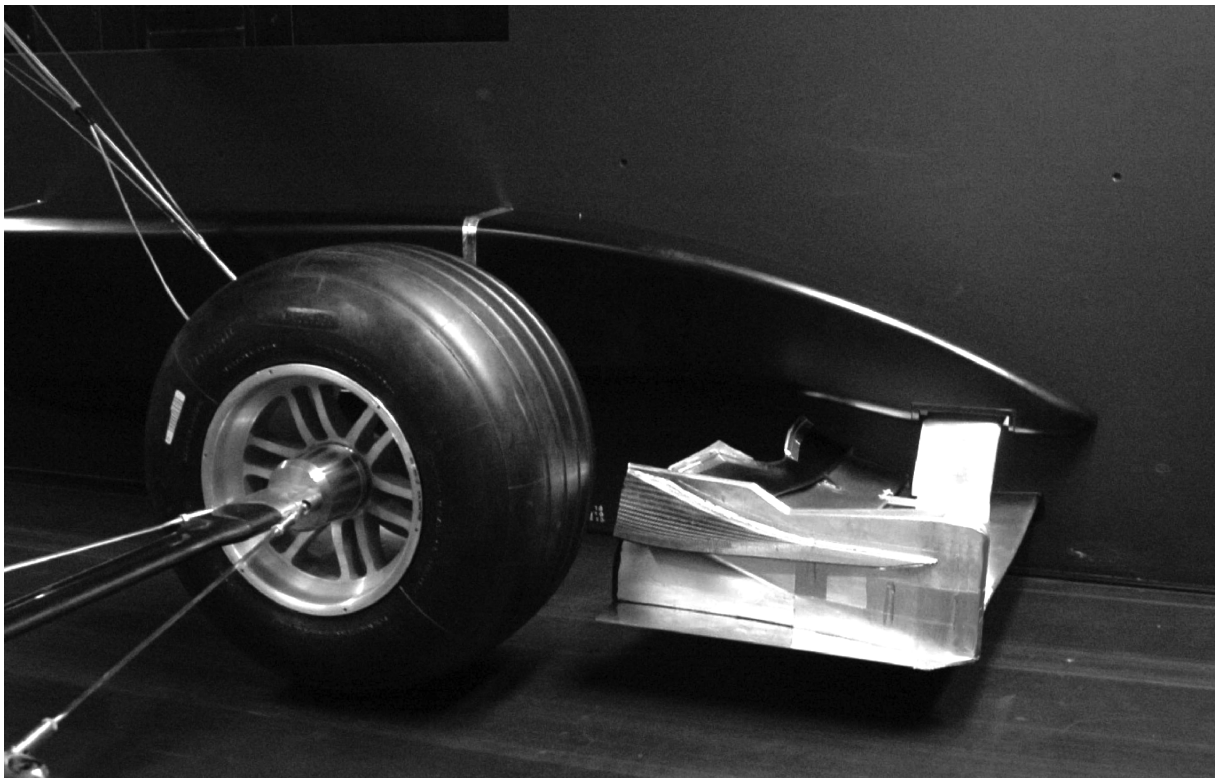


**Figure 6.6** – isolated wheel of the MP4-17D at 4° camber (Pegrum, 2006)

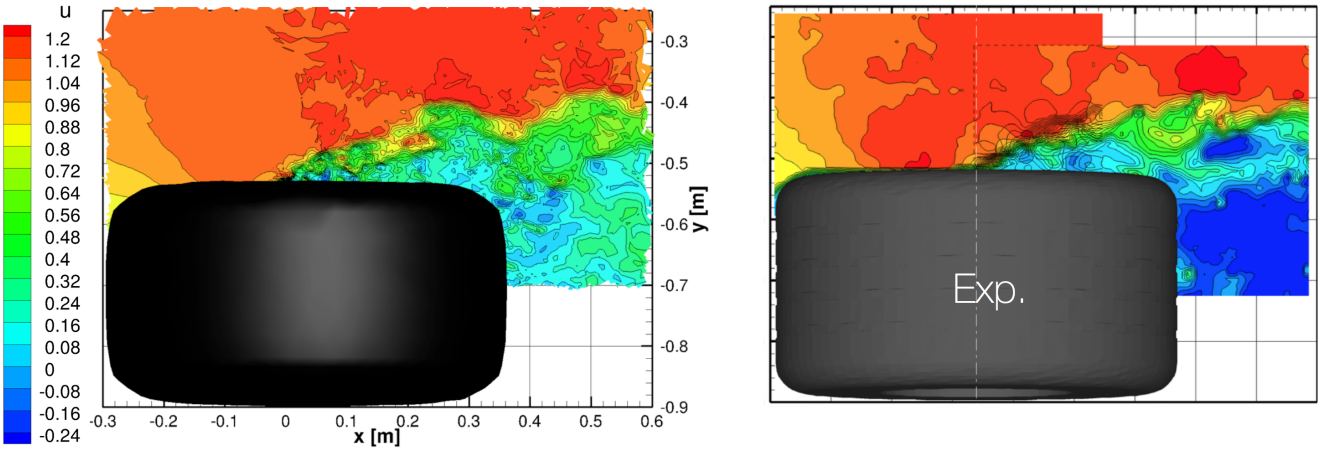



**Figure 6.7** – Instantaneous (top) streamwise velocity $u$ distribution in a $z/D = 0.04$ plane with a moving ground plane and $Re_c|MP = 2 \cdot 10^5$. LES (left), experimental results (Pegrum, 2006) (right).

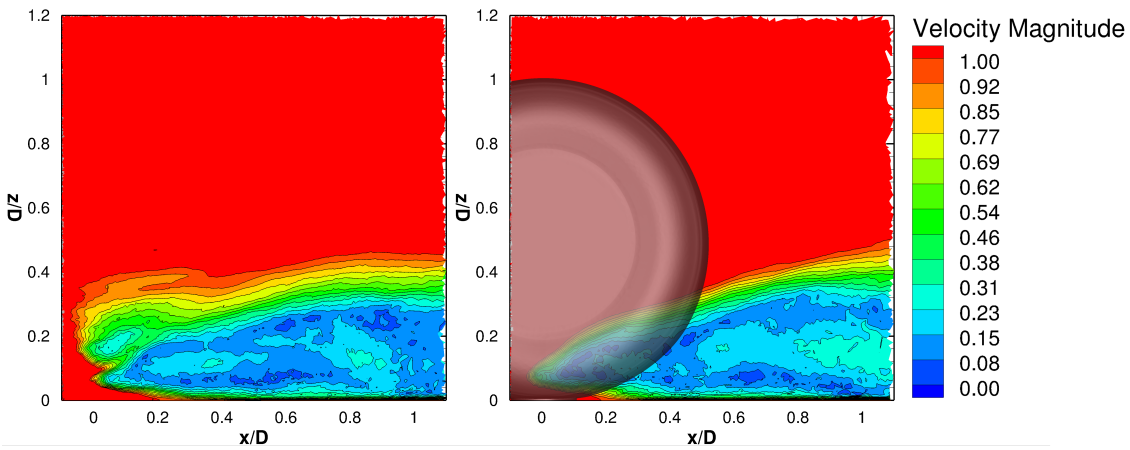



**Figure 6.8** – Time averaged velocity magnitude at $y = 0.5$ (left, smaller contact patch) and $y = 0.9$ (right, larger contact patch) with a moving ground plane and $Re_c|MP = 2 \cdot 10^5$. LES (left, smaller contact patch)

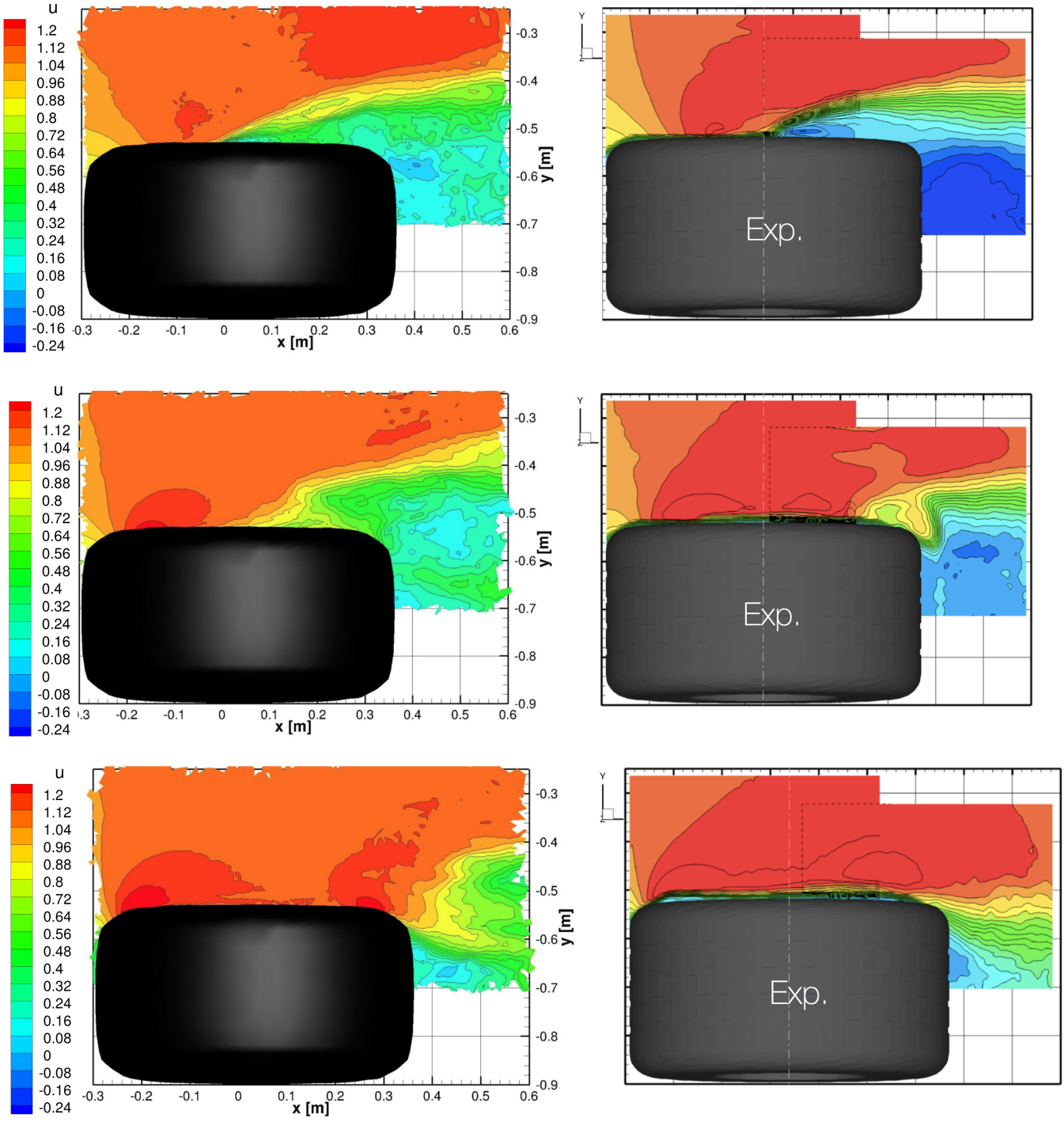



**Figure 6.9** – Time-averaged streamwise velocity $u$ distribution in a $z/D = 0.04$, $z/D = 0.19$, $z/D = 0.34$, plane with a moving ground plane and $Re_c|MP = 2 \cdot 10^5$. High-fidelity LES (left), experimental results (Pegrum, 2006) (right).

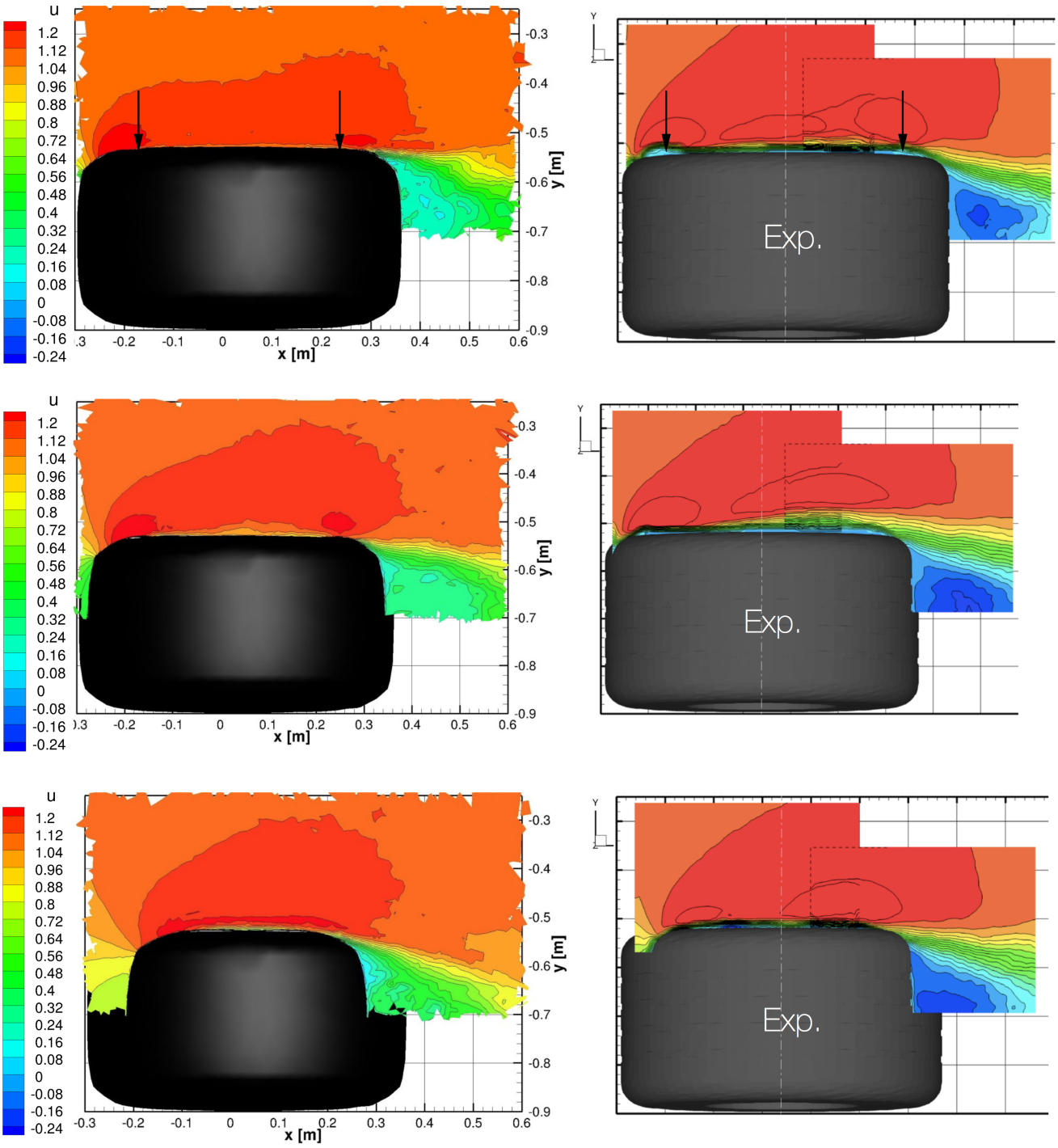



**Figure 6.10** – Time-averaged streamwise velocity $u$ distribution in a $z/D = 0.49$, $z/D = 0.64$, $z/D = 0.80$, plane with a moving ground plane and $Re_c|MP = 2 \cdot 10^5$. LES (left), experimental results (Pegrum, 2006) (right).

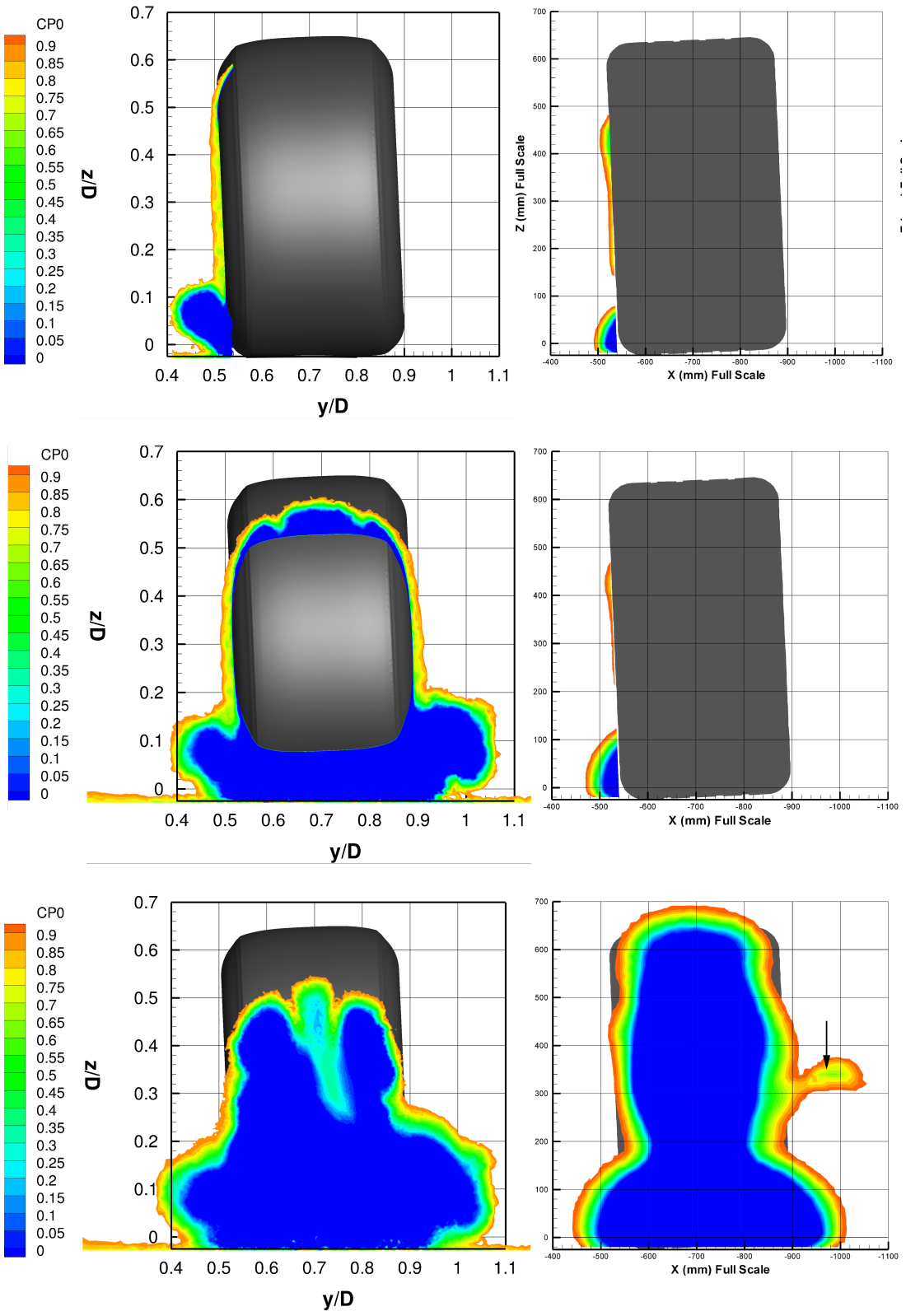



**Figure 6.11** – Time averaged total-pressure $CP_0$ distribution in planes at $y = 0.2$ (top), $y = 0.3$ (middle) and $y = 0.5$ (bottom) with a moving ground plane and $Re_c|MP = 2 \cdot 10^5$. LES (left), experimental results (Pegrum, 2006) (right).

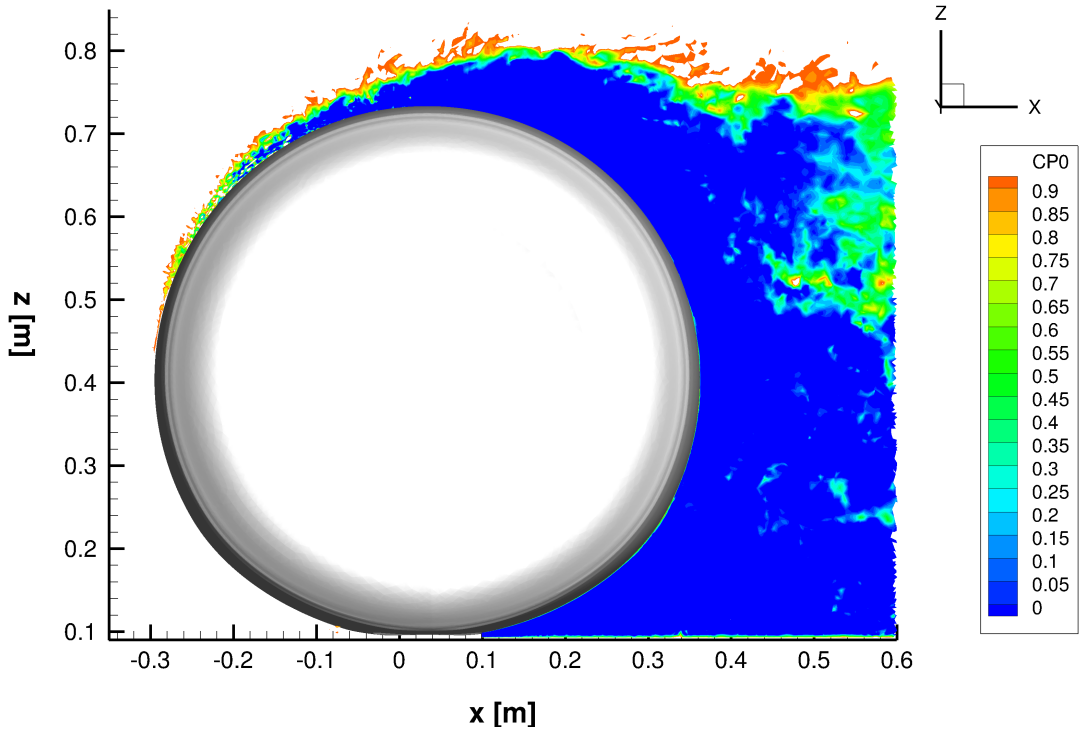



**Figure 6.12** – Time averaged total-pressure $CP_0$ distribution in planes at $y = -0.7$

## 6.4 MP4-17D front section.

This section compares the results from a LES of the front-wing and wheel assembly, referred to as the MP4-17D front-section. The wake produced by the front-wing and its interaction with the rolling wheel about the moving ground-plane is compared with experimental data. Iso-vorticity fields from the LES are compared to the experimental PIV results from Pegrum (2006). The geometry, in .stp format, the instantaneous flow field as well as the time-averaged flow field and the `Nektar++` session file are openly available upon request to the author.

**Motivation** This test case is particularly pertinent to the modelling and furthering of Formula 1 aerodynamics. The ultimate aim for the McLaren is to improve the design process that relies on numerical modelling of the flow in view of bettering the performance of the car on the track. Even though this front-wing geometry differs significantly from a 2018 front-wing, the challenges posed by the flow-physics are the same. Namely the sensitivity of the vortex generation on the footplate, endplate and canard to the diffusion and dispersion errors and the pressure induced separation at the top of the wheel. Even-though the number of vortex generating elements, most of which are low-aspect wings has increased significantly over the past 15 years the inherent challenges remain the same which is why this test case is pertinent to contemporary Formula 1 design. As the improvement in street-legal vehicles aerodynamics plateaus because of practical considerations (streamlining a sedan is limited by volume of the cabin, etc) focus is increasing on the internal and under-body flows both of which interact strongly with the rolling wheel. IN this context too, accurate modelling of the interaction between the vortices produced by the bumper, engine bay cooling, suspension system and wheel well is paramount for devising drag reduction in these regions of the car flow.

As such we propose this MP4-17D geometry as test case complementing the Ahmed body for improving the modelling methods for regions of the flow about a car where vortices interact with the rolling wheel.

From a purely numerical perspective this test case is also complex enough in terms of geometry and flow physics yet not overly complex (because of the limited number of elements on the front-wing). Building on the work of Vermeire *et al.* (2017) we believe this test case allows for a comparison of cost for the relative methods. In particular this test case will be proposed for the high-order workshop as a means of assessing both the technological readiness of high-order methods but also a comparison in terms of both correlation with experiment and cost with the incumbent lower-order methods.

**Computational setup and cost** The $5^{\text{th}}$ order accurate in space and second order accurate in time computation on the mesh consisting of $1.5 \cdot 10^6$ prisms and $4.3 \cdot 10^6$ tetrahedra required 8h per convective time-unit $t_{c|MP} = c_{MP}/U_\infty$, based on the chord of the main-plane, on 7680 mpi ranks on ARCHER. Both the mesh and the initial condition are available upon request.

### 6.4.1 Vorticity field

Despite the simulation requiring longer time acquisition, the vorticity fields associated to the structures identified in the experimental investigation seem to confirm the vortices are not well defined but rather seem to consist in the rollup of a large number of smaller structures as can be seen the three views comparing numerical and experimental results (Figs **??**) . Similarly to the experiment the four main vortical structures cannot be tracked downstream of the wheel (i.e. for $x > 0.4$). Increasing the resolution the resolution of the LES is required to assess the sensitivity of the solution to the mesh.

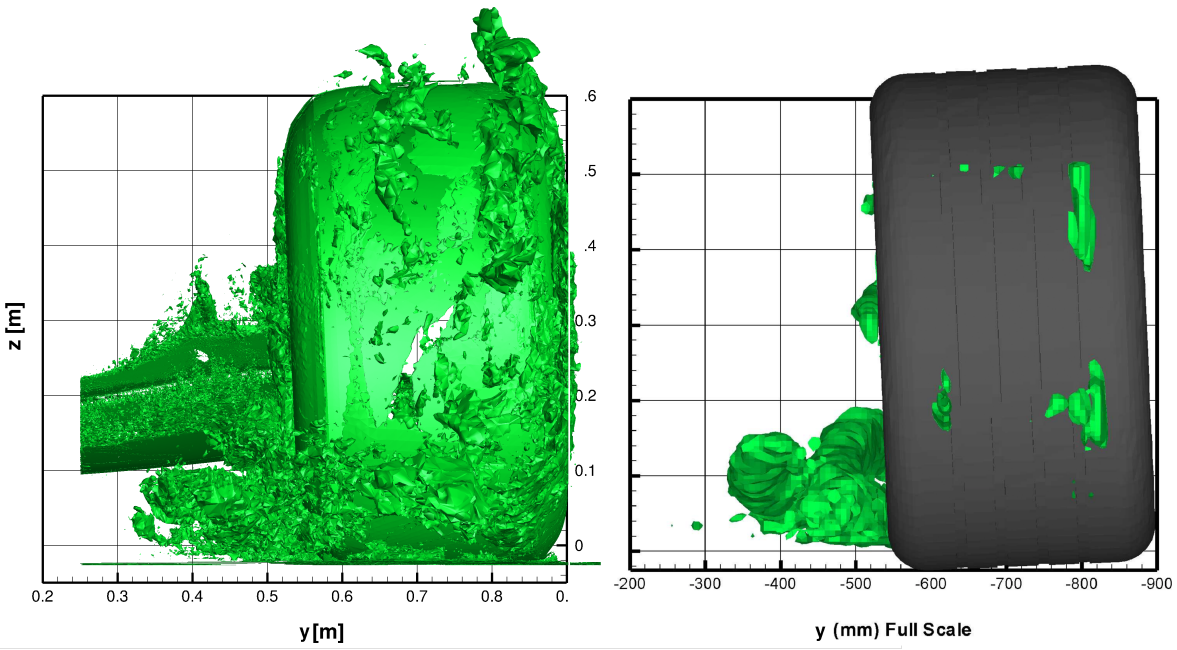



**Figure 6.13** – Time-averaged iso-vorticity contours ($\omega_x D/U_\infty = 8$) for the MP4-17D front-section at $Re_{c|MP} = R_{exp}$ with a ride-height of $h/c_m p = 0.48$ with a moving ground plane. Rear-view LES (left), experimental results (Pegrum, 2006) (right).

## 6.5 Chapter conclusion and outlook

Despite adequately capturing the number of main vortices, their formation, strength, location as well as stability over the front-wing, the wake of the front-wing, in the region

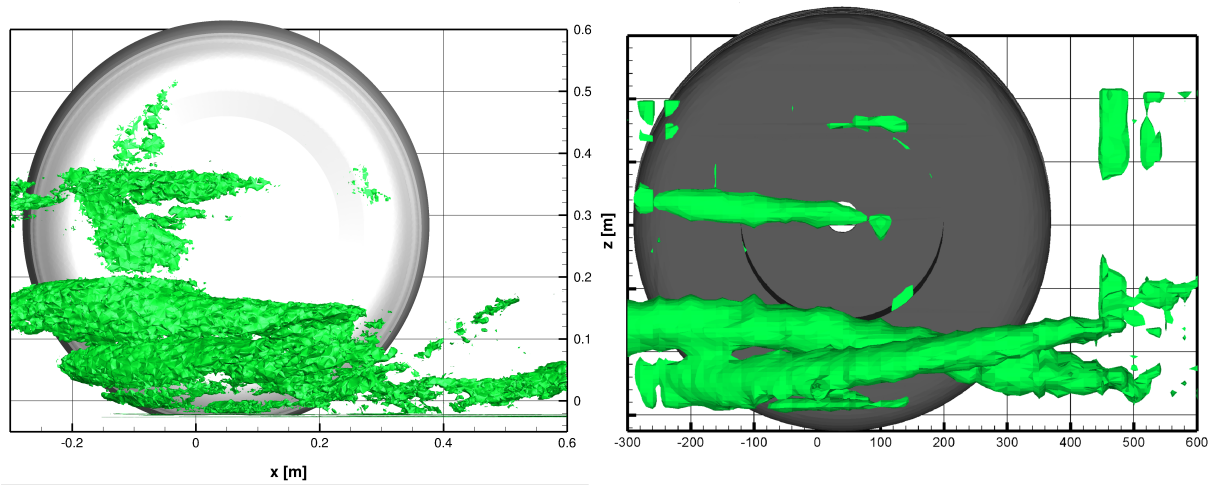



**Figure 6.14** – Time-averaged iso-vorticity contours ($\omega_x D/U_\infty = 8$) for the MP4-17D front-section at $Re_{c|MP} = R_{exp}$ with a ride-height of $h/c_m p = 0.48$ with a moving ground plane. Side view LES (left), experimental results (Pegrum, 2006) (right).

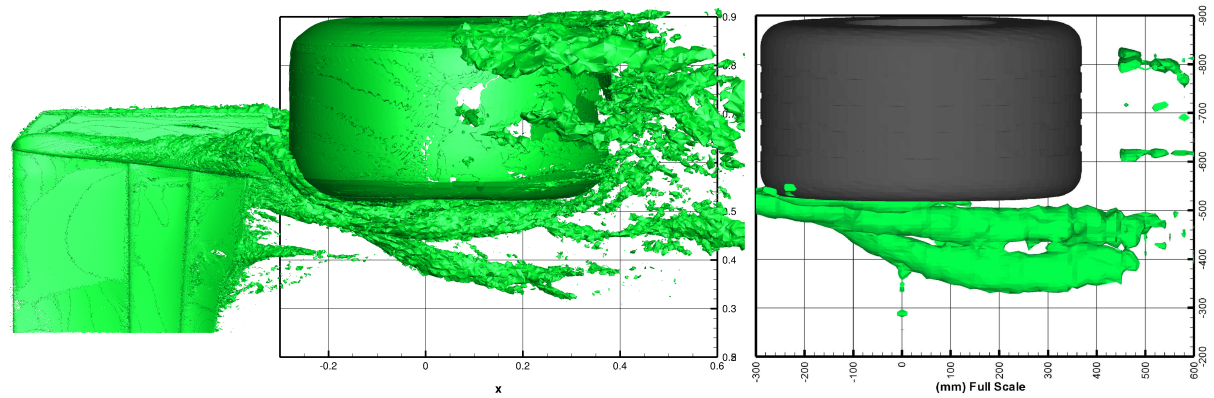



**Figure 6.15** – Time-averaged iso-vorticity contours ($\omega_x D/U_\infty = 8$) for the MP4-17D front-section at $Re_{c|MP} = R_{exp}$ with a ride-height of $h/c_m p = 0.48$ with a moving ground plane. Top view LES (left), experimental results (Pegrum, 2006) (right).

of the gurney flap, still does not correlate to the experimental results of Pegrum (2006). Qualitatively though, these results may be acceptable depending on the accuracy requirements. Contrary to the work horses of Formula One CFD that has become DES the more expensive LES alternative proposes is only attractive it is matched by a comparable improvement in correlation with experiment.

The wake of the wheel is not satisfactorily modelled either. The topology of the jetting vortices seem to indicate the geometric modelling of the contact region in the CFD does not correspond to the one that resulted from the experimental setup. Because of the coupling of the bottom and top parts of the wheel wake this discrepancy most likely contributes to the poor correlation with experimental data for the wake at $x = 0.4$ that is taller in the experiment.

Because these computations require tremendous resources relative to that available a rigorous mesh convergence study remains the first objective of future studies. Once this is achieved, it would be interesting to continue gaining a deeper understanding of the flow on the wing itself and how it affects the near wake studied. In particular it would be interesting to identify the source of the unsteadiness on the wing reported during the experiment.

Once these objectives have been achieved for the isolated front-wing and wheel, a study of the front-section (Figure 6.13) should be envisaged and numerical results should be compared with experiment as well as state of the art RANS and DES. It would also be interesting to see if the four vortices produced by the front-wing remain coherent, or burst, as they pass the rolling wheel and how they interact with the wake of the wheel. Pegrum (2006), MacCarthy (2010) both report these vortices seem to burst or merge with the wheel wake by $x = 0.5$ (in the reference frame of Pegrum (2006)). Because the experimental results were ensemble averaged (time-averaged and then averaged between experiments) it might be that these vortices do no burst or merge but meander more strongly. The averaging then blurs the signature of these vortices as they are drawn into the highly unsteady wake of the wheel.

# Chapter 7

# Conclusion and Outlook

> To do something well is so worthwhile that to die trying to do it better cannot be foolhardy. It would be a waste of life to do nothing with one's ability, for I feel that life is measured in achievement, not in years alone.
>
> Bruce McLaren

The motivation of this project was first to demonstrate that `Nektar++` was capable of meshing and resolving LES on a simplified Formula One front-section and second to continue developing a further understanding of the flow around a rolling wheel and front-wing. Experimental techniques have evolved considerably between the seminal work of Fackrell (1974) and the two most significant recent studies carried out by Pegrum (2006) and MacCarthy (2010). Comparatively state-of-the-art CFD methods have not benefited from the same rate of innovation mostly relying on models that were first tested for automotive flows in the late 90's. The development of the higher fidelity LES based on the spectral/hp element method aimed to address this shortcoming.

The study of the isolated wingtip, reported in Chapter 4, shows that this method produced better than previously reported correlation with experimental data as well as further insight into the nature of the wingtip vortex. In particular, the numerical results explained the presence of a kink in the trajectory of the vortex resulting from a secondary counter-rotating vortex (Figure 4.5).

To investigate the underlying flow physics associated with a rolling wheel wake and considering the high computational demands of this case even at lower Reynolds numbers we investigated the flow past a wheel at $Re_D = 1000$. At this Reynolds number a DNS was performed over one hundred convective time-units. This large data-set was then analysed to associate the flow structures associated to the strongest peaks in the PSD of

the force coefficients acting on the wheel surface. The total shear associated to each of these structures was computed and interpolated onto the surface of the wheel to identify the regions where the structure associated to a given frequency produced the strongest total shear. The spanwise symmetry breaking mode was identified as the meandering of secondary vortices that develop on the top rear quadrant of the wheel a reaction to the shedding hairpin vortices.

Finally the flow around the McLaren MP4-17D front-section, studied experimentally by Pegrum (2006) was investigated. Despite good general qualitative correlation with experiment the numerical results showed large discrepancies in terms of the reverse flow in the immediate wake of the isolated wheel. The isolated front-wing was also investigated numerically and good agreement in terms of total pressure distribution and location of the four main vortices identified by Pegrum (2006) is found. Downstream of the wing, at $x = 0.42$, the main and endplate (or top) vortex seem to be closer to merging than in the experiment. The next obvious step for understanding these discrepancies will be to study the sensitivity of these results to mesh refinement. An effort should also be made towards longer time-averaging closer to the time-horizons used during the experiment.

With the progress of computational facilities, the next step for these types of investigations is to :

1. identify the dominant flow structures and their dynamics for an isolated idealised wheel at practical Reynolds numbers ($Re_D = O(10^5)$).

2. report with greater detail the interaction between the front-wing vortices between the wing and the wheel as well as immediately downstream of the wheel where averaged experimental results could not resolve them,

3. finally both these cases should be compared against state of the art RANS, DES and Lattice-Boltzman to assess if the increased cost associated to high-fidelity LES comparatively increases correlation with experiment.

`Nektar++` should continue to be developed towards deployment on exa-scale facilities and the entire workflow, from meshing to post-processing, should be improved for it to be considered for integration into an industrial design workflow. A good challenge would be to resolve the flow on more recent Formula One, such as the McLaren MP4-29 (Figure 7.1), front-half to see the interaction of the $y_{250}$ vortex with the wheel wake and the side-pods.

The over-arching conclusion of this project is that high-order methods are now ready for meshing and computing the flow over complex geometries pertinent to Formula 1 design. For flows where the detachment and/or roll-up of vortices occurs over regions of smooth curvature high-order method offer better correlation with experiment than low-order methods. Rigorous mesh independence should be carried out to verify these claims

for the rounded wing-tip and the rounded delta-wing (not reported here). Motivated by access to this flow physics efforts should the next step towards integration of high-order methods in industrial settings should revolve around optimising the efficiency of the solver, particularly on larger computing facilities.




**Figure 7.1** – Onwards and upwards, towards high-fidelity modelling of the McLaren MP4-29 (Sutton, 2014)

# Bibliography

2017 http://www.grandprixhistory.org/mar711.htm.

AIKEN, WILLIAM 1981 William s. aiken,.

Aschwanden, Peter, Müller, Jürg & Knörnschild, Ulrich 2006 Experimental study on the influence of model motion on the aerodynamic performance of a race car. In *SAE Technical Paper*. SAE International.

Axerio-Cilies, John, Issakhanian, Emin, Jimenez, Juan & Iaccarino, Gianluca 2012 An aerodynamic investigation of an isolated stationary formula 1 wheel assembly. *JournalofFluidsEngineering* **134** (021101-1).

Axon, L., Garry, K. & Howell, J. 1998 n evaluation of cfd for modelling the flow around stationary and rotating isolated wheels. In *SAE International Congress and Exposition Detroit, Michigan,.*

Babuška, Ivo & Suri, Manil 1994 The p and h-p versions of the finite element method, basic principles and properties. *SIAM Rev.* **36** (4), 578–632.

Ballaban, Michael 2017 http://jalopnik.com/the-sleek-streamliners-that-broke-records-and-served-ev-1538151482.

Bao, Y, Palacios, R, Graham, JMR & Sherwin, SJ 2016 Generalized thick strip modelling for vortex-induced vibration of long flexible cylinders. *Journal of Computational Physics* .

Bareford, Michael, Johnson, Nick & Weiland, Michèle 2016 On the trade-offs between energy to solution and runtime for real-world cfd test-cases. In *Proceedings of the Exascale Applications and Software Conference 2016*, pp. 6:1–6:8. New York, NY, USA: ACM.

Basara, B, Beader, D & Przulj, V 2000 Numerical simulation of the air flow around a rotating wheel. In *3rd MIRA International Vehicle Aerodynamics Conference, Rugby, UK*, pp. 18–19.

Bearman, P.W. 1997 Near wake flows behind two- and three-dimensional bluff bodies. *Journal of Wind Engineering and Industrial Aerodynamics* **69**, 33 – 54.

Bearman, P.W. & Fackrell, J.E. 1975 Calculation of 2-dimensional and axisymmetric bluff-body potential flow. *JOURNAL OF FLUID MECHANICS* **72**, 229–241.

Bearman, P. W. 1978 *Some Effects of Free-Stream Turbulence and the Presence of the Ground on the Flow Around Bluff Bodies*, pp. 95–127. Boston, MA: Springer US.

Bearman, P. W. 1980 Bluff body flows applicable to vehicle aerodynamics. *JOURNAL OF FLUIDS ENGINEERING-TRANSACTIONS OF THE ASME* **102**, 265–274.

Bearman, P. W., Beer, D. De, Hamidy, E. & Harvey, J. K. 1988 The effect of a moving floor on wind-tunnel simulation of road vehicles. In *SAE Technical Paper*. SAE International.

Bearman, P. W. & Zdravkovich, M. M. 1978 Flow around a circular cylinder near a plane boundary. *Journal of Fluid Mechanics* **89** (1), 33–47.

van den Berg, M. A. & Zhang, X. 2009 The aerodynamic interaction between an inverted wing and a rotating wheel. *Journal of Fluids Engineering* **131** (10), 101104–101104–13.

Berger, E., Scholz, D. & Schumm, M. 1990 Coherent vortex structures in thewake of a sphere and a circular disk at rest and under forced vibrations. *Journal of Fluids and Structures* **4** (3), 231 – 257.

Bimbato, Alex Mendonca, Pereira, Luiz Antonio Alcantara & Hirata, Miguel Hiroo 2011 Study of the vortex shedding flow around a body near a moving ground. *Journal of Wind Engineering and Industrial Aerodynamics* **99** (1), 7 – 17.

Bisset, Mark 2015 https://primotipo.com/2015/07/12/wings-clipped-lotus-49-monaco-grand-prix-1969/.

Bolis, A., Cantwell, C. D., Kirby, R. M. & Sherwin, S. J. 2014 From h to p efficiently: optimal implementation strategies for explicit time-dependent problems using the spectral/hp element method. *International Journal for Numerical Methods in Fluids* **75** (8), 591–607.

Bolis, A., Cantwell, C. D., Moxey, D., Serson, D. & Sherwin, S. J. 2016 An adaptable parallel algorithm for the direct numerical simulation of incompressible turbulent flows using a Fourier spectral/hp element method and MPI virtual topologies. *Comput. Phys. Commun.* **206**, 17–25.

Bradshaw, P. 1973 Effects of streamline curvature on turbulent flow. *Tech. Rep.*. AGARD-AG-169.

Brizzi, Laurent-Emmanuel, Noel, Alain & Herbert, Vincent 2004 Phase average velocity field in the vicinity of an isolated wheel model. In *12th International Symposium on Applications of Laser Techniques to Fluid Mechanics*.

Broadhurst, M. 2007 Vortex stability and breakdown: Direct numerical simulation and stability analysis. PhD thesis, Imperial College London.

Brown, Allen 2017 http://www.oldracingcars.com/eagle/66/.

Cantwell, C. D., Moxey, D., Comerford, A., Bolis, A., Rocco, G., Mengaldo, G., de Grazia, D., Yakovlev, S., Lombard, J.-E., Ekelschot, D., Jordi, B., Xu, H., Mohamied, Y., Eskilsson, C., Nelson, B., Vos, P., Biotto, C., Kirby, R. M. & Sherwin, S. J. 2015 Nektar++: An open-source spectral/hp element framework. *Comput. Phys. Commun.* **192**, 205–219.

Cantwell, C. D., Sherwin, S. J., Kirby, R. M. & Kelly, P. H. J. 2011 From h to p efficiently: Selecting the optimal spectral/hp discretisation in three dimensions. *MATHEMATICAL MODELLING OF NATURAL PHENOMENA* **6**, 84–96.

Cantwell, C. D., Yakovlev, S., Kirby, R. M., Peters, N. S. & Sherwin, S. J. 2014 High-order spectral/hp element discretisation for reaction-diffusion problems on surfaces: Application to cardiac electrophysiology. *JOURNAL OF COMPUTATIONAL PHYSICS* **257**, 813–829.

Carmody, Thomas 1964 Establishment of the wake behind a disk. *Journal of Basic Engineering* **86** (4), 869–880.

Chauveau, Franck 2002 Aerodynamics of the frnot part of a formula 1 car: Numerical approach. PhD thesis, Lille 1 University.

Chen, Kevin K, Tu, Jonathan H & Rowley, Clarence W 2012 Variants of dynamic mode decomposition: boundary condition, koopman, and fourier analyses. *Journal of nonlinear science* **22** (6), 887–915.

Chow, J.S., Zilliac, G. & Bradshaw, P. 1997 Mean and turbulence measurements in the near field of a wingtip vortex. *AIAA Journal* **35** (10), 1561–1567.

Churchfield, Matthew & Blaisdell, Gregory 2008 *The Lag RST Turbulence Model Applied to a Vortex Flow*. American Institute of Aeronautics and Astronautics.

Churchfield, Matthew & Blaisdell, Gregory 2011 *A Reynolds Stress Relaxation Turbulence Model Applied to A Wingtip Vortex Flow*. American Institute of Aeronautics and Astronautics.

Churchfield, Matthew J. & Blaisdell, Gregory A. 2009*a* Numerical simulations of a wingtip vortex in the near field. *Journal of Aircraft* **46** (1), 230–243.

Churchfield, Matthew J. & Blaisdell, Gregory A. 2009*b* Numerical simulations of a wingtip vortex in the near field. *Journal of Aircraft* **46** (1), 230–243.

Churchfield, Matthew J. & Blaisdell, Gregory A. 2013 Reynolds stress relaxation turbulence modeling applied to a wingtip vortex flow. *AIAA Journal* **51** (11), 2643–2655.

Cogotti, A. 1983 Aerodynamic characteristics of car wheels. *International Journal of Vehicle Design* **SP3**, 173–196.

Cohen, J., Cantwell, C. D., Hong, N. P. Chue, Moxey, D., Illingworth, M., Turner, A., Darlington, J. & Sherwin, S. J. 2014 Simplifying the development, use and sustainability of hpc software. *J. Open Res. Soft.* **2** (1).

Constantinescu, George & Squires, Kyle 2004 Numerical investigations of flow over a sphere in the subcritical and supercritical regimes. *Physics of Fluids* **16** (5), 1449–1466.

Craft, T.J., Gerasimov, A.V., Launder, B.E. & Robinson, C.M.E. 2006 A computational study of the near-field generation and decay of wingtip vortices. *International Journal of Heat and Fluid Flow* **27** (4), 684 – 695, special Issue of The Fourth International Symposium on Turbulence and Shear Flow Phenomena - 2005 Special Issue of The Fourth International Symposium on Turbulence and Shear Flow Phenomena - 2005.

Croner, Emma, Bézard, Hervé, Sicot, Christophe & Mothay, Guillaume 2013 Aerodynamic characterization of the wake of an isolated rolling wheel. *International Journal of Heat and Fluid Flow* **43**, 233 – 243, 7th International Symposium on Turbulence Heat & Mass Transfer (THMT-7), Palermo Conference on Modelling Fluid Flow (CMFF'12).

D. Moxey, M. Hazan, J. Peiro & Sherwin, S. 2013 An isoparametric approach to high-order curvilinear boundary-layer meshing. *Comp. Meth. App. Mech. Eng.* .

Dacles-Mariani, Jennifer, Hafez, Mohamed & Kwak, Dochan 1997 *Prediction of wake-vortex flow in the near- and intermediate-fields behind wings*. American Institute of Aeronautics and Astronautics.

Dacles-Mariani, Jennifer, Kwak, Dochan & Zilliac, Gregory 1996 *Accuracy assessment of a wingtip vortex flowfield in the near-field region*. American Institute of Aeronautics and Astronautics.

Dacles-Mariani, J., Rogers, S., Kwak, D., Zilliac, G. & Chow, J. 1993 *A computational study of wingtip vortex flowfield*. American Institute of Aeronautics and Astronautics.

Dacles-Mariani, Jennifer, Zilliac, Gregory G., Chow, Jim S. & Bradshaw, Peter 1995 Numerical/experimental study of a wingtip vortex in the near field. *AIAA Journal* **33** (9), 1561–1568.

Dalla Longa, L., Morgans, A. S. & Dahan, J. A. 2017 Reducing the pressure drag of a d-shaped bluff body using linear feedback control. *Theoretical and Computational Fluid Dynamics* pp. 1–11.

Dassanayake, PRK, Ramachandran, D, Salati, L, Barber, TJ & Doig, GC 2012 Unsteady computational simulation of the flow structure of an isolated wheel in contact with the ground. In *Proceedings of the 18th Australasian Fluid Mechanics Conference, Launceston, Australia*, pp. 3–7.

DeMarco, Kathleen, Stratton, James, Chinavare, Kevin & VanHouten, Garry 2017 The effects of mass and wheel aerodynamics on vehicle fuel economy. In *SAE Technical Paper*. SAE International.

Devenport, William J., Rife, Michael C., Liapis, Stergios I. & Follin, Gordon J. 1996 The structure and development of a wing-tip vortex. *Journal of Fluid Mechanics* **312**, 67–106.

D'Hooge, Andrew, Palin, Robert B., Johnson, S., Duncan, Bradley & Gargoloff, Joaquin Ivan 2012 The aerodynamic development of the tesla model s - part 2: Wheel design optimization. In *SAE Technical Paper*. SAE International.

Diasinos, S. & Gatto, A. 2008 Experimental investigation into wing span and angle-of-attack effects on sub-scale race car wing/wheel interaction aerodynamics. *Experiments in Fluids* **45** (3), 537.

Dieterle, L., Ehrenfried, K., Stuff, R., Schneider, G., Coton, P., Monnier, J.C. & Lozier, J.F. 1999 Quantitative flow field measurements in a catapult facility using particle image velocimetry. In *Instrumentation in Aerospace Simulation Facilities, 1999. ICIASF 99. 18th International Congress on*, pp. 1/1–110.

Dimitriou, Ioannis & Klussmann, Sven 2006 Aerodynamic forces of exposed and enclosed rotating wheels as an example of the synergy in the development of racing and passenger cars. In *SAE Technical Paper*. SAE International.

Dominy, R G 1990 The influence of slipstreaming on the performance of a grand prix racing car. *Proceedings of the Institution of Mechanical Engineers, Part D: Journal of Automobile Engineering* **204** (1), 35–40.

Dong, S., Karniadakis, G.E. & Chryssostomidis, C. 2014 A robust and accurate outflow boundary condition for incompressible flow simulations on severely-truncated unbounded domains. *Journal of Computational Physics* **261** (0), 83 – 105.

Dreyer, Martin, Radespiel, Rolf, Körner, Matthias & Decker, Friedhelm 2007 Experimental and numerical simulation of the flow around the brake disk of a scaled-down vw phaeton model. In *SAE Technical Paper*. SAE International.

Dubief, Yves & Delcayre, Franck 2000 On coherent-vortex identification in turbulence. *Journal of turbulence* **1** (1), 011–011.

Duell, Edward G. & George, A. R. 1999 Experimental study of a ground vehicle body unsteady near wake. In *SAE Technical Paper*. SAE International.

Duraisamy, Karthikeyan & Baeder, James D. 2006 Numerical simulation of the effects of spanwise blowing on wing-tip vortex formation and evolution. *Journal of Aircraft* **43** (4), 996–1006.

Ekelschot, Dirk 2016 Mesh adaptation strategies for compressible flows using a high-order spectral/hp element discretisation. PhD thesis, Imperial College London.

Ekelschot, D., Moxey, D., Sherwin, S. J. & Peiró, J. 2017 A $p$-adaptation method for compressible flow problems using a goal-based error estimator. *Comput. Struct.* **181**, 55–69.

Evstafyeva, O, Morgans, A. S. & Dalla Longa, L. 2017 https://www.cambridge.org/core/journals/journal-of-fluid-mechanics/article/div-classtitlesimulation-and-feedback-control-of-the-ahmed-body-flow-exhibiting-symmetry-breaking-behaviourdiv/AED0A88BDDFF5C0630C7899D3255E7BB. *Journal of Fluid Mechanics* **817**.

Fabijanic, John & George, Albert 1996 *An experimental investigation of the aerodynamics of automobile wheel wells*. American Institute of Aeronautics and Astronautics.

Fabre, David & Jacquin, Laurent 2000 Stability of a four-vortex aircraft wake model. *Physics of Fluids (1994-present)* **12** (10), 2438–2443.

Fabre, D., Jacquin, L. & Loof, A. 2002 Optimal perturbations in a four-vortex aircraft wake in counter-rotating configuration. *Journal of Fluid Mechanics* **451**, 319–328.

Fackrell, John Edward 1974 The aerodynamics of an isolated wheel rotating in contact with the ground. PhD thesis, University of London.

Ferrari 2017 312 f1.

Fleig, Oliver, Iida, Makoto & Arakawa, Chuichi 2004 Wind turbine blade tip flow and noise prediction by large-eddy simulation. *Journal of Solar Energy Engineering* **126** (4), 1017–1024.

Fromm, Jacob E. & Harlow, Francis H. 1963 Numerical solution of the problem of vortex street development. *The Physics of Fluids* **6** (7), 975–982.

Gérardin, Fabien, Gentric, Caroline & Midoux, Noël 2014 Particle dispersion in the near-wake of an isolated rotating wheel: Experimental and cfd study. *Journal of Aerosol Science* **76**, 56 – 71.

Gérardin, Fabien & Midoux, Noël 2016 Attenuation of road dust emissions caused by industrial vehicle traffic. *Atmospheric Environment* **127**, 46 – 54.

Ghias, Reza, Mittal, Rajat, Dong, Haibo & Lund, Thomas 2005 *Study of Tip-Vortex Formation Using Large-Eddy Simulation*. American Institute of Aeronautics and Astronautics.

Giuni, M. 2013 Formation and early development of wingtip vortices. PhD thesis, University of Glasgow.

Giuni, Michea & Benard, Emmanuel 2011 *Analytical/Experimental Comparison of the Axial Velocity in Trailing Vortices*. American Institute of Aeronautics and Astronautics.

Giuni, Michea & Green, Richard B. 2013 Vortex formation on squared and rounded tip. *Aerospace Science and Technology* **29** (1), 191–199.

Godo, Matthew, Corson, David & Legensky, Steve 2009 *An Aerodynamic Study of Bicycle Wheel Performance Using CFD*. American Institute of Aeronautics and Astronautics.

Grazia, Daniele De 2016 Three-dimensional discontinuous spectral/hp element methods for compressible flows. PhD thesis, Imperial College London.

Green, S. I. & Acosta, A. J. 1991 Unsteady flow in trailing vortices. *Journal of Fluid Mechanics* **227**, 107–134.

Hashmi, Amir A. & Dimitriou, Ioannis 2006 Needs and possibilities for the correction of drag and lift wheel forces which have been derived by integrating its static pressure distribution. In *SAE Technical Paper*. SAE International.

Hein, S. & Theofilis, Vassilios 2004 On instability characteristics of isolated vortices and models of trailing-vortex systems. *Computers & Fluids* **33**, 741–753, lIDO-Berichtsjahr=2004,.

Henningson, Dan S., Lundbladh, Anders & Johansson, Arne V. 1993 A mechanism for bypass transition from localized disturbances in wall-bounded shear flows. *Journal of Fluid Mechanics* **250**, 169–207.

Heyes, A, Jones, R & Smith, D 2004 Wandering of wingtip vortices. In *12th Internation symposium on application of laser techniques to fluid mechanics*.

History, Grand Prix 2017 http://www.grandprixhistory.org/mar711.htm.

Hobeika, Teddy 2012 Investigation of tyre geometry influence on road vehicle aerodynamics. Master's thesis, Chalmers University of Technology, Gothenburg.

Hoëssler, J. 2011 Direct numerical simulations and stability analysis of vortex-dominated flows around complex geometries. PhD thesis, Imperial College London.

Hourigan, Anirudh Rao, Thompson, Mark C. & Kerry 2016 A universal three-dimensional instability of the wakes of two-dimensional bluff bodies. *Journal of Fluid Mechanics* **792**, 50–66.

Howard, Keith 2004 http://www.motorsportmagazine.com/archive/article/march-2004/69/mclaren-m7a.

Huang, Wei-Xi & Sung, Hyung Jin 2007 Vortex shedding from a circular cylinder near a moving wall. *Journal of Fluids and Structures* **23** (7), 1064 – 1076.

Issakhanian, Emin, Elkins, Chris J., Lo, Kin Pong & Eaton, John K. 2010 An experimental study of the flow around a formula one racing car tire. *Journal of Fluids Engineering* **132** (7), 071103–071103–8.

Jacquin, L., Fabre, D., Geffroy, P. & Coustols, E. 2001 *The properties of a transport aircraft wake in the extended near field - An experimental study*. American Institute of Aeronautics and Astronautics.

Jameson, Antony 2015 http://aero-comlab.stanford.edu/papers/cfd_past,present,future-scitech2015.pdf.

Jennings, S.G 1988 The mean free path in air. *Journal of Aerosol Science* **19** (2), 159 – 166.

Jiang, Li, Cai, Jiangang & Liu, Chaoqun 2008 Large-eddy simulation of wing tip vortex in the near field. *International Journal of Computational Fluid Dynamics* **22** (5), 289–330.

Jordi, B. E. 2015 Steady-state solvers for stability analysis of vortex dominated flows. PhD thesis, Imperial College London.

Jordi, B. E., Cotter, C. J. & Sherwin, S. J. 2014 Encapsulated formulation of the selective frequency damping method. *PHYSICS OF FLUIDS* **26** (ARTN 034101).

K. Duraisamy, G. Iaccarino 2005 Curvature correction and application of the v2 f turbulence model to tip vortex flows. *Tech. Rep.*. Center for Turbulence Research - Annual Research Briefs, Stanford, CA.

Kandasamy, Satheesh, Duncan, Bradley, Gau, Holger, Maroy, Fabien, Belanger, Alain, Gruen, Norbert & Schäufele, Sebastian 2012 Aerodynamic performance assessment of bmw validation models using computational fluid dynamics. In *SAE Technical Paper*. SAE International.

Karamanos, G.-S. & Karniadakis, G. E. 2000 A spectral vanishing viscosity method for large-eddy simulations. *J. Comput. Phys.* **163** (1), 22–50.

Karniadakis, G. & Sherwin, S. 2005 *Spectral/hp Element Methods for Computational Fluid Dynamics*, 2nd edn. Oxford University Press.

Karniadakis, G. E. 1990 Spectral element—fourier methods for incompressible turbulent flows. *Comput. Methods Appl. Mech. Eng.* **80** (1-3), 367–380.

Karniadakis, G. E., Israeli, M. & A., Orszag S. 1991 High-order splitting methods for the incompressible navier-stokes equations. *Journal of Computational Physics* **97** (2), 414 – 443.

Katz, Joseph & Dykstra, Lee 1994 Application of computational methods to the aerodynamic development of a prototype race car. In *SAE Technical Paper*. SAE International.

Katz, Joseph & Garcia, Darwin 2002 Aerodynamic effects of indy car components. In *SAE Technical Paper*. SAE International.

Kellar, Pearse & Savill 1999*a* Formula 1 car wheel aerodynamics. *Sports Engineering* **2** (4), 203–212.

Kellar, W. P., Savill, A. M. & Dawes, W. N. 1999*b* *Integrated CAD/CFD visualisation of a generic formula 1 car front wheel flowfield*, pp. 90–98. Berlin, Heidelberg: Springer Berlin Heidelberg.

Khoury, George K. EL, Andersson, Helge I. & Pettersen, Bjoornar 2010 Crossflow past a prolate spheroid at reynolds number of 10000. *Journal of Fluid Mechanics* **659**, 365–374.

Kirby, Robert M. & Karniadakis, George Em 2002 Coarse resolution turbulence simulations with spectral vanishing viscosity—large-eddy simulations (svv-les). *Journal of Fluids Engineering* **124** (4), 886–891.

Kirby, Robert M. & Sherwin, Spencer J. 2006 Stabilisation of spectral/hp element methods through spectral vanishing viscosity: Application to fluid mechanics modelling. *Computer Methods in Applied Mechanics and Engineering* **195** (23–24), 3128 – 3144, incompressible {CFD}.

Kothalawala, TD & Gatto, A 2016 Computational investigation into the influence of yaw on the aerodynamics of an isolated wheel in free air. *International Journal of Computational Science and Engineering* **13** (4), 333–345.

Lamballais, Eric, Fortuné, Véronique & Laizet, Sylvain 2011 Straightforward high-order numerical dissipation via the viscous term for direct and large eddy simulation. *Journal of Computational Physics* **230** (9), 3270 – 3275.

Landstrom, Christoffer, Josefsson, Linda, Walker, Tim & Lofdahl, Lennart 2012 Aerodynamic effects of different tire models on a sedan type passenger car. *SAE Int. J. Passeng. Cars - Mech. Syst.* **5**, 136–151.

Landström, Christoffer & Löfdahl, Lennart 2011 Investigation of aerodynamic wheel designs on a passenger car at different cooling air flow conditions (44403), 985–994.

Larsson, T., Sato, T. & Ullbrand, B. 2005*a* http://www.formula1-dictionary.net/big/supercomputing

Larsson, T., Sato, T. & Ullbrand, B. 2005*b* Supercomputing in f1 - unlocking the power of cfd. In *Proceedings of 2nd European Automotive CFD Conference*.

Leclerc, Cédric 2008 Reduction de la trainee d'un vehicule automobile simplifie a l'aide du controle actif par jet synthetique. PhD thesis, Polyetchnique de Toulouse.

Leśniewicz, P, Kulak, M & Karczewski, M 2014 Aerodynamic analysis of an isolated vehicle wheel. *Journal of Physics: Conference Series* **530** (1), 012064.

Lin, John C 2002 Review of research on low-profile vortex generators to control boundary-layer separation. *Progress in Aerospace Sciences* **38** (4), 389 – 420.

Lombard, J.-E. W., Moxey, D., Sherwin, S. J., Hoessler, J. F. A., Dhandapani, S. & Taylor, M. J. 2016 Implicit large-eddy simulation of a wingtip vortex. *AIAA J.* **54** (2), 506–518.

Longa, Laurant Dalla 2018 Simulation, modelling et feedback control of the flow around a square back vehicle. *Tech. Rep.*. Imperial College.

MacCarthy, Nigel Hugh 2010 An Experimental Study of the Aerodynamics of Exposed Wheels. PhD thesis, Imperial College London.

Maday, Y., Patera, Anthony T. & Rønquist, Einar M. 1990 An operator-integration-factor splitting method for time-dependent problems: Application to incompressible fluid flow. *Journal of Scientific Computing* **5** (4), 263–292.

Mankowski, Oliver, Sims-Williams, David, Dominy, Robert, Duncan, Bradley & Gargoloff, Joaquin 2011 The bandwidth of transient yaw effects on vehicle aerodynamics. *SAE Int. J. Passeng. Cars – Mech. Syst.* **4**, 131–142.

McAlister, K. W. & Takahashi, R. K. 1991 Avscom technical report 91-a-003 naca 0015 wing pressure and trailing vortex measurements. *Tech. Rep.*. Nasa Tecnical Paper 3151.

McManus, James & Zhang, Xin 2005 A computational study of the flow around an isolated wheel in contact with the ground. *Journal of Fluids Engineering* **128** (3), 520–530.

Mears, A. P., Crossland, S. C. & Dominy, R. G. 2004 An investigation into the flow-field about an exposed racing wheel. In *SAE Technical Paper*. SAE International.

Mears, A. P., Dominy, R. G. & Sims-Williams, D. B. 2002 The air flow about an exposed racing wheel. In *SAE Technical Paper*. SAE International.

Mengaldo, G., Grazia, D. De, Moxey, D., Vincent, P.E. & Sherwin, S.J. 2014 Dealiasing techniques for high-order spectral element methods on regular and irregular grids. *Journal of Computational Physics* .

Menter, F. R. 1994 Two-equation eddy-viscosity turbulence models for engineering applications. *AIAA Journal* **32** (8), 1598–1605.

Mercker, E. & Berneburg, H. 1991 On the simulation of road driving of a passenger car in a wind tunnel using a moving belt and rotating wheels. In *Proceedings of 3rd international conference on innovation and reliability*.

Moura, R.C., Mengaldo, G., Peiró, J. & Sherwin, S.J. 2017 On the eddy-resolving capability of high-order discontinuous galerkin approaches to implicit les / under-resolved dns of euler turbulence. *J. Comput. Phys.* **330** (C), 615–623.

Moura, R.C., Sherwin, S.J. & Peiró, J. 2015 Linear dispersion-diffusion analysis and its application to under-resolved turbulence simulations using discontinuous galerkin spectral/hp methods. *Journal of Computational Physics* .

Moura, R.C., Sherwin, S.J. & Peiró, J. 2016 Eigensolution analysis of spectral/hp continuous galerkin approximations to advection–diffusion problems: Insights into spectral vanishing viscosity. *Journal of Computational Physics* **307**, 401 – 422.

Moxey, D., Cantwell, C.D., Kirby, R.M. & Sherwin, S.J. 2016*a* Optimising the performance of the spectral/ element method with collective linear algebra operations. *Computer Methods in Applied Mechanics and Engineering* **310**, 628 – 645.

Moxey, D., Cantwell, C. D., Kirby, R. M. & Sherwin, S. J. 2016*b* Optimizing the performance of the spectral/hp element method with collective linear algebra operations. *Comput. Meth. Appl. Mech. Eng.* **310**, 628–645.

Moxey, D., Ekelschot, D., Keskin, Ü., Sherwin, S. J. & Peiró, J. 2016*c* High-order curvilinear meshing using a thermo-elastic analogy. *Comput. Aided Design* **72**, 130–139.

Moxey, D., Green, M. D., Sherwin, S. J. & Peiró, J. 2015*a* An isoparametric approach to high-order curvilinear boundary-layer meshing. *Computer Methods in Applied Mechanics and Engineering* **283**, 636–650.

Moxey, D., Green, M. D., Sherwin, S. J. & Peiró, J. 2015*b* *On the generation of curvilinear meshes through subdivision of isoparametric elements*, pp. 203–215. Springer.

n/a 2017*a* Jamais-contente.

n/a 2017*b* Mclaren firestone.

Nakagawa, Masaki, Kallweit, Stephan, Michaux, Frank & Hojo, Teppei 2016 Typical velocity fields and vortical structures around a formula one car, based on experimental investigations using particle image velocimetry. *SAE Int. J. Passeng. Cars - Mech. Syst.* **9**, 754–771.

Newbon, Joshua, Sims-Williams, David & Dominy, Robert 2017 Aerodynamic analysis of grand prix cars operating in wake flows. *SAE Int. J. Passeng. Cars - Mech. Syst.* **10**, 318–329.

Nishino, Takafumi, Roberts, Graham T. & Zhang, Xin 2007 Vortex shedding from a circular cylinder near a moving ground. *Physics of Fluids* **19** (2), 025103.

Pasquetti, R. 2005 Spectral vanishing viscosity method for les: sensitivity to the svv control parameters. *Journal of Turbulence* **6**.

Pasquetti, Richard 2006 Spectral vanishing viscosity method for large-eddy simulation of turbulent flows. *Journal of Scientific Computing* **27** (1-3), 365–375.

Pasquetti, R., Séverac, E., Serre, E., Bontoux, P. & Schäfer, M. 2008 From stratified wakes to rotor–stator flows by an svv–les method. *Theoretical and Computational Fluid Dynamics* **22** (3-4), 261–273.

Patera, Anthony T 1984 A spectral element method for fluid dynamics: Laminar flow in a channel expansion. *Journal of Computational Physics* **54** (3), 468 – 488.

Pegrum, J.M. 2006 Experimental study of the vortex system generated by a formula front wing. PhD thesis, Imperial College London.

Persson, P.O. & Peraire, J. 2009 Curved mesh generation and mesh refinement using Lagrangian solid mechanics. In *Proc. 47th AIAA Aerospace Sciences meeting*.

Persson, Per-Olof & Peraire, Jaime 2006 *Sub-Cell Shock Capturing for Discontinuous Galerkin Methods*. American Institute of Aeronautics and Astronautics.

Piccioni, Carlo Fabio, Cianetti, Filippo & Paolotti, Alessio 1997 Numerical investigations on the front fender of a motorcycle. In *SAE Technical Paper*. SAE International.

Piola, Giorgio 2017*a* https://www.motorsport.com/f1/photo/main-gallery/ferrari-f2008-and-f60-top-view-comparison-11440683/?sz=&y=2009&s=-6&oft=363&id=11440683&i=338.

Piola, Giorgio 2017*b* https://www.motorsport.com/f1/photos/main-gallery/?r=164459&e=575440&y=2002&event_type_id=giorgio-piola-archive.

Pirozzoli, Sergio, Orlandi, Paolo & Bernardini, Matteo 2012 The fluid dynamics of rolling wheels at low reynolds number. *Journal of Fluid Mechanics* **706**, 496–533.

Prandtl, L. 1920 Göttinger wind tunnel for testing aircraft models.

Prince, Justin 2015 Coupled 1D-3D simulation of flow in subway transit networks. PhD thesis, Imperial College London.

Purvis, AR 2003 The wake behind a deformable racing tyre. Master's thesis, Cranfield University.

Rao, A., Passaggia, P.-Y., Bolnot, H., Thompson, M.C., Leweke, T. & Hourigan, K. 2012 Transition to chaos in the wake of a rolling sphere. *Journal of Fluid Mechanics* **695**, 135–148.

Rao, Anirudh, Thompson, MC, Leweke, Thomas & Hourigan, Kerry 2015 Flow past a rotating cylinder translating at different gap heights along a wall. *Journal of Fluids and Structures* **57**, 314–330.

REICHL, P., HOURIGAN, K. & THOMPSON, M. C. 2005 Flow past a cylinder close to a free surface. *Journal of Fluid Mechanics* **533**, 269–296.

Rider, Bill 2014 Lessons from the history of cfd.

Rigas, G, Oxlade, AR, Morgans, AS & Morrison, JF 2014 Low-dimensional dynamics of a turbulent axisymmetric wake. *Journal of Fluid Mechanics* **755**, R5.

Rocco, G. & Sherwin, S. J. 2015 The role of spanwise forcing on vortex shedding suppression in a flow past a cylinder. *Fluid Mechanics and its Applications* **107**, 105–110.

Rocco, G., Zaki, T. A., Mao, X., Blackburn, H. M. & Sherwin, S. J. 2015 Floquet and transient growth stability analysis of a flow through a compressor passage. *AEROSPACE SCIENCE AND TECHNOLOGY* **44**, 116–124.

Roshko, Steinolfson & Chattoorgoon 1975 Flow forces on a cylinder near a wall or near another cylinder. In *Second US Conference on Wind Engineering Research*.

Roshko, Anatol 1954 On the drag and shedding frequency of two-dimensional bluff bodies. *Tech. Rep.*. California Institute of Technology.

Rossow, Vernon J. 1999 Lift-generated vortex wakes of subsonic transport aircraft. *Progress in Aerospace Sciences* **35** (6), 507 – 660.

Rouméas, Mathieu, Gilliéron, Patrick & Kourta, Azeddine 2009 Analysis and control of the near-wake flow over a square-back geometry. *Computers and Fluids* **38** (1), 60 – 70.

Saddington, A. J., Knowles, R. D. & Knowles, K. 2007 Laser doppler anemometry measurements in the near-wake of an isolated formula one wheel. *Experiments in Fluids* **42** (5), 671.

Sagaut, Pierre 2001 *Large Eddy Simulation for Incompressible Flows*. Springer Berlin Heidelberg.

Salati, L. 2012 Detached eddy simulations on a fully exposed rotating wheel in contact with a moving ground. Master's thesis, University of New South Wales.

Sardou, Max 1988 The sensitivity of wind-tunnel data to a high-speed moving ground for different types of road vehicles. In *SAE Technical Paper*. SAE International.

Satti, Rajani, Li, Yanbing, Shock, Richard & Duncan, Brad 2011 *Computational Analysis of a Wingtip Vortex in the Near-Field using LBM-VLES Approach*. American Institute of Aeronautics and Astronautics.

Satti, Rajani, Li, Yanbing, Shock, Richard & Noelting, Swen 2012 Unsteady flow analysis of a multi-element airfoil using lattice boltzmann method. *AIAA Journal* **50** (9), 1805–1816.

Sawley, M.L. & Richter, R. 1997 Mumerical simulation of the flow around a formula 1 racing car. *EPFL Supercomputing Review* .

Schmid, P. J. & Henningson, D. S. 2001 *Stability and Transition in Shear Flows*, *Applied Mathematical Sciences*, vol. 142. Springer.

Serson, Douglas & Meneghini, JR 2015 Numerical study of wings with wavy leading and trailing edges. *Procedia IUTAM* **14**, 563–569.

Serson, D, Meneghini, JR & Sherwin, SJ 2016 Velocity-correction schemes for the incompressible navier-stokes equations in general coordinate systems. *Journal of Computational Physics* **316**, 243–254.

Severac, E. & Serre, E. 2007 A spectral vanishing viscosity for the les of turbulent flows within rotating cavities. *J. Comput. Phys.* **226** (2), 1234–1255.

Sherwin, S.J. & Casarin, M. 2001 Low-energy basis preconditioning for elliptic substructured solvers based on unstructured spectral/hp element discretization. *J. Comp. Phys* **171**, 394–417.

Sims-Williams, David 2001 Self-excited aerodynamic unsteadiness associated with passenger cars. PhD thesis, Durham University.

Somerfield, Matthew 2017 http://www.somersf1.co.uk/2014/04/bahrain-post-race-test-technical-image.html.

Spalart, Philippe R. 1998 Airplane trailing vortices. *Annual Review of Fluid Mechanics* **30** (1), 107–138.

Sprot, A. J., Minto, J. B., Sims-Williams, D. B. & Dominy, R. G. 2011 Aerodynamic investigation on the effect of varying through-hub flow on a formula one front wheel assembly. *SAE Int. J. Passeng. Cars – Mech. Syst.* **4**, 929–944.

Sprot, A. J., Sims-Williams, D. B. & Dominy, R. G. 2012 The aerodynamic characteristics of a fully deformable formula one wind tunnel tyre. *SAE Int. J. Passeng. Cars - Mech. Syst.* **5**, 1026–1041.

Stapleford, W. R., Carr, G. W. & Association., Motor Industry Research 1969 *Aerodynamic characteristics of exposed rotating wheels*. Lindley [England]: Motor Industry Research Association.

Stewart, B. E., THOMPSON, M. C., LEWEKE, T. & HOURIGAN, K. 2010*a* Numerical and experimental studies of the rolling sphere wake. *Journal of Fluid Mechanics* **643**, 137–162.

Stewart, B. E., Thompson, M. C., Leweke, T. & Hourigan, K. 2010*b* The wake behind a cylinder rolling on a wall at varying rotation rates. *Journal of Fluid Mechanics* **648**, 225–256.

Sutton 2014 .

Szepessy, S. & Bearman, P. W. 1992 Aspect ratio and end plate effects on vortex shedding from a circular cylinder. *Journal of Fluid Mechanics* **234**, 191–217.

Tadmor, Eitan 1989 Convergence of spectral methods for nonlinear conservation laws. *SIAM Journal on Numerical Analysis* **26** (1), 30–44.

Taneda, Sadatoshi 1965 Experimental investigation of vortex streets. *Journal of the Physical Society of Japan* **20** (9).

Thompson, D.H. 1983 Aerodynamics note 421 : A flow visualization study of tip vortex formation. *Tech. Rep.*. Defence Science and Technology Organisation Aeronautical Research Laboratories, Melbourne Australia.

Turner, Michael 2017 High-order mesh generation for cfd solvers. PhD thesis, Imperial College London.

Turner, Michael, Moxey, David, Sherwin, Spencer J & Peiró, Joaquim 2016 Automatic generation of 3d unstructured high-order curvilinear meshes. In *Proceedings of the European Congress on Computational Methods in Applied Sciences and Engineering*.

Turner, M., Peiró, J. & Moxey, D. 2017 Curvilinear mesh generation using a variational framework. Under review in Comput. Aided Design.

Tzortzis, Konstantinos N, Roney, Caroline H, Qureshi, Norman A, Ng, Fu Siong, Lim, Phang Boon, Sherwin, Spencer J, Peters, Nicholas S & Cantwell, Chris D 2015 Influence of left atrial geometry on rotor core trajectories in a model of atrial fibrillation .

Uzun, Ali & Hussaini, M. Yousuff 2010 Simulations of vortex formation around a blunt wing tip. *AIAA Journal* **48** (6), 1221–1234.

Uzun, Ali, Hussaini, M. Yousuff & Streett, Craig L. 2006 Large-eddy simulation of a wing tip vortex on overset grids. *AIAA Journal* **44** (6), 1229–1242.

Vdovin, Alexey 2013 Investigation of aerodynamic resistance of rotating wheels on passenger cars. Master's thesis, Chalmers University of Technology, Gothenburg, Sweden.

Vdovin, Alexey, Bonitz, Sabine, Landstrom, Christoffer & Lofdahl, Lennart 2013 Investigation of wheel ventilation-drag using a modular wheel design concept. *SAE Int. J. Passeng. Cars - Mech. Syst.* **6**, 308–315.

Vdovin, Alexey, Lofdahl, Lennart & Sebben, Simone 2014 Investigation of wheel aerodynamic resistance of passenger cars. *SAE Int. J. Passeng. Cars - Mech. Syst.* **7**, 639–645.

Vermeire, B.C., Witherden, F.D. & Vincent, P.E. 2017 On the utility of {GPU} accelerated high-order methods for unsteady flow simulations: A comparison with industry-standard tools. *Journal of Computational Physics* **334**, 497 – 521.

Volino, Pascal & Thalmann, N Magenat 1998 The spherigon: a simple polygon patch for smoothing quickly your polygonal meshes. In *Computer Animation 98. Proceedings*, pp. 72–78. IEEE.

VonNeumann, J. & Richtmyer, R. D. 1950 A method for the numerical calculation of hydrodynamic shocks. *Journal of Applied Physics* **21** (3), 232–237.

Vos, Peter E. J., Chun, Sehun, Bolis, Alessandro, Eskilsson, Claes, Kirby, Robert M. & Sherwin, Spencer J. 2011 A generic framework for time-stepping pdes: General linear methods, object-oriented implementations and applications to fluid problems. *International Journal of Computational Fluid Dynamics* **25**, 107–125.

Wang, Z.J., Fidkowski, Krzysztof, Abgrall, Rémi, Bassi, Francesco, Caraeni, Doru, Cary, Andrew, Deconinck, Herman, Hartmann, Ralf, Hillewaert, Koen, Huynh, H.T., Kroll, Norbert, May, Georg, Persson, Per-Olof, van Leer, Bram & Visbal, Miguel 2013 High-order cfd methods: current status and perspective. *International Journal for Numerical Methods in Fluids* **72** (8), 811–845.

Wäschle, Alexander 2007 The influence of rotating wheels on vehicle aerodynamics - numerical and experimental investigations. In *SAE Technical Paper*. SAE International.

Wäschle, Alexander, Cyr, Stephane, Kuthada, Timo & Wiedemann, Jochen 2004 Flow around an isolated wheel - experimental and numerical comparison of two cfd codes. In *SAE Technical Paper*. SAE International.

Wieselsberger, C. 1921 New data on the laws of fluid resistance. *Tech. Rep.*. National Advisory comittee for aeronautics.

Wikipedia 2017 https://en.wikipedia.org/wiki/mclaren_m2b.

Williams, Samuel, Waterman, Andrew & Patterson, David 2009 Roofline: An insightful visual performance model for multicore architectures. *Commun. ACM* **52** (4), 65–76.

Wittmeier, Felix, Kuthada, Timo, Widdecke, Nils & Wiedemann, Jochen 2014 Model scale based process for the development of aerodynamic tire characteristics. In *SAE Technical Paper*. SAE International.

Wolf-Heinrich Hucho, Gino Sovran 1993 Aerodynamics of road vehicles. *Annual Review of Fluid Mechanics* **25** (1), 485–537.

Xiu, D., Sherwin, S. J., Dong, S. & Karniadakis, G. E. 2005 Strong and auxiliary forms of the semi-lagrangian method for incompressible flows. *Journal of Scientific Computing* **25** (1), 323–346.

Xu, Chuanju 2006 Stabilization methods for spectral element computations of incompressible flows. *Journal of Scientific Computing* **27** (1-3), 495–505.

Xu, Hui, Hall, Philip & Sherwin, Spencer 2014 Effect of curvature modulation on gortler vortices in boundary layers. In *APS Meeting Abstracts*.

Xu, Hui, Lombard, Jean-Eloi W. & Sherwin, Spencer J. 2017*a* Influence of localised smooth steps on the instability of a boundary layer. *Journal of Fluid Mechanics* **817**, 138–170.

Xu, Hui, Mughal, Shahid M, Gowree, Erwin R, Atkin, Chris J & Sherwin, Spencer J 2017*b* Destabilisation and modification of tollmien–schlichting disturbances by a three-dimensional surface indentation. *Journal of Fluid Mechanics* **819**, 592–620.

Xu, H, Sherwin, SJ, Hall, P & Wu, X 2016*a* The behaviour of tollmien-schlichting waves undergoing small-scale localised distortions. *JOURNAL OF FLUID MECHANICS* **792**, 499–525.

Xu, Hui, Sherwin, Spencer J., Hall, Philip & Wu, Xuesong 2016*b* The behaviour of tollmien–schlichting waves undergoing small-scale localised distortions. *Journal of Fluid Mechanics* **792**, 499–525.

Yakovlev, S., Moxey, D., Sherwin, S. J. & Kirby, R. M. 2016 To CG or to HDG: a comparative study in 3D. *J. Sci. Comp.* **67** (1), 192–220.

Zdravkovich, Momchilo M 2003 *Flow around Circular Cylinders: Volume 2: Applications*, , vol. 2. Oxford university press.

Zdravkovich, M. M., Brand, V. P., Mathew, G. & Weston, A. 1989 Flow past short circular cylinders with two free ends. *Journal of Fluid Mechanics* **203**, 557–575.

Zdravkovich, M. M., Flaherty, A. J., Pahle, M. G. & Skelhorne, I. A. 1998 Some aerodynamic aspects of coin-like cylinders. *Journal of Fluid Mechanics* **360**, 73–84.

Zuhal, L.R. 2001 Formation and near-field dynamics of a wingtip vortex. PhD thesis, California Institute of Technology.

Zuhal, Lavi & Gharib, Morteza 2001 *Near field dynamics of wing tip vortices*. American Institute of Aeronautics and Astronautics.